Mesoporous Materials Supported Vernonia oil Esters and Their Immobilization with Silver Nanoparticles for Catalytic Applications

Gutta Gonfa

A Thesis Submitted to

Chemistry Department

Presented in Fulfillment of the Requirements for the Degree of Doctor of Philosophy (Inorganic Chemistry)

Addis Ababa University
Addis Ababa, Ethiopia

October 2018

Addis Ababa University

School of Graduate Studies

This is to certify that the thesis prepared by Gutta Gonfa entitled "**Mesoporous Materials Supported Vernonia Oil Esters and Their Immobilization with Silver Nanoparticles for Catalytic Applications**"and submitted in fulfillment for the degree of Doctor of Philosophy (Inorganic Chemistry) complies with the regulations of the university and meets the accepted standards with respect to originality and quality.

Signed by the Examining Committee

Examiner_____Signature_____Date_____

Examiner_____Signature_____Date_____

Advisor_____Signature_____Date_____

Advisor_____Signature_____Date_____

Abstract

In our world of rapidly increasing population and fast industrialization, design of value added and ecofriendly high performance organic–inorganic nanocomposites with higher stability for environmental remediation is becoming an active area of research in the field of inorganic material chemistry. The major objectives of this study are to design some typical surface hydrophobic ordered mesoporous nanocomposites by surface modification of their hydrophilic surfaces by supporting with native vernonia oil derivatives and immobilization by silver nanoparticles as potential heterogeneous catalyst for degradation of model organic dyes.

In the first part of this work, vernonia oil with unique natural epoxy moiety was extracted from *vernonia galamensis* seed, which was purified and then derivatized to more active forms such as vernolic acid and vernolic acid mono alkyl esters like methyl, ethyl and propyl esters as well as their mercapto imidazole functionalized derivatives, i.e. methyl ester-IFVAME, ethyl ester-IFVAEE and propyl ester-IFVAPE. The presences of the functional groups were confirmed by FT-IR, ^{1}H and ^{13}C NMR spectroscopy and CHNS elemental analysis. In the second part of this work, vernolic acid methyl ester-VAME, and its mercapto imidazole functionalized (IFVAME) derivatives were supported on three types of ordered mesoporous nanomaterials with different surface properties and pore sizes: OMMs: Al-MCM-41 (Si/Al=3 & 15), SBA-15 & periodic mesoporous organo silica-PMO. The supported materials were studied by powder X ray diffraction, thermogravimetric analysis, FT-IR spectroscopy and nitrogen sorption isotherms. In the third part of this work, silver nanoparticles were synthesized on VAME and IFVAME supported Al-MCM-41, SBA-15, and PMO. The formations of the silver

nanoparticles were confirmed from wide angle powder XRD and the final distribution of the metal nanoparticles were studied using Transmission Electron Microscopy. Finally, the potential catalytic applications of Ag-impregnated mOMMs were tested for degradation of model organic dyes (methyl orange and methylene blue) which was found to be promising.

Acknowledgements

First of all, I would like to express my sincere gratitude and deepest respect to my supervisors, Dr. Yonas Chebude and Prof. Isabel Diaz for their thoughtful guidance, continuous supervision, valuable comments and encouragement through all the stages of this thesis. Really, I am very thankful for their utmost dedication in providing research facilities and materials necessary for my research work here including the great support for further provision of scientific instruments for running TGA, nitrogen sorption isotherms, CHNS analysis, TEM and mesoporous materials at the Instituto de Catálisis y Petroleoquímica, CSIC, Madrid, Spain to generate valuable data.

My sincere thanks go to Prof.Negussie Reta and Prof. V.J.T Raju for their thoughtful comments and encouragements. I am also thankful to Prof. Ermias Dagne and his research group for running NMR and UV-Vis measurements, Prof. Wendimagegn Mamo and his research group for providing research facilities, thoughtful comments and encouragements, Dr.Negash Getachew for running Powder X-ray diffraction and his encouragement, and Dr. Tegene Desalegn for his valuable comments at the beginning of my research work.

I am also very thankful to my friends of the group Dr.Taju Sani, Dr.Lijalem Ayele, Dr. Kiros Guesh, and Dr. Wendimagegn Mammo, Tesfaye Haile, Masresha Amare and Yaregal Awoke for their support, encouragement, and constructive suggestions throughout my research work. Here, a very special thanks is also extended to Yaregal Awoke for providing me with additional mesoporous materials from Prof. Isabel Diaz at the Instituto de Catálisis y Petroleoquímica, CSIC, Madrid, Spain. I also thank all the

PhD students of organic stream and other streams and all laboratory technicians of the Department of Chemistry of Addis Ababa University for their encouragement and technical supports.

I would also like to express my gratitude to Addis Ababa University, Department of Chemistry and its staff members for their unreserved cooperation. I also want to thank Jimma University for giving me the study leave to pursue my PhD at AAU and for financial support.

Last but not least, I am very thankful to my relatives, my mother, brothers and sisters for their love and encouragement and also my very special thanks extends to my family, my wife Mitike Haile, my daughters, Hawi Gutta, Sena Gutta and Sifan Gutta for their, love, encouragement, technical support, understanding and endless patience.

Table of Contents

Abstract iii

Acknowledgements v

List of Abbreviations xi

List of Figures xiv

List of Schemes xvii

List of Tables xix

1. Introduction 1

1.1. Background of the study 1

1.1.1. *Veronica Galamensis* plant seed oil 2

1.1.2. Structure, composition, reactivity and derivatizations of Vernonia oil 5

1.2. Ordered mesoporous materials 10

1.2.1. General overview of ordered mesoporous materials (OMMs) 10

1.2.2. Ordered mesoporous materials of this work 17

1.2.3. Modification of ordered mesoporous materials in this work 19

1.3. Immobilization of silver nanoparticles on OMMs 20

1.3.1. General overview of metal nanoparticles 20

1.3.2. Immobilization of silver nanoparticles on modified OMMs (AgmOMMs) and their catalytic test 22

1.4. Significance of the study 22

1.5. Objective of the study 23

1.6. References 24

2. Characterization Techniques 30

2.1. Nuclear Magnetic Resonance Spectroscopy (NMR) 30

2.2. CHNS Elemental Analysis....32
2.3. Fourier Transform Infrared Spectroscopy (FT-IR) 32
2.4. Powder X-ray Diffraction (PXRD) 33
2.5. Thermogravimetric analysis (TGA) 35
2.6. Nitrogen Adsorption-desorptions Isotherms....36
2.7. Transmission Electron Microscopey (TEM)....43
2.8. UV-Vis Spectroscopy....44
2.9. References....46
3. Materials and Methods....48
3.1. Extraction and Purification of Vernonia Oil....48
3.1.1. Conventional refining method....50
3.1.2. Solid phase extraction....51
3.2. Derivitization of Vernonia Oil....53
3.2.1. Derivitization to Vernolic Acid (VA)....53
3.2.2. Derivatization to metyl, ethyl and propyl esters (VAME/VAEE/VAPE)....54
3.2.3. Functionalization with mercaptoimidazole groups....56
3.3. Surface Modification of OMMs with VAME and IFVAME....56
3.3.1. Suport of Vernolic Acid Methyl Ester (VAME) on ordered mesoporous material (OMMs)....56
3.3.2. Loading of Ag on modified OMMs....57
3.4. Test for catalytic activity of modified OMMs....58
3.5. References....60
4. Results and Discussion....63
4.1. Characterization of crude (CVO) and neutral vernonia oil (NVO)....63

4.1.1. ^{1}H and ^{13}C NMR measurements of CVO and NVO 64
4.1.2. FT-IR studies on CVO and NVO 69
4.2. Characterizations of Vernolic Acid (VA) 70
4.2.1. ^{1}H NMR and ^{13}C NMR spectral studies of VA 70
4.2.2. FT-IR Spectral studies of VA 72
4.3. Characterizations of Vernolic Acid Alkyl Ester (VAME/VAEE/VAPE) 73
4.3.1. ^{1}H and ^{13}C NMR Spectral studies of VAME/VAEE/VAPE 74
4.3.2. FT-IR studies of VAME/VAEE/VAPE 78
4.4. Characterization of mercapto imidazole functionalized VAME (IFVAME) 79
4.4.1. ^{1}H and ^{13}C NMR characterization of IFVAME 81
4.4.2. FT-IR studies of IFVAME 83
4.4.3. CHNS Elemental Analysis of IFVAME and VAME 84
4.5. References 86
5. Results and Discussion on Surface Modification of OMMs with VAME and IFVAME 89
5.1. Surface modification of Al-MCM-41(3 and 15), SBA-15 and PMO with VAME 89
5.1.1. FT-IR Spectral Analysis 90
5.1.2. Powder XRD studies 93
5.1.3. Thermogravimetric Analysis 94
5.1.4. Nitrogen adsorption-desorption isotherms 99
5.2. Surface modification of Al-MCM-41(3 and 15), SBA-15 and PMO with IFVAME 104
5.2.1. FT-IR Spectral Analysis 105
5.2.2. Powder XRD studies 107
5.2.3. Thermogravimetric Analysis 109
5.2.4. Nitrogen adsorption-desorption Isotherms 111
5.3. References 114
6. Results and Discussion on Loading of Ag on VAME/IFVAME Modified OMMs 116
6.1. Loading of Ag on VAME supported MCM (3 &15)1, SBA1 and PMO1 116

6.1.1. FT-IR Spectral Analysis 117
6.1.2. Powder XRD Studies 119
6.1.3. Transmission Electron Microscopy Studies 120
6.2. Loading of Ag on IFVAME Supported SBA1 and PMO1 126
6.2.1. FT-IR Spectral Analysis 126
6.2.2. Powder XRD studies 128
6.2.3. Transmission Electron Microscopy Studies 129
6.3. Catalytic Tests on Ag modified OMMs 132
6.3.1. Photocatalytic degradation test of MO by AgmOMMs 133
6.3.2. Chemodegradation of Methylene blue by Silver nanocomposite 136
6.4. References 139
7. Conclusion 142
8. Appendices 145

List of Abbreviations

Al- MCM-41	Aluminosilica Mobil composition matter number 41(Si/Al=3& 15)
Ag-IFVAME-OMMs	Ag immobilized on IFVAME supported ordered mesoporous materials
AgmOMMs	VAME supported & silver nanoparticles immobilized ordered mesoporous materials
AgifmOMMs	IFVAME supported & silver nanoparticles immobilized ordered mesoporous materials
AgNPs	Silver nanoparticles
AgifmOMMs	Ag immobilized on IFVAME supported ordered mesoporous materials
AgifmPMO	Ag immobilized on IFVAME supported PMO
AgifmSBA1	Ag immobilized on IFVAME supported on SBA1
AgmOMMs	Ag immobilized on VAME supported ordered mesoporous materials
AgmMCM (3)1	Ag immobilized on 13 % VAME supported Al-MCM-41 (Si/Al=3)1
AgmMCM (15)1	Ag immobilized on 13 % VAME supported Al-MCM-41 (Si/Al=15)1
AgmSBA1	Ag immobilized on 13% VAME supported SBA-15(1)
AgmPMO1	Ag immobilized on 13% VAME supported PMO1
AOP	Advanced Oxidation Process
BET	Brunauer-Emmett-Teller
BJH	Barrett-Joyner-Halenda
CVO	Crude Vernonia oil

CTAB	Cetyltrimethylammoniumbromide
DTG	Derivative Thermogravimetry
FT-IR	Fourier Transform Infrared Spectroscopy
FFA	Free Fatty Acid
IFVAME-OMM	Imidazole functionalized VAME supported on OMMs
IPA	Isopropyl alcohol
MOF	Metal-organic frame work
mMCM (3)	modified alumina silica mobil composition matter No 41(Si/Al=3))
mMCM (15)	modified alumina silica mobil composition matter No 41(Si/Al=15)
mPMO	modified periodic mesoporous organosilica
mSBA	modified Santa Barbara Amorphous No 15
MB	Methylene Blue
MO	Methylene Orange
NVO	Neutral Vernonia oil
OMMs	Ordered Mesoporous materials
PMO	Periodic Mesoporous organosilica
S_{BET}	BET Surface Area
SEM	Scanning Electron Microscope
Si-SBA-15	Siliceous Santa Barbara Amorphous No 15
TEM	Transmission Electron Microscope
TEOS,	Tetraethyl Orthosilicate
TGA	Thermogravimetric Analysis
TLC	Thin Layer Chromatography
UV-Vis	Ultraviolet-Visible spectroscopy

VA	Vernolic Acid
VAEE	Vernolic acid Ethyl Ester
VAME	Vernolic acid Methyl Ester
VAPE	Vernolic acid Propyl Ester
VAME-OMMs	Vernolic acid Methyl Ester supported on ordered mesoporous materials
VO	Vernonia Oil
PXRD	Powder X-ray Diffraction

List of Figures

Figure 1. 1: Regions and route of germplasm collection for *Vernonia galamensis* in Ethiopia [10]. 4

Figure 1. 2 *Vernonia Galamensis* plant (left side) and its seed (right side [19] 5

Figure 1. 3: a) Vernonia oil, b) vernolic acid and c) vernolic acid alkyl ester (R = CH_3, CH_2CH_3, or $CH_2CH_2CH_3$) 6

Figure 1. 4: Reactivity of Vernonia oil 6

Figure 1. 5: Framework and surface structure of ordered mesoporous aluminosilicate material .. 18

Figure 1. 6: Framework and surface structure of Pure Silica ordered mesoporous material 19

Figure 1. 7: The outer surface structure of PMO 19

Figure 2. 1: Bragg's scattering of X-rays from parallel planes with d representing inter-planar spacing 34

Figure 2. 2: Classification of physisorption isotherms [9] 37

Figure 2. 3: Classification of hysteresis loops [9] 39

Figure 4. 1: ^{1}H NMR (ppm, 400 MHz, $CDCl_3$) spectrum of NVO compared to that of CVO 65

Figure 4. 2: ^{13}C NMR spectrum of NVO compared to that of CVO 68

Figure 4. 3: FT-IR spectrum of NVO compared to that of CVO. 69

Figure 4. 4: ^{1}H NMR spectrum of vernolic acid (VA) (δppm, 400 MHz, $CDCl_3$). 71

Figure 4. 5: ^{13} C NMR spectrum of vernolic acid (δ ppm, 400 MHz, $CDCl_3$) 72

Figure 4. 6:.FT-IR spectra of VA (red-top) and VO (black bottom) 73

Figure 4. 7: The ^{1}H NMR spectra δ (ppm), 400 MHz, $CDCl_3$) of VAME/VAEE/VAPE. 76

Figure 4. 8: ^{13}C NMR spectra (δ (ppm), 400 MHz, $CDCl_3$) of VAME /VAEE and VAPE..... 77

Figure 4. 9: FT-IR spectra of NVO and vernolic acid alkyl (methyl/ethyl/ propyl) esters (Top to bottom NVO (a), VAPE (b), VAME (c) & VAEE (d)..... 79

Figure 4. 10: a) ^{1}H NMR and b) ^{13}C NMR spectra of IFVAME compared to that of VAME..... 82

Figure 4. 11: FT-IR spectrum of VAME (top red) and IFVAME (bottom black)..... 83

Figure 5. 1: FT-IR Spectra of: (A) Al-MCM-41 (3) in red solid line and (15) in red dashed line, and their modified ones in green. (B) SBA-15 in red solid line and PMO in red solid line, and their modified ones in green. VAME is also included in black line in both cases for comparison. 92

Figure 5.2: Wide angle PXRD patterns of VAME supported on (A) Al-MCM-41(3) and Al-MCM-41(15) and (B) on SBA-15 and PMO with a 0.13 VAME/VAME+OMM ratio..... 93

Figure 5. 3: Low angle PXRD patterns of VAME supported on (A) Al-MCM-41 (3) and Al-MCM-41 (15) and (B) on SBA-15 and PMO with a 0.13 VAME/VAME+OMM ratio..... 93

Figure 5. 4: TGA and derivatives of (A) mMCM (3) and (B) mMCM (15), at varying loading ratios of VAME to OMMs. 96

Figure 5. 5: TGA and DTG of (A) mSBA1-4 and (B) mPMO1-3, at varying loading ratios of VAME to OMM. 97

Figure 5. 6: N_2 Adsorption-desorption isotherms of the VAME supported on (A) MCM (3) and (B) mMCM (15). 100

Figure 5**. 7**: N_2 Adsorption-desorption isotherms of the VAME supported on (A) SBA-15, and (B) PMO..... 101

Figure 5. 8 FT-IR spectra of ifm- OMMs compared to that of OMMs: (A) Al-MCM-41(3) in red solid line and (15) in blue line, and their modified ones in red and blue dashed lines, respectively. (B) SBA-15 in black solid line and PMO in blue solid line, and their modified ones in black and

blue dashed line, respectively. VAME also included in purple line in both case for comparison. 106

Figure 5. 9 Wide angle PXRD pattern of: (A) IFVAME supported MCM (3&15) compared with their pristine materials and (B) IFVAME supported SBA & PMO compared with their pristine materials. 108

Figure 5. 10: Low angle Powder XRD of ifm-OMMs at low angle mode. 108

Figure 5. 11: TGA/DTG curves of: (A) ifm-MCM (3) and ifm-MCM (15) and (B) ifm-SBA and ifm-PMO. 110

Figure 5. 12: Nitrogen sorption isotherms of (A) ifm-MCM (3) and ifm-MCM (15); and (B) ifm-SBA and ifm-PMO. 112

Figure 6. 1**:** FT-IR Spectra of AgmOMM1 118

Figure 6. 2: Powder XRD of AgmSBA1, AgmPMO1, AgmMCM (3& 15)1. 119

Figure 6. 3: TEM micrographs of AgmMCM (3)1 at different direction and magnifications 121

Figure 6. 4: TEM images of AgmMCM (15)1 at outer and inner surfaces and different magnifications 122

Figure 6. **5:** TEM images of AgmSBA1 at varying surface and magnifications 123

Figure 6. 6**:** TEM images of AgmPMO1 at outer and inner surfaces and different magnifications 124

Figure 6. **7:** FT-IR of AgifmSBA and AgifmPMO1 nanocomposites compared to their precursors SBA1 and PMO1 127

Figure 6. 8**:** Wide angle Powder XRD pattern of AgifmSBA1 and AgifmPMO1. 128

Figure 6. 9**:** TEM images of AgifmSBA1 at outer surface and inner hexagonal symmetry pore channels of mesopore structure with different magnifications. 130

Figure 6. 10**:** TEM images of AgifmPMO1 at outer surface and inner hexagonal symmetry pore channels of mesopore structure with different magnifications. 131

Figure 6. 11**:** a) Structure of MO and b) UV-Vis Spectrum of MO 134

Figure 6. 12**:** UV-vis spectroscopy of MO after degradation test: a) by AgmMCM, AgmPMO and presence of only UV light compared with that of AgmSBA1 at preliminary test. b) by AgmSBA1 at varying time compared with that of its preliminary test result of AgmSBA1 135

Figure 6. 13: UV-Vis Spectrum of AgmSBA1 in 1M NaOH solution. 136

Figure 6. 14: a) UV-vs spectra of Methylene blue after degradation test by different AgmOMMs (catalyst compared with that of $NaBH_4$ and b) the resulted color changes 137

List of Schemes

Scheme 1. 1: Routes for the preparation of valuable products from vegetable oils. 7

Scheme 1. 2: Hydrolysis of vernonia oil 8

Scheme 1. 3: Esterification of vernonia oil 8

Scheme 1. 4: Transesterification of Vernonia oil 8

Scheme 1. 5: Thiolene coupling reaction [16] 9

Scheme 1. 6: Mechanism of thiolene coupling reaction [22] 10

Scheme 1. 7: Classification of Porous Materials 11

Scheme 1. 8: Hierarchical self-assembly of micelles forming MCM-41[23]. 12

Scheme 1. 9: a) Post synthesis functionalization of OMMs by grafting b) Co-condensation and c) Synthesis of PMO with a bridged organosilane [28] 16

Scheme 3. 1: Extraction, purification and hydrolysis of vernonia oil 49

Scheme3. 2: Summary of the procedure for the synthesis of the esters and their functionalization with mercapto imidazole 55

Scheme 3. 3: Surface Modification of OMM with VAME and IFVAME 57

Scheme 3. 4: Synthesis of Ag nanoparticles on the supported VAME/IFVAME on OMMs 58

Scheme 3.5: Test for photo/chemo degradation catalytic activity of AgmOMMs on model organic dyes (methyl orange and methylene blue) 59

Scheme 4. 1: Synthesis of Vernolic Acid by hydrolysis of Vernonia oil 70

Scheme 4. 2: Derivatization of VO (a) and VA (b) to VAME/VAEE/VAPE 74

Scheme 4. 3: Functionalization of VAME to form IFVAME. 81

Scheme 5. 1: The proposed reaction scheme for surface functionilization of OMMs with VAME 89

Scheme 5. 2: The proposed reaction scheme for supporting of VAME on OMMs 104

Scheme 5. 3: Scheme of the modification process in this section 105

Scheme 5. 4: Reaction scheme showing supporting of IFVAME on OMMs 113

Scheme 6. 1: Synthesis of AgNps by immobilization in-situ with metal salt in DMF solution. . 117

Scheme 6. 2: Synthesis of AgmOMMs by in-situ impregnation of metal salt 126

Scheme 6. 3: Synthesis of AgifmOMMs by in-situ impregnation of metal Salt. 132

Scheme 7. 1**:** Schemes showing sample support of vernonia oil derivatives on ordered mesoporous nanomaterials and Ag NPs immobilization (top side) and potentail catalytic

degradation test of methylene blue and methyl orange by the synthesized AgmOMM1 nanocomposites (bottom side) 144

List of Tables

Table 4. 1: ^{1}H NMR of crude (CVO) and neutral vernonia oil (NVO) 65

Table 4. 2: ^{13}C NMR spectra of crude (CVO) and neutral vernonia oil (NVO). 68

Table 4. 3: FT-IR Spectra of CVO and NVO. 69

Table 4. 4**:** Data of ^{1}H NMR Spectrum of VAEE & VAPE compared with VAME 76

Table 4. 5: Data of ^{13}C NMR of VAEE/VAPE and VAME 77

Table 4. 6: Summary of FT-IR spectral analysis of NVO, VAME, VAEE & VAPE 78

Table 5. 1: Surface modification of OMM: Al-MCM-41(3 and 15), SBA-15, PMO with VAME 90

Table 5. 2: FT-IR band assignments for m-MCM (3) 3, m-MCM (15) 3, m-SBA3 and m-PMO3. 92

Table 5. 3: Data of weight losses obtained from the TGA curves of mOMMs 98

Table 5. 4: Textural properties of VAME supported on OMMs 100

Table 5. 5: Supporting of OMMs with IFVAME using a mass ratio of 0.13 and 15 ml of n-hexane. 105

Table 5. 6: FT-IR Spectral Analysis of ifm-MCM (3), ifm-MCM (15), ifm-SBA and ifm-PMO. 107

Table 5. 7: Data of weight losses obtained from the TGA curves of ifmOMMs 110

Table 5. 8: Textural properties of IFVAME supported on OMMs (ifm-OMMs) 112

Table 6. 1**:** FT-IR band assignments for AgmMCM (3)1, AgmMCM (15)1, AgmSBA1 and AgmPMO1 118

Table 6. 2: FT-IR Spectral Analysis of AgifmOMMs (AgifmSBA & AgifmPMO) 127

1. Introduction

1.1. Background of the study

In the present world of high population growth and fast industrialization, environmental pollution is becoming a major problem and hence while designing material synthesis for the desired purpose in academic or commercial sectors, the environmental issues like the sustainability/or renewability, biodegradability/biocompatibility of chemicals or materials to be used or synthesized must be considered. The use of non-renewable, non-biodegradable petrochemicals (with rapidly increasing price) as starting materials or finished goods or the production of non-ecofriendly by-products during industrial processing is contributing much to environmental pollution. On top of this, there is dye effluent from the textile industry as one of the first major water pollutants next to agricultural waste. Report from World Bank showed that about 20 % of global industrial pollution comes from the textile industry, due to its higher consumption of water (1.6 million liters) for production of about 3600 types of chemicals like methyl orange and methylene blue by using more than 8000 chemicals [1, 2]. Various classical methods such as adsorption, sedimentation, coagulation, ultra-filtration, etc. have been used to treat such effluent. However, these methods generate secondary pollutants, which need further treatment. Advanced Oxidation Processes (AOP) on nanomaterials based heterogeneous photocatalysis/chemo-catalysis is currently an emerging technology for the treatment of organic dye effluent. In photocatalysis, semiconducting nanoparticles are used for photo-degradation of organic dyes. Such catalytic mechanism involves the photo excitations of electrons to form the excited electron-positive hole pairs. The excited

electron generates HO^* free radical, which together with the positive holes helps in the degradation of organic dyes [1, 3]. Many methods have been used to decrease the band gaps of semiconducting nanoparticles like the most widely investigated titanium oxide semiconducting nanoparticles, Recently silver nanoparticles have attracted much attention due to their lower band gap that facilitates the photodegradation of organic dyes both under UV and visible light via surface plasmon resonance mechanism [1, 3].

In order to have efficient catalytic performance in liquid media, high stability and dispersion capacity of silver nanoparticles is very important [1]. In this research, work attempt is made to use vernolic acid methyl ester and its mercapto imidazole derivative as a source of a surface active modifier of some ordered mesoporous materials, which are used for immobilization of silver nanoparticles as potential nanocatalyst for degradation of model organic dyes.

1.1.1. *Veronica galamensis* plant seed oil

Vegetable oils are green renewable natural resources attracting increasing research interest in academia and the chemical industry as oleochemicals to replace or blend with non-renewable petroleum-based petrochemicals.

Vegetable oils are triglycerides of long chain fatty acids which are a source of oleochemicals. Oleochemicals are derived from oil and fats like fatty acids, fatty alcohols, fatty amines, fatty acid alkyl esters, glycerols, etc. Oleochemicals are used in a wide range of applications, [4-8] i.e. surfactants, personal care, soaps, detergents, biodiesel, lubricants, and food additives.

Vernonia oil is a special type of vegetable oil mainly composed of triglycerides of vernolic acid with much more research interest because of its unique property of having naturally epoxidized moiety. Thus, a number of research works have been done to investigate the availability of the vernonia oil source (*Vernonia galamensis* plant seed), composition and structure of the oil, the chemistry and reactivity of the oil for modifications into the number of value-added chemicals for multipurpose applications [9-18].

The source of vernonia oil, *vernonia galamensis* plant is of sunflower family of the genus vernonia (Asteraceae), having about 1000 species in the world and 200 species in Africa of which about 50 species are found in Ethiopia. The subspecies *galamensis* grows in the wild in Eritrea, Ethiopia, Malawi, Tanzania, and Kenya.

Ethiopia is endowed with an indigenous *Vernonia galamensis* plant, which usually grows as a weed (ironweed). *Vernonia galamensis* subspecies *galamensis* variety *ethiopica* was first identified by Perdue in 1964 in eastern part of the country along the Harar-Jijiga road at 9°14' N and 42°35' E. Geographical locations of *Vernonia galamensis* sub-species *galamensis* varieties in Ethiopia are found at Gelemso (08° 49' N, 40° 31' E), Yirgalem (06° 42' N, 38° 21' E), Leku (06° 52' N, 38°.27' E), Melkabelo (09°.12' N,41° 25' E), Awassa (06° 52' N, 38° 27' E), Harar Zuria (09° 19' N, 42° 07' E), Areka (06° 48' N, 37° 43' E), Metta (09° 25' N, 41° 34' E) and Arsi-Negele (07°.00' N, 38° 35' E) as shown in figure 1.1 [10].

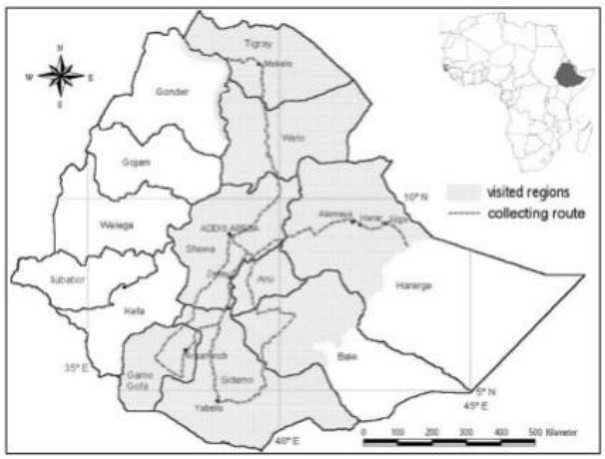

Figure 1. 1: Regions and route of germplasm collection for *Vernonia galamensis* in Ethiopia [10].

Due to its high oil and vernolic acid content and its relatively low shattering nature, the Vernonia seed plant subspecies, *galamensis variety ethiopica* has been the major focal point of research aimed at domestication and commercialization of the crop as a potential industrial oilseed crop for the export market for oleochemical industry and domestic uses. In the area of commercialization of the crop, some essential steps have been taken by the Ethiopian government to attract foreign investors/business firms for commercial production of vernonia oilseed (figure 1.2). The British firm Vernique Biotech has shown an interest in purchasing large quantities of vernonia oil by signing a material transfer agreement with Ethiopia's government in 2006 on the patent and use of the native vernonia seed. It is currently being cultivated at Adet Agricultural Research Center of the Amhara region of Ethiopia. Thus, the uses of such locally available, non-edible and eco-friendly renewable resources and their value-added products for industrial feedstock are the bases for sustainable development of developing countries.

Figure 1. 2 *Vernonia Galamensis* plant (left side) and its seed (right side [19]

The very important properties of *Vernonia galamensis* plant is that it can be grown at desert and semi-desert, non-arable land with sandy-loam soil that is non-competitive with food crops. Regarding geographical and climatic condition, it can be grown well with a location near the equator with a minimum rainfall of 200 mm per year at an elevation ranging from 700 to 2400 m and temperature ranges from 15-37 ºC.

1.1.2. Structure, composition, reactivity, and derivatizations of Vernonia oil

Vernonia oil is non-edible with a high potential substitute for petrochemicals which are non-renewable and non-ecofriendly with increasing price from time to time. As widely reported in the literature [13, 16-18], seeds from this plant contain about 40-42 % vernonia oil, with 73-80 % vernolic acid (figure 1.3).

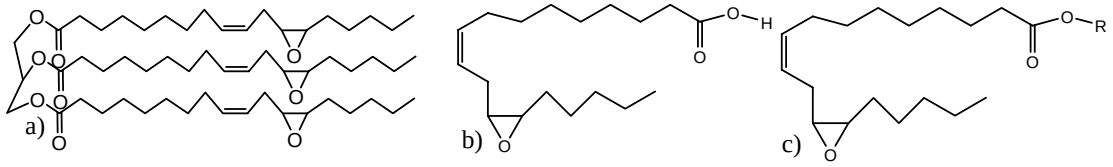

Figure 1. 3: a) Vernonia oil, b) vernolic acid and c) vernolic acid alkyl ester (R = CH_3, CH_2CH_3, or $CH_2CH_2CH_3$)

Vegetable oils in general and vernonia oil or its derivatives like vernolic acid and vernolic acids methyl esters, in particular, have many reactive active sites (figure 1. 3) and hence are important platform chemicals for the production of advanced functional materials for diverse applications in oleochemical industry by various modification reactions (figure 1.4).

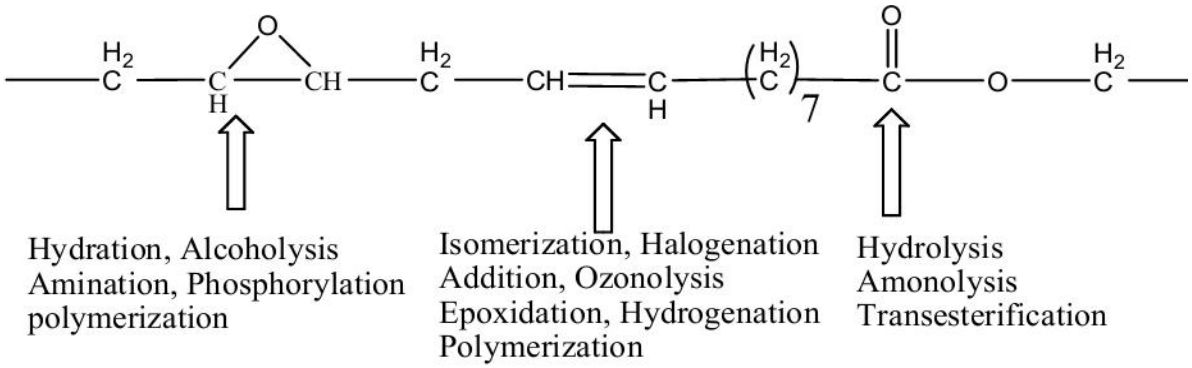

Figure 1. 4: Reactivity of Vernonia oil

Based on the reactive sites of vegetable oil in general and vernonia oil in particular, or its derivatives, many research works have been reported [4-18] on its modification. The flow chart below (scheme 1.1**)** summarizes the modifications of vegetable oil for the preparation of valuable products.

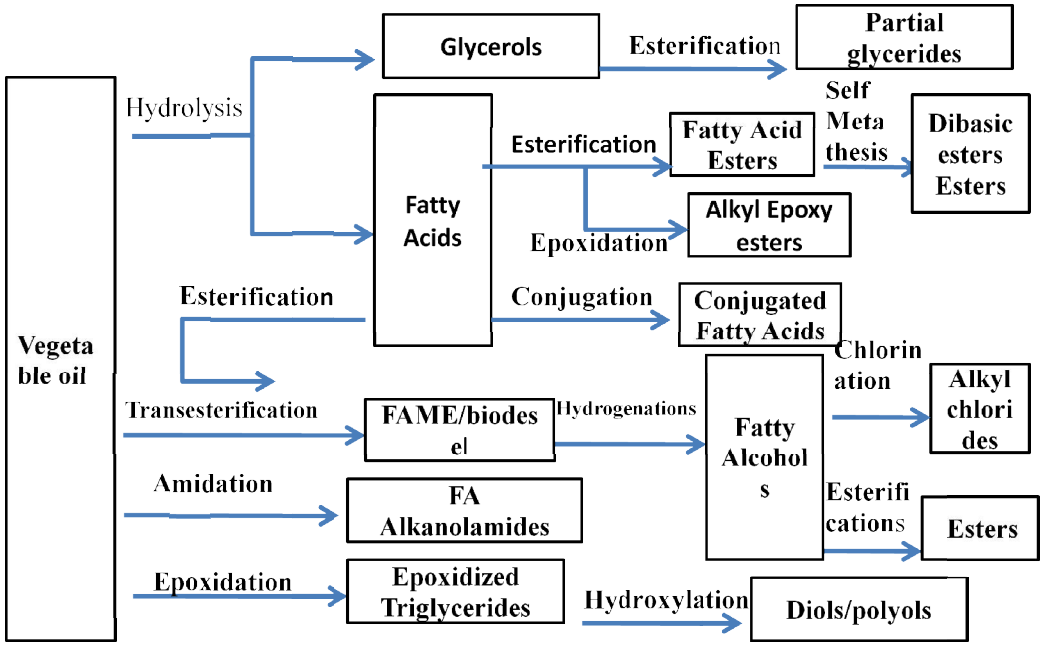

Scheme 1. 1: Routes for the preparation of valuable products from vegetable oils.

In the present work attempts were made for the modification of vernonia oil by hydrolysis, esterification, transesterification reactions on the ester carbonyl reactive site so as to get vernolic acid or vernolic acid methyl/ethyl/propyl ester and thiolene coupling reactions on the double bond active site of vernolic acid/methyl/ethyl/propyl ester for their functionalization with 2-mercapto-1-methyl imidazole. The reaction used for the modifications of Vernonia oil in this work includes the following:

Hydrolysis reaction is the conversion of triglyceride esters into fatty acids by saponification and acidification reaction. Based on this, the conversion of neutralized VO into VA was carried out by saponification and then acidification reactions as shown in scheme 1.2.

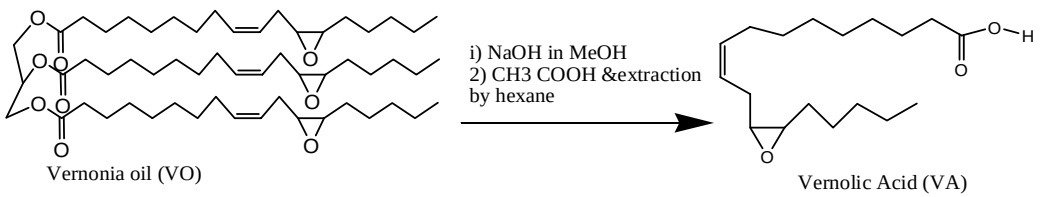

Scheme 1. 2: Hydrolysis of vernonia oil

The esterification reaction is the reaction of an acid with alcohol to get esters**.** In this project, it is the conversion of vernolic acid with methanol/ethanol/propanol in acidic or basic catalyst to get vernolic acid alkyl esters (methyl/ethyl/propyl ester) (scheme 1. 3).

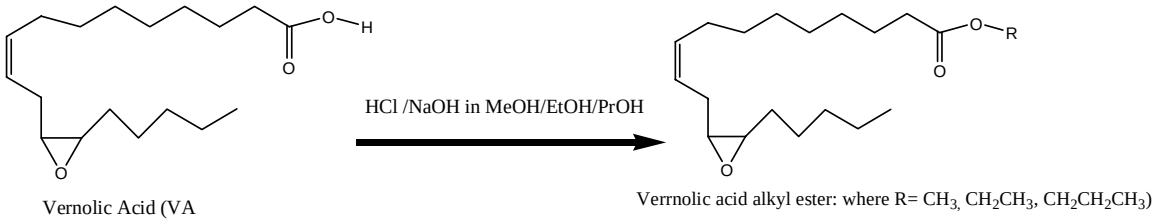

Scheme 1. 3: Esterification of vernonia oil

Transesterification is the conversion of triglycerides of oils into monoesters**.** Consequently, by transesterification reaction, NVO is directly converted into VAME/VAEE/VAPE in the presence of ethanol/ethanol/propanol and acidic or basic catalyst (Scheme 1.4). This is done because plant oils with linear carbon chains and carboxylic acid end groups as well as double bonds in different positions and numbers with high purity are very useful renewable raw materials [20].

Scheme 1. 4: **Transesterification of Vernonia oil**

Thiolene coupling reaction is the reaction of alkenes or unsaturated triglycerides/fatty acids with thiol under UV irradiation. Bromberg, L et al. 2010 [21] reported the synthesis of the oleic acid-2-mercaptoimidazole conjugate by thiol-ene coupling reaction as shown in scheme 1.5. It is one of the most efficient and simple modifications for alkenes or unsaturated esters/fatty acids. .

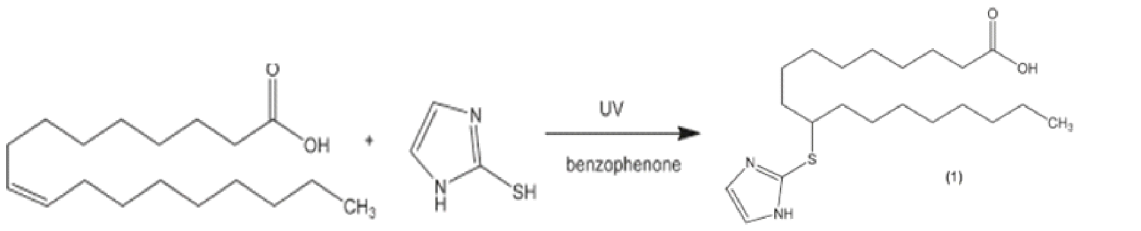

Oleic acid 2-mercaptoimidazole Oleic acid-2-mercaptoimidazole conjúgate

Scheme 1. 5: Thiolene coupling reaction [16]

The earliest report on the thiolene to unsaturated compounds dates back to 1905 in which Posner discussed that mercaptans add to double bonds in an anti-Markonkov manner and the structure of the unsaturated compounds strongly influences the product of the reaction. The general reported mechanism of thiolene coupling reaction is as shown in scheme 1.6.

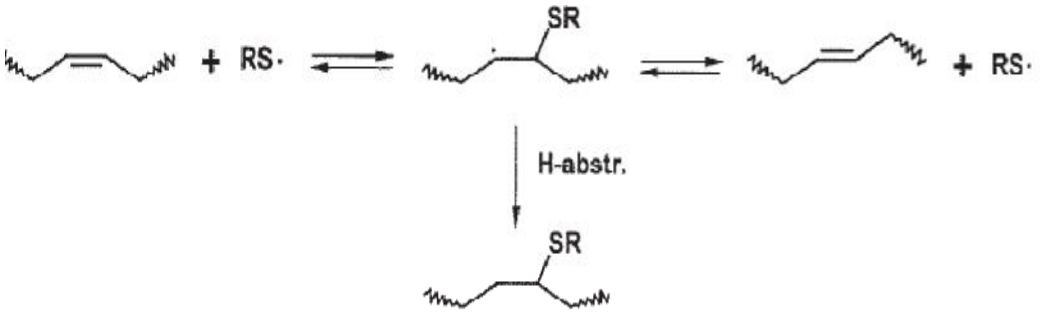

Scheme 1. 6: Mechanism of thiolene coupling reaction [22]

Reports on the relative reactivity shows that it increases if the radical is stabilized by resonance or electron donating groups on the olefins and also terminal double bonds are more reactive than internal ones for open chain olefins and increase of strain increases reactivity for cycloalkenes [20].

In this project, attention has been given on the use of VAME/VAEE/VAPE and its imidazole derivatives, as surface functional and stabilizing agents for surface modification of ordered mesoporous silica materials on which silver nanoparticles are immobilized with potential catalytic applications. The following section gives a brief discussion of ordered mesoporous materials.

1.2. Ordered mesoporous materials

1.2.1. A general overview of ordered mesoporous materials (OMMs)

Porous solids are materials with pores or voids formed during crystallization or subsequent treatments. They are of academic and technological interest due to their ability to interact with atoms, ions and molecules not only at their surfaces but throughout the bulk of the material and have been used a long time in human history as adsorbent

and molecular sieves. In this section, a brief overview of classes of porous materials, their synthetic techniques, post-synthesis modifications, and applications in heterogeneous catalysis will be described. Based on their pore size or framework structure nanoporous materials can be generally classified into various groups as shown in scheme 1.7.

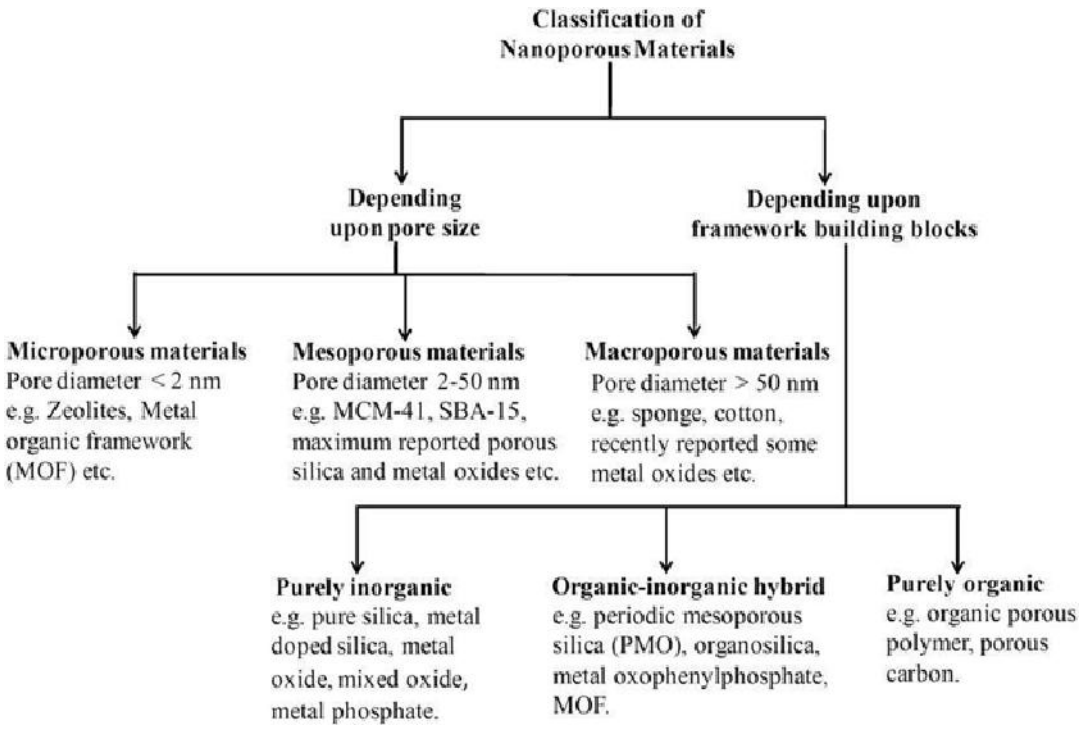

Scheme 1. 7: Classification of Porous Materials

Silica and organosilica ordered mesoporous materials represent a unique class of silica-based materials which possess high specific surface area (S_{BET}>700 m^2 g^{-1}), large pore volume, uniform pore size (2-50 nm), thicker pore walls with high hydrothermal stability, uniform pore opening with narrow pore size distribution and rich silanol surface chemistry. The hexagonal arrangement structure is obtained from hierarchically ordered pore system by agglomeration of a uniform array of micelles as shown in scheme 1.8**.**

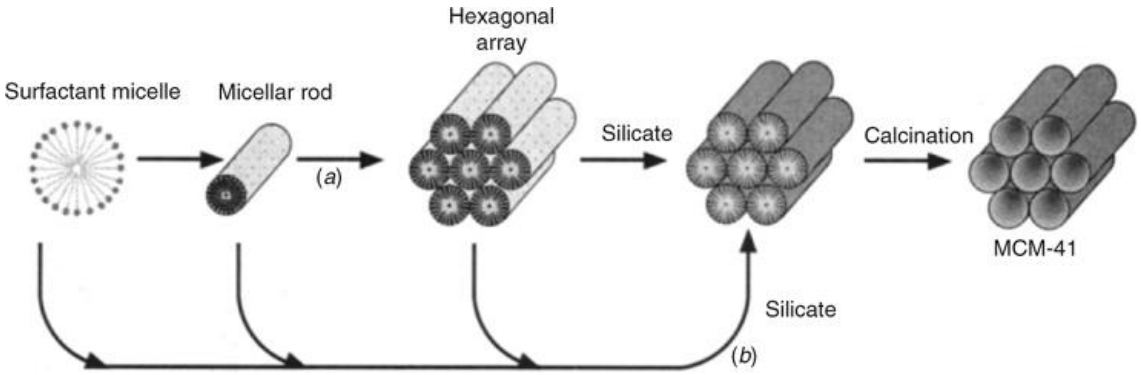

Scheme 1. 8: Hierarchical self-assembly of micelles forming MCM-41[23]**.**

Due to their important properties mentioned above, OMMs have received widespread interest as potential supports for catalysis, separation, selective adsorption, novel functional materials, and used as hosts to confine guest molecules for drug delivery, energy storage, sensors, nanotechnology, and biotechnology.

Typical examples of ordered mesoporous materials that gained much popularity include Mobil Composition of Matter number 41, MCM-41 [23] aluminum loaded MCM-41 (Al-MCM-41) [24, 25], Santa Barbara amorphous No-15 (SBA-15) [26], and periodic mesoporous organosilica-PMO [27].

Pure silica, metallosilica, and organosilica ordered mesoporous materials can be generally synthesized by sol-gel or hydrothermal methods from silica precursors (like TEOS, fused silica, sodium silicate or from extracts of Si & Al-rich minerals or plant remains) in the presence of surfactants like Cetyltrimethylammoniumbromide–CTAB or Pluronic-P123 ($EO_{20}PO_{30}EO_{20}$) as template or structure directing agent in basic or acidic media [24-27].

The morphology and surface properties of these materials can be tuned during synthesis by variation of the reactant stoichiometry, the nature of the surfactant molecule, the

auxiliary chemicals, the reaction conditions, or by post-synthesis functionalization techniques.

The amorphous silica walls associated with the synthesized OMMs generally limit their applications in catalysis due to limited, hydrothermal stability, and absence of doped metals in the framework of pure silica. OMMs also have limited acidity and functionality. On the other hand, their surface can be easily functionalized by organic molecules [28, 29] and these hybrid materials promise great opportunities for a generation of new functional materials with improved and tailored properties for diverse applications in various fields. Therefore, surface functionalization of these materials with organic molecules like amines, thiols, carboxylic acid, sulfonic acid, vinyl and nitrogen-based heterocyclic and others have emerged as one of the most important research areas in the field of advanced functional materials.

In particular, mesoporous siliceous matrices like SBA-15 and MCM-41 and PMOs are ideal candidates for functionalization due to their large surface area (~1000 m^2/g), large and tunable pore sizes (2-50 nm), hydrothermal stability and thicker walls that can be easily functionalized using simple silanol chemistry. Basically, functionalization of such OMMs can be done by one of the following three conventional methods [28-33].

1. Grafting or post-synthesis functionalization by organic functional groups to modify hydrophilicity/hydrophobicity of surface silanols (scheme 1.9a) and functionalization by immobilization with metals to modify the acidity of the silica centers as well as the pore size and thickness of the mesoporous materials. Grafting conventionally refers to the process by which the surfaces

of pre-made mesoporous silica materials are modified by organic groups using organosilane coupling agents. This process is often carried out by simply reacting mesoporous silica with organosilanes of the type trialkoxysilane $(R'O)_3SiR$, or less frequently chlorosilanes $ClSiR_3$ or silazanes $HN(SiR_3)_3$. The reaction leads to the conjugation between the free silanol groups of the parent mesoporous silica material and the incoming organosilane. This process often leaves the mesostructure of the parent material intact; however, it inherently leads to non-homogeneous distribution of the organic groups in the material, where higher density of functional groups are formed around the pore mouth and less density in the middle of the cylindrical channel pores of the material leading to problem of pore blocking.

2. Direct or co-condensation (Scheme 1.9b) refers to an alternative method to synthesis of organic functionalized mesoporous silica or organosilica materials which are achieved by one-pot co-condensation of the silica precursors, in the presence of functionalizing and templating agents. This leads to mesostructured materials with the organic functional groups anchored covalently to the walls of the material. In this case, the organic functionality is homogeneously dispersed on the surface and pore blocking and leaching due to silane breaking do not occur. The most notable drawback of the co-condensation synthetic method is that the incorporation of the organosilane can hinder the ordering of the material at high loading and must be limited to 40 mol %.

3. The third method of organic functionalization of ordered mesoporous material is by hydrolysis and condensation of bridged the type $(R'O)_3$-Si-R-Si-$(OR')_3$ in the presence of a structure directing agent as shown in scheme 1.9c, where R is organic group and R' is a methyl or ethyl group This was the method by which periodic mesoporous organosilica materials (PMOs) were synthesized for the first time in 1999 [28]. Such methods result in 100% loading of the bridged precursor with no problem of pore blocking and leaching. The obtained materials show large pores, high surface areas and good hydrothermal and mechanical stability. The drawback of PMO synthesis is that only relatively small and rigid organic group linkers generate a well-ordered material.

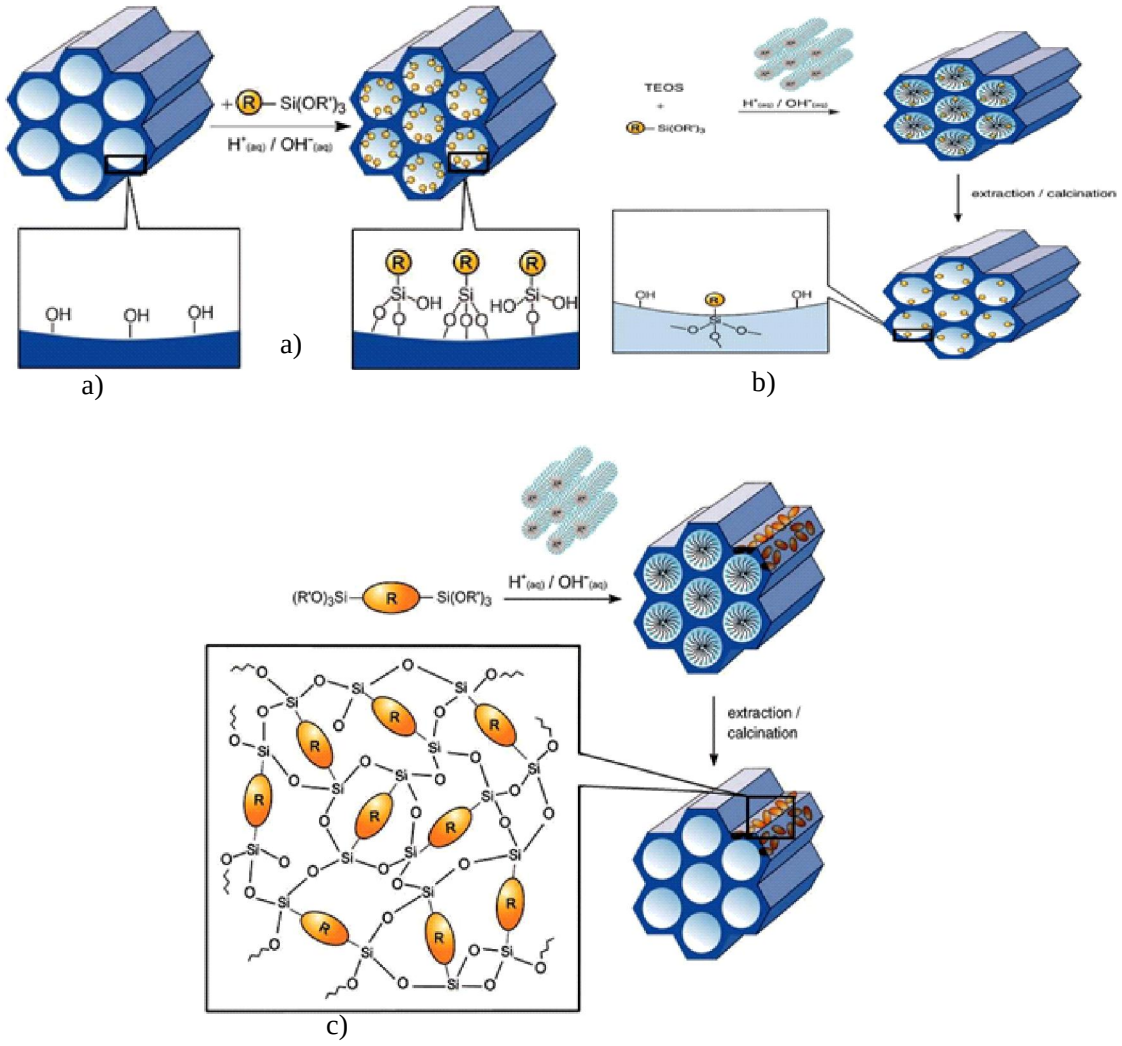

Scheme 1. 9: a) Post synthesis functionalization of OMMs by grafting b) Co-condensation and c) Synthesis of PMO with a bridged organosilane [28]

In general, recent literature shows that attempts have been made to tune surface modification by varying the templating and co-templating agents for co-stabilizing agents and the use of oleic acid as co-templating and stabilizing agent [34, 35]. Apart from this, there is also literature report on the functionalization of ordered mesoporous silica materials (MCM-41 & SBA-15) by silylated long chain fatty acid ester like methyl oleate, methyl linoleate as bulky co-templating precursors to sustain the order of the material [36]. Such functionalized ordered mesoporous materials may have potential

application as a hard template in the preparation of metal nanoparticles as catalysts. There are also literature reports on functionalization of MCM-41[29] and SBA-15 [26] OMMs for application as catalysts [37], PMOs for biomedical applications [40], mesoporous silicate materials in sensing [38], Al-MCM-41 as catalyst for methanol dehydration [24], catalytic properties of acid functionalized ordered mesoporous organosilica-PMO for advanced applications [27], and as adsorbents [39]. To the best of our knowledge, there is no research report on the use of vernolic acid or its derivatives for surface modification of ordered mesoporous materials and their applications as potential hard templates for immobilization of silver nanoparticles.

1.2.2. Ordered mesoporous materials of this work

The following sections give brief overview including surface properties of three groups of ordered mesoporous materials, namely aluminum doped ordered mesoporous aluminosilicate Mobil Composition of Matter No 41 (Al-MCM-41), Pure silica Santa Barbara Amorphous No 15 (SBA-15) and Periodic Mesoporous Organosilica (PMO). These materials were surface modified by supporting vernolic acid methyl/ethyl/propyl esters and their mercapto imidazole derivatives, as well as immobilizing silver nanoparticles on them for the subsequent potential catalytic applications.

An aluminum modified form of MCM-41 ordered mesoporous material was developed in 1992. It has aluminum in addition to silicon in its framework structure and silanol groups on inner pore surface and an outer surface of the material as shown in figure 1.5. Thus, it possesses the properties of Lewis acidity at the aluminum center and acts as Lewis acid in heterogeneous catalysis like microporous alumino-silica-zeolite. As the Al to Si ratio increases its acidity also increases. Generally, the hydrophilic surface properties of

ordered mesoporous aluminosilicate materials impart their less affinity to hydrophobic materials to be supported on these materials [24].

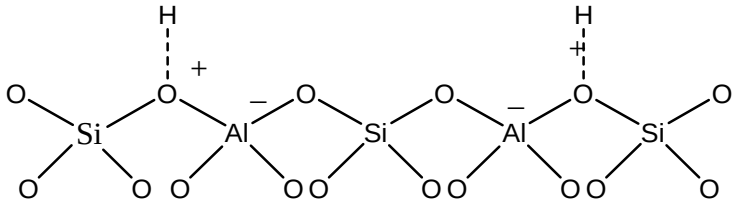

Figure 1. 5: Framework and surface structure of ordered mesoporous aluminosilicate material

Santa Barbara Amorphous No 15 (SBA-15) is one of the pure silica mesoporous materials. SBA-15 has been first synthesized in 1998. It has two-dimensional hexagonal structures and is the most widely used of the SBA groups. The strong popularity of SBA-15 silica is attributed to its main features like: (i) it can be easily and reproducibly prepared within a wide range of temperatures (35–130 ^{0}C) using tetraethylene orthosilicate or sodium silicate; (ii) it is a hexagonally ordered silica material with tailorable uniform mesopores and micropores in the mesopore walls; and (iii) it has thick pore walls (2–6 nm), leading to improved thermal and hydrothermal stability.

Due to the presence of only silica in its central framework structure and silanol (SiOH) groups on its outer and inner amorphous pore surfaces, the pure silica SBA-15 has neutral and hydrophilic surface properties as shown in figure 1.6. Consequently, it shows less affinity for hydrophobic materials and higher affinity for polar materials to be supported. However, it is less polar than Al-MCM-41 and has a higher affinity for hydrophobic material loading (figure 1.6). Apart from this, it possesses higher surface area and thicker pore walls than the pure silica MCM-41 and higher hydrothermal stability. It also possesses unique surface property in that it has some micropores connecting the

mesopores and hence it is good for nanoparticle preparation by hard template methods in nanotechnology

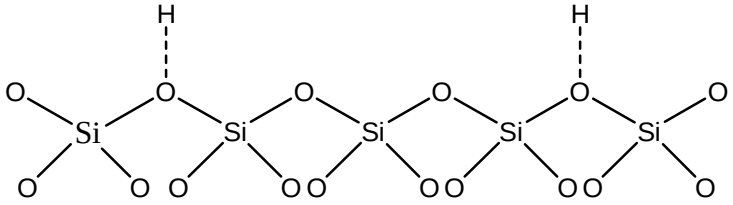

Figure 1. 6: Framework and surface structure of Pure Silica ordered mesoporous material PMO is an organic-inorganic hybrid ordered mesoporous material, which was synthesized first in 1999. It is an organo-silica with a small chain and rigid organic bridging functional groups as shown in (figure 1.7) and thus possesses more surface hydrophobic than the alumino-silica Al-MCM-41 and the pure silica SBA-15. Thus, PMO material has the highest affinity for hydrophobic material loading when compared to Al-MCM-41 and SBA-15. It also possesses a higher surface area and good for higher loading and higher mass transfer..

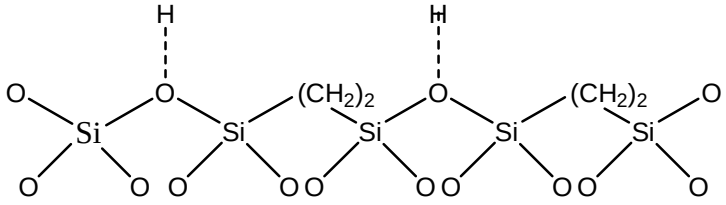

Figure 1. 7: The outer surface structure of PMO

1.2.3. Modification of ordered mesoporous materials in this work

After the synthesis of vernolic acid methyl ester (VAME) and its mercapto-imidazole derivates (IFVAME) in the first part of this work, they are supported on the above mentioned ordered mesoporous materials (OMM). In the second part of the work,

VAME-OMMs and IFVA/IFVAME-OMM modified products were obtained and fully characterized. To optimize the modifications the ratio of the mass of VAME to OMM and IFVA/IFVAME to OMMs were varied according to the literature report [34].

Since vernolic acid methyl ester and its imidazole derivatives have large organic alkyl group with C-18, they are more hydrophobic and show less affinity for more surface hydrophilic and less acidic ordered mesoporous materials. Confirmation of the success of such modifications was obtained by characterization by nitrogen adsorption-desorption isotherms, FT-IR spectroscopy, Thermogravimetric Analysis-TGA, powder XRD and CHN elemental analysis.

1.3. Immobilization of silver nanoparticles on OMMs

1.3.1. General overview of metal nanoparticles

Nanoparticles are materials in the range of 1-100 nm size scale. Nanoparticles of noble metals and nanoporous silica nanoparticles have diverse applications in catalysis, electronic devices, sensors, optical devices, magnetic devices, antibacterial activities etc. because of their special size-dependent physical and chemical properties. A variety of preparation methods of nanoparticles have been proposed so far. However, such inorganic nanoparticles are highly unstable and easily agglomerate and have poor dispersion in organic solvents [34], which need hard templating and stabilizing methods using mesoporous materials as host.

Metal nanoparticle modified mesoporous solids have been considered for a wide range of heterogeneous catalysis reactions. Immobilizations of the active centers by nanoparticle can improve the overall efficiency of the catalytic processes because:

1) It is easier to retain the solid catalyst in the reactor or to separate it from the liquid process stream by filtration (compared to extraction and distillation requirement for homogeneous processes);
2) Often the catalyst can be regenerated and recycled;

Confinement of the catalyst within the mesopores provides a means of introducing size and/ or shape selectivity and thereby greater specificity for reactions. Unlike organic polymers, this mesostructured confinement avoids swelling, dissolution & leaching of the functional groups. This confinement of catalyst within the mesopore channels can also enhance catalyst turnover and safe handling of the higher acidic surface. Recently, syntheses of metal nanoparticles by hard templating methods by using mesostructured materials have been reported [40-43].

Furthermore, synthesis of reactive silver metal coordinate imidazole functionalized fatty acid methyl esters being used for hydrolysis of organophosphorus pesticides [21] and for the photo-degradation of organic dye by titanium containing SBA-15 and silver nanoparticles immobilized on packed quartz bed have been reported [1, 44]. To the best of our knowledge, there is no literature report on the immobilization of silver nanoparticles on vernolic acid and its derivative on modified ordered mesoporous silica having potential catalytic application for photo-degradation of model organic dye effluent.

1.3.2. Immobilization of silver nanoparticles on modified OMMs (AgmOMMs) and their catalytic test

The silver nanoparticles were immobilized on ordered mesoporous materials that have been modified with VAME /IFVAME. This happens because the inner-pore surface of these materials possesses carboxylate of ester as well as nitrogen for imidazole derivative functionalized VAME that have an affinity for silver ion or metal after reduction by use of an appropriate reducing agent. Finally, catalytic properties of VAME modified OMMs were tested for photocatalytic/chemocatalytic degradation of model organic dyes, namely methyl orange and methylene blue.

1.4. Significance of the study

Vernolic acid and its derivatives may be used for the production of many value-added materials like surface functionalized ordered mesoporous materials such as aluminum loaded Mobil Composition Matter No 41 (Al-MCM-41), Santa Barbara Amorphous No 15 (SBA-15), and periodic mesoporous organosilica (PMOs). These modified materials and their silver nanoparticles supported ones can be used for diverse applications such as photo-degradation of dye effluent in textile factories and as a potential catalyst for detoxification of phosphate ester of phosphorous pesticides in agricultural sectors as well as potential adsorbent applications of wastewater treatment for removal of heavy metals. It may also be used as a baseline on further modification of ordered mesoporous materials with other fatty acids derived from renewable resources to get other value-added chemicals.

1.5. The objective of the study

- **Major objective:** To support vernolic acid methyl/ethyl/propyl ester and its mercapto imidazole derivatives on OMMs and immobilize silver nanoparticles on OMMs for catalytic applications.

- **Specific objectives**

- To extract vernonia oil from native *vernonia galamensis* seed and derivatize it to acids and monoalkyl esters.
- To functionalize vernolic acid methyl/ethyl/propyl ester with 2-mercapto-1-methylimidazole
- To support vernolic acid methyl ester and its mercaptoimidazole conjugates on Al-MCM-41, SBA-15 and PMOs.ordered mesoporous nanomaterials,
- To immobilize silver nanoparticles on the three-modified ordered mesoporous nanomaterials.
- To evaluate the potential catalytic properties of the VAME/IFVAME supported and AgNps immobilized ordered mesoporous materials for degradation of model organic dyes.

1.6. References

1. Zhou R, Srinivasan MP: **Photocatalysis in a packed bed: Degradation of organic dyes by immobilized silver nanoparticles**. *J of Envir Chem Engin* 2015, **3**(2):609-616.
2. Kant R: **Textile dyeing industry an environmental hazard**. *Natural Sci* 2012, **04**(01):22-26.
3. Colpini LMS, Lenzi GG, Urio MB, Kochepka DM, Alves HJ: **Photo-discoloration of textile reactive dyes on Ni/TiO_2 prepared by the impregnation method: Effect of calcination temperature**. *J of Envir Chem Engin* 2014, **2**(4):2365-2371.
4. Karmakar G, Ghosh P, Sharma B: **Chemically Modifying Vegetable Oils to Prepare Green Lubricants**. *Lubricants* 2017, **5**(4):44.
5. Samarth NB, Mahanwar PA: **Modified Vegetable Oil Based Additives as a Future Polymeric Material—Review**. *Open J of Organic Polymer Materials* 2015, **05**(01):1-22.
6. Singh AK: **Castor oil-based lubricant reduces smoke emission in two-stroke engines**. *Industrial Crops and Products* 2011, **33**(2):287-295.
7. Ulf Schuchardta U, Serchelia R, Vargas RM: **Transesterification of Vegetable Oils: a Review**. *J Braz Chem Soc,* 1998, **9**(1):199-210.
8. Carlson KD, Schneider1 WJ, Chang SP, Princen LH: **Vernonia galamensis Seed Oil: A New Source for Epoxy Coatings**. *Am. Oil chem. Soc.* 1981, **11**:297-318.
9. Zeleke TD, Segne TA, Chebude Y: **Synthesis and Characterization of Starch Vernolates in Organic Solvents**. *Am J of Applied Chem.* 2016, **4**(6):212-220.

10. Baye T, Becker HC: **Exploration of *Vernonia galamensis* in Ethiopia, and Variation in Fatty Acid Composition of Seed Oil**. *Genetic Resources and Crop Evolution* 2005, **52**(7):805-811.

11. Mann N, Mendon SK, Rawlins JW, Thames SF: **Synthesis of Carbonated Vernonia Oil**. *J Am Oil Chem Soc* 2008, **85**:791-796.

12. Shimelis H, Mashela PW, Hugo A: **Performance of Vernonia as an Alternative Industrial Oil Crop in Limpopo Province of South Africa**. *Crop Sci* 2008, **48**(1):236.

13. Mbugua MN, Yusuf AO, Gitu PM, Bhatt BM: **Conversion of *Vernonia galamensis* Oil to Pyridinyl-Vernolamides and their Antimicrobial Activities**. *Bull Chem Soc, Ethiop* 2007, **21**(1):108-110.

14. Grinberg S, Linder C, Kolot V, Waner T, Wiesman Z, Shaubi E, Heldman E: **Novel Cationic Amphiphilic Derivatives from Vernonia Oil: Synthesis and Self-Aggregation into Bilayer Vesicles, Nanoparticles, and DNA Complexants**. 2005, **21**: 7638-7645.

15. Casebolt ED, Mote BE, Trumbo DL: **Applications of Vernonia oil in thermoset coatings II**. *Progress in Organic Coatings* 2002, **44**:147-151.

16. Ayorinde FO, Saeed KA, Price E, Morrow A, Collins WE, McInnis F, Pollack SK, Eribo BE: **Production of poly-(β-hydroxybutyrate) from saponified Vernonia galamensis oil by Alcaligenes eutrophus**. *J of Industrial Microbiology and Biotechnology* 1998, **21**(1):46-50.

17. Ayorinde FO, Nana EY, Nicely PD, Woods AS, Price EO, Nwaonicha CP: **Syntheses of 12-aminododecanoic and 11-aminoundecanoic acids from vernolic acid**. *J of the Am. Oil Chem. Soc.* 1997, **74**(5):531-538.

18. Mambo CK, Gitu PM, Bhatt BM, Chweya J, Grinberg S, Mills D: **Synthesis of Vernolamide Containing Tertiary Amino Groups from *Vernonia galamensis* Oil and Their Biological Activities**. *Bull Chem Soc, Ethiop* 1998, **12**(2):121-128.

19. Shimelis H, Gwata ET: **Evaluation of the Agronomic Performance of Vernonia (*Vernonia galamensis*) Germplasm**. *Intech chapter 6* 2013.

20. Türünç O, Meier MAR: **The thiol-ene (click) reaction for the synthesis of plant oil derived polymers**. *Eur J of Lipid Sci and Techn* 2013, **115**(1):41-54.

21. Bromberg L, Chen L, Chang EP, Wang S, Hatton TA: **Reactive Silver and Cobalt Nanoparticles Modified with Fatty Acid Ligands Functionalized by Imidazole Derivatives**. *Chemistry of Materials* 2010, **22**(18):5383-5391.

22. Samuelsson J, Jonsson M, Brinck T, Johansson M: **Thiolene coupling reaction of fatty acid monomers**. *J of Polymer Sci Part A: Polymer Chemistry* 2004, **42**(24):6346-6352.

23. Beck JS, VartUli JC, Roth WJ, Leonowicz ME, Kresge CT, Schmitt KD, Chu CT-W, Olson DH, Sheppard EW, McCullen SB *et al*: **A New Family of Mesoporous Molecular Sieves Prepared with Liquid Crystal Templates**. *J Am Chem Soc*, 1992, **114**: 10834-10843.

24. Naik SP, Bui V, Ryu T, Miller JD, Zmierczak W: **Al-MCM-41 as methanol dehydration catalyst**. *Applied Catalysis A: General* 2010, **381**(1-2):183-190.

25. Araújo S, Costa FT, Maia DAS, Sant`Ana HB, Cavalcante Jr. C.L.: **Synthesis and Characterization of Al- and Ti-MCM-41 Materials: Application to oxidation of Anthracene**. *Brazilian J of Chem Engin* 2007, **24**:135-141.

26. Huirache-Acuna R, Nava R, Peza-Ledesma CL, Lara-Romero J, Alonso-Nuez G, Pawelec B, Rivera-Munoz EM: **SBA-15 Mesoporous Silica as Catalytic Support for Hydrodesulfurization Catalysts-Review**. *Materials* 2013, **6**(9):4139-4167.

27. Park SS, Santha Moorthy M, Ha C-S: **Periodic mesoporous organosilicas for advanced applications**. *NPG Asia Materials* 2014, **6**(4):e96.

28. Hoffmann F, Cornelius M, Jrgen Morell J, Froba M: **Silica-Based Mesoporous Organic-Inorganic Hybrid Materials**. *Angew Chem Int Ed* 2006, **45**: 3216 – 3251.

29. Aghapoor K, M. Amini M, Jadidi K, Reza Darabi H: **N-functionalized L-proline anchored MCM-41: A novel organic-inorganic hybrid material for solvent-free aminolysis of styrene oxide under microwave irradiation**. *Acta Chimica Slovenica* 2015, **62**(1).

30. Yang Q, Liu J, Zhang L, Li C: **Functionalized periodic mesoporous organosilicas for catalysis**. *J of Materials Chemistry* 2009, **19**(14):1945-1955.

31. Pal N, Bhaumik A: **Soft templating strategies for the synthesis of mesoporous materials: Inorganic, organic-inorganic hybrid and purely organic solids**. *Advances in Colloid and Interface Sci* 2013, **189-190**:21-41.

32. Alothman Z: **A Review: Fundamental Aspects of Silicate Mesoporous Materials**. *Materials* 2012, **5**(12):2874-2902.

33. Wei Y, Li X, Zhang R, Liu Y, Wang W, Ling Y, El-Toni AM, Zhao D: **Periodic Mesoporous Organosilica Nanocubes with Ultrahigh Surface Areas for Efficient CO(2) Adsorption**. *Scientific reports* 2016, **6**:20769.

34. Li Z, Zhu Y: **Surface-modification of SiO_2 nanoparticles with oleic acid**. *Applied Surface Science* 2003, **211**(1-4):315-320.

35. Choi J, Han Y, Park S, Park J, Kim H: **Pore Characteristics and Hydrothermal Stability of Mesoporous Silica: Role of Oleic Acid**. *J. of Nanomaterials* 2014, **2014**:8.

36. El Kadib A, Katir N, Finiels A, Castel A, Marcotte N, Molvinger K, Biolley C, Gaveau P, Bousmina M, Brunel D: **Mesostructured fatty acid-tethered silicas: sustaining the order by co-templating with bulky precursors**. *Dalton transactions* 2013, **42**(5):1591-1602.

37. Esquivel D, Van Der Voort P, J. Romero-Salguero F: **Designing advanced functional periodic mesoporous organosilicas for biomedical applications Electrodes**. *AIMS Materials Sci.* 2014, **1**(1):70-86.

38. Melde BJ, Johnson BJ, Charles PT: **Mesoporous Silicate Materials in Sensing**. *Sensors* 2008, **8**(8):5202-5228.

39. Park J, Kim H, Park J: **Characteristics of Thiol-Functionalized Mesoporous Silica and Its Application to Silver and Cadmium Ion Removal**. *Int J of Env Sci and Development* 2012, **3**(2).

40. Lin D-H, Jiang Y-X, Wang Y, Sun S-G: **Silver Nanoparticles Confined in SBA-15 Mesoporous Silica and the Application as a Sensor for Detecting Hydrogen Peroxide**. *J. of Nanomaterials* 2008, **2008**:10.

41. Ivashchenko NA, Gac W, Tertykh VA, Yanishpolskii VV, Khainakov SA, Dikhtiarenko AV, Pasieczna-Patkowska S, Zawadzki W: **Preparation, Characterization and Catalytic Activity of Palladium Nanoparticles Embedded in the Mesoporous Silica Matrices**. *World J of Nano Sci. and Engin.* 2012, **02**(03):117-125.

42. Wu H, Pantaleo G, Venezia A, Liotta L: **Mesoporous Silica Based Gold Catalysts: Novel Synthesis and Application in Catalytic Oxidation of CO and Volatile Organic Compounds (VOCs)**. *Catalysts* 2013, **3**(4):774-793.

43. Bhosale RR, Kulkarni AS, Gilda SS, Aloorkar NH, Osmani RA, Harkare BR: **Innovative Eco-friendly Approaches for Green Synthesis of Silver Nanoparticles**. *Int J, of Pharma Sci and Nanotech* 2014, **7**(1):2328-2337.

44. Yang L, Jiang Z, Lai S, Jiang C, Zhong H: **Synthesis of Titanium Containing SBA-15 and Its Application for Photocatalytic Degradation of Phenol**. *Int J of Chem Engin* 2014:1-7.

2. Characterization Techniques

The use of feasible characterization techniques is a key step and an indispensable work for gathering information to ensure the formation or applications of a particular material of interest in a research work involving the synthesis of such material with potential applications [1]. In this chapter, the different techniques used in this study are briefly described. The techniques used include those employed to identify the nature of the vernolic acid and its derivatives, These techniques are Nuclear Magnetic Resonance Spectroscopy (NMR), CHN Elemental Analysis and Fourier Transform Infrared Spectroscopy (FT-IR), while for the characterization of the Ordered Mesoporous Materials upon modification, Powder X-ray Diffraction (PXRD), Thermogravimetric Analysis (TGA), Nitrogen adsorption-desorption isotherms and Transmission Electron Microscopy (TEM) have been utilized. Finally, Ultraviolet-Visible Spectroscopy (UV-Vis) is employed to follow the catalytic reaction employed to test our Ag-mOMM materials.

2.1. **Nuclear Magnetic Resonance Spectroscopy (NMR)**

NMR spectroscopy is one of the most powerful tools to investigate the structure and dynamics of a molecular system in the liquid phase [1-4]. Atomic nuclei such as ^{1}H, ^{11}B, ^{13}C, ^{15}P, ^{19}F, which consist of an odd number of protons and/or neutrons, possess quantized magnetic moment (μ) with quantized energy states due to Zeeman effect when an external magnetic field is applied. This will result in transitions of electrons during the absorption of a photon.

The fundamental property of the atomic nucleus involved in nuclear magnetic resonance is the nuclear spin (I) which has values of 0, ½, 1, 1½, etc., in the unit of h/2π (where h is the Plank's constant). The nuclear magnetic moment (μ) is directly proportional to the spin, i.e. (Equation 7)

$$\mu = \frac{\gamma I h}{2\pi} \quad (Equation\ 7)$$

Where γ is the proportionality constant called magnetogyric ratio and is constant for each particular nucleus. When a magnetic field is applied, the nuclear moments orient themselves with only certain allowed orientation, a nucleus of spin I have 2I+1 possible orientation, which is given by the value of the magnetic quantum number m_I. m_I has values of -I, -I+1, …, I-1, I. The energy of interaction is proportional to the nuclear moment and the applied field. The selection rule for NMR transition is that mI can only change by one unit, i.e. ΔmI = ±1. Therefore, the net transition energy and frequency are given respectively as follows (equation 8):

$$\Delta E = \frac{\gamma h B}{2\pi} \quad or\ \nu = \frac{\gamma B}{2\pi} \quad (Equation\ 8)$$

where B is the applied field.

The chemical shift interaction arises from secondary local magnetic fields induced by the interaction of the electrons surrounding the nucleus to which the external magnetic field is applied. The induced local field opposes the external magnetic field and hence shields the nucleus under observation. Thus, the chemical shift is defined as the nuclear shielding divided by the applied field. It is only a function of the nucleus and its environment, i.e. it is a molecular quantity. It is always measured from the suitable compound, this may be

an external reference or more commonly the reference compound is added to the solution investigated (internal reference). Mathematically, the chemical shift is defined as

$$\delta = \frac{B_{sample} - B_{refrence}}{B_{refrence}} \times 10^6\ ppm\ \ or\ \frac{sample - \nu_{refrence}}{\nu_{Oscillator(Hz)}} \times 10^6 \quad (Equation\ 9)$$

For ^{1}H NMR, the recommended reference is tetramethylsilane (TMS), whose peak appears at 0 in the δ-scale. TMS is also the recommended reference for ^{13}C NMR, giving rise to only one peak under normal operation.

In this study, ^{1}H NMR spectra of vernolic acid methyl ester, its precursors and mercapto-imidazole functionalized was recorded on a 400 MHz Bruker 400 Ultra-Shield NMR with operating frequencies 270 MHz (^{1}H) and 68 MHz (^{13}C) with tetramethylsilane (TMS) as a reference and the deuterated solvent used is chloroform-d.

2.2. CHNS Elemental Analysis

Elemental analysis (EA) is a technique used to determine the elemental composition of an organic sample [3]. The sample's content of carbon, hydrogen, sulfur, and nitrogen can be quantified by burning the sample in an excess of oxygen. The combustion products thus formed are carbon dioxide, water, nitrogen dioxide, and sulfur dioxide. These gases are then separated by gas chromatography and detected quantitatively.

2.3. Fourier Transform Infrared Spectroscopy (FT-IR)

Fourier transforms infrared (FT-IR) spectroscopy deals with the vibration of chemical bonds in a molecule at various frequencies depending on the elements and types of bonds. After absorbing electromagnetic radiation the frequency of vibration of a bond

increases leading to transition between a ground state and several excited states. These absorption frequencies represent excitations of vibrations of the chemical bonds and thus are specific to the type of bond and the group of atoms involved in the vibration [1-4]. The energy corresponding to these transitions corresponds to the infrared region (4000–400 cm^{-1}) of the electromagnetic spectrum in which range the main functional groups' materials under study is included.

In this study, FT-IR spectra of synthesized samples are recorded using the Perkin Elmer Spectrum 65 FT-IR Spectrometer.

2.4. Powder X-ray Diffraction (PXRD)

Powder X-ray diffraction is a powerful technique that helps to identify the structure, phase purity, degree of crystallinity and unit cell parameters of a given sample [1, 3, 5, 6]. The mesoporous materials exhibit characteristic high-intensity peaks in the low angle region between $2\theta = 0.5\text{-}10^{o}$. The XRD patterns are recorded by the measurements of the angles at which the X-ray beams are diffracted by the periodicity of the sample. The relation between the distance between two *hkl* planes *(d)* and the angle of diffraction (2θ) is given by Bragg's equation based on figure 2.1.

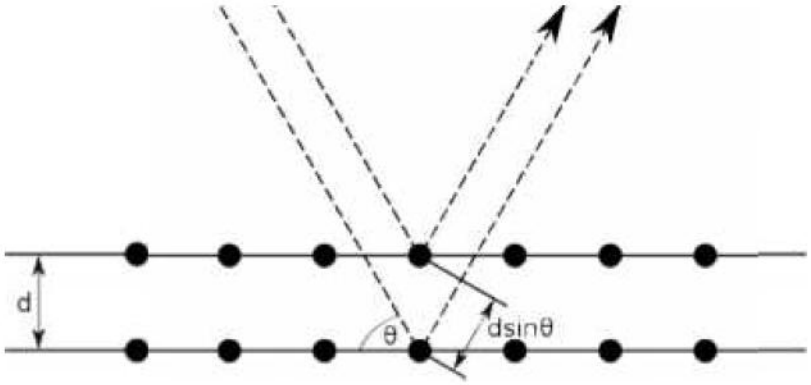

Figure 2. 1: Bragg's scattering of X-rays from parallel planes with d representing inter-planar spacing

$$n\lambda = 2dsin\theta \qquad (Equation\ 10)$$

Where λ = wavelength of X-rays, n= an integer known as the order of reflection (*h, k,* and *l* represent Miller indices of respective planes). From the diffraction patterns, the uniqueness of the mesoporous structures, phase purity, degree of crystallinity, and unit cell parameters can be determined. The identification of phase is based on a comparison of a set of reflections of the sample with that of pure reference phases distributed by International Center for Diffraction Data (ICDD). The unit cell parameter (a_o) of a hexagonal lattice can be determined by the following equation:

$$a_0 = \frac{2d_{hkl}}{3^{\frac{1}{2}}} \ (Equation\ 11)$$

Where d is the distance between two consecutive parallel planes having Miller indices *h, k,* and *l.*

The widths of the diffraction lines are closely related to the size, distribution, defects, and strain in nanocrystals. As the size of the nanocrystals decreases, the line width is broadened due to loss of long-range order relative to the bulk. For most crystalline materials, the diffraction pattern recorded between 2θ of typically 10-90 degrees provides all information needed for the detail of structural order and can also allow refinement of the data to obtain information about molecular packing and inter-atomic distances. According to the Bragg's equation the lower angle the larger inter-planar spacing, *d*. For mesoporous materials which have much larger *d*-spacing than the typical crystalline materials, the diffraction patterns only show peaks at a low angle, generally between 2θ of 2-8 degrees. In addition, the mesoporous materials only have a regular arrangement of pores but no short-range inter-atomic order as the structure of the pore wall is amorphous. Therefore, the structural information that usually obtained from X-ray diffraction for mesoporous materials is the *d*-spacing and the symmetry or packing arrangement of the pores relative to each other.

In this work, the low and wide angle powder X-ray diffraction data were recorded for the synthesized solid composite materials at an ambient temperature on Rigaku Miniflex 600 Powder X-ray diffractometer operating in the reflection geometry from 2θ of 0.5 to 10^0 and 1 to 80° respectively with a step size of 0.02°.

2.5. Thermogravimetric analysis (TGA)

Thermogravimetric analysis or TGA is a technique in which the weight loss of a sample is studied with increasing temperature [3]. It is a highly sensitive technique, which provides information about the weight percentage of moisture, volatiles, solvent, organic /inorganic contents, etc. It is done by placing the sample in a sensitive thermo-balance

and heating the sample at a controlled rate. The weight loss is studied in various ambient atmospheres like nitrogen or air. TGA is widely used for studying the weight percentage of templates in mesoporous material synthesis and to estimate the organic/inorganic contents in modified mesoporous materials.

In this particular study the thermal stability analysis of the synthesized vernolic acid methyl ester supported on Al-MCM-41, SBA-15 and PMO ordered mesoporous silica and organosilica materials were carried out in air with a Perkin-Elmer TGA 7 instrument in the temperature range of 30-900 ^{o}C and at a heating rate of 20 ^{o}C/min by taking sample of 3 to 5 mg weight.

2.6. Nitrogen Adsorption-desorptions Isotherms

Nitrogen gas adsorption-desorption measurements are widely used for evaluating the surface area, pore size, pore volume and pore size distribution of porous solids, pigments, ceramics, industrial adsorbent, etc. In this technique, the amount of gas adsorbed by a solid is measured, which is in turn is directly related to the porous properties and pore structure of the material. The volume of gas adsorbed by the solid is measured over a wide range of relative pressures, and a plot of the volume adsorbed with varying relative pressure (p/p_o) is called the adsorption isotherm. N_2 adsorption isotherm at sub atmospheric pressures and -196 ºC is routinely used for determining pore information and pore size distributions in microporous, mesoporous and macroporous range.

Regarding the types of isotherms, the original 1985 IUPAC recommendations physisorption isotherms were grouped into six types [7, 8]. However, these classifications have been refined and updated to the 2015 IUPAC classification [9] due to the identification of various new types of isotherms over the past three decades as shown in

figure 2.2**.**

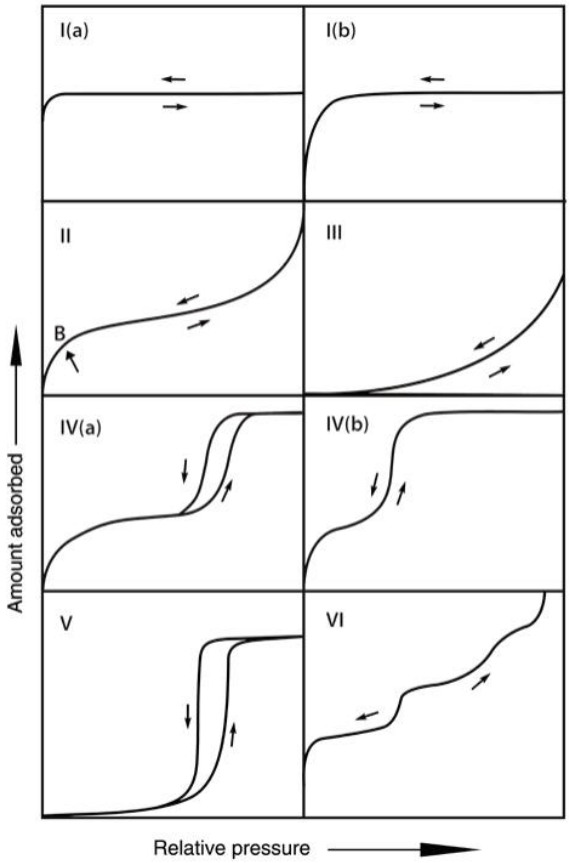

Figure 2. 2: Classification of physisorption isotherms [9]

Type I reversible isotherms are exhibited by microporous solids. Based on updated IUPAC classification, there are two sub-types of type I isotherms namely type Ia and type Ib. Type Ia isotherms are given by microporous materials having mainly narrow micropores (of width < ~ 1 nm); Type Ib isotherms are found with materials having pore size distributions over a broader range including wider micropores and possibly narrow mesopores (< ~ 2.5 nm).Type II reversible isotherms are the normal form of isotherms obtained with a non-porous or macroporous adsorbent. Type III isotherms are rarely seen

for weak adsorbate-adsorbent interaction like for nitrogen on polyethylene with no monolayer formation. Type IV isotherm is given by mesoporous adsorbent. According to updated IUPAC classifications, this has two sub-types namely Type IVa isotherms in which capillary condensation is accompanied by hysteresis loops for adsorbent pore wider than 4 nm and Type IVb reversible isotherms with adsorbents having mesopores of smaller width than 4 nm or for conical and cylindrical mesopores that are closed at the tapered end. Type V isotherms are related to the type III isotherm in that the interaction between adsorbent-adsorbate is weak; this is uncommon but can be obtained with certain porous adsorbent. Type VI reversible isotherms represent stepwise multilayer adsorption on a uniform non-porous surface. Such isotherm is given from certain system such as argon or krypton on graphitized carbon blacks at liquid nitrogen temperature.

Studies of types of hysteresis loops show the following. According to more recent findings the type IV isotherms exhibited is classified in to six distinct types [9] of which types H1, H2 (a), H3 and H4 (figure 2.3) were identified in the original IUPAC classification of 1985 [7, 8]. Each of these six characteristic types is fairly closely related to particular features of the pore structure and underlying adsorption mechanism.

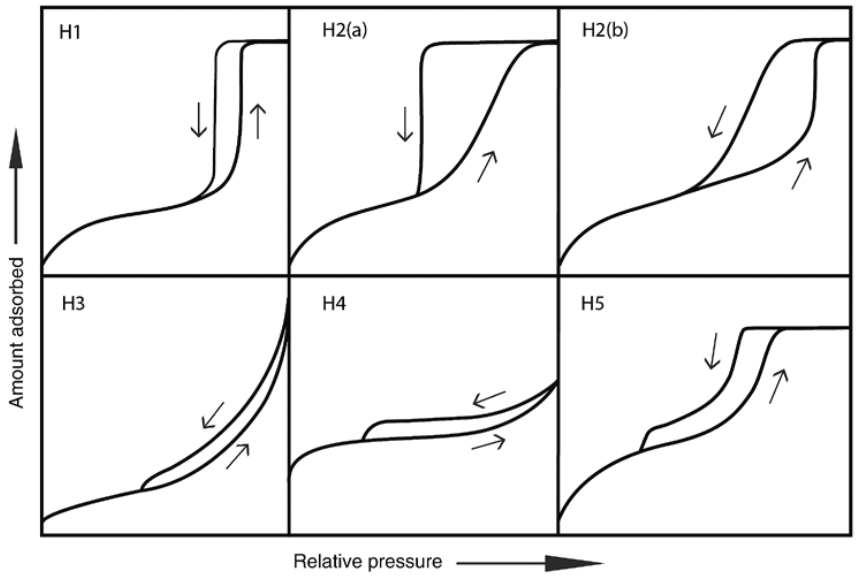

Figure 2. 3: Classification of hysteresis loops [9]

The type H1 steep and narrow loop is usually exhibited by pores of materials like MCM-41 and SBA-15 with regular shape and narrow pore size distribution; The type H2 loop is usually associated with pores with narrow necks and wide bodies; The very steep desorption branch, which is a characteristic feature of H2 (a) loop, can be attributed either to pore-blocking/percolation in a narrow range of pore necks or to cavitations-induced evaporation. The type H2 (b) loop is also associated with pore blocking, but the size distribution of neck width is now much larger. Examples of this type of hysteresis loops have been observed with meso-cellular silica foams and certain mesoporous ordered silicas after hydrothermal treatment. The type H3 loops are usually associated with a non-rigid aggregate plate-like particles of certain clays. The type H4 loop is usually associated with slit-like pores. Although the type H5 loop is unusual, it has a distinctive form associated with certain pore structures containing both open and partially blocked mesopores.

Determination of surface area is based on the principle of Brauner-Emmett-Teller (BET) equation based on monolayer adsorption of gases [7, 9]. This method continues to be the most widely used procedure for evaluating the surface area of porous and finely-divided materials, in spite of the weakness of its theoretical foundations. Indeed, under certain carefully controlled conditions, the BET-area of a nonporous, macroporous or a mesoporous solid (i.e., giving a well-defined type II or a type IVa isotherm) can be regarded as the 'probe accessible area'.

Two stages are involved in the application of the BET method. First, it is necessary to transform a physisorption isotherm into the 'BET plot' and from it derive a value of the BET monolayer capacity, n_m. In the second stage, the BET-area, a (BET), is calculated from n_m by adopting an appropriate value of the molecular cross-sectional area, σ. The BET equation is given in linear equation 1.

$$\frac{p/p'}{n\left(1-\frac{p}{p'}\right)} - \frac{1}{n_m C} + \frac{C-1}{n_m C}\left(\frac{p}{p'}\right) \quad (\textbf{\textit{Equation 1}})$$

Where n is the specific amount adsorbed at the relative pressure p/p° and n_m is the specific monolayer capacity. Thus, The BET surface area is given by equation 2:

$$a_s(BET) = n_m L \sigma_m / m \quad (\textit{Equation 2})$$

where a_s (BET) is the BET specific area of the adsorbent (of mass m).

Alternatively, the BET equation in terms of volume of adsorbed N_2 adsorption/desorption isotherm is given as follows (equation 3),

$$\frac{p}{v(p_0-p)} = \frac{1}{V_m c} + \frac{C-1}{V_m c} \times \frac{p}{p'} \quad (\textit{Equation 3})$$

where v is volume of N_2 adsorbed by the sample under pressure p/po is equal to saturated vapor pressure at the same temperature, v_m is volume of N_2 adsorbed when the surface is covered with monolayer, and C is BET constant for a given adsorbate equation suggests that the plot of p/v (p_o- p) versus p_o/p should be linear, and from the intercept $1/v_m c$ and slope $(c-1)/v_m c$, the values of v_m and c can be determined. Thus, the specific surface area (S) of a sample can be determined as follows (*Equation 4)*:

$$S = \frac{N_o v_m A}{22414m} \quad (Equation\ 4)$$

Where N_o is Avogadro number, m is mass of solid adsorbent, A is a cross-section of the gas molecules (16.2 Å for N_2), and S is expressed in $cm^2\ g^{-1}$ unit.

The determination of pore size distribution and pore volume is based on the physical adsorption and a capillary condensation in the pore. Several computational procedures are available for the derivation of the pore size distribution of mesoporous samples from physisorption isotherms. Most popular among them is the Barrett-Joyner-Halenda (BJH) computational model [10], which is based on speculative emptying of the pores by a stepwise reduction of p/p_o, and allowance being made for the contraction of the multilayer in those pores already emptied by the condensate. The mesopores size distribution is usually expressed as a plot of dVp/dr_p versus r_p, where Vp is equal to mesopore volume, and r_p is equal pore radius. It is assumed that the mesopores volume is completely filled at high p/p_o. In addition, the BJH method is normally related to

desorption of nitrogen at 77 K. At the first desorption step (j=1), when the relative pressure is reduced from $\left(\frac{P}{p_0}\right)_1$ to $\left(\frac{\boldsymbol{P}}{\boldsymbol{p_o}}\right)_2$ a volume ΔV(1) will be desorbed from the pore, which results in the reduction of the thickness of the physically adsorbed layer by an amount of Δt_1. Across the relative pressure reduction, the average change of the thickness is $\left(\frac{\boldsymbol{\Delta t1}}{\boldsymbol{2}}\right)$, therefore, the pore volume may be expressed as follows (*Equation 5*)

$$V_{p1} = \Delta V(1)\left[\frac{r_{p1}}{r_{K1} + \frac{\Delta t_1}{2}}\right]^2 \quad \textit{(Equation 5)}$$

Where r_p is pore radius r_k is the inner capillary radius

In general, the calculation of the pore volume at various relative pressures may be summarized as follows (equation 6**)**:

$$V_{pn} = \left[\frac{r_{pn}}{r_{Kn} + \frac{\Delta t_n}{2}}\right]^2 \left[\Delta V(n) - \Delta t_n \sum_{j=1}^{n-1} Ac_j\right] \quad \textit{(Equation 6)}$$

In the experimental procedure**,** prior to the determination of adsorption isotherm, surface area, and pore size distribution, all the physisorbed species must be removed from the adsorbent surface. This is typically carried out by outgassing at low pressure and, normally, elevated temperature. The analysis is performed at 77 K (e.g. under liquid nitrogen). The small amounts of adsorbate gas are admitted in the step into the evacuated sample chamber.

In this work nitrogen, adsorption-desorption isotherms of vernolic acid methyl ester supported ordered mesoporous materials at varying ratios were recorded in a

Micromeritics ASAP 2420 physisorption analyzer. Usually, OMM samples are degassed at 350 ºC for 16 h prior to data collection, except for the samples modified that was degassed at 150 ºC.

2.7. Transmission Electron Microscopy (TEM)

Transmission Electron Microscope (TEM) is an important analytical instrument with very high ability to provide structural and chemical information over a range of length scale down to the atomic dimensions [11]. The topographic information obtained by TEM in the vicinity of atomic resolution can be utilized for structural characterization and identification of various phases of mesoporous materials, viz. hexagonal, cubic or lamellar. TEM also provides real space image on the atomic distribution in the bulk and surface of a nanocrystal. Thus, it has been developed into an indispensable tool for scientists for characterization of microstructure and chemical composition of nanostructured materials and nanocomposites.

The TEM technique involves the irradiation of a very thin sample by a high energy electron beam, which is diffracted by the lattice of a crystalline or semi-crystalline material and propagated along with different directions. A beam of accelerated electrons can interact with specimen in a TEM in either elastic scattering, whereby the electrons change their path in the specimen without a loss of energy, or inelastic scattering resulting in a loss of energy due to an interaction of the impinging electrons with the orbital electrons surrounding the nucleus of each atom in the object. Those electrons, which are not scattered, contribute positively to the image, whereas, considerably scattered electrons are prevented from doing so by apertures in the optical path. Consequently, differences in light intensity (contrast) are created in the final image,

which relates to areas in the object with different scattering potentials. As the atomic number increases, their scattering efficiency will also increase. Hence, heavy metals can form images with good contrast. The modern TEM machines can achieve resolution below 0.5 angstroms (A^0) (50 pm) at magnifications above 50 million times.

2.8. UV-Vis Spectroscopy

Ultraviolet-visible molecular absorption spectroscopy is an analytical technique based upon the absorption of electromagnetic radiation in the wavelength region between 160 to 789 nm [1, 3]. The method is useful for the quantitative determination of a large variety of inorganic and organic species. The method is useful for the quantitative determination of a large variety of inorganic and organic species. The technique is based on the measurement of the absorbance A or transmittance T of solutions in transparent cells with path length l (cm). The concentration of the analyte is directly proportional to the absorbance of the solution or inversely proportional the logarithms of transmittance or directly proportional to logarithmic ratio of transmitted intensity (I) to incident intensity (I_o) of the solution as shown by Beer Lambert's law (equation 13)

$$A = log\frac{I}{Io} = \varepsilon Cl \; or A = \frac{logI}{Io} = -logT \quad (Equation 13)$$

Where A is absorbance I_0 is the intensity of light incident upon sample cell, I is the intensity of light leaving sample cell, C is a molar concentration of solute, l is path length of sample cell (cm.) and ε is molar absorptivity

The technique is mainly used for assaying of analyte although it can also be used in identification and determination of metal-ligand mole ratio in a complex .which helps in structural identification.

From the Beer-Lambert law, it is clear that the greater the number of` molecules capable of absorbing light of a given wavelength, the greater the extent of light absorption. It may also be used for estimation of metal nanoparticles formation at certain characteristic maximum wavelength absorption. However, its limitation lies in interferences and instrumental limitations. As the experimental procedure of getting the spectrum, Sample usually in solutions (may also in gases or solids) is put in a sample holder (made of glass or pure silica) and a filtered and split beam of light is passed through the sample cell and reference cell. Then the emerging beams are compared at the detector (photodiode) after which the absorption is obtained as a function of wavelength.

In this study, the extent of discoloration of methyl orange and methylene blue model dyes solutions by photodegradation and chemo degradation in the present samples of synthesized silver nanocomposites as catalyst was done by recording the UV-Vis spectra of the solutions by T60 UV-Visible spectrophotometer.

2.9. References

1. Nworie1 FS, Nwabue1 FI, Oti1 WJO: **Comparison of Analytical Techniques in the Characterization of Complex Compounds**. *ACS* 2015, **9**(2):1-19.

2. Roberts JD, Caserio MC: **Separation, Purification, and Identification of Organic Compounds by Spectroscopic Techniques BSOC chapter 9, second edition, Benjamin, Inc., Menlo Park,** *Caltech* 1977:258-348.

3. Atkins PW, Overton TL, Rourke JP, Weller MT, Armstrong. FA: **Physical techniques in inorganic chemistry chapter 8, W. H. Freeman and Company, 41 Madison Avenue, New York, NY 10010**. *Book* 2010:1-813.

4. Silverstein RM, Webster FX, Kiemle DJ: **Spectrometric Identification of Organic Compounds 7th ed, John Wiley and Sons, INC.** 2005.

5. Solovyov LA: **Diffraction analysis of mesostructured mesoporous materials**. *ChemSocRev,* 2013, **42**(3708).

6. Charurvedi S, Dave PN: **Microscopy in Nanotechnology** *FORMATEX* 2012(946-952).

7. Sink KSW, D. H. Everett DH, R.A.W H, Moscou L, Pierotti RA, Rouquerol J, Siemieniewska T: **Reporting Physisorption data for gas-solid systems with Special Reference to Determination of Surface Area and Porosity**. *Pure & Appl Chem,* 1985, **57**(4):603—619.

8. Alothman Z: **A Review: Fundamental Aspects of Silicate Mesoporous Materials**. *Materials* 2012, **5**(12):2874-2902.

9. Thommes M, Kaneko K, Neimark AV, Olivier JP, Rodriguez-Reinoso F, Jean Rouquerol J, Sing KSW: **Physisorption of gases, with special reference to the evaluation of surface area and pore size distribution (IUPAC Technical Report)**. *Pure Appl Chem* 2015, **87**(9-10):1051-1069.

10. Barrett EP, Joyner E, Halenda P: **The Determination of Pore Volume and Area Distributions in Porous Substances. I. Computations from Nitrogen Isotherms** *The volume and Area distribution in porous Substances* 1951, **53**:373-380.

11. Smith DJ: **Characterization of Nanomaterials Using Transmission Electron Microscopy, Chapter 1**. *RSC* 2015:1-29.

3. Materials and Methods

3.1. Extraction and Purification of Vernonia Oil

Extraction of crude vernonia oil (CVO) was done according to the procedure reported in the literature with slight modification [1-4]. First, the *V. galamensis* seeds were sun-dried, cleaned and cooled in a refrigerator, heated in an oven for 1 hour at 90 ºC for lipase deactivation and powdered seeds of *V. galamensis* were extracted with n-hexane as a solvent for three hours using Soxhlet extraction systems. Then the extract was filtered, kept overnight in a refrigerator and decanted to separate unnecessary solid wastes and then the solvent was removed by vacuum drying using rotary evaporator. Finally, NMR and FT-IR analysis were done for the dried sample of crude vernonia oil.

In addition to triglycerides; the crude vernonia oil contains variable amounts of objectionable substances, which must be removed to produce pure VO. Some of these impurities are of the non-glycosides type such as the free fatty acids, which may be built up due to enzymatic processes (lipase) resulting from damage to the seed. While others are of the non-oil kind such as the mucilage volatile including moisture and solvent, pigment or coloring materials, primary and secondary oxidation products, waxes and saponifiable and odoriferous materials which are to be refined. Thus, after extraction of crude vernonia oil, its purification was done either by conventional refining method as reported in the literature [1-4] or via modified solid phase extraction by chromatography methods [5-7] followed by deacidification method [8-11] to get neutral vernonia oil (scheme 3.1).

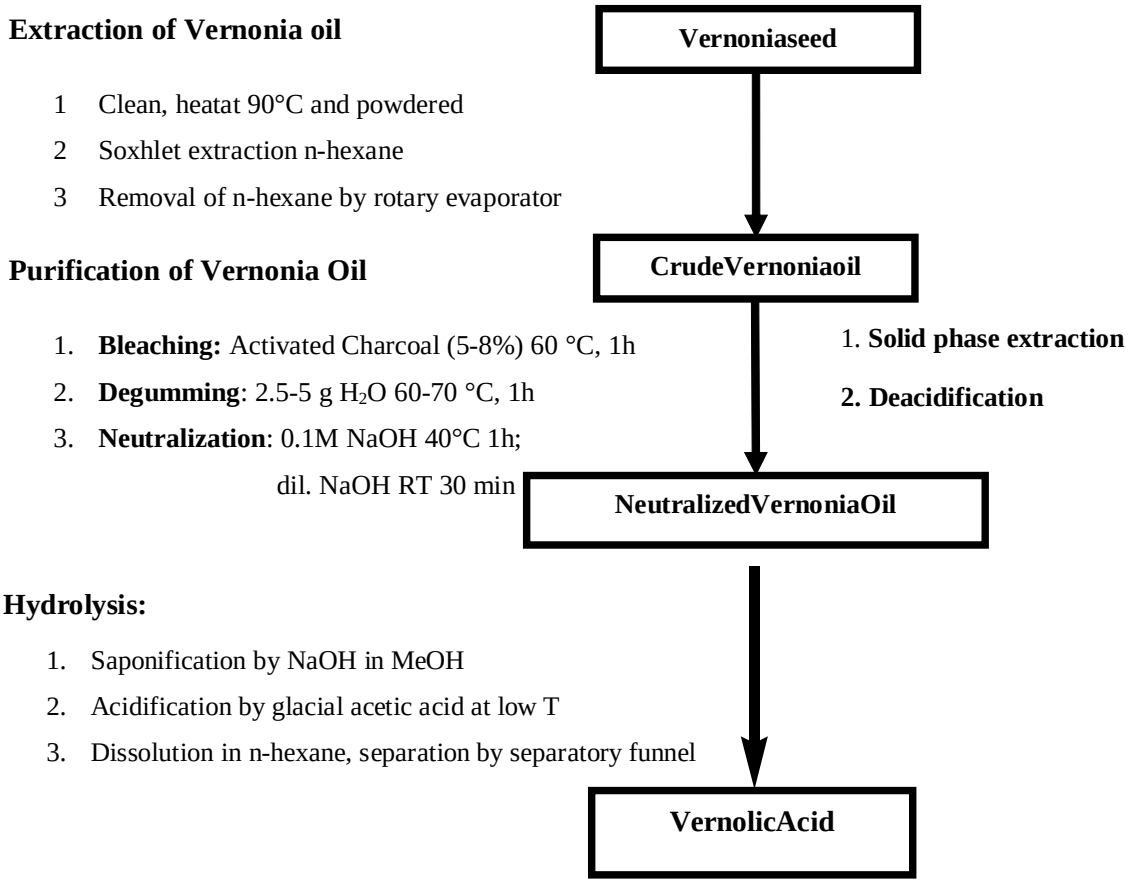

Scheme 3. 1: Extraction, purification, and hydrolysis of vernonia oil

In **Solid phase extraction** of scheme 3.1 above, 10-20 g of CVO was dissolved in 10-20 ml n-hexane and mixed with 35 % activated carbon was introduced from the top of 60 g packed silica gel. Then three different fractions were collected by enough amount of n-hexane, 1:1 volume ratio of n-hexane to diethyl ether and methanol respectively to get separated glycerides and non-glycerides.as shown in section 3.1.2.

In deacidification scheme 3.1 above, solvent extraction was done by taking 1:1 v/v ratio of ethanol to hexane/diethyl ether into which certain amount of oil is dissolved completely by stirring or shaking and allowed to stand for some time and repeatedly extracted for 2 to 3 times with subsequent stripping of solvent under vacuum drying to get the neutral oil. Alternatively, an appropriate size packed column (containing ca. 20 g

basic or neutral alumina) is saturated with 80 mL isopropyl alcohol (IPA), which is used as an eluting solvent. Then 20 g of crude vernonia oil is dissolved in 80 mL of IPA and transferred onto the column, where the eluent is collected over a 70 minutes period. The column is then rinsed with 80 mL portion of IPA followed by 240 mL of hot water (ca. 85 °C.). Then the solvent is stripped off under vacuum to get the neutral oil.

3.1.1. Conventional refining method

The major steps incorporated in the conventional refining steps include bleaching, degumming, and neutralization steps which are described briefly as follows.

Bleaching is usually used as the first stage of conventional refining steps in order to remove colorant impurities. Crude vernonia oil was bleached with 5 % to 8 % by weight of activated charcoal mixed with the oil and heated at a temperature of 60 ^{0}C by continuous stirring for one hour. The decolorized oil was isolated by hot filtration.

Degumming is the second stage of conventional purification which is meant to remove phospholipids and other polar impurities in the colloidal state or dissolved in the oil, which was carried out immediately before neutralization or concurrently with it. Crude vernonia oil was degummed by stirring with 2.5-5 g by weight of distilled water, heated at 60-70 ºC for one hour followed by centrifugation at 5,000 rpm. Gum and oil were separated and the oil was dried at 60 ºC on a rotary evaporator.

Neutralization is the third step of the conventional and chemical deacidification method which involves saponification or hydrolysis by sodium hydroxide to remove organic acids called free fatty acid (FFA), which are always dissolved in the oil. This step is the most challenging step in the oil refining due to the fact that for oil with high FFA contents there is high loss of neutral oil due to saponification and emulsification during

the neutralization [9]. Literature report [10] shows that to resolve such problems a repeated pre-esterification of the oils with a methanolic solution of acids like sulfuric acid or hydrochloric acid is done until the acid value of the oil become less than 1 mg of KOH/g of oil. In line with this, a number of parameters like the effect of the amount of the acid and the ratio of methanol to the acid during the esterification or effect of concentrations of the alkali sodium hydroxide, effect of temperature and effect of time were studied and optimized [10]. Thus, for oil with the recommended optimum acid value, the acid is usually removed by saponification or hydrolysis with sodium hydroxide solution according to the literature report [1-4]. Here, the degummed VO was mixed with sodium hydroxide solution and then heated to 40 ºC followed by stirring for 30 minutes. From the mixer, the oil-soap stock suspension passes through the centrifugal separator, which separates the soap stock from the neutral oil. The oil was dried for one hour on a rotary evaporator at 60 ºC. Separation occurs easily because the resulting soaps are practically insoluble in the neutral oil under standard operating conditions.

In the neutralization processes, sodium hydroxide solution of different concentrations is used according to the FFA content and quality of the oils. For FFA contents below one percent, more dilute solution (8 % to 12 %) is employed, whereas for higher FFA contents strength of about 15 % is required. Consequently, determination of acid value or FFA content of oil was done by titration of ethanolic solution of 0.5 g of the oil sample with 0.1 M KOH in the presence of 2 drops of phenolphthalein solution indicator.

3.1.2. Solid phase extraction

Solid-phase extraction (SPE) is a modified method derived a form of liquid-solid chromatographic extraction [12] which follows almost the same principles of high-

performance liquid chromatography. In this SPE process, the lipidic components of interest are retained in the adsorbent of disposable extraction mini-columns and later on eluted by appropriate solvents for effective purification [7]. In this study, solid phase extraction method was done as reported in the literature [5]. In this procedure, 10-20 g of CVO was dissolved in 10-20 ml n-hexane and mixed with 35 % activated carbon introduced from the top of 60 g packed silica gel. Then three different fractions were collected by enough amount of n-hexane, 1:1 volume ratio of n-hexane to diethyl ether and methanol, respectively to get glycerides and non-glycerides separated. This was followed by deacidification by solvent extraction or activated alumina to get the neutral oil [8-11]. The solvent extraction as deacidification method is a softer method carried out at room temperature and atmospheric pressure with less energy consumption and no change in physical properties of oil to be purified and hence has more advantages than chemical refining [9]. In this study, a mixture of ethanol and n-hexane or diethyl ether with a certain volume ratio was used for decalcification of the extracted oil. Alternatively, chromatographic deacidification by activated alumina was also done [11]. Of many chemical deacidification methods of high free fatty acid oils [9] supercritical fluid extraction and enzymatic deacidification, may be effective with no change in physical properties and no loss of neutral oil for the low thermal and oxidative stability vernonia oil, unfortunately, supercritical fluid extraction system and enzyme are not available here in our laboratory.

3.2. Derivitization of Vernonia Oil

3.2.1. Derivitization to Vernolic Acid (VA)

Hydrolysis of VO to VA was done based on procedures reported in the literature [5]. 50 mL methanol and 5 g (0.125 mol) sodium hydroxide are placed in a 250 mL distilling flask, equipped with a magnetic stirrer bar. The flask was then fitted with a condenser and the mixture was heated to reflux until complete dissolution of the sodium hydroxide. Vernonia Oil was added to the hot alkaline solution 5.12 g (5.53 mmol). The resulting brownish solution was refluxed with continuous stirring for 10 minutes, after which it was immediately transferred into a beaker and allowed to form a semisolid on cooling. About 100 g of ice was added, mixed thoroughly, followed by addition of 100 mL water with mixing. The cold mixture was vacuum-filtered to afford white solid soap in the filter bed. The soap was transferred into a beaker and mixed with 100 g ice and 100 mL water, then acidified with 4 mL glacial acetic acid. The acidified mixture was immediately vacuum filtered to afford a white solid acid. The cold white solid was transferred into a beaker, containing 100 mL hexane, with mixing to dissolve the acid and the resulting mixture was transferred into a separatory funnel to allow separation of the organic and aqueous phases. The hexane layer was stripped to afford crude VA.

Purification of the acid was accomplished by low-temperature recrystallizations. Hexane (50 mL) was added to a 150 mL beaker containing the crude vernolic acid and the beaker was placed in a freezer for 24 hours. The resulting solid was vacuum-filtered and rinsed with an additional 50 mL ice-cold hexane to get the pure acid. Alternatively, the purity of VA was checked first by thin layer chromatography (TLC) and then it was also purified by column chromatographic and solvent extraction methods.

3.2.2. Derivatization to methyl, ethyl and propyl esters (VAME/VAEE/VAPE)

Preparation of vernolic acid methyl ester (VAME), vernolic acid ethyl ester (VAEE) and vernolic acid propyl ester (VAPE) were accomplished by esterification of vernolic acid and transesterification of the neutral oil with methanol, ethanol & propanol respectively according to the procedure in scheme 3.2 reported in the literature [13]. First methanolic, ethanolic and propanoic hydrochloride acids solution were prepared by adding 2.5 mL of acetyl chloride to 50 mL of respective anhydrous alcohols in an ice bath and the mixture was left (closed) for 15 minutes. Then for transesterification reaction, 5 mL of methanolic, ethanolic or propanoic hydrochloric acid was mixed with 0.5 g of the vernonia oil dissolved in 3 mL of diethyl ether and refluxed for 3 minutes. Vernolic acid was esterified in the absence of diethyl ether. After cooling, the refluxed solution was transferred into a separatory funnel and mixed with 10-15 ml saturated NaCl solution. Then it was washed twice with 10 ml diethyl ether, and the lower phase was discarded. Finally, the diethyl phase was washed with 5-10 ml saturated NaCl solution and dried with 0.5 g sodium sulfate for 30 minutes which was then separated from solvent under vacuum drying.

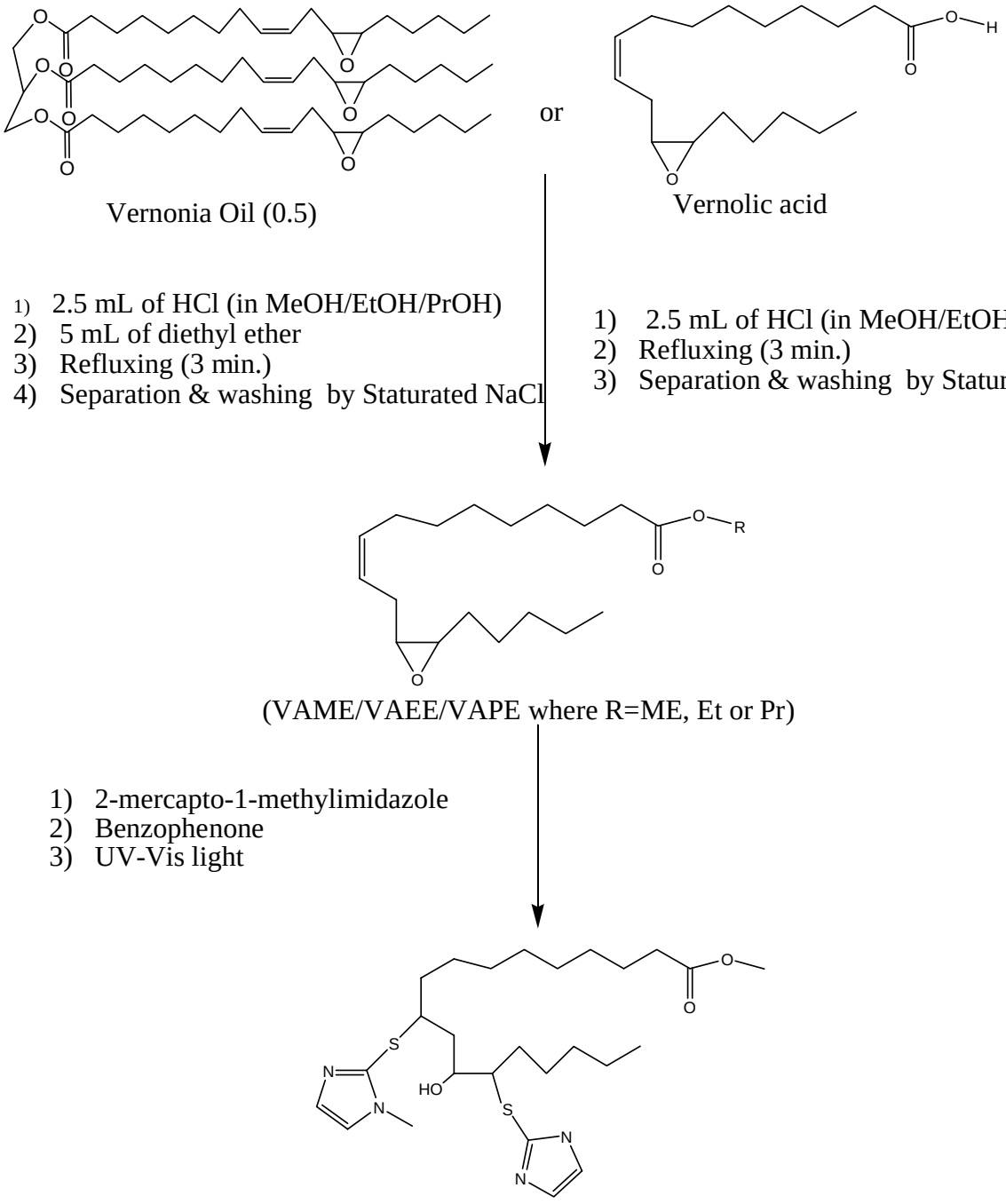

Scheme3. 2: Summary of the procedure for the synthesis of the esters and their functionalization with mercapto imidazole

3.2.3. Functionalization with mercaptoimidazole groups

Functionalization of vernolic acid methyl/ethyl/propyl ester with mercapto-imidazole was done according to the procedure reported in the literature with slight modifications [14] **(**scheme 3.2**).** A solution of vernolic acid methyl ester 1.42 mmol (0.40 g) 2-mercaptoimidazole mmol (0.1416 g), and benzophenone (20 mg), 4 mL dry methanol was placed in a glass quartz vial, which was subsequently sealed and irradiated using a UV-vis lamp of 150 W. The resulting orange solution was equilibrated at ambient temperature and vacuum-evaporated. The products were tested by TLC for their purities and separated by column chromatography using hexane-ethyl acetate solvent (90:10 v/v).

3.3. Surface Modification of OMMs with VAME and IFVAME

3.3.1. Support of Vernolic Acid Methyl Ester (VAME) on ordered mesoporous material (OMMs)

As reported in the literature [15], oleic acid is used as surface ligands for stabilization of nanocrystals. In a similar manner, we have tried to adopt procedures reported in the literature [16] to use VAME and IFVAME as the surface modification of OMMs. For a similar purpose, vernolic acid methyl ester was supported on three types of OMMs, namely ordered mesoporous aluminosilicate (Al-MCM-41 with Si/Al=15 & 3), siliceous Santa Barbara amorphous No-15 (SBA-15) & periodic mesoporous organosilica-PMO. Different ratios were tested in order to optimize the final composite as shown in scheme 3.3.

In a similar way to that of VAME, mercapto-imidazole functionalized VAME (IFVAME) was supported on the three OMMs based on optimum loading ratio resulted from VAME

loading according to the procedure given in the literature with slight modifications [16] (scheme 3.3).

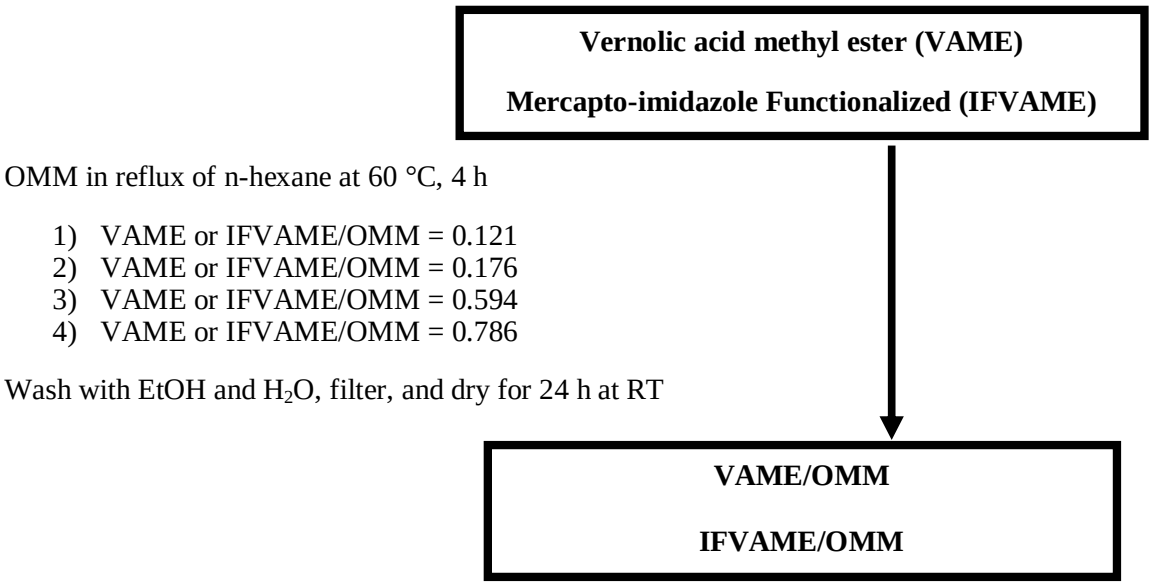

Scheme 3. 3: Surface Modification of OMM with VAME and IFVAME

3.3.2. Loading of Ag on modified OMMs

Impregnation or in-situ preparation of Ag nanoparticles on VAME or IFVAME supported OMMs (Al-MCM-41(Si/A=3 &15), SBA-15 and PMO) were done according to the literature reports with modification [17, 18] in order to prepare smaller size silver nanoparticles with less aggregation and higher stability with higher capacity in liquid phase catalysis. Thus, 0.15 g of VAME/IFVAME-OMMs was suspended in 15 mL of DMF solution of 1.2 g $AgNO_3$. The mixture was equilibrated by stirring for 12 h. Freshly prepared DMF solution of 120 mg of $NaBH_4$ in 15 mL DMF was added to the mixture dropwise at a reduced temperature (3–5 ºC) with constant stirring. The color change of

the solution is recorded during the addition of $NaBH_4$ to check for the formation of silver nanoparticles. The mixture was then further stirred for 2 h. Then it was filtered, washed with acetone, vacuum dried and labeled as Ag-mOMMs (Ag-mMCM-3, Ag-mOMM-15, Ag-mSBA & Ag-mPMO). This is summarized in scheme 3.4.

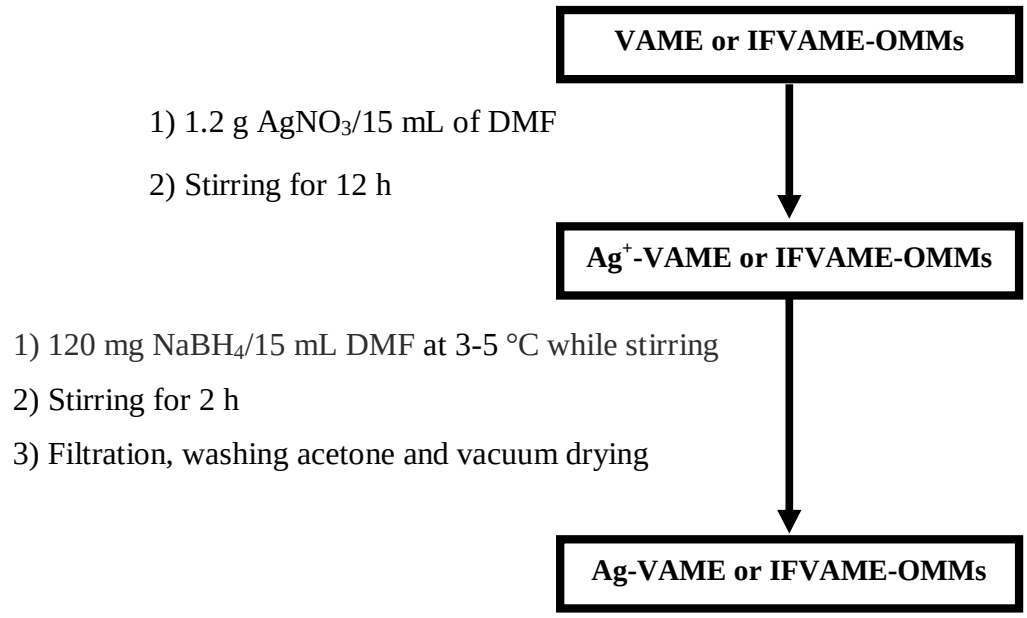

Scheme 3. 4: Synthesis of Ag nanoparticles on the supported VAME/IFVAME on OMMs

3.4. Test for the catalytic activity of modified OMMs

The preliminary photodegradation test was done based on the procedure reported in the literature [19, 20] with slight modification (scheme 3.5)**.** After preparation of 100 mL of methyl orange (MO) solution, 4 mL of 10 ppm of MO was added to a quartz cuvette and 3 mg of Ag-mSBA was added, stirred and tied inside the quartz glass nearer to UV reactor lamp of 150 W at one inlet, As a control test, an additional 4 mL of methyl orange without the catalyst was tied and put in a similar way at the other inlet. Thereafter, it was irradiated with UV light of a UV reactor for 8 h. Furthermore, for AgmSBA

photodegradation test was done at varying time by taking 166 mg of AgmSBA in 500 mL of 10 ppm MO dye [20] under oxygen purge and magnetic stirring in 150 W lamp UV reactor. Apart from this, chemo degradation test of methylene blue (MB) model organic dye by AgmOMMs was carried out according to the procedure reported in the literature [21]. In this procedure, 1 mg of each of Ag-VAME-OMMs was dispersed into the MB dye (0.5 $x10^{-4}$ M) solution in water (2.8 mL) followed by rapid injection of 0.5 mL of an aqueous solution containing $NaBH_4$ (0.01M) under stirring. Then finally, the change in color is observed and the UV- Visible spectra were recorded for all the samples.

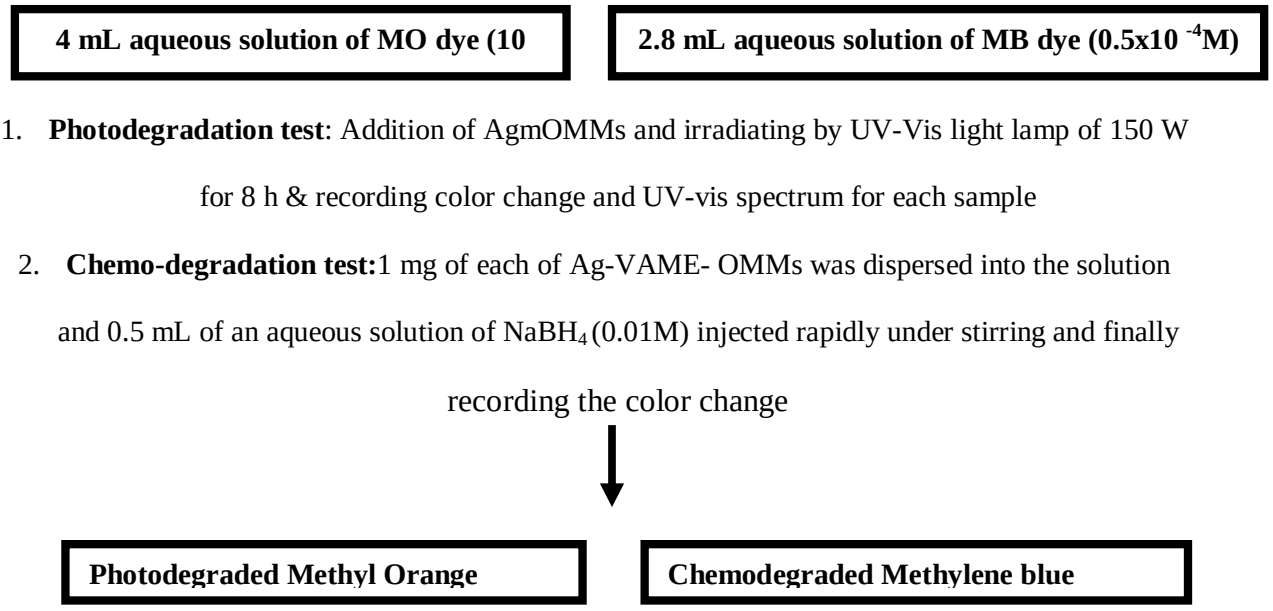

Scheme 3.5: Test for photo/chemo degradation catalytic activity of AgmOMMs on model organic dyes (methyl orange and methylene blue)

3.5. References

1 Mbugua MN, Yusuf AO, Gitu PM, Bhatt BM: **Conversion of *Vernonia galamensis* Oil to Pyridinyl-Vernolamides and their Antimicrobial Activities**. *Bull Chem Soc, Ethiop* 2007, **21**(1):108-110.

2. Ayorinde FO, Saeed KA, Price E, Morrow A, Collins WE, McInnis F, Pollack SK, Eribo BE: **Production of poly-(β-hydroxybutyrate) from saponified *Vernonia galamensis* oil by Alcaligenes eutrophus**. *J. of Industrial Microbiology and Biotechnology* 1998, **21**(1):46-50.

3. Ayorinde FO, Nana EY, Nicely PD, Woods AS, Price EO, Nwaonicha CP: **Syntheses of 12-aminododecanoic and 11-aminoundecanoic acids from vernolic acid**. *JAOCS* . 1997, **74**(5):531-538.

4. Mambo CK, Gitu PM, Bhatt BM, Chweya J, Grinberg S, Mills D: **Synthesis of Vernolamide Containing Tretiary Amino Groups from Vernonia galamensis Oil and Their Biological Activities**. *Bull Chem Soc, Ethiop* 1998, **12**(2):121-128.

5. Neff WE, Adlof RO, Konishi1 H, Weisleder D: **High-Performance Liquid Chromatography of the Triacylglycerols of *Vernonia galamensis* and *Crepis Alpina* Seed Oils**. *JAOCS*, 1993, **70**:449-455.

6. Nilsson UJ: **Solid-phase extraction for combinatorial libraries**. *J of Chr, A* 2000, **885**(1):305-319.

7. Ruiz-Gutiérrez V, Pérez-Camino MC: **Update on solid-phase extraction for the analysis of lipid classes and related compounds**. *J. of Chr. A* 2000, **885**(1):321-341.

8. Abd El-Salam ASM, Doheim MA, Sitohy MZ, Ramadan MF: **Deacidification of High-acid Olive Oil**. *J. of Food Processing & Technology* 2015, **5**.

9. Christianne ECR, Goncalves CB, Batista E, Antonio JAM: **Deacidification of Vegetable Oils by Solvent Extraction**. *Recent Patents on Engineering* 2007, **1**(1):95-102.

10. Ding J, Xia Z, Lu J: **Esterification and Deacidification of a Waste Cooking Oil for Biodiesel Production**. *Energies* 2012, **5**(12):2683-2691.

11. Ayorinde FO, Hassan M: **Deacidification of vegetable oils**. In Google Patents; 1995.

12. Roberts JD, Caserio MC: **Separation, Purification and Identification of Organic Compounds by Spectroscopic Techniques BSOC Chapter 9, second edition, Benjamin, Inc., Menlo Park,** *Caltech* 1977:258-348.

13. Christie WW: **Preparation of Ester Derivatives of Fatty Acids For Chromatographic Analysis, Oily Press, Dundee** *JAOCS* 1983: 69-111.

14. Bromberg L, Chen L, Chang EP, Wang S, Hatton TA: **Reactive Silver and Cobalt Nanoparticles Modified with Fatty Acid Ligands Functionalized by Imidazole Derivatives**. *Chemistry of Materials* 2010, **22**(18):5383-5391.

15. Liu B, Deng X, Xie Z, Cheng Z, Yang P, Lin J: **Thiol-Ene Click Reaction as a Facile and General Approach for Surface Functionalization of Colloidal Nanocrystals**. *Advanced materials* 2017, **29**(36).

16. Li Z, Zhu Y: **Surface-modification of SiO_2 nanoparticles with oleic acid**. *Applied Surface Sci.* 2003, **211**(1-4):315-320.

17. Gupta R, Ganesan V: **Gold nanoparticles impregnated mesoporous silica spheres for simultaneous and selective determination of uric acid and ascorbic acid**. *Sensor and Actuator B: Chemical* 2015, **218**:139-145.

18. Huang R-S, Hou B-F, Li H-T, Fu X-C, Xie C-G: **Preparation of silver nanoparticles supported mesoporous silica microspheres with perpendicularly aligned mesopore channels and their antibacterial activities**. *RSC Advances* 2015, **5**(75):61184-61190.

19. Zhou R, Srinivasan MP: **Photocatalysis in a packed bed: Degradation of organic dyes by immobilized silver nanoparticles**. *J. of Envir. Chem Engin.* 2015, **3**(2):609-616.

20. Colpini LMS, Lenzi GG, Urio MB, Kochepka DM, Alves HJ: **Photodiscoloration of textile reactive dyes on Ni/TiO_2 prepared by the impregnation method: Effect of calcination temperature**. *J. of Envir.l Chem. Engin.* 2014, **2**(4):2365-2371.

21. Chen L, Hu J, Qi Z, Fang Y, Richards, R: **Gold Nanoparticles Intercalated into the Walls of Mesoporous Silica as a Versatile Redox Catalyst**. *Ind Eng Chem Res* 2011, **50**:13642–13649.

4. Results and Discussion

4.1. Characterization of crude (CVO) and neutral vernonia oil (NVO)

The crude vernonia oil extracted from the seeds of *vernonia galamensis* (40 % yield) was purified yielding deep golden yellow neutral vernonia oil via conventional methods (bleaching, degumming & neutralization). The results achieved are in good agreement with the results found in the literature [1-4]. The process of conventional deacidification with aqueous sodium hydroxide solution during neutralization is effective only for oil of free fatty acid (FFA) content not exceeding 8-10 %. For oils with greater FFA content, deacidification can be performed with high neutral oil losses by hydrolysis during neutralization and by emulsion during washing and the biochemical process by lipase enzyme, with the formation of much soap that cannot be separated from the neutral oil [5-7]. In order to minimize the loss of vernonia oil, a new method of solid phase extraction with slight modification as reported in the literature [5] was used. As a result, the obtained percent recovery by conventional deacidification method is found to be less than that of solid phase extraction method supported by other deacidification methods such as solvent extraction [8] and liquid chromatographic treatment by activated alumina in the presence of isopropanol as eluent [9]. The TLC test in a varying ratio of n-hexane to ethyl acetate shows more than one spot due to the fact that an attempt to purify by recrystallization in n-hexane at a lower temperature was ineffective. This may be due to the formation of free fatty acid and a mixture of glyceride impurities, which may result from base catalyzed neutralization and hydrolysis reaction and water moisture used during the work up. Thus, further purification was done by column chromatographic

separation and solvent extraction. The other major factors that affect percentage yield of the oil content of the seed includes the type of the seed (ecotype), the solvent used, the particle size of the flour, age of seeds, the storage temperature of seeds and the time of extraction [10]. After extraction of CVO and the necessary purification steps to get NVO, the ^{1}H NMR, ^{13}C NMR, and FT-IR spectra were recorded to identify the major functional groups namely: the ester, the double bond and the epoxide moiety.

4.1.1. ^{1}H and ^{13}C NMR measurements of CVO and NVO

Figure 4.1 shows the ^{1}H NMR spectra of CVO and NVO containing the different protons as assigned in table 4.1. Apart from the data given in table 4.1, there are also peaks at 3.60 ppm and 3.5-3.8 ppm which indicate the presence of free fatty acids (FFA) and free glycerol, respectively.

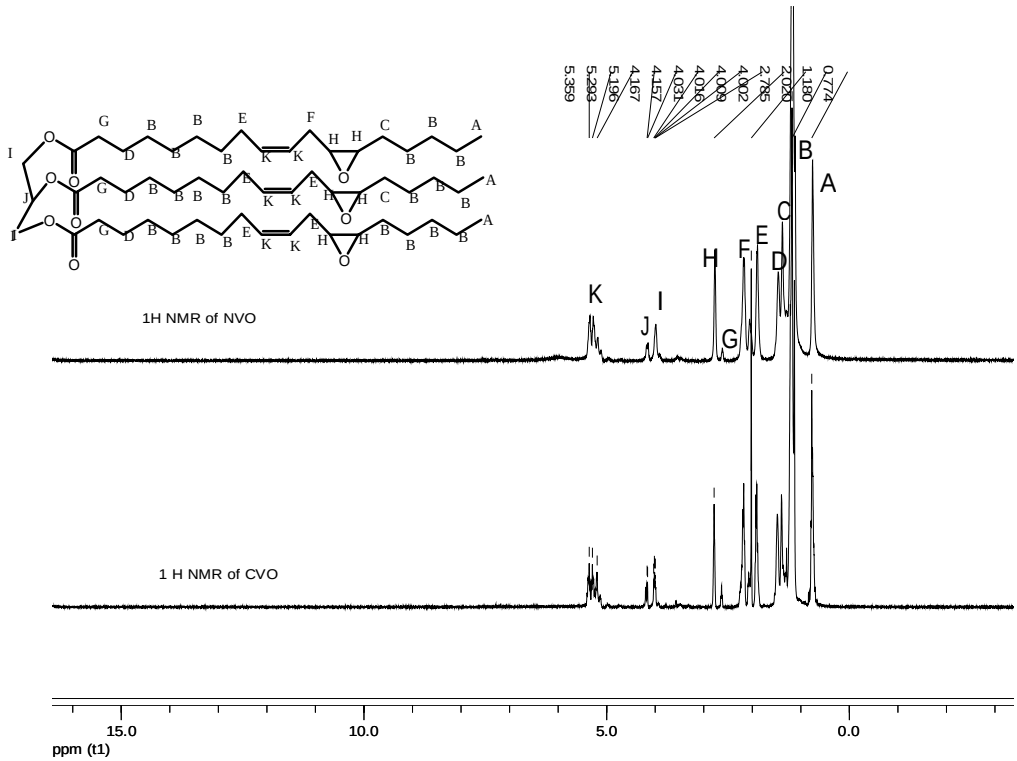

Figure 4. 1:[1]H NMR (ppm, 400 MHz, $CDCl_3$) spectrum of NVO compared to that of CVO

Table 4. 1: [1]H NMR of crude (CVO) and neutral vernonia oil (NVO)

Types of Protons	δ (ppm)	
	CVO	NVO1
Glyceryl ($-CH_2$)	5.20-5.26	5.24-5.44
Glyceryl ($-CH_2$)	5.20-5.36	5.24-5.44
Glyceryl ($-CH_2$)	4.00-4.20	4.04-4.24
Epoxy (-O-C-H)	2.63-2.79	2.68-2.85
Methylene($-CH_2-CH=CH-CH_2-$)	2.02-2.18	1.97-2.25
Methylene $(-CH_2)_n$	1.18-1.40	1.26-1.56
Methyl ($-CH_3$)	0.77	0.82

The epoxide content of the oil is 1.5 (= 3/2) epoxide groups per triglyceride. Thus, the

vernolic acid content in the oil is 50 % (=1.5/3). This value is consistent with the proton count of the alpha CH of the oxirane group observed at 1.46 ppm. Vernolic acid also has a unique characteristic peak between 2.16-2.17 ppm is due to the content of the CH amid the double bond and epoxy ring. Using the integral value of 2.47 suggests that 41 % of NVO is composed of VA. The peak at 3.89 ppm shows the presence of hydroxyl protons. The integrals of secondary and primary hydroxyl protons ratio give 1 and 3.27 protons instead of 1 and 4, respectively. Moreover, there are also about four separate peaks observed in the olefinic proton peaks region which indicate that the NVO oil is not purely in the form of triglycerides i.e. free fatty acids mono- and diglycerides are also present due to the biochemical conversion of triglycerides. The NMR spectrum result generally shows that there is an insignificant change of characteristic functional groups of crude oil during purification and work up. Furthermore, the characterization result is in good agreement with the literature report [10]. The purified vernonia oil obtained by solid phase extraction alternative method reported in the literature with slight modification [5] showed a similar result on characterization by ^{1}H NMR spectroscopy. Purified vernonia oil PVO separated by modified solid phase extraction, the epoxide content of the oil is 1.82=3.64/2 and the vernolic acid content of the oil is 60 %. Using alpha CH proton amid double bond and epoxy groups, the integral value of characteristic VA peaks at 2.00-2.17 gives 35 % of the oil is VA. Thus, the VA content of PVO is 35-60 % which is greater than that of the NVO from the conventional method.

The spectrum in Figure 4.2 and Table 4.2 correspond to the ^{13}C NMR data showing carbonyl carbon, olefinic carbons, glyceryl carbons, epoxy carbons, methylene, and methyl carbon. There is also a small peak at 177.28 ppm, which may indicate the

presence of saturated fatty acids in the crude vernonia oil. The peaks at around 127 and 130 ppm also indicate the presence of unsaturated fatty acids. The characteristic functional group's spectral result is in good agreement with the literature report [1-4]. The results obtained indicate that the major functional groups such as the carbon-carbon double bond, epoxy group and triglyceride ester characteristic components of vernonia oil remain intact throughout the extraction and purification processes. The neutral vernonia oil possesses additional peaks because of the presence of other saturated triglyceride oils corresponding to fatty acids such as stearic acid, palmitic acid, and arachidic acids. This can be confirmed from the peak at 177.28 ppm in $^{\text{the}}$ ^{13}C NMR spectrum of crude vernonia oil. The ^{13}C NMR spectrum of purified vernonia oil by modified solid phase extraction gave similar result except for the appearance of peaks of free fatty acids at 178.57 ppm in addition to peaks at 130 & 127 ppm. Consequently, it was deacidified by solvent extraction and chromatographed with activated alumina for further use.

Table 4. 2: ^{13}C NMR spectra of crude (CVO) and neutral vernonia oil (NVO).

: Types of Protons	δ (ppm)	
	CVO	NVO
Vernonyl Carbonyl (O=C)	172.50-173.40	172.70-173.64
Olefinic (CH=CH)	123.83-132.25	123.80-132.41
Glyceryl (CH)	68.88	68.84
Glyceryl (CH_2)	61.91-64.79	62.00-64.87
Epoxy (O-C-H)	56.41-57.17	56.49-57.18
Methylene $(CH_2)_n$	22.55-34.51	22.52-34.35
Methyl (CH_3)	13.95	13.93.

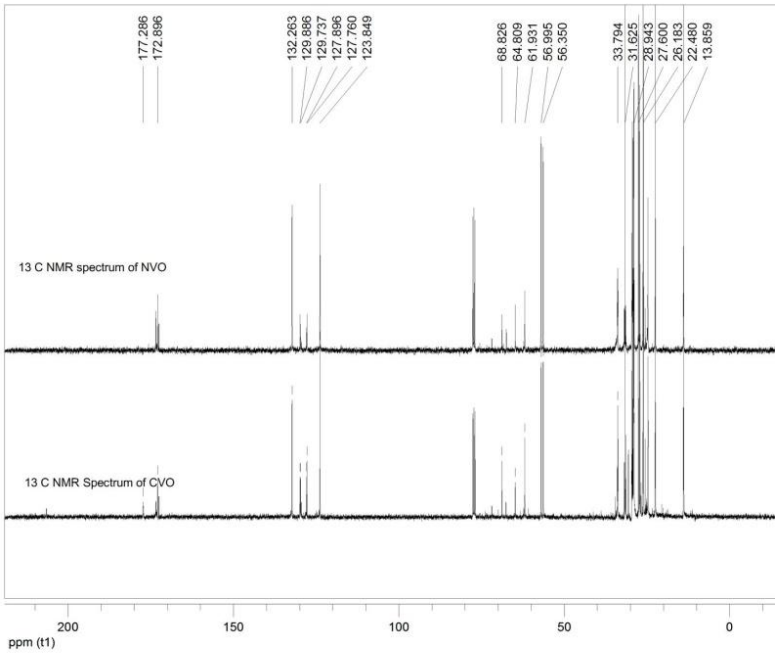

Figure 4. 2: ^{13}C NMR spectrum of NVO compared to that of CVO

4.1.2. FT-IR studies on CVO and NVO

The FT-IR spectra of CVO and NVO recorded in chloroform solution are as shown in Figure 4.3, and the assigned bands are listed in Table 4.3.

Table 4. 3: FT-IR Spectra of CVO and NVO.

Functional group (mode of vibration & intensity)	Wave number (cm^{-1})	
	CVO	NVO
Olefinic =CH (cis) (str.)	3010	3010
Methyl -C-H (CH_3) (str. as.)	2928	2928
Methylene –C-H (CH_2)	2856	2856
Carbonyl C=O of ester (str.)	1741	1738
Olefinic Carbon (-C=C-) (str.)	1521	1522
CH, CH_2 (ben, ciss.)	1466	
C-O of oxirane group	929	758
$(CH_2)_n$ rocking	758	758

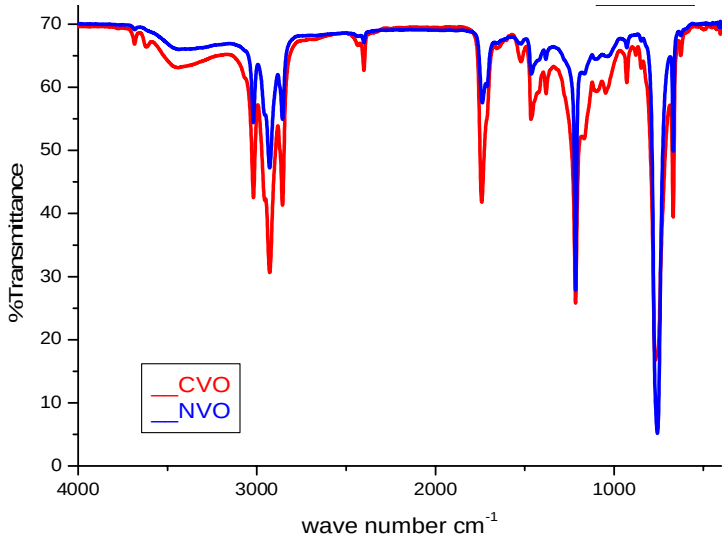

Figure 4. 3: FT-IR spectrum of NVO compared to that of CVO.

The spectra show characteristic functional groups of the oil, namely the olefinic C-H stretching bands at 3010 cm^{-1} with olefinic C=C stretching bands at 1521 cm^{-1}, C-H

stretching of methyl bands at 2928 cm^{-1} & bending at 1466 cm^{-1}, C-H of Methylene stretching bands at 2856 cm^{-1}& bending at 1466 cm^{-1}, carbonyl stretching bands of ester at 1738-1741 cm^{-1}, epoxy stretching bands at 758-929 cm^{-1} and long-chain methylene stretching at 758 cm^{-1} confirming the existence of the oil functional groups which remain intact during purification. This result is consistent with that reported in the literature [1-4]. The crude vernonia oil contains hydroxyl monomer around 3600 cm^{-1} which may be due to the presence of free fatty acids.

4.2. Characterizations of Vernolic Acid (VA)

Vernonia oil was derivatized to vernolic acid by hydrolysis of NVO and purification of the acid by solvent extraction according to the literature report [3], as shown in scheme 4.1.

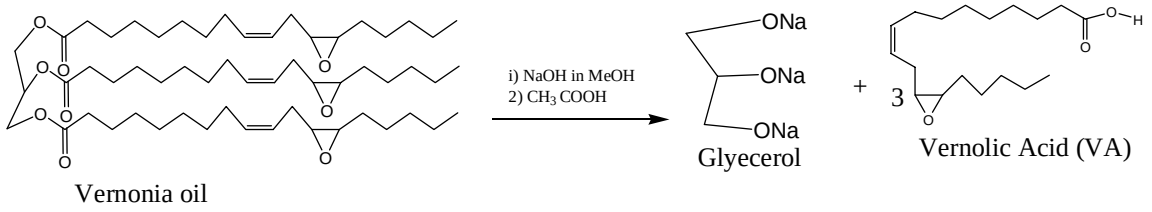

Scheme 4. 1: Synthesis of Vernolic Acid by hydrolysis of Vernonia oil

4.2.1. ^{1}H NMR and ^{13}C NMR spectral studies of VA

The ^{1}H NMR and ^{13}C NMR spectral analysis of vernolic acid was done to show the presence of major functional groups of the acid. Figure 4.4 shows the ^{1}H NMR data of the vernolic acid indicating the presence of hydroxylic protons (-O<u>H</u>) at 10.85 ppm, olefinic protons (C<u>H</u>=C<u>H</u>) at 5.33-5.44 ppm, epoxy protons (O-C-<u>H</u>) at 2.74-2.96 ppm, protons of

methylene attached to olefinic group (-C<u>H</u>$_2$-CH=CH-C<u>H</u>$_2$-) at 2.02-2.32 ppm, protons of methylene groups (C<u>H</u>$_2$)$_n$ at 1.25-1.63 ppm, and protons of methyl (C<u>H</u>$_3$) group at 0.87 ppm. The characteristic functional groups' spectral result is in good agreement with the literature report [1-4].

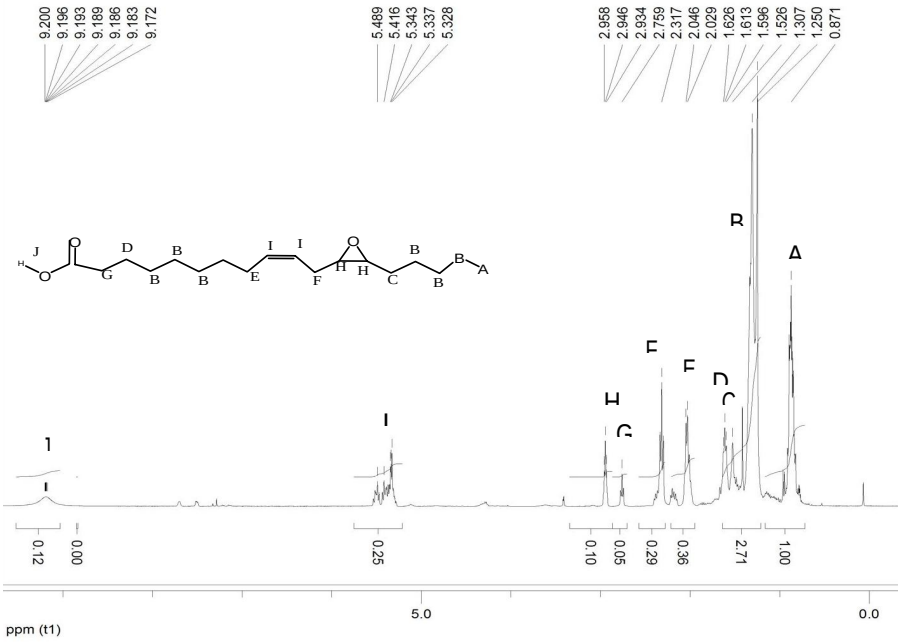

Figure 4. 4: ^{1}H NMR spectrum of vernolic acid (VA) (δppm, 400 MHz, $CDCl_3$)**.**

It can be noted from the spectrum (Figure 4.4) that the new peak corresponding to hydroxyl proton of vernolic acid and the disappearance of glycerol proton in the region 4.00-4.34 after the hydrolysis also confirms the success of hydrolysis of vernonia oil.

The ^{13}C NMR spectrum of the VA (Figure 4.5) shows the presence of the carbonyl carbon (O=<u>C</u>) at 179.67-179.74, olefinic carbons (<u>C</u>H=<u>C</u>H) at 124.38-132.92, epoxy carbons (O-C-H) at 56.02-56.59, methylene carbons (<u>C</u>H$_2$)$_n$ at 22.60-34.21, and methyl carbon (<u>C</u>H$_3$) at 14.41 which are characteristic peaks of vernolic acid.

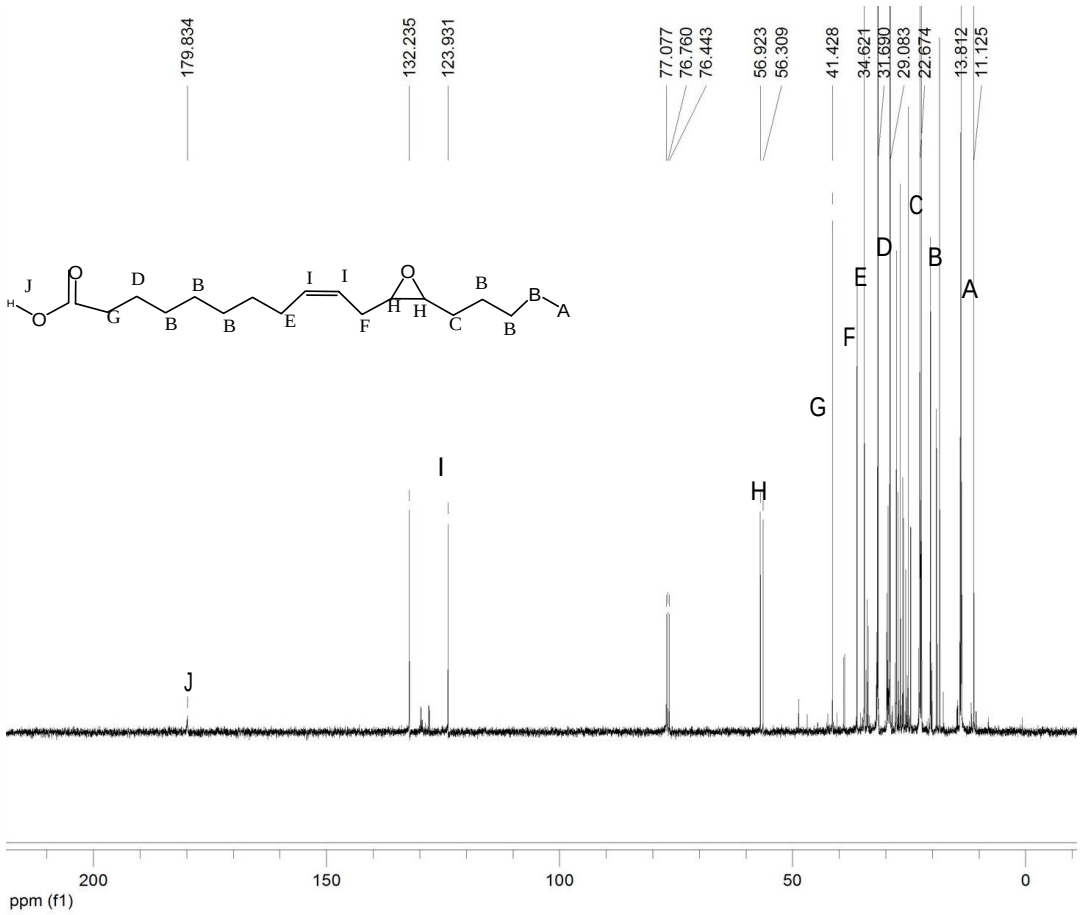

Figure 4. 5: ^{13} C NMR spectrum of vernolic acid (δ ppm, 400 MHz, $CDCl_3$)

4.2.2. FT-IR Spectral studies of VA

In general, during the extraction of vernolic acid by saponification and acidification of neutral VO, it can be noted that the disappearance of peaks characteristic of glyceryl proton and carbons (CH, CH_2) and the appearance of OH peak characteristic of vernolic acid confirms its formation (figure 4.6).

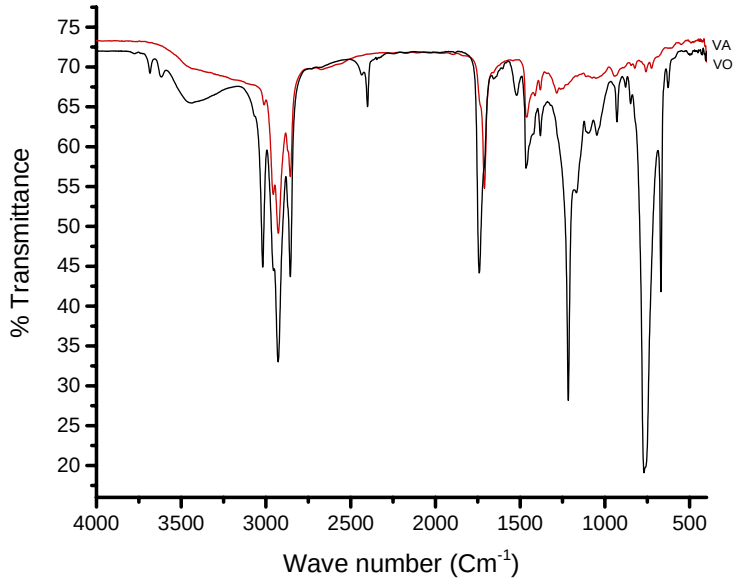

Figure 4. 6:.FT-IR spectra of VA (red-top) and VO (black bottom)

Note the weak peak at about 2970 cm^{-1}, a strong and broad peak from 3300 to 2900 cm^{-1} and peak of carbonyl of acid at about 1713 cm^{-1} confirms the formation of vernolic acid during hydrolysis. The absence of peaks at 1711 cm^{-1} in the FTIR spectrum of vernonia oil shows the absence of significant free fatty acids. Note also that the peak of carbonyl stretching peak shifted from 1741 cm^{-1} of the VO ester to 1713 cm^{-1} of the VA which also confirms the acid formation.

4.3. Characterizations of Vernolic Acid Alkyl Ester (VAME/VAEE/VAPE)

Vernolic acid methyl/ethyl/propyl ester was synthesized according to procedures reported in the literature [11] via acid catalyzed esterification of VA or transesterification of NVO (scheme 4.2).

The percentage recovery yield of VAME synthesized by acid catalyzed transesterification of veronia oil was 45 %, which is found to be a better result than that of acid catalyzed the esterification of vernolic acid synthetic route (30 % yield). Furthermore, the synthesis of vernolic acid methyl ester via esterification reaction is a long process that involves first saponification of the neutral oil and then acidification of the oil to get vernolic acid and finally esterification of the neutral oil to get vernolic acid methyl ester, whereas in the case of transesterification synthetic route, vernonia oil is directly converted to the methyl ester. Thus, the transesterification synthetic root was chosen for the synthesis of VAME, VAEE and VAPE and the obtained products were used for characterization and functionalization work.

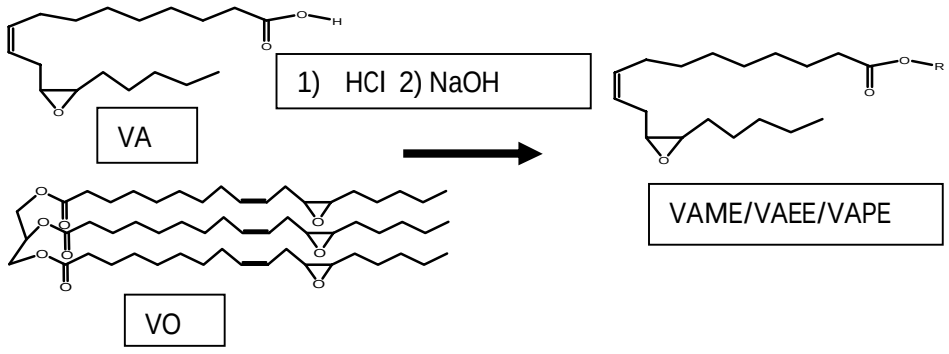

Scheme 4. 2: Derivatization of VO (a) and VA (b) to VAME/VAEE/VAPE

4.3.1. ^{1}H and ^{13}C NMR Spectral studies of VAME/VAEE/VAPE

The esters of VA were purified by column chromatographic separation based on TLC purity test result. The ^{1}H & ^{13}C NMR spectra of vernolic acid alkyl ester (VAME/VAEE/VAPE) were analyzed as follows to show major functional groups according to the literature report [11]. ^{1}H NMR spectrum of VAME is shown in figure 4.7

as an example where we could identify the presence of major functional groups and absence of glycerol protons at 4.04-4.24 ppm as indicated in table 4.4. All the indexing data are collected in Table 4.4. The peak areas of the double bond, epoxy and methyl functional groups of VAME are 1, 0.83 & 1.67, respectively compared to 1, 1, & 1.5 of their theoretical values for VAME. The epoxy group has undergone partial ring opening. It also indicates that the integrated peak areas of the double bond, epoxy, and ethyl functional groups of VAEE are 1, 0.43 & 1.79 respectively, whereas such integral peak areas of a double bond, epoxy, and propyl functional groups of VAPE are 1, 0.68 & 3.08 respectively compared to their corresponding theoretical values. This result generally shows that there are less epoxy functional groups (higher partial epoxy ring opening) and higher proton number of ethyl group of VAEE or propyl group of VAPE compared to the methyl group of VAME. Note also that VAME, VAEE and VAPE show additional peaks at 3.79-3.88 ppm and 3.28-3.29 ppm, which may also be due to partial epoxy ring opening by in-situ generated HCl catalyst that in turn introduces chloro & hydroxo substituents, respectively. This is also the main reason of intensity reduction in the epoxy protons signal. Similarly, the ^{13}C NMR spectrum (figure 4.8) shows the main functional groups of the alkyl (methyl/ethyl/propyl) esters as the data indexed in table 4.5. Apart from the given data, new peaks appeared at 67.41-67.88 & 73.44 ppm. These may be due to the hydroxo and cloro substituents resulting from partial ring opening of an epoxy group whose intensity is diminished. Furthermore, the unusual different integral peak values for VAEE compared to that of VAPE may be due to the less purity of VAEE because of the presence of unsaturated free fatty acid esters as shown by peaks at 127 and 130 ppm in the ^{13}C NMR spectrum. The ^{13}C NMR spectra of the VAME/VAEE/VAPE

are shown in Figure 4.8 and the indexing data are collected in Table 4.5.

Table 4. 4: Data of ^{1}H NMR Spectrum of VAEE & VAPE compared with VAME

Type of Proton	δ (ppm)		
	VAME	VAEE	VAPE
Olefinic(CH=CH-)	5.20-5.40	5.29-5.48	5.30-5.43
Glyceryl(-CH)	-	-	-
Glyceryl (-CH_2)	-	-	-
Alkoxy (-O-Me/Et/Pr)	3.30-3.40	3.61	3.56-3.57
Epoxy (-O-C-H)	2.73	2.51-2.71	2.46-2.54
Methylene (-CH_2-CH=CH-CH_2-)	2.20-2.27	2.23-2.24	2.17-2.21
Methylene groups (-CH_2)$_n$	1.20-1.21	1.20-1.77	1.21-1.96
Methyl /Ethyl/Propyl(-Me/Et/Pr)	0.77	0.84	0.84

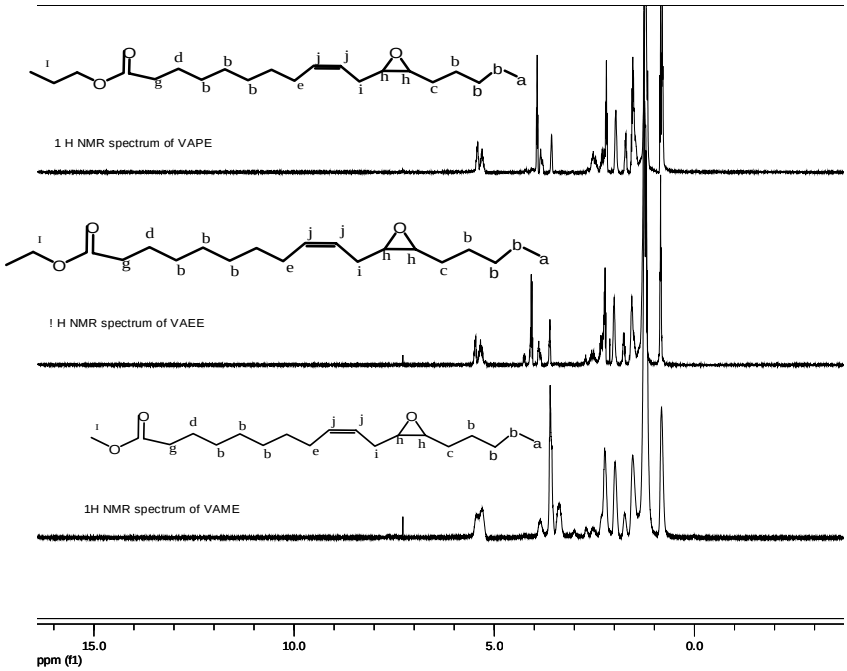

Figure 4. 7: The ^{1}H NMR spectra δ (ppm), 400 MHz, $CDCl_3$) of VAME/VAEE/VAPE.

Table 4. 5: Data of ^{13}C NMR of VAEE/VAPE and VAME

Type of Carbon	δ (ppm)		
	VAME	VAEE	VAPE
Vernonyl Carbonyl C (O=C)	174.05	173.80	173.78
Olefinic(CH=CH)	124.3-132.1	124.26-133.20	124.35-133.01
Epoxy (O-C-H)	57.9	57.88	
Alkoxy C (O-Me/Et/Pr)	51.3	51.37	51.99
00Methylene C $(CH_2)_n$	22.41-34.8	22.47-34.27	21.93-34.24
Methyl/Ethyl/Propyl C (Me/Et/Pr)	13.95	14.19	13.91

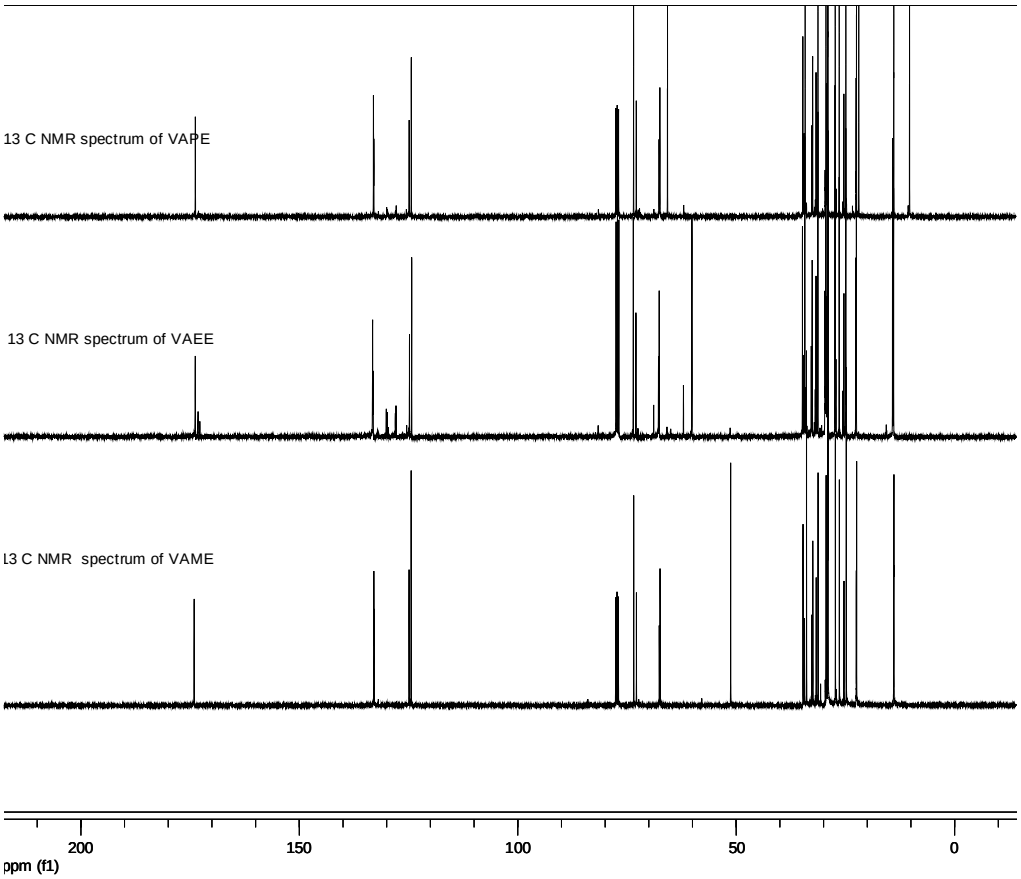

Figure 4. 8: ^{13}C NMR spectra (δ (ppm), 400 MHz, $CDCl_3$) of VAME /VAEE and VAPE

4.3.2. FT-IR studies of VAME/VAEE/VAPE

FT-IR spectra of VAME, VAEE, and VAPE are presented in Figure 4.9 and compared with that of NVO. Theoretically, VAME/VAEE/VAPE and its precursor (NVO) group bond vibrations bands like X-H single bond stretching (O-H & C-H) appear in the range 3600-2700 cm^{-1}, H-bonded stretching 3300-2500 cm^{-1}, double bond stretching (C=O, C=C) 2400-1550 cm^{-1}, C-O-C stretching of esters 1200-1050 cm^{-1}. Thus, in line with this, the indicated stretching frequencies of the functional groups (olefinic, hydroxyl, methyl/ethyl/propyl, methylene, alkoxy (methoxy, ethoxy/propoxy) (table 4.8) are in agreement with the results obtained from the spectra [11].

Table 4. 6: Summary of FT-IR spectral analysis of NVO, VAME, VAEE & VAPE

The functional group (mode of vibration)	Frequency (cm^{-1})			
	NVO	VAME	VAEE	VAPE
Hydroxyl H-bond (OH) (str.)	3448	3482	3476	3473
Olefinic =CH (cis) (str.)	3027	3008	3008	3008
Methyl -C-H (CH_3) (str. As.)	2928	2929	2929	2929
Methylene –C-H (CH_2) (str.)	2856	2856	2856	2857
Carbonyl C=O of ester (str.)	1738	1743	1740	1739
Olefinic (-C=C-) (str.)	1522	1655	1648	1630
CH, CH_2 (bend. Scis.)	1465	1465	1466	1466
C-H(CH_3) (bend.)	1381	1379	1378	1381
Alkoxy C-O-C (str.)	900-1220	900-1250	900-1250	900-1250
Epoxy group C-O (str.)	943	870	860	858
$(CH_2)_n$(bend., rock.)	758	727	727	728

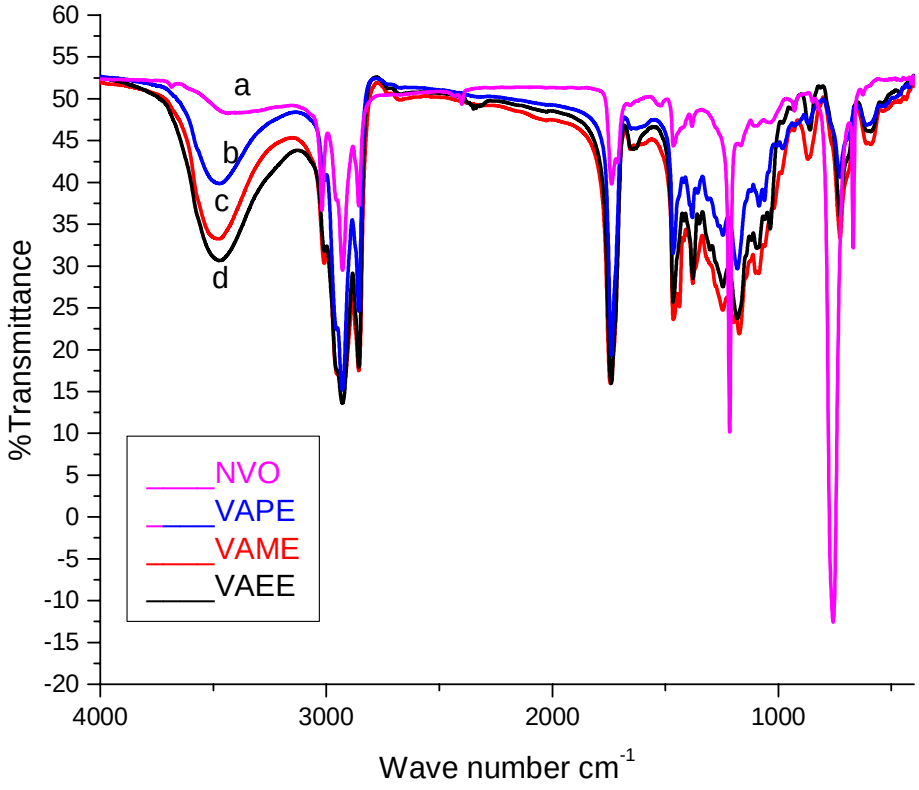

Figure 4. 9: FT-IR spectra of NVO and vernolic acid alkyl (methyl/ethyl/ propyl) esters (Top to bottom NVO (a), VAPE (b), VAME (c) & VAEE (d).

4.4. Characterization of mercapto imidazole functionalized VAME (IFVAME)

Photo-initiated thiol-ene reaction is the addition of thiols to an alkene. Such reaction is developed since 1905 [12] and recently studied extensively [13, 14] to functionalize fatty acid molecules and their derivatives from vegetable oils because of their relatively low cost, renewability, and biodegradability (environmental compatibility). However, the reactivity of their double bonds are generally weak and hence need special conditions for the optimum reaction [14]. In principle, fatty acids/esters with double bonds at or near

terminal positions with less steric hindrance [12] and the high thiolene ratio increases the efficiency of the reaction conversion [13]. To increase the functionality of vernolic acid alkyl esters, in this study functionalization with 2-mercapto-1-methyl imidazole was conducted on VAME by thiol-ene coupling reaction according to the procedure reported in the literature [15]. The light golden yellow color of the starting reaction mixture finally changed to orange color after UV light irradiation and equilibration time. After vacuum drying, the crude yield was 60% with respect to 2-mercapto-1-methyl imidazole or 32 % with respect to VAME. To increase the optimum yield, the mercapto-imidazole to VAME ratio was increased up to 4 to 1 molar ratio. The purity of the product was checked by TLC test, which showed many spots due the presence of many components including unreacted precursor materials and then purification was done by solvent extraction and/or column chromatographic separation in 70:30 n-hexane: ethyl acetate. Thus, IFVAME is formed as indicated in scheme 4.3.

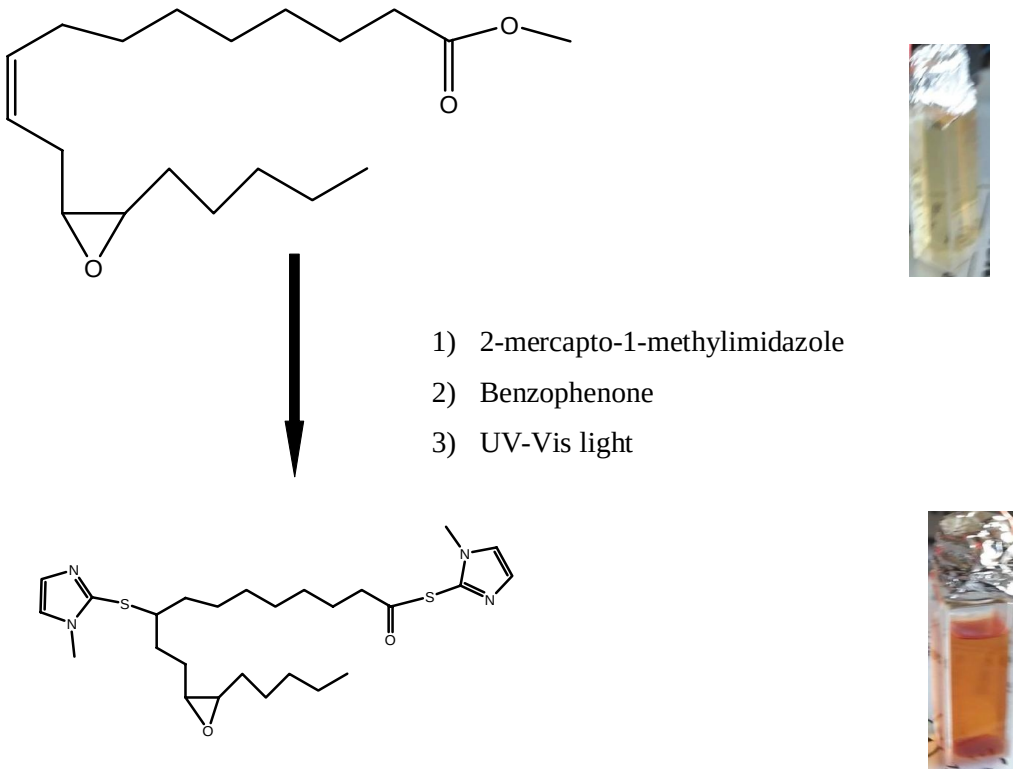

Scheme 4. 3: Functionalization of VAME to form IFVAME.

4.4.1. ^{1}H and ^{13}C NMR characterization of IFVAME

The ^{1}H &^{13}C NMR data of IFVAME was recorded and compared with ^{1}H &^{13}C NMR of VAME as shown in figure 4.10

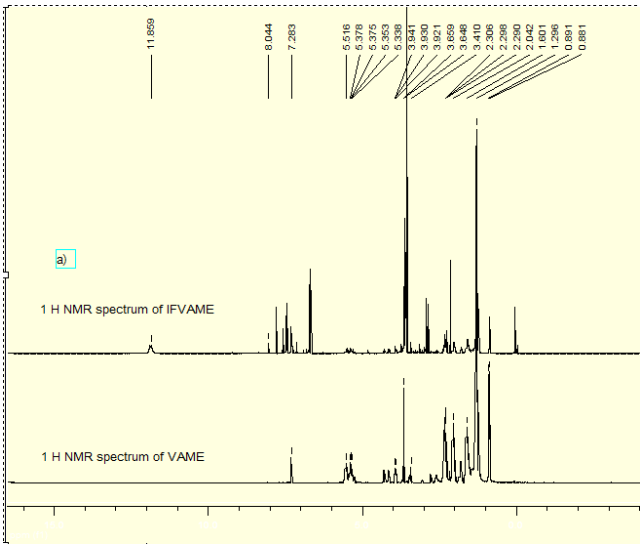

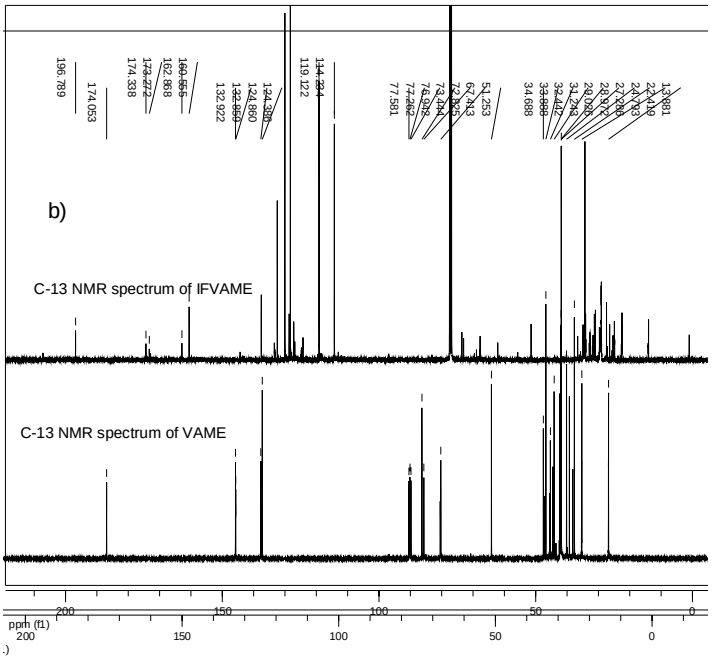

Figure 4. 10: a) ^{1}H NMR and b) ^{13}C NMR spectra of IFVAME compared to that of VAME

The analysis of ^{1}H NMR spectrum shows the characteristic aromatic imidazole ring protons at 6.99–7.09 ppm and CH_3 proton attached to imidazole ring at 3.67 ppm in addition to other functional groups existing on VAME. The ^{13}C NMR spectrum of

IFVAME also shows the presence of imidazole olefinic carbons (C=C and C=N) peaks at 132.43 to 119.12 ppm, peaks of VAME carbon bonded to mercapto imidazole by thiolene coupling reaction at about 36.60 ppm, carbonyl carbon peaks bonded with mercaptoimidazole group at 196.79 ppm confirms that VAME is functionalized with 2-mercapto-1-methylimidazole.

4.4.2. FT-IR studies of IFVAME

The FT-IR spectral analysis of IFVAME (figure 4.11) shows that there is a characteristic band at 3126 cm^{-1} which may be assigned to C-H stretching band of CH=CH of the imidazole ring overlapped with C-H of $–CH_3$ attached to imidazole ring, in addition, the normal C-H stretching of structure on VAME at 2928 cm^{-1}.

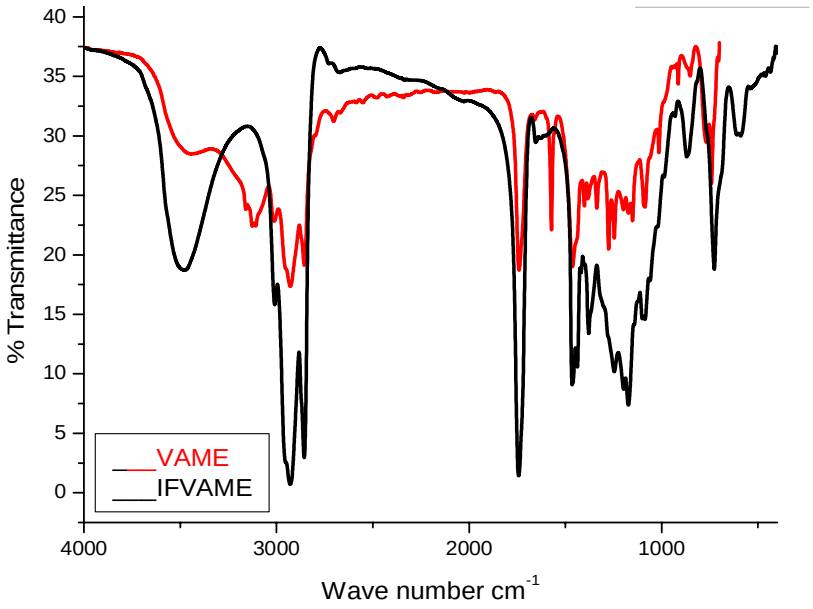

Figure 4. 11: FT-IR spectrum of VAME (top red) and IFVAME (bottom black)**.**

The band at 1572 cm^{-1} may be assigned to N=C of the imidazole ring. There is also C-C-S bands at 741 cm^{-1}. Major functional group bond vibrations of X-H single bond

stretching (H-bond & C-H) occur in the range 3600-2700 cm^{-1}, double bond stretching (C=O, C=N, C=C) in the range 2400-1550 cm^{-1}, and C-O-C stretching of esters occur between 1200-1050 cm^{-1}, which is in agreement with the result obtained. Thus, the result of FT-IR spectral analysis also ensures the functionalization of VAME by imidazole derivative. Note that the disappearance of C=C of VAME during functionalization with mercapto imidazole may not be observed clearly from FT-IR because of overlapping of such double bond region with the introduced double bonds on the ring from mercapto imidazole functionalization.

4.4.3. CHNS Elemental Analysis of IFVAME and VAME

The CHNS elemental analysis were recorded for VAME and IFVAME summarized in table 4.7

Table 4.7: CHN elemental analysis of VAME and IFVAME

Compound	Molecular formula	Weight (g/mol)	Theoretical(Experimental) Elemental Composition (%)				
			C	H	N	S	O
VAME	$C_{19}H_{34}O_3$	310	73.54 (68.52)	10.97 (10.01)	- (0.12)	-	15.48 (21.33)
IFVAME	$C_{26}H_{42}\ N_4\ O_2S_2$	506	61.61 (59.36)	8.30 (8.12)	11.07 (9.89)	12.64 (11.31)	6.32 (11.31)

Note that the experimental values of CHN/S elemental composition of VAME and IFVAME (table 4.7) are consistent with their expected theoretical values with slight deviation for some elements. The lower experimental values of C & H for VAME and C, H, N & S for IFVAME may be due to the less composition of VA/VAME from proton

NMR spectrum of the tri-ester from the purified oil and the loss of methanol from the monoester by hydrolysis of VAME at carbonyl carbon center by mercapto imidazole in addition to thiolene coupling reaction at olefinic carbon. On the other hand, the relatively higher oxygen content for both VAME and IFVAME may be due to the presence of associated water moisture through H-bonding.

In summary, the ^{1}H & ^{13}C NMR and FT-IR spectral studies additional characteristic peaks of IFVAME that differ from VAME precursor material due to mercapto imidazole functional groups and the CHNS elemental analysis for IFVAME with additional N and S composition characteristic to it also confirmed that functionalization of VAME with mercapto imidazole has been successful.

4.5. References

1. Mbugua MN, Yusuf AO, Gitu PM, Bhatt BM: **Conversion of Vernonia galamensis Oil to Pyridinyl-Vernolamides and their Antimicrobial Activities**. *Bull Chem Soc, Ethiop* 2007, **21**(1):108-110.

2. Ayorinde FO, Saeed KA, Price E, Morrow A, Collins WE, McInnis F, Pollack SK, Eribo BE: **Production of poly-(β-hydroxybutyrate) from saponified Vernonia galamensis oil by Alcaligenes eutrophus**. *J. of Industrial Microbiology and Biotechnology* 1998, **21**(1):46-50.

3. Ayorinde FO, Nana EY, Nicely PD, Woods AS, Price EO, Nwaonicha CP: **Syntheses of 12-aminododecanoic and 11-aminoundecanoic acids from vernolic acid**. *J.Am.Oil Chem.Soc.* 1997, **74**(5):531-538.

4. Mambo CK, Gitu PM, Bhatt BM, Chweya J, Grinberg S, Mills D: **Synthesis of Vernolamide Containing Tertiary Amino Groups from Vernonia galamensis Oil and Their Biological Activities**. *Bull Chem Soc, Ethiop* 1998, **12**(2):121-128.

5. Neff WE, Adlof RO, Konishi1 H, Weisleder D: **high-performance Liquid Chromatography of the Triacylglycerols of Vernonia galamensis and Crepis Alpina Seed Oils**. *J.Am.Ojl Chem.Soc.*, 1993, **70**:449-455.

6. Nilsson UJ: **Solid-phase extraction for combinatorial libraries**. *J of Chr, A* 2000, **885**(1):305-319.

7. Ruiz-Gutiérrez V, Pérez-Camino MC: **Update on solid-phase extraction for the analysis of lipid classes and related compounds**. *J. of Chr. A* 2000, **885**(1):321-341.

8. Christianne ECR, Goncalves CB, Batista E, Antonio JAM: **Deacidification of Vegetable Oils by Solvent Extraction**. *Recent Patents on Engin.* 2007, **1**(1):95-102.

9. Ayorinde FO, Hassan M: **Deacidification of vegetable oils**. In.: Google Patents; 1995.

10. Shah DU: **Towards Sustainable Polymers and Plastics: NMR Spectroscopic Analysis and Characterisation of Vernonia Seed (Vernonia galamensis) Oil and Epoxidised Soya Bean Seed (Glycine Max) Oil**. *The Sci-Tech* 2014, **01**(12):13-29.

11. Christie WW: **Preparation of Ester Derivatives of Fatty Acids For Chromatographic Analysis, Oily Press, Dundee** *J.Am.Oil Chem.Soc.* 1983:. 69-111.

12. Samuelsson J, Jonsson M, Brinck T, Johansson M: **Thiolene coupling reaction of fatty acid monomers**. *J. of Polymer Sci. Part A: Polymer Chem.* 2004, **42**(24):6346-6352.

13. Türünç O, Meier MAR: **The thiolene (click) reaction for the synthesis of plant oil derived polymers**. *European J. of Lipid Sci. and Technology* 2013, **115**(1):41-54.

14. Liu B, Deng X, Xie Z, Cheng Z, Yang P, Lin J: **Thiol-Ene Click Reaction as a Facile and General Approach for Surface Functionalization of Colloidal Nanocrystals**. *Advanced materials* 2017, **29**(36).

15. Bromberg L, Chen L, Chang EP, Wang S, Hatton TA: **Reactive Silver and Cobalt Nanoparticles Modified with Fatty Acid Ligands Functionalized by Imidazole Derivatives**. *Chemistry of Materials* 2010, **22**(18):5383-5391.

5. Results and Discussion on Surface Modification of OMMs with VAME and IFVAME

5.1. Surface modification of Al-MCM-41(3 and 15), SBA-15 and PMO with VAME

In the second part of this work, we have supported VAME on three types of ordered mesoporous materials: MCM-41 (Mobil Composition of Matter No. 41) with two different compositions, Si/Al=3 and 15, Siliceous Santa Barbara Amorphous No 15 (SBA-15) and Periodic Mesoporous Organosilica (PMO). The aim is to investigate the effect of the chemistry of the pore surface on the final immobilization process. The surface modifications were done with vernolic acid methyl ester (VAME) in a varying ratio according to the reported literature [1, 2] so as to introduce surface ligands with increased hydrophobicity for further immobilization of silver metal nanoparticles. In the first set of experiments, several ratios were tested in order to optimize the relationship between the amount of VAME and the porosity in the final composite. The general proposed a scheme for the process of such transesterification reaction of VAME with some surface hydroxyl of all the three OMMs (SBA-15, Al-MCM-41(Si/Al=3 &15), & PMO) can be given as follows respectively (scheme 5.1), where x varies as collected in table 5.1.

a) $SiO_2(OH)_n + x(H_3COOCC_{17}H_{30}O) \longrightarrow SiO_2(OH)_{n-x}(OOC_{17}H_{30}O)_x + xCH_3OH$

b) $(SiO_2/Al_2O_3)/(OH)_n + x(H_3COOCC_{17}H_{30}O) \longrightarrow SiO_2/Al_2O_3)/(OH)_{n-x} + (OOCC_{17}H_{30})O)_x + xCH_3OH$

c) $(SiO_2/C_2H_4)/(OH)_n + x(H_3COOCC_{17}H_{30}O) \longrightarrow SiO_2/C_2H_4)/(OH)_{n-x}(OOCC_{17}H_{30})O)_x + xCH_3OH$

Scheme 5. 1: The proposed reaction scheme for surface functionalization of OMMs with VAME

The optimum ratio for VAME loading is the one that allows surface modification of the OMM while avoiding pore blocking or complete loss of pore volume since potential catalytic or catalytic support property is highly attained. At the same time, the nature of the pore wall of the OMM determines an optimum surface chemistry for efficient loading of VAME.

Table 5. 1: Surface modification of OMM: Al-MCM-41(3 and 15), SBA-15, PMO with VAME

Mass of VAME (g)	Mass of OMM (g)	VAME/VAME+OMM (g)	Name
0.06	0.40	0.13	mMCM(3)1
0.03	0.14	0.18	mMCM(3)2
1.00	0.68	0.59	mMCM(3)3
0.06	0.40	0.13	mMCM(15)1
0.03	0.14	0.18	mMCM(15)2
1.00	0.68	0.59	mMCM(15)3
1.00	0.14	0.78	mMCM(15)4
0.06	0.40	0.13	mSBA1
0.03	0.14	0.18	mSBA2
1.00	0.68	0.59	mSBA3
0.50	0.14	0.78	mSBA4
0.06	0.40	0.13	mPMO1
0.03	0.14	0.18	mPMO2
1.00	0.68	0.59	mPMO3

5.1.1. FT-IR Spectral Analysis

The FT-IR spectra of the mOMMs composites loaded with 50 % VAME, labeled as mOMM3 were recorded in the wave number range of 4000 to 400 cm^{-1} using KBr pellets. Table 5.2 collects all the bands' assignments, whereas the spectra are presented in Figure 5.1. Figure 5.1A plots the two supports of mMCM (3 & 15, (Si/Al=3 & 15) with ratio of

58 % VAME loading i.e mMCM (3) 3 & mMCM (15) 3. Similarly, figure 5.1B contains SBA-15 and PMO with the ratio of 58 % VAME loading i.e mSBA3 and mPMO3. The results of spectral analysis of the mOMMs show the characteristic CH stretching of CH_3 & CH_2 as well as C=O stretching functional groups of VAME as indicated in table 5.2. Note that the C=O stretching frequencies for mOMMs (1742 cm^{-1} for mMCM3 and 1741 cm^{-1} for mPMO3 are lower compared to that of pristine VAME (1743 cm^{-1}) as shown in table 4.6, which confirms its incorporation into the modified composite without altering functional groups. Furthermore, the results of spectral analysis of the mOMMs also show a characteristic band of silanol hydroxyl groups stretching with a change in intensity upon loading of VAME .This may show a change in surface chemistry of mOMMs from hydrophilic to hydrophobic thereby resulting in a promising surface ligand for further silver metal immobilization. Note that the presence of ν_{OH} (H_2O) stretching is confirmed by the presence of broad bands shifted to a lower frequency in the hydroxyl region of FT-IR spectrum, in addition, its bending frequency at around 1630-1638 cm^{-1}.which may be overlapped with ν ($_{C=C}$) bands.

In summary, the surface modification of OMMs with VAME has been achieved without altering the functional groups of VAME which is in good agreement with what is reported in the literature [3-8].

Table 5. 2: FT-IR band assignments for m-MCM (3) 3, m-MCM (15) 3, m-SBA3 and m-PMO3.

Functional group (mode of vibration & intensity)	ν(cm^{-1})			
	mMCM(3)3	mMCM(15)3	mSBA3	mPMO3
Silanol H-bond (OH) (str.)	3435	3426	3437	3427
Methyl -C-H (CH_3) (str. As.)	2930	2929	2929	2929
Ethylene-C-H (CH_2) (str.)	2857	2856	2857	2857
Ester carbonyl of VAME	1724	1742	1741	1741
Adsorbed H_2O OH (str.)	1638	1630	1635	1634
Methyl -C-H (CH_3) (bend.) (VAME)	1467	1464	1464	1460
Ethylene–C-H(CH_2)(bend,) of VAME	1383	1378	1384	1379
Si-O-Si- bond (str.)	1066	1076	1088	1030
Al-SiO_2 (str.)	799	802	-	-

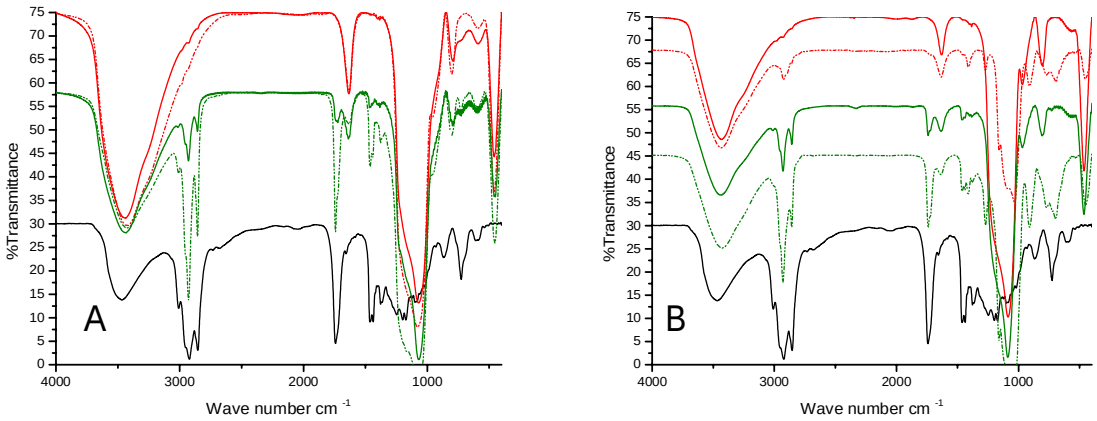

Figure 5. 1: FT-IR Spectra of (A) Al-MCM-41 (3) in red solid line and (15) in red dashed line, and their modified ones in green. (B) SBA-15 in red solid line and PMO in red solid line, and their modified ones in green. VAME is also included in the black line in both cases for comparison.

5.1.2. Powder XRD studies

Wide and low angle powder X-ray diffraction patterns of modified & unmodified OMMs are presented in Figures 5.2 and Figure 5.3, respectively.

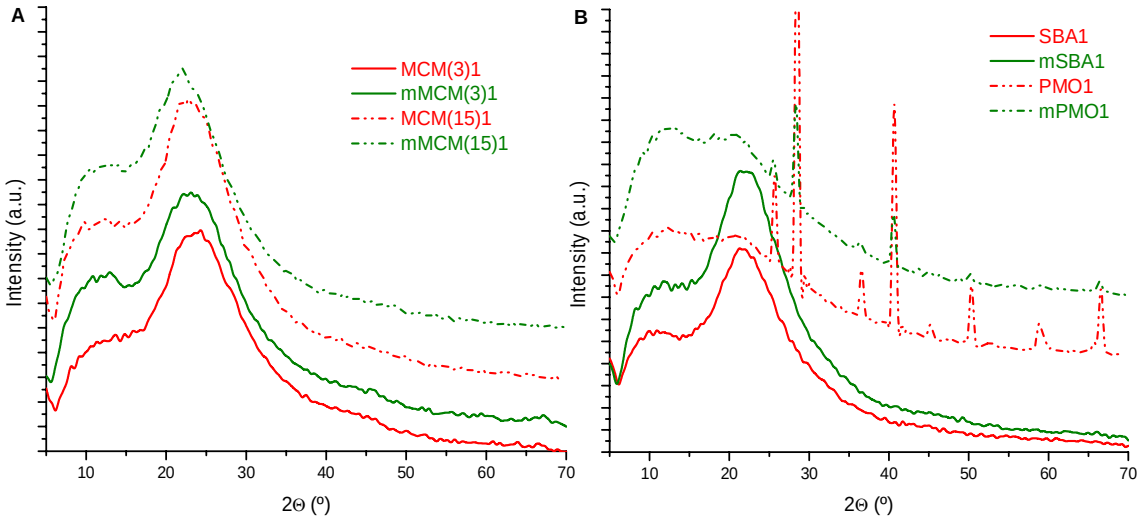

Figure 5.2: Wide angle PXRD patterns of VAME supported on (A) Al-MCM-41(3) and Al-MCM-41(15) and (B) on SBA-15 and PMO with a 0.13 VAME/VAME+OMM ratio.

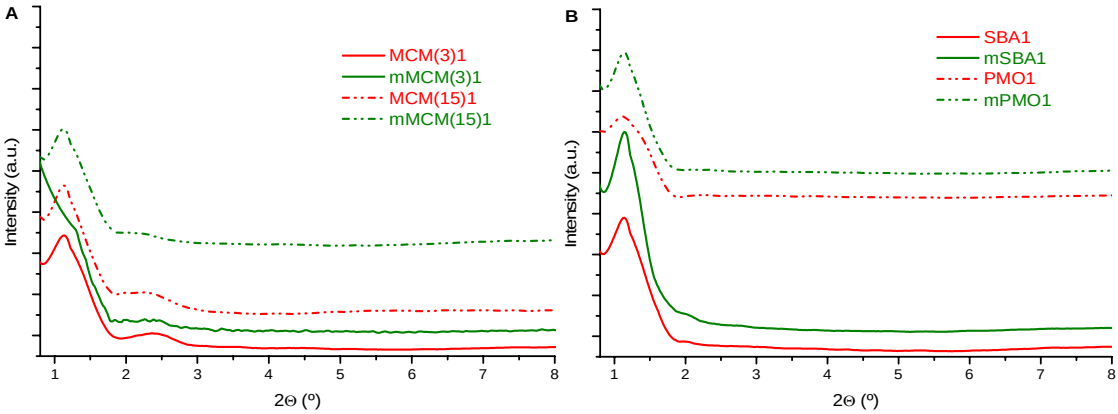

Figure 5. 3: Low angle PXRD patterns of VAME supported on (A) Al-MCM-41 (3) and Al-MCM-41 (15) and (B) on SBA-15 and PMO with a 0.13 VAME/VAME+OMM ratio.

As can be observed from the wide angle diffraction patterns, ordered mesoporous materials are amorphous. In Al-MCM-41 the tetrahedral of aluminosilicate is randomly distributed within the pore walls, and in SBA-15 the SiO_2 is condensed forming amorphous 2, 3 and 4 coordinated silicate framework. The broad intensity peak at 10 to

30° indicates that either the parent supports or after VAME loading, the materials remain the same. There is only one exception, which is the PMO support. In this case, the periodicity given by the ethylene groups forming the pore walls (organic bridging groups) is responsible for the sharp diffraction peaks observed [9, 10]. After loading of VAME, the nature of the pore wall remains intact. In the low angle range (Figure 5.3), OMMs usually show sharp intense diffraction peaks due to the periodicity given by the hexagonal packing of mesopores [3, 4, 7, 8]. However, the profiles are not well resolved due to instrumental resolution limitation at such a low angle of 2θ below 5^0. Nevertheless, Figure 5.3 shows relatively high intense peaks at 2Θ 1.11 to 1.13^0 for Al-MCM-41 and PMO supports and even sharper for SBA-15 case in which 100 and 110 reflections could be clearly seen confirming the two-dimensional hexagonal structure. In general, upon VAME loading, the intensity of the diffraction peaks decrease due to a commonly observed effect given by a change of refraction index within the periodic system [3, 7, 8, 10]. This could be indirect evidence that the VAME is indeed entering the porous systems at this low VAME/OMM ratio.

5.1.3. Thermogravimetric Analysis

Figure 5.4 plots the TGA and DTG curves of the two series of MCM-41 based materials and figure 5.5 shows the curves corresponding to the SBA-15 and PMO systems. Table 5.3 collects the weight losses of all the samples prepared using different values of VAME/OMMs ratios. For mMCM(3)1-3, the analysis of TGA/DTG curves (figure 5.5A) shows a total weight loss ranging from 9 % in mMCM (3)1 to 22 % in mMCM (3) 3 in the temperature range of 150 to near 900 ^{o}C. The curves generally show that there are three phases of weight loss. The first weight loss up to 150 ^{o}C (6 to 11 wt %) may refer to

desorption of physically adsorbed water and hexane solvent adsorbed on the outer surface of the mMCM modified material. The second weight loss (6 to 15 wt %) between 150 to 500 ºC may be due to loss of VAME that has been loaded on the outer and pore wall surface of the MCM (3) materials and third weight loss (3 to 7 wt %) at T > 500 ^{0}C may be due to the loss of water released from the structural silanol condensation forming defects in the pore walls of the MCM-41.

In summary, this result indicates that the thermal stability of VAME in mMCM (3) (Si/Al=3) is up to 150 ºC and the approximate percent yield of VAME incorporation is 37 to 73 %, with the 13 % initial loading ratio as highest optimum loading.

The TGA/DTG curves of mMCM (15) with Si/Al=15 (figure 5.5B) show that the total amount loaded is ranging between 55.84 % for mMCM (15)4 to 55.94 % in mMCM (15)1 at a temperature of T>150 ºC. As indexed in table 5.3, the approximate percent yield of VAME incorporation or efficiency of VAME loading gets the highest optimum value at 13 % VAME loading. Note that there are two clear groups with similar patterns namely the first group corresponds to first two lower ratios of VAME loading with VAME/ (MCM (15) 1 & 2) (0.13 and 0.18) and second group corresponds to the last two ratio of VAME loading VAME/ (MCM (15) 3 & 4) (0.59 & 0.78)

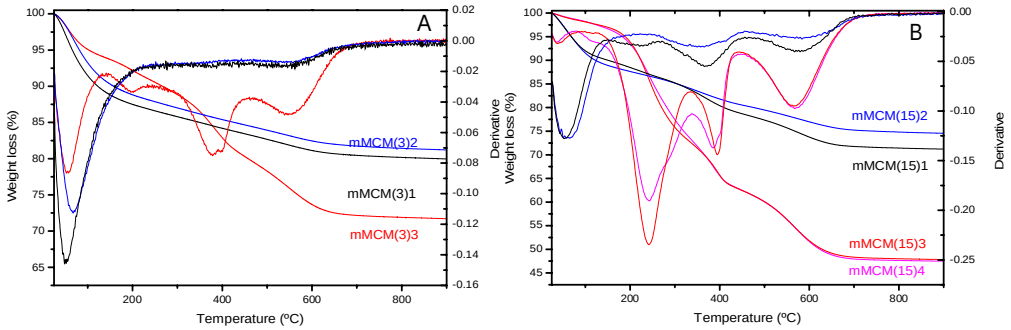

Figure 5. 4: TGA and derivatives of (A) mMCM (3) and (B) mMCM (15), at varying loading ratios of VAME to OMMs.

TGA/DTG curves of mMCM (15) 1-4 show three distinct phases of weight loss as indexed in table 5.3 resembling that of mMCM (3)1-3. The first weight loss at T<150 ^{0} C is due to desorption of physically adsorbed water which is higher at lower precursor ratio of loading (VAME/ (MCM (15) 1 & 2) as shown in table 5.3 which may be due to the higher pore size and hydrophilicity of mesopore surfaces Al acidic site in extra framework that attracted much water during loading. The second weight loss at a temperature range of 150 to 500 ^{0} C corresponds to decomposition of organic VAME from mMCM (15). Note also that, mMCM (15)1 and 2 show less organic content than mMCM (15) 3 and 4, confirming the desired loading increasing along with the initial VAME/MCM (15). as shown in table 5.3. In these cases, the third weight loss centered at T>500 ºC may not only be due to the release of water due to silanol condensation but also indicative of some stronger interactions of the VAME with the strong acid sites of the Al-MCM-41 with Si/Al=15, stronger than mMCM (3) (Si/Al=3). The weight loss between 500 and 900 ºC shows an increasing amount of organic substances as the ratio increases. This may be due to the presence of lower coordination number of Al at such composition that leads to the larger active site. This, in turn, leads to stronger polar interactions between VAME and Al-MCM-41 carboxylic and epoxy functional groups of VAME

with acid sites of Al-MCM-41 that leads to much higher loading of on MCM (15) compared to MCM (3) which is consistent with the literature report [4].

In the case of SBA-15 and PMO (figure 5.5), both have larger pore size so it is expected that more VAME would be loaded.

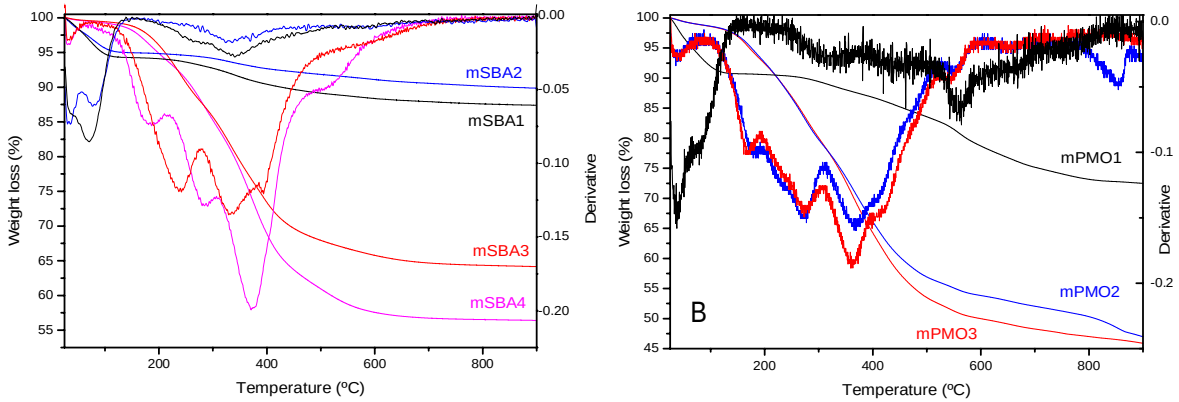

Figure 5. 5: TGA and DTG of (A) mSBA1-4 and (B) mPMO1-3, at varying loading ratios of VAME to OMM..

The TGA/DTG curves of mSBA1-4 and mPMO1-3 are different from that of the MCM (15) 1-4 case, showing that a maximum weight loss (i.e. loading) is achieved around 400 ºC, with no weight loss centered at 600 ºC. Thermogravimetric analysis of mSBA1-4, shows that there is a total weight loss from 5 to 42 wt % at a temperature of T >150 ºC. Similarly, TGA analysis of mPMO 1-3 shows that there is higher weight loss of 12 to 45 wt % at a temperature of T >150 ºC due to the combined higher pore volume and higher affinity and the hydrophobicity of PMO towards VAME that leads to higher immobilization of VAME in the channels of the PMO, while the small losses above 600 ºC are due to structural water condensation and the decomposition of the bridging organic

groups of the mPMO. The mPMO has a weight loss due to the organic bridging groups forming the walls, which amounts to 6 wt % and that weight loss has been substracted from the modified samples.

Note that for 13 to 78 % ratio of VAME loading at T value between 150 to 600 ºC, the highest percentage weight loss of mPMO (47 wt %) greater than that of mSBA (41 wt %) due to the greater hydrophobic pore surface of PMO that loads more VAME. Thus, these materials seem to be thermally stable up to 150 ºC with the incorporation of VAME and are feasible for catalytic application at a higher temperature.

Table 5. 3: Data of weight losses obtained from the TGA curves of mOMMs

Sample	VAME/VAME+OMM(g)	TGA weight loss (%)			T > 150 ºC Total weight loss (%)	Yield of VAME incorporation (%)
		T < 150 ºC	150 < T< 500 ºC	T > 500 ºC		
mMCM(3)1	0.13	11.18	6.15	2.71	8.86	73.41
mMCM(3)2	0.18	9.70	6.37	2.72	9.09	51.72
mMCM(3)3	0.59	6.30	15.43	6.56	21.99	36.99
mMCM(15)1	0.13	9.97	12.68	6.14	18.82	155.94
mMCM(15)2	0.18	11.08	9.44	4.92	14.36	81.70
mMCM(15)3	0.59	3.00	36.92	12.25	49.17	82.70
mMCM(15)4	0.78	3.34	36.61	12.55	49.16	55.84
		T < 150 ºC	150 <T < 600 ºC	T > 600 ºC		
mSBA1	0.13	5.73	5.90	0.96	6.86	56.84
mSBA2	0.18	5.03	3.86	1.25	5.11	29.07
mSBA3	0.59	1.18	33.04	1.62	34.66	58.30
mSBA4	0.78	1.80	40.63	1.16	41.79	53.16
mPMO1	0.13	9.27	12.02	6.23	11.98*	99.26
mPMO2	0.18	3.07	43.10	6.86	43.69*	248.58
mPMO3	0.59	3.07	46.95	4.09	44.77*	75.30
Parent PMO					6.27	

* 6.27 have been substracted from these values.

In summary, the TGA studies showed that the highest percentage yield of approximate VAME incorporation is generally observed for the lowest 13 % of VAME loading ratio

on OMMs may be due to least pore blocking (table 5.3) for MCM (3 &15) with 73.41 & 155.92 % respectively except a slight variation for SBA and PMO with higher pore size and some anomalous results for PMO2 may be due to larger pore size, pore size fluctuation due to swelling or random error.

5.1.4. Nitrogen adsorption-desorption isotherms

In order to evaluate the remaining porosity in the final loaded supports and the textural properties of the mOMM materials, N_2 sorption isotherms studies were carried out. The obtained isotherms follow type IV as per the IUPAC classification indicating uniform mesopores that are not significantly changed during the modification with VAME, except for the loss of surface area and pore volume. The loading of VAME may diminish the mesoporosity of mOMM either by fully filling the channels or pore blocking. Figure 5.6 depicts the isotherms of the Al-MCM-41 systems, 5.6A for mMCM (3)1-3 and mMCM (15)1-4, respectively. Figure 5.7A and 5.7B plot the isotherms of mSBA1-4 and mPMO1-3 sets of samples, respectively. Table 5.4 collects the textural properties of all the samples compared with the parent supports.

Table 5. 4: Textural properties of VAME supported on OMMs

Sample	Mass ratio	S_{BET} (m^2/g)	Pore Volume(cm^3g^{-1})	Pore diam (nm)	Sample	Mass ratio	S_{BET} (m^2/g)	Pore Volume(cm^3/g)	Pore diam. (nm)
Al-MCM(3)	-	722		-	SBA-15	-	609	1.00	8
mMCM(3)1	0.13	594.0	0.75	2	mSBA1	0.13	460.1	0.85	-
mMCM(3)2	0.18	566.5	0.69	-	mSBA2	0.18	502.2	0.90	6
mMCM(3)3	0.59	154.4	0.4	-	mSBA3	0.59	157.2	0.30	-
Al-MCM(15)	-	799.0			mSBA4	0.78	75.2	0.16	-
mMCM(15)1	0.13	656.6	1.20	2	PMO	-	882	1.00	7.1
mMCM(15)2	0.18	794.4	1.32	-	mPMO1	0.13	588.1	0.68	6
mMCM(15)3	0.59	49.1	0.58	-	mPMO2	0.18	15.4	0.08	-
mMCM(15)4	0.78	44.3	0.52	-	mPMO3	0.59	15.5	0.09	-

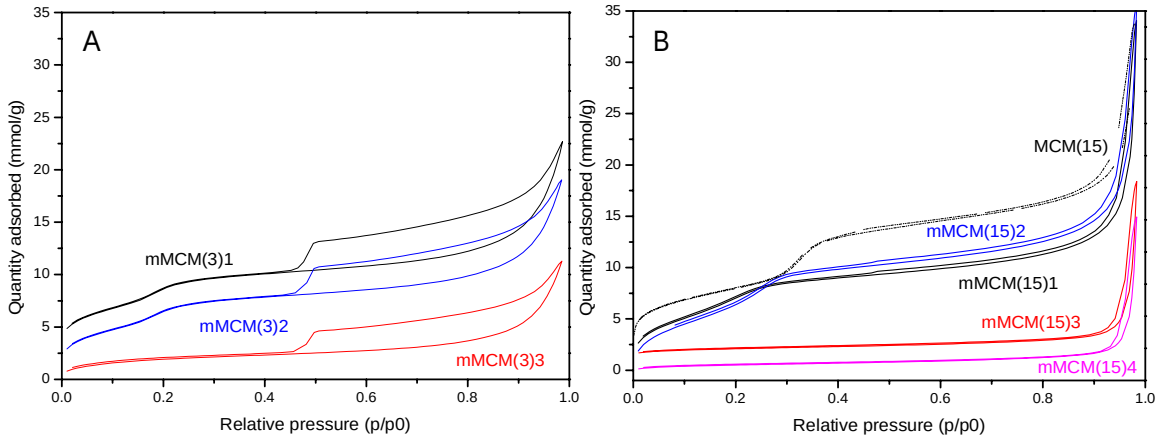

Figure 5. 6: N_2 Adsorption-desorption isotherms of the VAME supported on (A) MCM (3) and (B) mMCM (15).

The N_2 adsorption-desorption studies (table 5.4) of mMCM (3)1-3 revealed that as loading ratio of VAME to MCM (3) increases from 0.13 to 0.59, there is a decrease of S_{BET} from 594 for mMCM(3)1 to 154 m^2/g for mMCM (3)3 when compared to

unmodified MCM(3) with S_{BET} of 722 m^2/g and hence a decrease of BJH pore volume from 0.75 to 0.4 cm^3 /g as a result of pore surface functionalization during VAME loading. Such a large decrease in S_{BET} and BJH pore volume of mMCM (3) is consistent with the decrease of weight losses observed by TGA from 8.86 to 21.99 wt % at a temperature range of T >150 ^oC. The hysteresis loop observed in these samples is due to textural porosity, related to a small crystal size, and thus the pores between particles which could also be responsible of the loading of VAME as it was observed in the TGA.

The S_{BET} of mMCM (15)1-4, decreased from 799.0 m^2/g in the pristine material to 656.6 m^2/g in mMCM (15)1 and to 49 m^2/g in mMCM (3)1-3, as the precursor mass ratio increased from 0.13 to 0.78. This may be due to the total filling of the mesoporoes as it was observed in the TGA a result of stronger interaction of the greater surface hydrophobic VAME with increased hydrophobicity of MCM (15) compared to that of MCM (3) which resulted from increased value of Si/Al ratios.

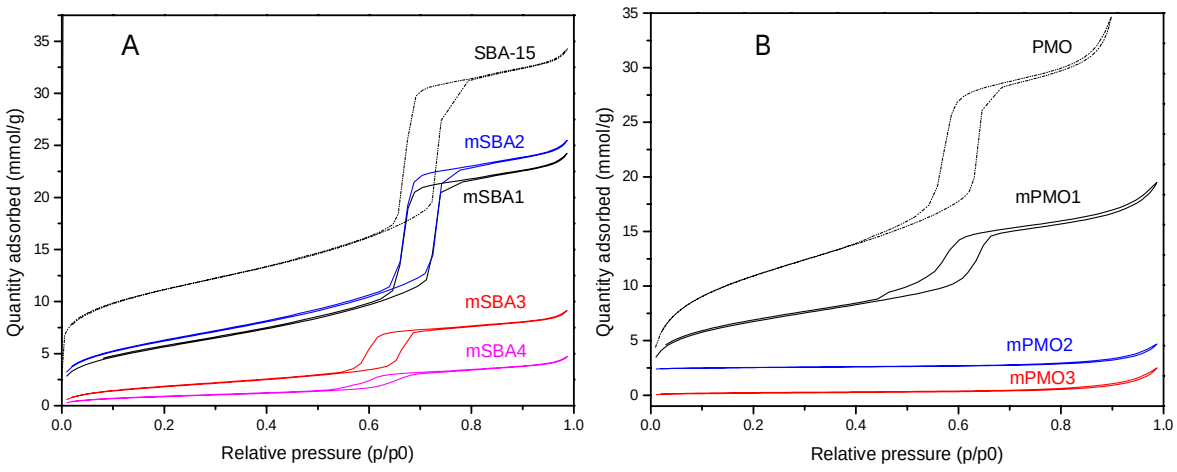

Figure 5. 7: N_2 Adsorption-desorption isotherms of the VAME supported on (A) SBA-15, and (B) PMO.

In the case of the SBA-15 system, the relatively larger initial pore size of 8 nm allows for fine tuning of the loading of VAME. For 0.13 to 0.78 variations of precursors mass ratios, the BET surface area of 609 m^2/g for a parent SBA-15 decreased to 460.1, 502.2, 157.2 & 75.2 m^2/g for mSBA1, mSBA2, mSBA3 & mSBA4, respectively, which show generally a decrease of the BET surface area, as well as a decrease of the BJH pore volume (1.00 to 0.16 cm^3/g). As indexed in table 5.4 the mesopore pore size of the BJH pore size of 6 nm for mSBA2 also shows that there is mesoporosity of the material. The obtained textural properties of mSBA-15 is consistent with higher weight loss observed in TGA (5.11 to 41.79 wt %) at T >150 ^{0}C due to the larger pore size of SBA-15 which can accommodate much more VAME during loading as compared to MCM (3) & MCM (15). Thus, the modified materials with 0.13 to 0.18 precursors mass ratios, having both microporosity and mesoporosity are potentially the best or more feasible for metal nanoparticle immobilization (Chapter 6).

For mPMO1-3 there is a more significant decrement in porosity in mPMO2 and mPMO3 due to higher VAME loading leading to blockage of pores. It is clear that for PMO & mPMO1 there is a steep increase in adsorption at P/P^0=0.4-0.7 due to capillary condensation of the nitrogen in the mesopore. The calculated data of BET surface area & BJH pore volume and pore diameter are presented in table 5.4.This is in good agreement with the literature report [3]. The parent PMO showed higher BET surface area (882 m^2/g) compared with modified materials (588.1, 15.4 & 15.5 for PMO1, PMO2 & PMO3, respectively) and hence VAME loading on PMO significantly decreased the BET surface area of the material for mPMO2 and mPMO3. This is attributed to the pore blocking by VAME loading as a result of higher pore size of PMO and its higher

hydrophobicity that facilitates a dominant diffusion of VAME. The textural properties result is consistent with higher weight loss as observed in TGA values (11.98 to 44.77 wt %) which may be due to higher pore size (7.1 nm). Thus, the mPMO1 with 13 % VAME loading have high BET surface area and BJH pore size and volume as indexed in table 5.4, with retained microporosity and mesoporosity during modification seems to be the best support for metal nanoparticle immobilization for catalytic application in chapter 6.

In summary, the degree of VAME loading on OMMs (Al-MCM-41(3&15), SBA-15, and PMO depends on the ratio of VAME to OMMs (with the lowest 13 % VAME loading being the best ratio for further work). The pore size (higher VAME loading with larger pore size), the surface hydrophobicity/hydrophilicity (the more surface hydrophobicity matching with higher loading of more hydrophobic VAME) and framework acidity (Si/Al-ratios) of the mesoporous materials (more acidic Al-O Lewis acid center attracts more hydroxyl of epoxy group or carboxylate of VAME leading to more loading). Note that VAME loading is higher for Al-MCM-41(15) than for Al-MCM-41(3) due to it's less Al content with less acidity or higher hydrophobicity of Al-MCM-41 (15). This result matches the result reported in the literature [4]. The N_2 adsorption-desorption isotherm and powder XRD show that the mesoporosity of the material is retained intact with slight change in values of textural properties during loading and the TGA/DTG curves show that the modified materials (mOMMs) have thermal stability approximately up to a temperature of 150 ^{0}C with desorption of physisorbed water on the external and internal pore surface.

Thus, the modified materials with optimum 13 % VAME loading with a highest percentage yield of VAME incorporation seem potentially feasible as VAME

functionalized mMCM catalyst or catalyst support for encapsulation of Ag nanoparticles with dimension less than the pore size of the modified materials. The sample proposed scheme of such reaction is as given in scheme 5.2.

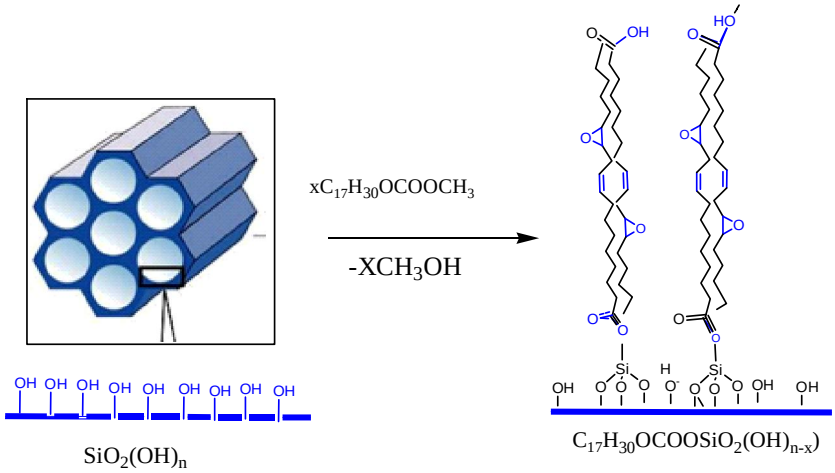

Scheme 5. 2: The proposed reaction scheme for supporting of VAME on OMMs

5.2. Surface modification of Al-MCM-41(3 and 15), SBA-15 and PMO with IFVAME

2-Mercapto-1-methyl-imidazole functionalized VAME (IFVAME) was supported on Al-MCM-41(Si/Al=3 &15), SBA-15 and PMO according to the procedure reported in the literature [11] as indexed in table 5.6. Note that the selection was made based on the optimum capacity of 13 % VAME loading on OMMs as discussed in section 5.1

The general scheme for the process of such transesterification reaction of IFVAME with some surface hydroxyl of all the three OMMs (SBA-15, Al-MCM-41(Si/Al=3 &15), & PMO) can be given as follows respectively (scheme 5.3), where x value stands for data as collected in table 5.5.

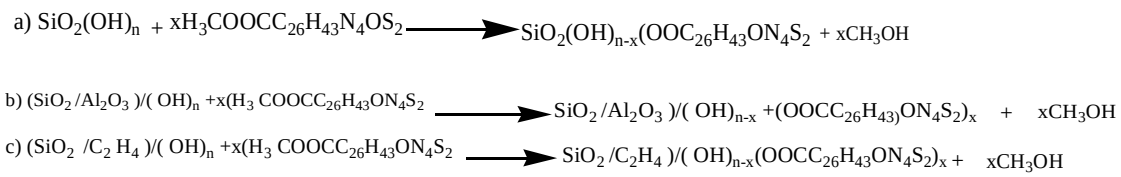

Scheme 5. 3: Scheme of the modification process in this section

Table 5. 5: Supporting of OMMs with IFVAME using a mass ratio of 0.13 and 15 ml of n-hexane.

Name	Mass of IFVAME(g)	Mass of OMMs (g)	Mass of product (g)
ifm-MCM(3)	0.03	0.20	0.22
Ifm-MCM(15)	0.03	0.20	0.22
Ifm-SBA-15	0.03	0.20	0.24
Ifm-PMO	0.03	0.20	0.24

ifm = IFVAME.

Based on the obtained mass of the products the higher IFVAME loading on OMMs is observed for SBA-15 and PMO as a result of their larger pore size and higher hydrophobicity of PMO.

5.1.1. FT-IR Spectral Analysis

To investigate the change in surface chemistry of MCM (3), MCM (15), SBA-15 and PMO during loading of IFVAME, the FT-IR spectra were recorded for samples of ifm-MCM (3), ifm-Al-MCM-41(15), ifm-SBA an ifm-PMO compared with that of their precursors (figure 5.8A and B) in the wavenumber range of 4000 to 400 cm^{-1} to show the charcterstic functional groups as indicated in the table 5.6.

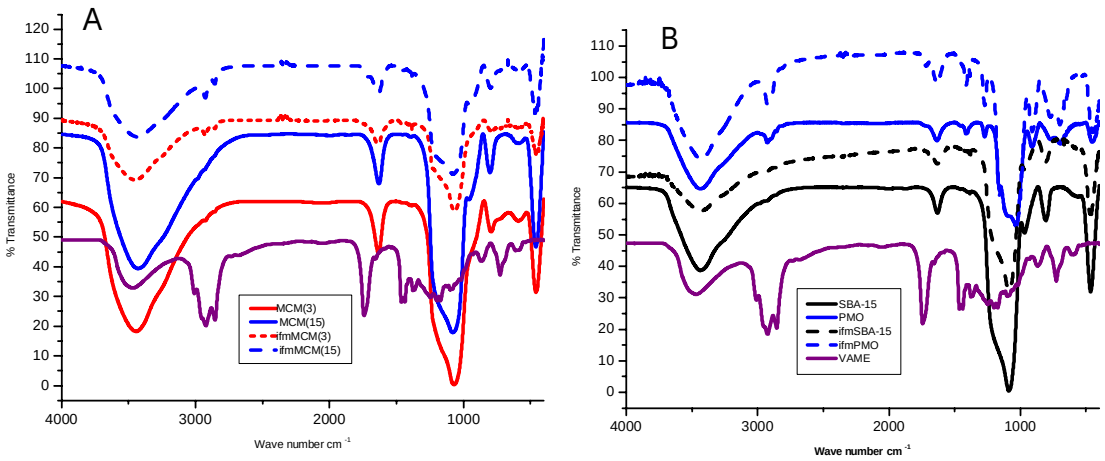

Figure 5. 8 FT-IR_spectra of ifm- OMMs compared to that of OMMs: (A)_Al-MCM-41(3) in red solid line and (15) in blue line, and their modified ones in red and blue dashed lines, respectively. (B) SBA-15 in black solid line and PMO in blue solid line, and their modified ones in black and blue dashed line, respectively. VAME also included in purple line in both case for comparison.

The important functional groups of the ifm-OMMs derived from their precursors are observed as indexed in table 5.6 and the grafting of IFVAME on OMMs was confirmed by the decrease in intensity of silanol hydroxyl groups on loading and the incorporation of the IFVAME functional groups like methyl and methylene alkyl groups and carbonyl groups on the FT-IR spectra of the ifm-OMMs material.

Table 5. 6: FT-IR Spectral Analysis of ifm-MCM (3), ifm-MCM (15), ifm-SBA and ifm-PMO.

Functional group (mode of vibration & Intensity)	$\nu(cm^{-1})$			
	ifmMCM(3)	ifmMCM(15)	ifmSBA	ifmPMO
Silanol H-bond (OH) (str.)	3457	3427	3416	3434
Methyl -C-H (CH_3) (str. As.)	2925	2928	2936	2927
Ethylene-C-H (CH_2)	2853	2856	2858	2808
Ester Carbonyl of VAME	1735	1725	1715	1720
Adsorbed H_2O OH (str.)	1639	1630	1636	1631
Methyl -C-H (CH_3) (bend.) (VAME)	1463	1464	1420	1420
Ethylene–C-H(CH_2)(bend,) of VAME	1384	1384	1383	1383
Si-O-Si- bond (str.)	1066	1078	1084	1030
Al-SiO_2 (str.)	799	797	-	-

5.2.2. Powder XRD studies

The wide angle and low angle powder x-ray diffraction patterns of IFVAME modified & unmodified OMMs were recorded and presented in figures 5.9 and 5.10.

The wide angle profiles show a broad band between 20 and 30º indicating amorphous nature of the pore wall in Al-MCM-41. Even after supporting IFVAME the characterstic amorphous band remains intact with no new extra peaks. In the case of ifm-PMO, the appearance of sharp diffraction peaks at high angle indicates the homogeneous distribution or periodicity of the organic bridging groups in the PMO support [11]. The low angle powder XRD of ifmOMMs materials has been carried out in X´Pert Pro PANalytical diffractometer (CuK_α radiation, λ=0.15406 nm) with a mode of low angle (Figure 5.10). The profiles show a well resolved diffraction peak at 2-theta below 2 ºC with differences between the four materials due to their initial structure and unit cell

dimensions. ifmMCM (3) and (15) show a typical Al-MCM-41 band not very well resolved, whereas ifm-SBA and ifm-PMO show a sharp intense peak at 1^{o} corresponding to the 100 reflections of hexagonal *p*6mm symmetry with two weaker peaks, 110 and 200 at slightly higher angle. This is in good agreement with the literature report [12].

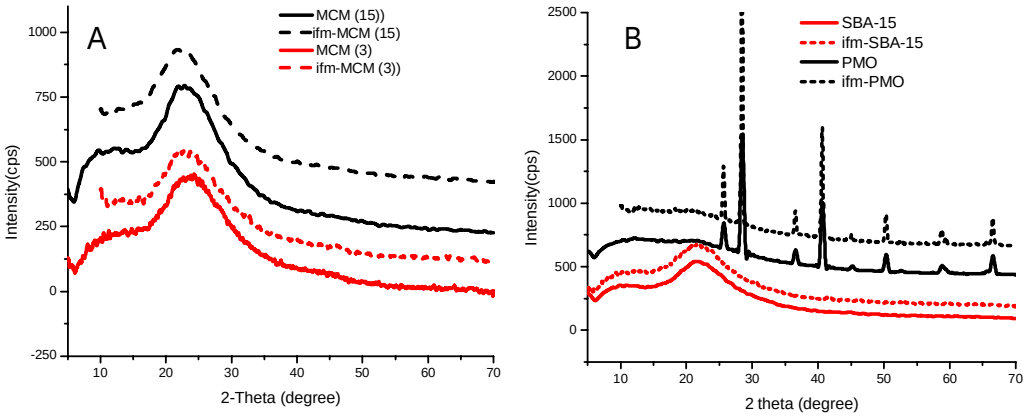

Figure 5. 9 Wide angle PXRD pattern of: (A) IFVAME supported MCM (3&15) compared with their pristine materials and (B) IFVAME supported SBA & PMO compared with their pristine materials.

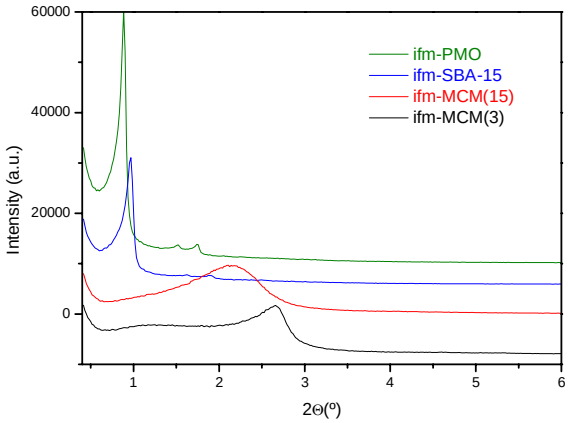

Figure 5. 10: Low angle Powder XRD of ifm-OMMs at low angle mode**.**

In general, upon IFVAME loading, the intensity of the diffraction peaks decrease due to a commonly observed effect given by a change of refraction index within the periodic system [3, 7, 8, 10]. This could be indirect evidence that the IFVAME is indeed entering the porous systems at this low IFVAME/OMM ratio.

5.2.3. Thermogravimetric Analysis

In order to evaluate the thermal stability and quantify the total incorporation of IFVAME in ifm-OMMs, their TGA/DTG curves are plotted in figure 5.11, and the weight losses extracted from the plots collected in table 5.7.

For the ifm-OMMs, the summary results of values of weight loss from TGA curves at a temperature range of 25 to 900 ^{0}C are indicated in table 5.7. As can be observed, the total weight loss in the two MCM-41 systems is higher than 13 % indicating more than 100 % yield in the incorporation of the IFVAME due to the extra weight loss of the remaining solvent that is not easily separated in this case. SBA-15 and PMO a small decrement in the amount of organic incorporated, yet a 10 % value is observed for SBA-15, close to the theoretical 13 %. In fact, these values follow the trend of the same ratio of 0.13 in the VAME modified samples of the previous chapter at temperature >150 ºC (mOMM1). In these cases the analysis into temperature ranges is rather, overlapped although the slope of the TGA curves allows speculating about the different interaction between the IFVAME and the different supports.

For ifm-MCM (3), a first weight loss is clearly observed up to 300 ºC, with 6.04 wt %, which in the case of ifm-MCM (15) broadens up to 400 ºC with a weight loss of almost 9 %. After that, in ifm-MCM (3) there is another clear weight loss with rather a sharp curve with almost 8 % weight loss indicating a sharp release of organic material, probably due

to remaining form a strongly bonded IFVAME on the surface of the acid sites in a Al-mMCM-41 material with Si/Al = 3.

Table 5. 7: Data of weight losses obtained from the TGA curves of ifmOMMs

Sample	TGA weight loss (%)		Total weight loss (%)	Yield of IFVAME incorporation (%)
	T < 300 ºC	T > 300 ºC		
ifm-MCM(3)	6.04	7.66	13.7	105.4
	T < 400 ºC	T > 400 ºC		
ifm-MCM(15)	8.8	4.4	13.2	101.5
	T < 400 ºC	T > 400 ºC		
ifm-SBA	7.65	2.36	10.01	77
	T < 300 ºC	T > 300 ºC		
ifm-PMO	10.06	5.64	15.7*	74.61

* 6% has beed substracted due to the PMO support

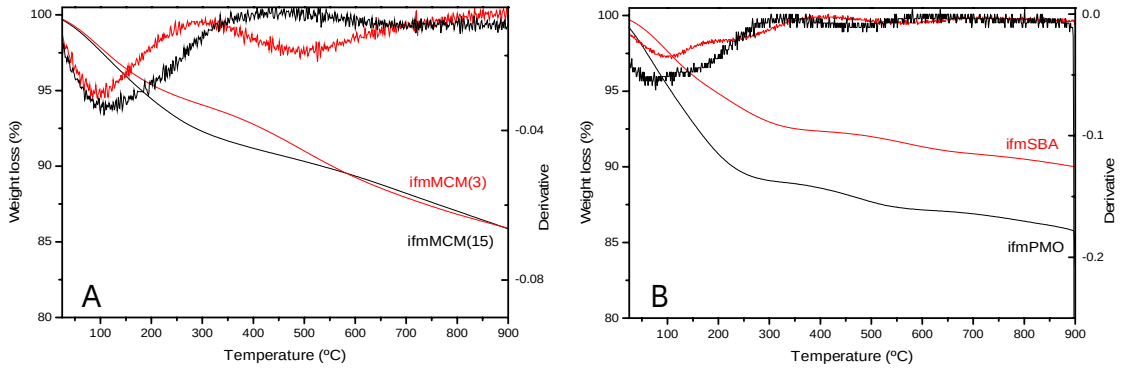

Figure 5. 11: TGA/DTG curves of: (A) ifm-MCM (3) and ifm-MCM (15) and (B) ifm-SBA and ifm-PMO.

On the other hand, in ifm-MCM (15) there is a slow slope of progressive decomposition of 4.4 % above 400 ºC indicating a smoother decomposition and release of the IFVAME.

For ifm-SBA, the derivative curve reveals a two-step decomposition of the IFVAME up to 400 ºC with 8 % of organic weight loss and ifm-PMO shows a sharp weight loss below 300 ^{o}C corresponding to 10.%. In both cases, the higher temperature weight loss is very small and mainly due to the decomposition of the framework rather than the decomposition and release of IFVAME. In particular, for PMO, there is a 6 % approximately weight loss due to the ethylene groups of the pore walls. The fast release in these two cases may be related to the large pore size of these supports, and the temperature range may be indicating that there is a stronger interaction with the OH-based surface of SBA-15 rather than with the ethylene bridging surface of PMO.

In summary, as indexed in table 5.7, the approximate percent yield of IFVAME incorporation for ifm-MCM (3), ifm-MCM (15) and ifm-SBA1 for 13 % IFVAME loading is found to be higher than that of VAME incorporation, which may be due to the stronger affinity due to an additional thio-imidazole moiety of IFVAME.

5.2.4. Nitrogen adsorption-desorption Isotherms

Nitrogen sorption Isotherms studies (figure 5.11) give information about the pore shape, pore size, and pore volume. The Nitrogen sorption isotherms of the synthesized ifm-MCM (3 &15) suggest type IV isotherms as per the IUPAC classification with H_1 hysteresis indicating uniform cylindrical pore arrangement of hexagonal symmetry order is not significantly changed during the modifications. Note that the deformation in sorption isotherm of ifm-SBA may be due to deformation of pore walls as a result of IFVAME loading and less hydrothermal stability during aging.

Table 5. 8: Textural properties of IFVAME supported on OMMs (ifm-OMMs)

Sample	S_{BET} (m^2/g)	Pvol (cm^3g^{-1})	Pd (nm)	Sample	S_{BET} (m^2/g)	Pvol (cm^3/g)	Pd (nm)
Al-MCM(3)	722			SBA-15	609	1.00	8
ifmMCM(3)	434.9	0.59	3.4	ifmSBA	486.2	0.56	2.5
Al-MCM(15)	799.0			PMO	882	1.00	7.1
ifmMCM(15)	591.1	0.79	5.2	ifmPMO	773.1	1.05	2.8

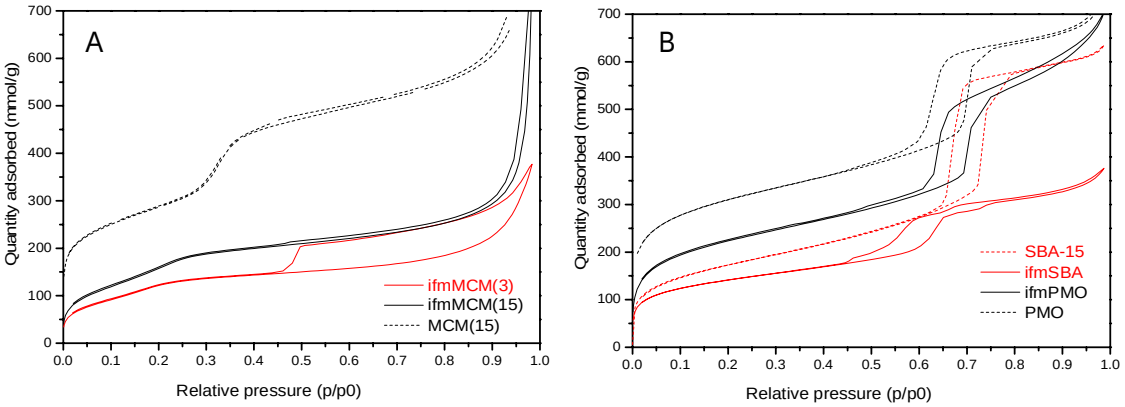

Figure 5. 12: Nitrogen sorption isotherms of (A) ifm-MCM (3) and ifm-MCM (15); and (B) ifm-SBA and ifm-PMO.

As can be observed from the data collected in table 5.8 the BET surface area of ifm-OMMs decreases slightly compared to their pristine materials as well as that of the previous 13 % VAME loading case. The same tendency is observed in the BJH pore volume and pore sizes also slightly decrease, which may be attributed to the successful interaction of IFVAME with OMMs as a result of the presence of more hydrophilic thio-imidazole functional moiety on IFVAME that may lead to tightly grafted modifier on the surface of the materials. These observations are consistent with the higher weight loss in the TGA analysis of ifm-OMM compared to that of lower weight loss of 0.96 to 6.23 wt % for mOMM1.

Thus, in general, the resulting composite materials show promising textural properties with 13 % IFVAME loading and with higher percent yield of IFVAME incorporation compared to that of 13 % incorporation for mOMM1. Both systems, with special emphasis on IFVAME systems, will be impregnated to obtain Ag nanoparticles (Chapter 6)

The proposed scheme showing formation of ifmOMMs is given below (scheme 5.4).

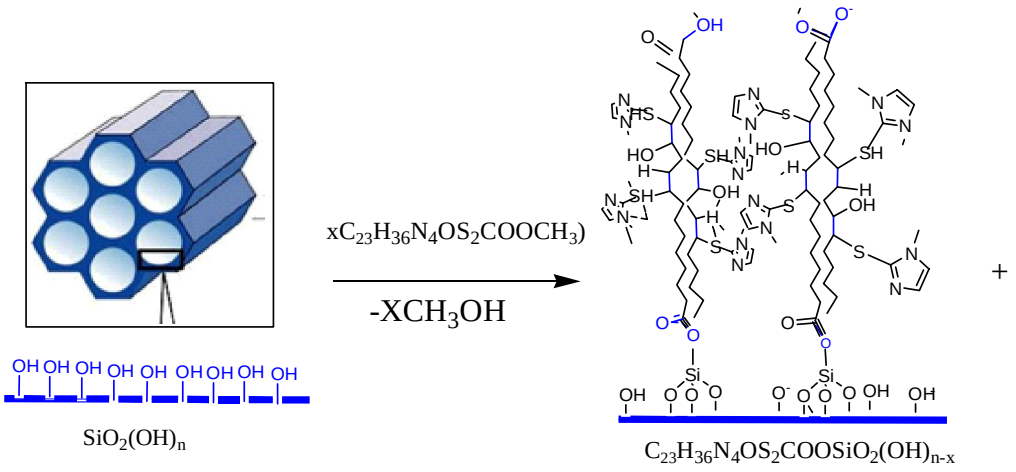

Scheme 5. 4: Reaction scheme showing supporting of IFVAME on OMMs

5.3. References

1. Li Z, Zhu Y: **Surface-modification of SiO_2 nanoparticles with oleic acid**. *Applied Surface Sci.* 2003, **211**(1-4):315-320.
2. Liu B, Deng X, Xie Z, Cheng Z, Yang P, Lin J: **Thiolene Click Reaction as a Facile and General Approach for Surface Functionalization of Colloidal Nanocrystals**. *Advanced materials* 2017, **29**(36).
3. Aghapoor K, M. Amini M, Jadidi K, Reza Darabi H: **N-functionalized L-proline anchored MCM-41: A novel organic-inorganic hybrid material for solvent-free aminolysis of styrene oxide under microwave irradiation**. *Acta Chimica Slovenica* 2015, **62**(1).
4. Naik SP, Bui V, Ryu T, Miller JD, Zmierczak W: **Al-MCM-41 as methanol dehydration catalyst**. *Applied Catalysis A: General* 2010, **381**(1-2):183-190.
5. La-Salvia N, Lovón-Quintana JJ, Lovón ASP, Valença GP: **Influence of Aluminum Addition in the Framework of MCM-41 Mesoporous Molecular Sieve Synthesized by Non-Hydrothermal Method in an Alkali-Free System**. *Materials Research* 2017, **20**(6):1461-1469.
6. Araújo S, Costa FT, Maia DAS, Sant`Ana HB, Cavalcante Jr. C.L.: **Synthesis and Characterization of Al- and Ti-MCM-41 materials: application to oxidation of Anthracene**. *Brazilian J of Chem Engin* 2007, **24**:135-141.
7. Xie W, Hu L: **Mesoporous SBA-15 Silica-supported Diisopropylguanidine: An Efficient Solid Catalyst for Interesterification of Soybean Oil with Methyl Octanoate or Methyl Decanoate**. *J. of oleo sci.* 2016, **65**(10):803-813.

8. Freitas LBdO, Bravo IJG, Macedo WAdA, de Sousa EMB: **Mesoporous silica materials functionalized with folic acid: preparation, characterization and release profile study with methotrexate**. *J. of Sol-Gel Sci. and Techn.* 2015, **77**(1):186-204.

9. Figueira P, Lourenço MAO, Pereira E, Gomes JRB, Ferreira P, Lopes CB: **Periodic mesoporous organosilica with low thiol density – a safer material to trap Hg(II) from water**. *J. of Envir. Chem. Engin.* 2017, **5**(5):5043-5053.

10. Park SS, Park, D.H, Chang-Sik Ha C-S: **Free-Standing Periodic Mesoporous Organosilica Film with a Crystal-like Wall Structure**. *Chem Mater* 2007, **19,** :2709-2711

11. Pal N, Bhaumik A: **Soft templating strategies for the synthesis of mesoporous materials: Inorganic, organic-inorganic hybrid and purely organic solids**. *Advances in Colloid and Interface Sci.* 2013, **189-190**:21-41.

12. Zhao Y, Yue Qi Y, Wei Y, Y Zhang Y, Zhang S, Yang Y, Liu Z: **Incorporation of Ag nanostructures into channels of nitrided mesoporous silica**. *Microporous and mesoporous materials* 2008, **111**:300-306.

6. Results and Discussion on Loading of Ag on VAME/IFVAME Modified OMMs

6.1. Loading of Ag on VAME supported MCM (3 &15)1, SBA1 and PMO1

Supported silver nanoparticles have long been extensively used industrially as an oxidizing catalyst for epoxidation of ethylene [1]. It is also found to be a potential candidate for selective hydrogenation of chloronitrobenzenes to chloroanilines [2], an intermediate for chemicals such as agrochemicals, pharmaceuticals, and dyestuffs. Recently, Silver nanoparticles supported on the silica-based porous inorganic framework have attracted great research interest in catalysis due to their smaller size, high surface area, and greater stability. In chapter 5 of this work, VAME supported OMMs were synthesized to improve their surface functionality and hydrothermal stability. In this work, we are interested in the preparation of small size silver nanoparticles with high surface area and hence higher catalytic properties. To date, many methods have been developed but there is a limitation on the stability and dispersion of the silver nanoparticles in liquid phase catalysis. Apart from this, most of the conventional methods of silver nanoparticle synthetic methods occur at high temperature in the presence of non-ecofriendly stabilizers as surface ligands and supporting matrices. To alleviate such problems, in this work we are interested in immobilization of Ag NPs on methyl vernolate (VAME) supported on ordered mesoporous nanomaterials as a surface ligand to decrease their size and sintering effect thereby increasing their stability for long term catalytic applications. The synthesis of

smaller size AgNps with high catalytic efficiency is also governed by other factors such as the type of solvent, reducing agent and condition of reaction media like pH. The use of non-aqueous solvents like DMF and strong reducing agent like $NaBH_4$ which create basic media facilitate the formation of smaller size silver metal nanoparticles with decreased state of aggregation as reported in the literature [3-5] and have been considered here.

Consequently, in this work, a series of Ag nanoparticles impregnated mOMMs were prepared according to the reported procedures [6, 7] with slight modifications. Modified OMMs with optimum 13 % VAME loading (AgmMCM (3 & 15)1, AgmSBA1 and AgmPMO1) with different surface nature were used and evaluated according to the results described in Chapter 5. The resulting process can be described as follows (Scheme 6.1).

mOMMs $\xrightarrow{AgNO_3}$ Ag^+-mOMMs $\xrightarrow{NaBH_4}$ Ag-mOMMs where m stands for VAME

Scheme 6. 1: Synthesis of AgNps by immobilization in-situ with metal salt in DMF solution.

6.1.1. FT-IR Spectral Analysis

Investigation of the change in surface chemistry of the VAME modified OMMs as a result of silver nanoparticles impregnation was initially evaluated by FT-IR of the four Ag-mOMMs (figure 6.1 and table 6.1). The spectra show similar profile as the mOMMs with the presence of characteristic broad bands of silanol and siloxane groups combined with the presence of alkyl CH_3 and CH_2 as well as carbonyl functional groups. The carbonyl group bands of VAME of mOMMs (1724-1742 cm^{-1}) shifted to a lower frequency of 1652 cm^{-1} for VAME of AgmOMMs and presence of Ag-O bands at around

550-582 cm^{-1} as indicated in Table 6.1 confirm the silver impregnation. Such frequency shift toward the lower value may be mainly due to the coordination of Ag with the oxygen of carbonyl group that reduces electron cloud around and hence lower its frequency.

Table 6. 1: FT-IR band assignments for AgmMCM (3)1, AgmMCM (15)1, AgmSBA1 and AgmPMO1

Functional group (mode of vibration & Intensity)	ν(cm^{-1})			
	AgmMCM(3)1	AgmMCM(15)1	AgmSBA1	AgmPMO1
Silanol H-bond (OH) (str.)	3416	3416	3408	3432
Methyl -C-H (CH_3) (asy. str)	2922	2925	2923	2923
Methylene -C-H (CH_2) (str.)	2856	2856	2856	2848
Ester Carbonyl (str.)	1652	1652	1652	1652
Si-O-Si- bond (str.)	1060	1078	1082	1029
Ag-O (str.)	582	577	468	450
Al-SiO_2(from Al_MCM-41)	799	802	-	-

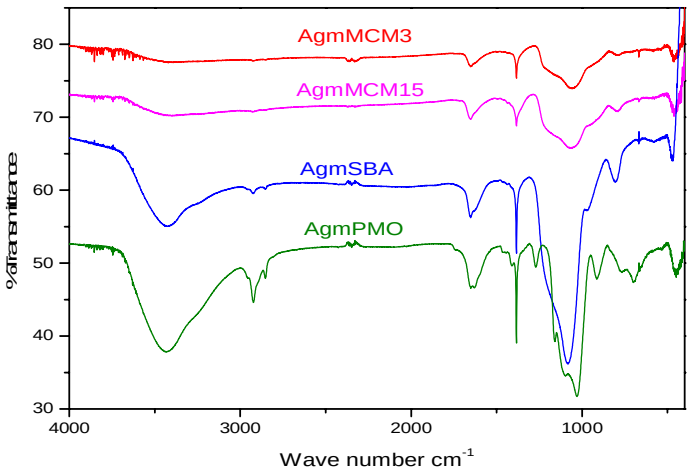

Figure 6. 1: FT-IR Spectra of AgmOMM1

Note that the nearly similar stretching of C=O & C-H for the first three AgmOMMs may be due to the fact that all the OMMs are composed of the same modifier material VAME whose (VAME-OMMs) carbonyl group coordinated with silver.

6.1.2. Powder XRD Studies

The wide angle region of powder XRD of all the four VAME supported and Ag impregnated ordered mesoporous materials (AgmMCM (3)1 and (15)1, AgmPMO1, & AgmSBA1.) are shown in figure 6.2.

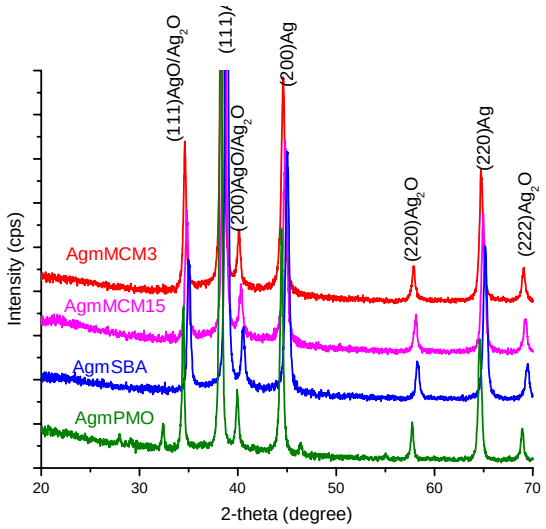

Figure 6. 2: Powder XRD of AgmSBA1, AgmPMO1, AgmMCM (3& 15)1.

Note that the sharp intense peaks at 2-theta=38, 45 & 65^0 which are indexed as indicated in figure 6.2 correspond to silver (Ag^0) present in the composites VAME-OMMs. Additional low intense peaks at 34, 40, 58 & 69^0 which are indexed as indicated in figure 6.2 correspond to the formation of some Ag_2O & AgO stabilized with mOMMs. This result is consistent with the results reported in the literature [8-12]. Note also that based

on the Scherrer equation and the value of full width at high maximum (FWHM) of highest intensity peak calculated using JADE MDI powder XRD software, the Ag NPs size in the AgmOMM nanocomposite is from 2.59 nm for AgmMCM (15)1 to 5.49 nm for AgmSBA1 and the minor Ag (I/II) oxide nanoparticle size formed in the same nanocomposite is 2.32 nm for AgmMCM (15)1 to 5.74 nm for AgmSBA1 which are consistent with the given pore size of mOMMs in section 5.2 of chapter 5.

6.1.3. Transmission Electron Microscopy Studies

The surface morphology and size of the incorporated silver nanoparticles on VAME-OMMs samples were investigated by TEM. Note that most of the obtained nanoparticles (Silver (I/II) Oxide) nanoparticles for AgmOMMs are well dispersed with a spherical shape with a retained hexagonal structure of the mesopore matrix as shown in figures 6.3 to 6.6. In the bright field TEM images, the mesopores are observed due to the contrast pore-wall density. However, the loading of VAME would not be visible due to the very poor scattering power of C-based materials [13]. On the other hand, Ag provides contrast due to its higher electron density. Thus, in the images silver particles will show as strong dark contrasts, whereas the mesoporous matrix shows as a pore white- wall-grey contrast scheme.

In the case of MCM (3 &15)1 it has to be mentioned that MCM (3)1 is formed by very small domains of hexagonal mesopores, while MCM (15)1 is formed by larger ordered particles. In both cases, the pore size is rather small as compared to the pore sizes of mOMMs described in section 5.2. Figures 6.3 to 6.6 show TEM images of AgmMCM (3)1, AgmMCM (15)1, AgmSBA1 and AgmPMO1.

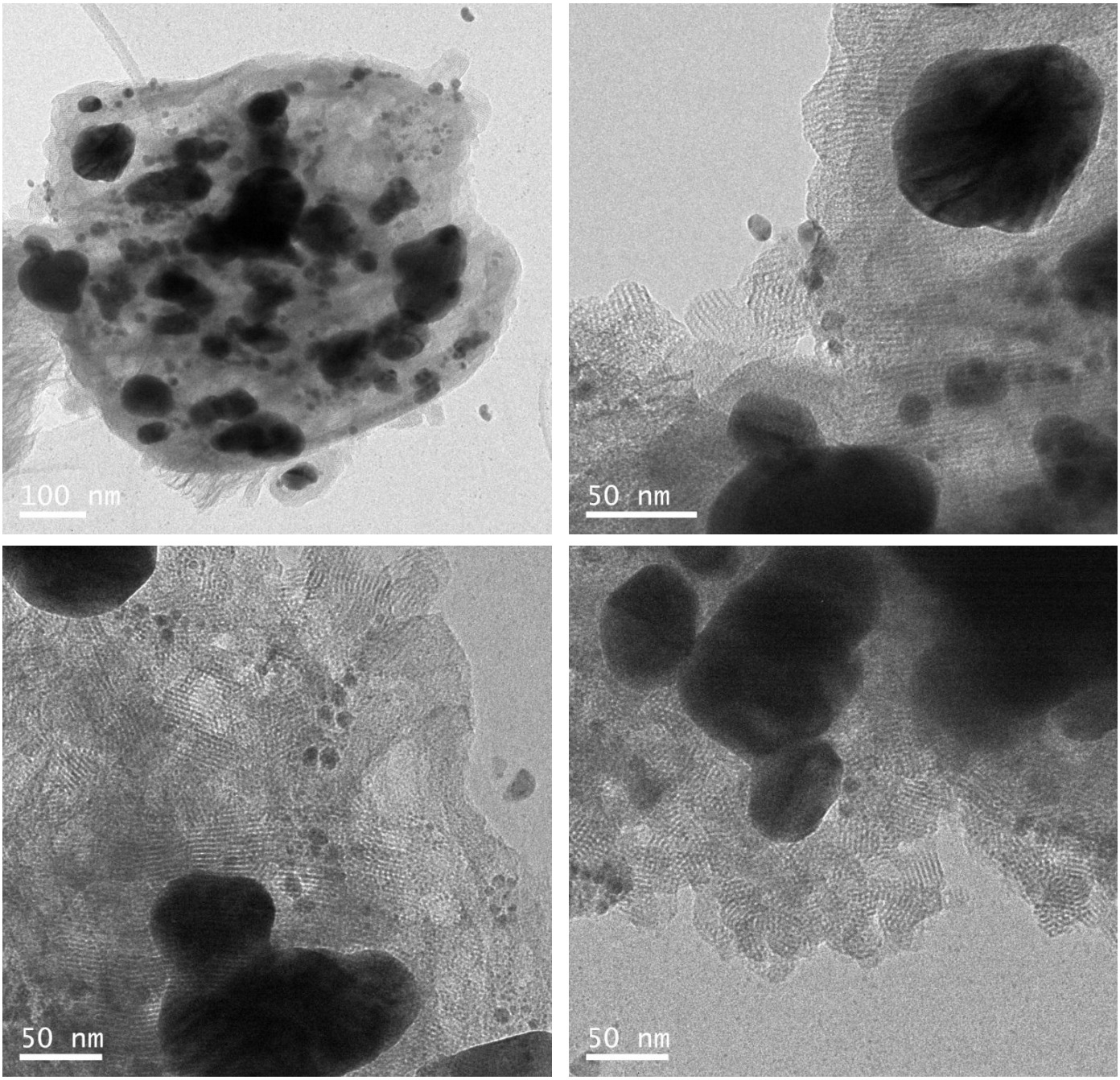

Figure 6. 3: TEM micrographs of AgmMCM (3)1 at different direction and magnifications

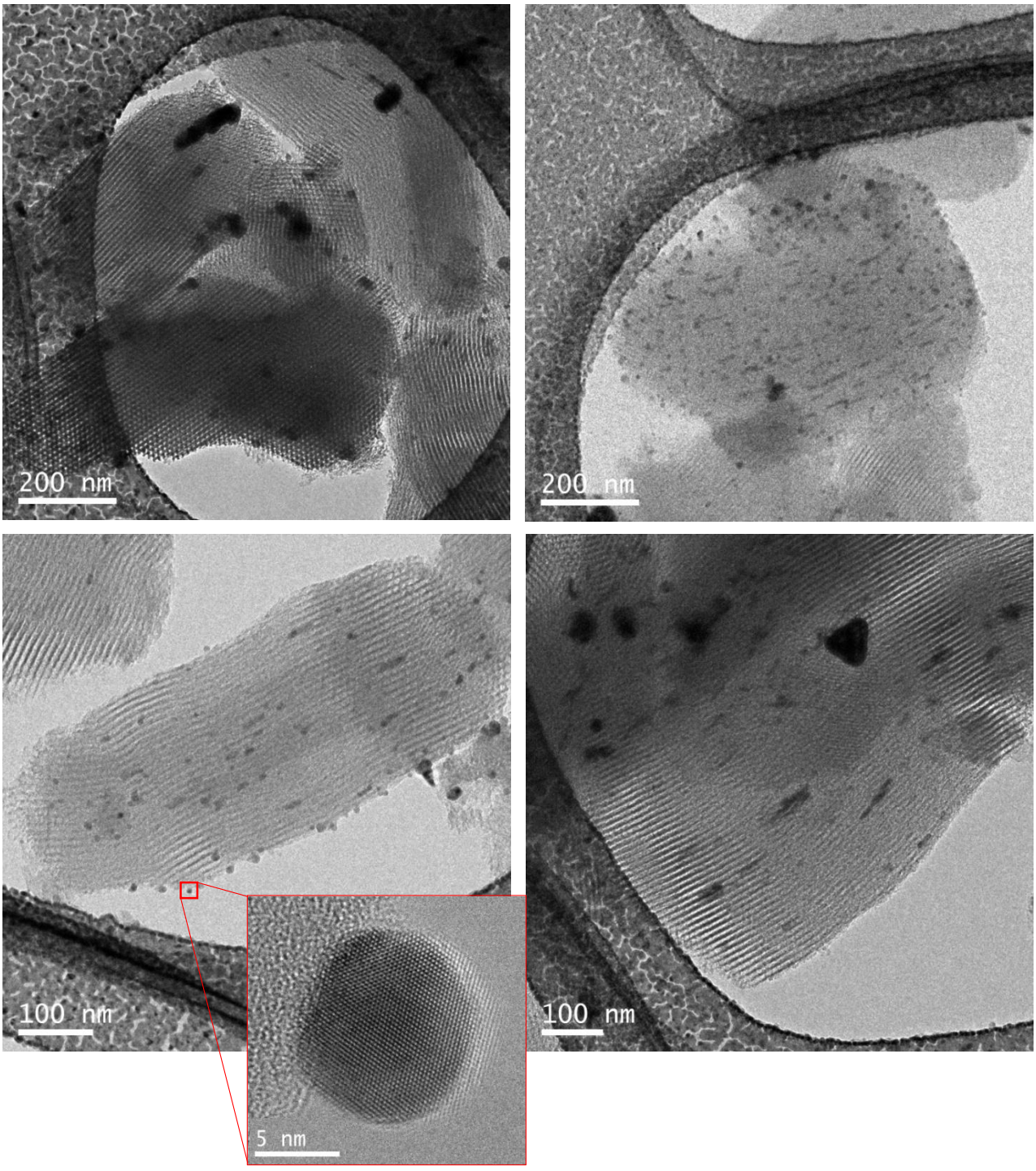

Figure 6. 4: TEM images of AgmMCM (15)1 at outer and inner surfaces and different magnifications

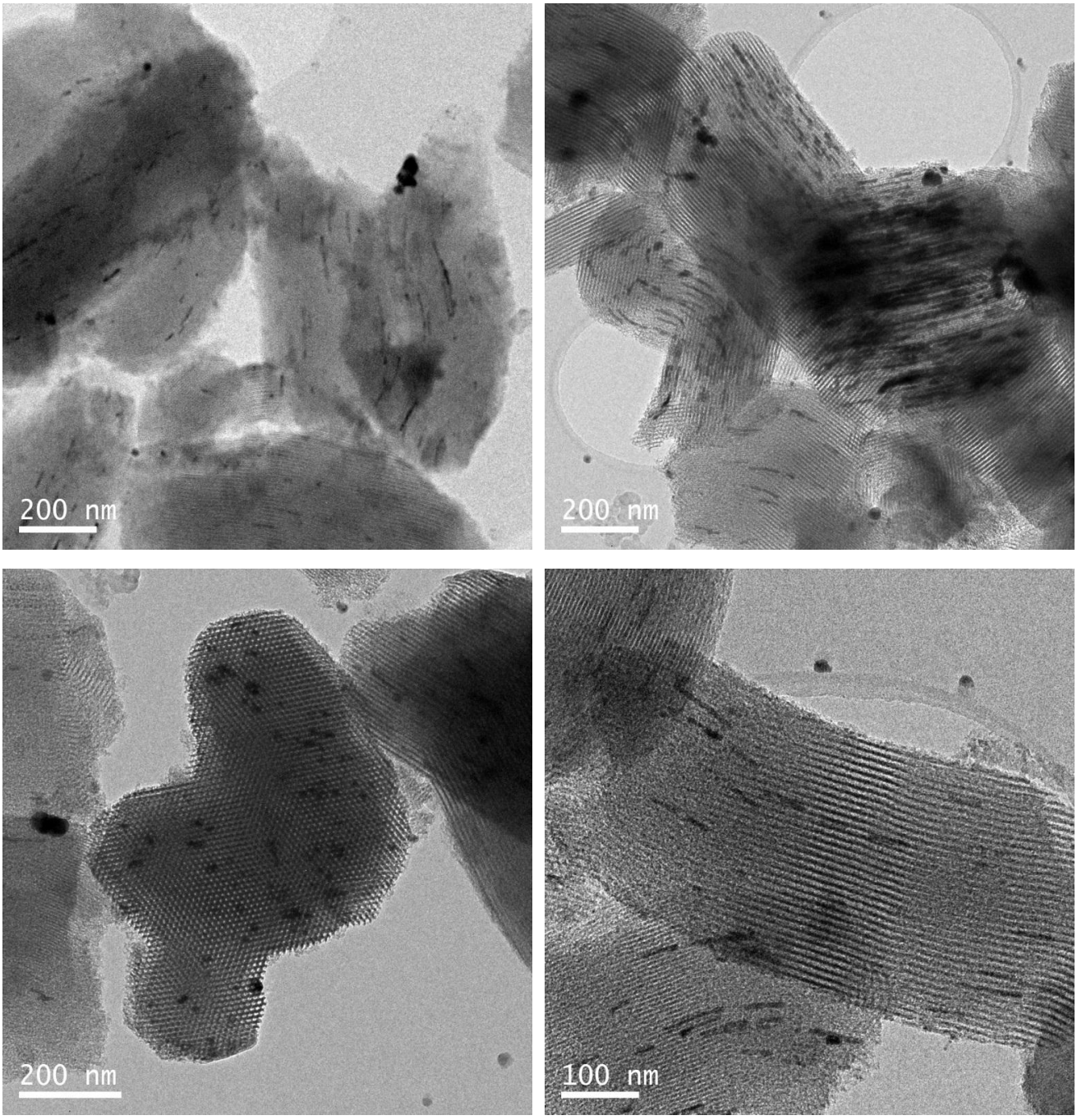

Figure 6. 5: TEM images of AgmSBA1 at varying surface and magnifications

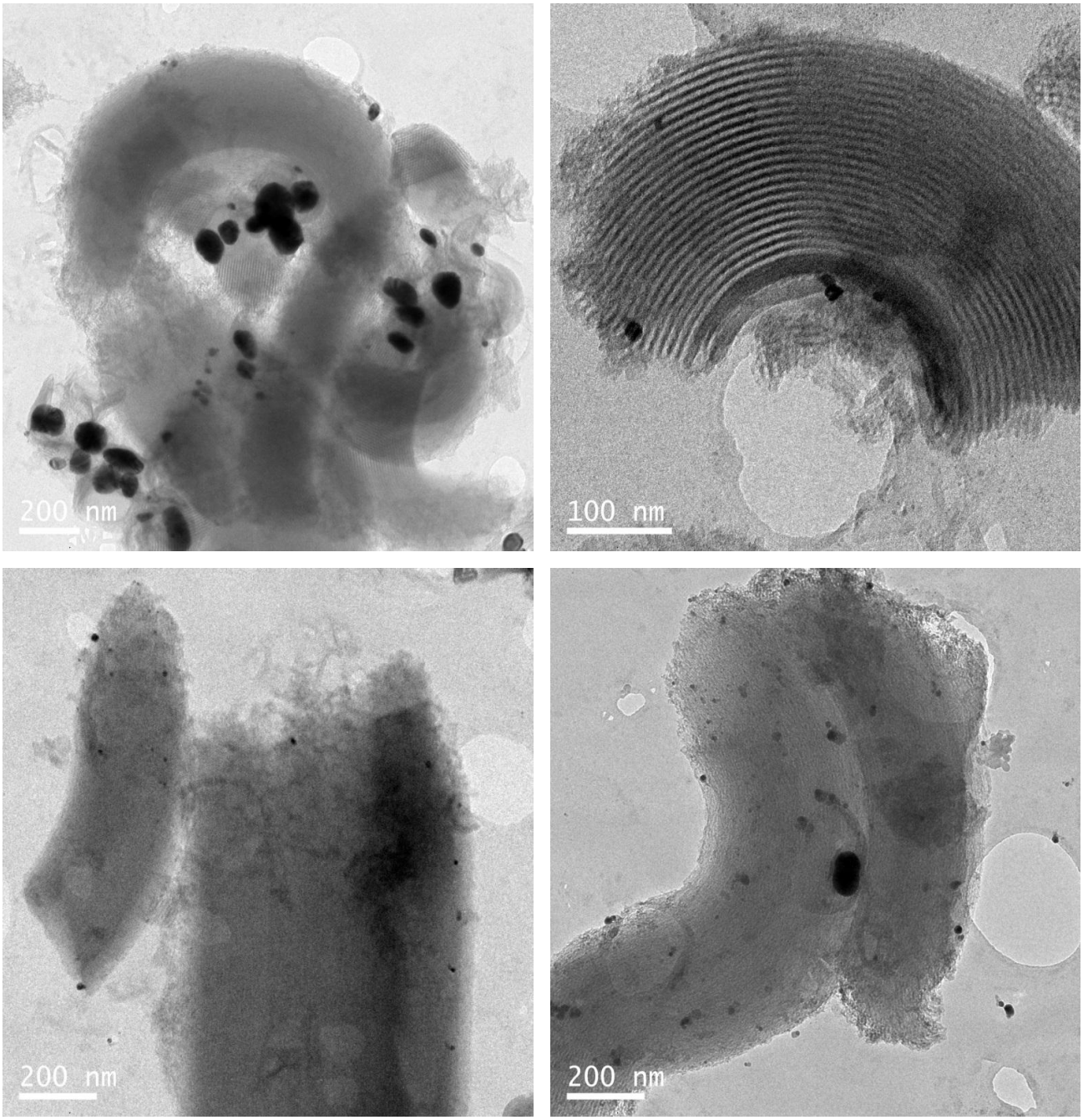

Figure 6. 6: TEM images of AgmPMO1 at outer and inner surfaces and different magnifications

Note also that TEM images of AgmOMM composites showed that the mOMM part of the composite retained well-ordered mesoporous channels arranged in two dimensional hexagonal structure symmetry and also indicates silver or silver (I/II) oxide nanoparticles are well dispersed on the outer surface and inner mesopore channel surface of the hexagonal symmetry with less aggregation and spherical shape.TEM images also show the formation of some Ag nanorods as well which is consistent with the literature report [14]. Note also that the smallest size of silver/silver (I/II) oxide particle size calculated using ImageJ software for AgmOMMs is from 2 nm to 40 nm for Ag mMCM (15)1 and the largest size is from 4 nm to 72 nm for AgmSBA1. This result is in agreement with the result obtained in the literature [7, 8, 10, 11, 15]. Finally, it could be concluded from the images that PMO support may be too hydrophobic for the diffusion of $AgNO_3$, leading to a less loaded material.

In summary, the characterization results of AgmOMMs from FT-IR, PXRD, and TEM images confirm the formation of Ag NPs with appropriate size for catalytic applications.

In general, the proposed reaction scheme for AgmOMMs synthesis as indicated in Scheme 6.2.

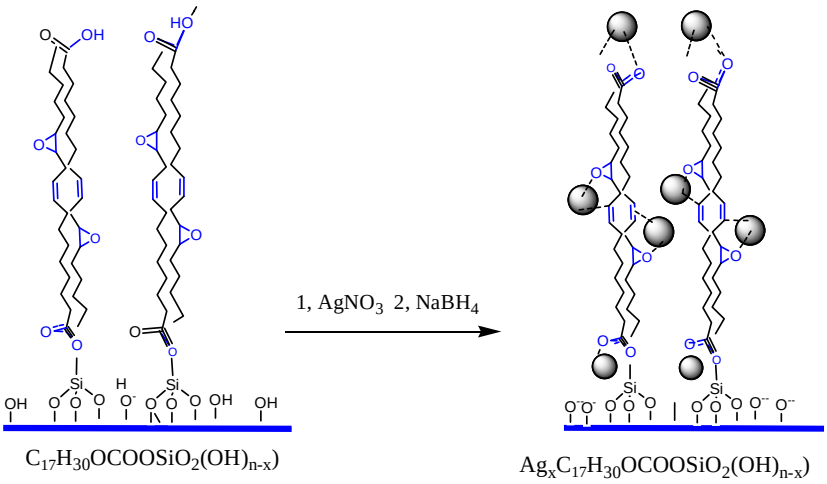

Scheme 6. 2: Synthesis of AgmOMMs by in-situ impregnation of metal salt

6.2. Loading of Ag on IFVAME Supported SBA1 and PMO1

Ordered mesoporous materials surface supported with mercaptoimidazole functionalized vernolic acid methyl ester (IFAME) with additional and softer S and N binding sites that fits the softer Ag metals are good potential candidates for more AgNPs immobilization with increased stability. Consequently, in this section Ag NPs impregnated ifmSBA1 & ifmPMO1 were prepared according to the reported procedures [6, 7] with slight modifications in a similar way to Ag immobilizations on mOMMs. in sección 6.1,

6.2.1. FT-IR Spectral Analysis

FT-IR spectra of the four AgmOMMs (figure 6.7) were recorded whose result is shown in the table 6.2. The characterization result showed a change in the carbonyl stretching of the carboxylate groups due to coordination of AgNPs with electron rich oxygen of the

carboxylate as well as sulfur and nitrogen from mercapto imidazole substituent of the IFVAME.

Table 6. 2: FT-IR Spectral Analysis of AgifmOMMs (AgifmSBA & AgifmPMO)

Functional group (mode of vibration & Intensity)	ν(cm^{-1})	
	AgifmSBA1	AgifmPMO1
Silanol H-bond (OH) (str.)	3424	3435
Methyl -C-H (CH_3) (str. as,.)	2924	2924
Methylene -C-H (CH_2) of VAME	2856	2848
Ester Carbonyl of VAME	1654	1631
Si-O-Si- bond (str.)	1082	1031
Ag-O (str.)	806	778
Al-SiO_2(from Al_MCM-41)	-465	460-

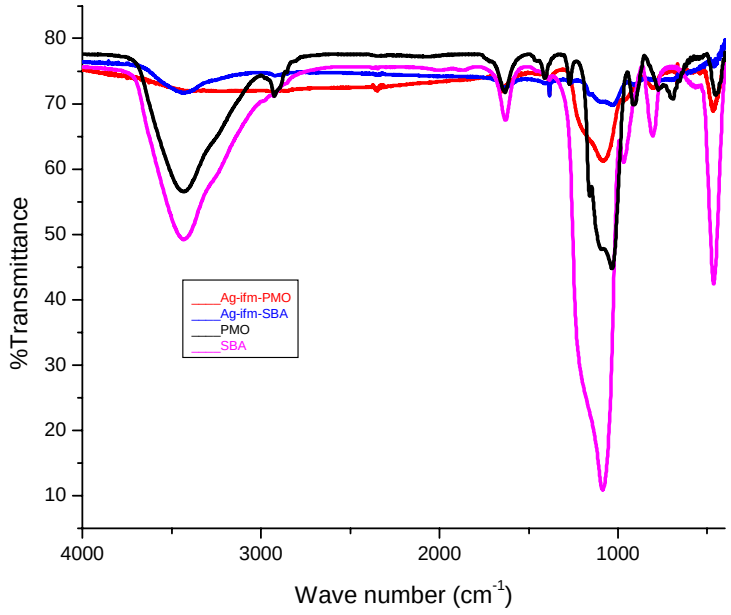

Figure 6. 7: FT-IR of AgifmSBA and AgifmPMO1 nanocomposites compared to their precursors SBA1 and PMO1

6.2.2. Powder XRD studies

The wide angle region of powder XRD of two IFVAME supported and Ag –impregnated ordered mesoporous materials (AgifmPMO1, & AgifmSBA1), are as shown in figure 6.8.

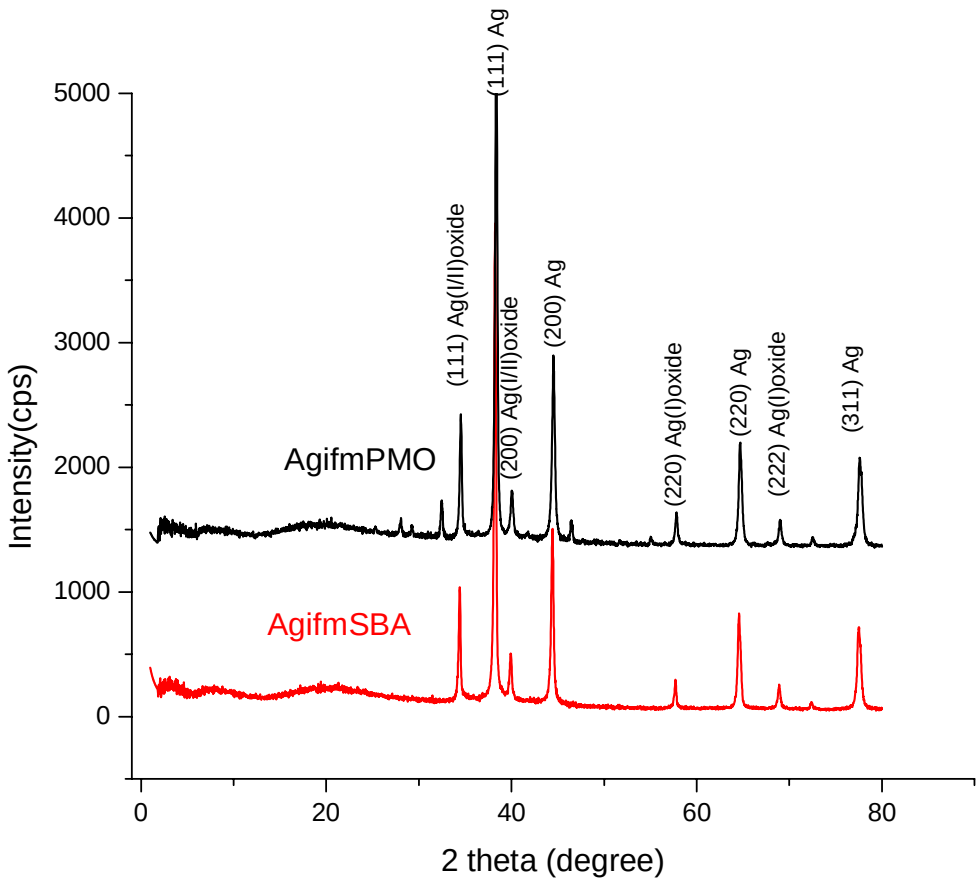

Figure 6. 8: Wide angle Powder XRD pattern of AgifmSBA1 and AgifmPMO1.

Note that peaks at 2-theta=38, 45, 65 & 78^0 indicate crystalline silver nanoparticles formed in AgifmOMMs nanocomposite as indexed in figure 6.8, while the observed additional peaks at 34, 40, 58 & 72^0 may be due to some silver (I/II) oxide formed as a result of the silver metal oxidation by air on exposure to light in the nanocomposite as

indexed in the same figure. Note also that based on the Scherrer equation and the value of full width at high maximum (FWHM) of highest intensity peak calculated from JADE MDI powder XRD software, the Ag nanoparticle size formed in AgifmSBA1 nanocomposite is 5.39 nm and the minor Ag (I/II) oxide nanoparticle size formed in the same nanocomposite as a result of Ag oxidation is 5.6 nm which are consistent with the given pore size of ifmOMMs in section 5.2 of chapter 5. This value is consistent with the literature cited for AgmOMMs nanocomposites.

Note that there is a shift of peaks of AgifmSBA1 & AgifmPMO1 to the left and right of their original precursor OMMs may be due to contraction and swelling of the pore size respectively.

Broad diffraction peaks for both AgifmOMMs at 2-theta 20^0 indicates the presence of surface wall amorphous OMMs.

6.2.3. Transmission Electron Microscopy Studies

Similar to that of Ag nanoparticle formation in AgmOMMs nanocomposites, the bright TEM images of AgifmSBA1 & AgifmPMO1 also show that well dispersed and nearly spherical and rod-shaped Ag Nps which is in agreement with literature report [14] with some amount of silver (I/II) oxide nanoparticles are formed in the nanocomposite during silver loading with higher concentration on the outer surface and with slightly higher degree of aggregation. The manually calculated average crystallite size of the obtained spherical shaped nanoparticle silver/silver (I/II) oxide using ImageJ software is 8 to 63 nm for AgifmSBA1 nanocomposites & 2 to 67 nm for AgifmPMO1.

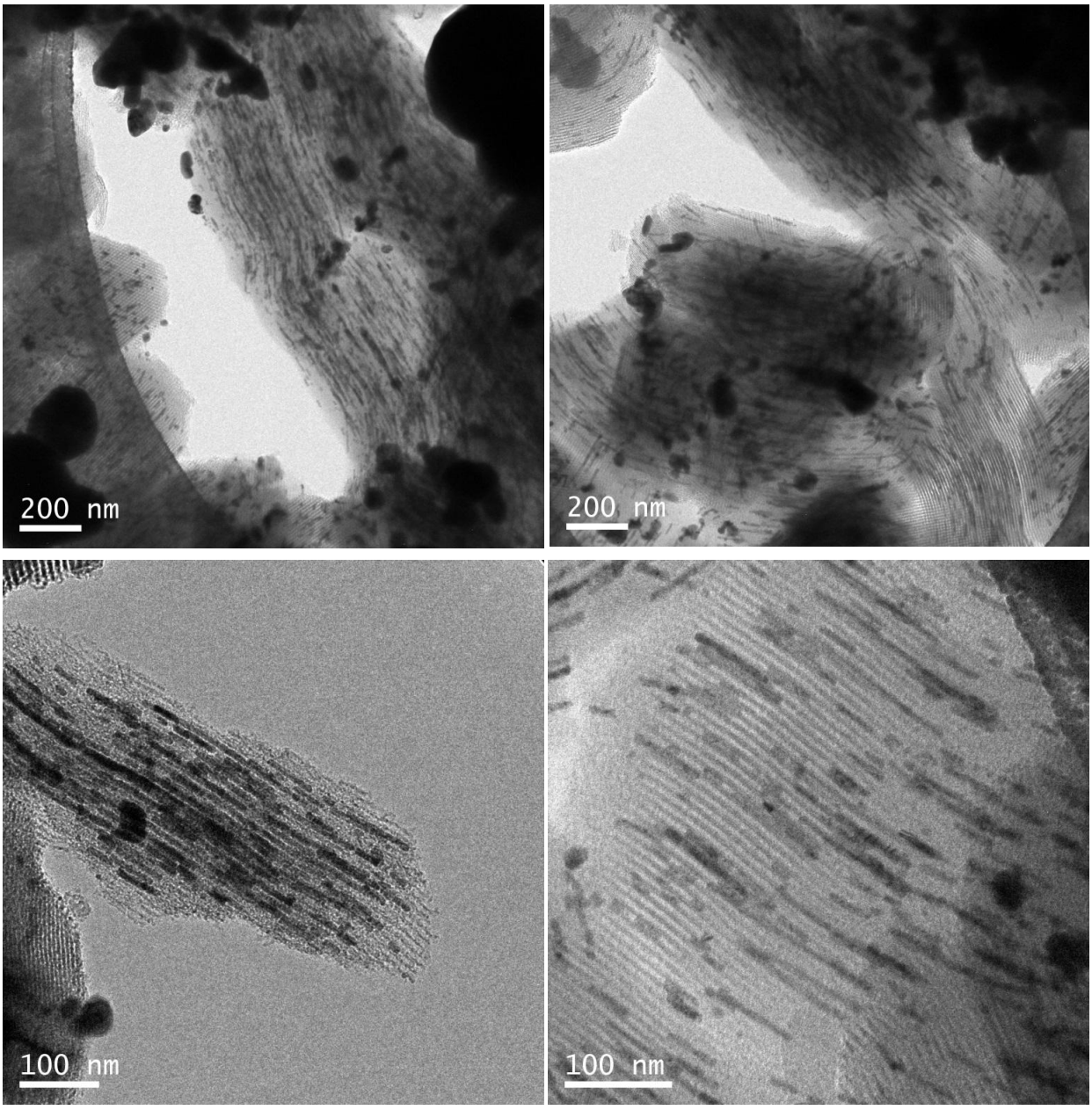

Figure 6. 9: TEM images of AgifmSBA1 at outer surface and inner hexagonal symmetry pore channels of mesopore structure with different magnifications.

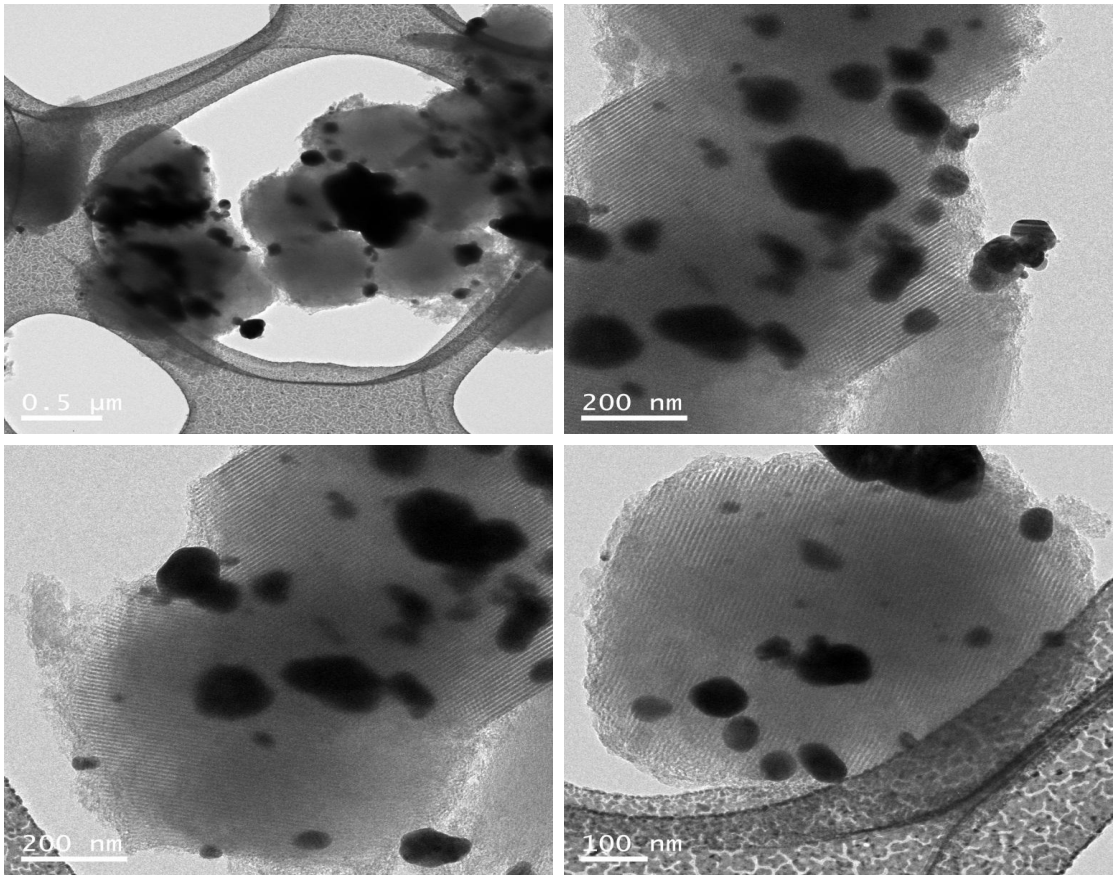

Figure 6. 10: TEM images of AgifmPMO1 at outer surface and inner hexagonal symmetry pore channels of mesopore structure with different magnifications.

In summary, the characterization results from FT-IR, PXRD and TEM images of Agifm nanocomposites in correlation with textural properties of the pristine materials confirms for the formation of spherical and rod shaped Ag Nps with potential catalytic applications

In general, the proposed reaction scheme for AgifmOMMs is given in the scheme 6.3.

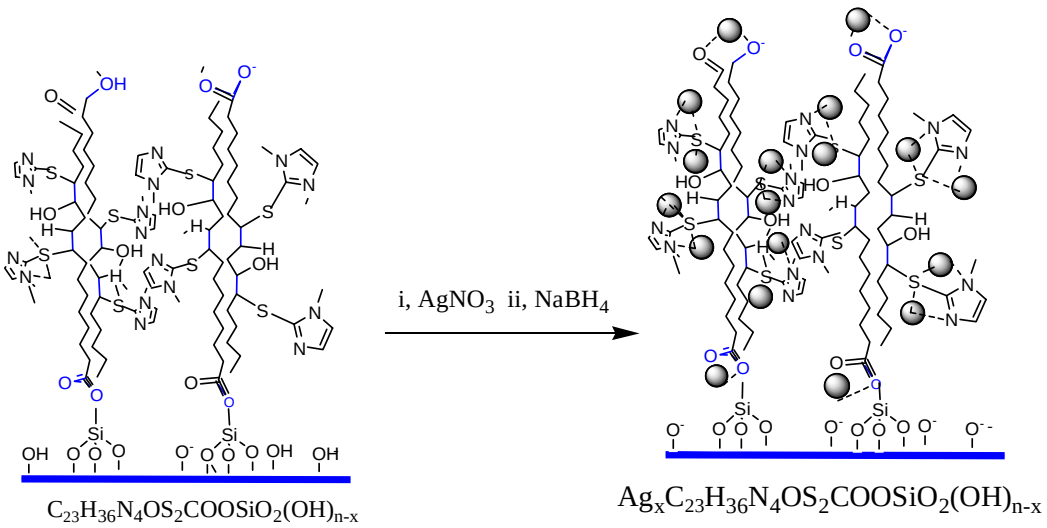

Scheme 6. 3: Synthesis of AgifmOMMs by in-situ impregnation of metal Salt.

6.3. Catalytic Tests on Ag modified OMMs

In the present world of rapidly increasing populations and industrialization, organic dye effluent from the textile industry have become one of the major water pollutants next to that of agricultural waste. Report from World Bank showed that about 20 % global industrial pollution comes from the textile industry due to its higher consumption of water (1.6 million Liter) for production about 3600 types of chemicals by using more than 8000 chemicals [16]. Various classical methods such as adsorptions, sedimentation,

coagulation, ultra-filtration, etc. have been used to treat effluent. However, such methods generate secondary pollutants, which need further treatment. Heterogeneous photocatalysis/chemocatalyst which belongs to the emerging, and destructive technology called advanced oxidation process uses semiconducting nanoparticles for photo degradations of organic dyes. Such catalytic mechanism involves the photo excitations of electrons to form the excited electron-positive hole pairs. The excited electron generates HO^* free radical which together with the positive holes helps in the degradation of organic dyes [17]. Many methods have been used to decrease the band gaps of semiconducting nanoparticles like the most widely investigated titanium oxide semiconducting nanoparticles [18]. Recently, the silver nanoparticle has attracted much attention due to its lower band gap that facilitates the photodegradation of organic dyes both under UV and Visible light via surface plasmon resonance mechanism [17]

In order to have efficient catalytic performance in liquid media, high stability and dispersion capacity of silver nanoparticles is very important [17].

In this study, Photocatalytic and chemo catalytic, degradation test of model organic dye Methyl orange (MO) and Methylene blue (MB) by Ag-mOMMs are presented whose results were analyzed by using UV-vis spectroscopy.

6.3.1. Photocatalytic degradation test of MO by AgmOMMs

A Model dye methyl orange (MO) is a known acid-base indicator with the following structures (figure 6.11) and two UV-vis absorption maxima less intense band at 271 nm and more intense band at 465 nm (figure 6.11) [19]. The later intense band was used to monitor the photocatalytic degradation of MO by the synthesized nanocomposite.

a) 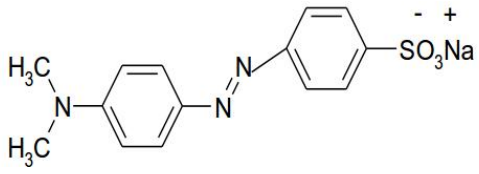

b) 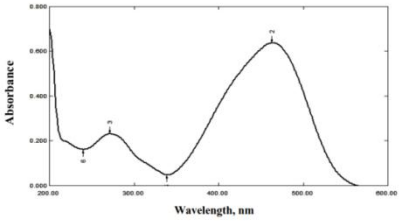

Figure 6. 11: a) Structure of MO and b) UV-Vis Spectrum of MO

In this study, initially, a preliminary photodegradation test was done based on the procedure reported in the literature [16, 17] with slight modification. After preparation of 100 mL of methyl orange solution, 4 mL of 10 ppm of methyl orange was added to a quartz Cuvette and 3 mg of AgmSBA1 was added, stirred and tied inside the quartz glass of UV reactor nearer of 150 W lamp at one inlet. As a control test, an additional 4 mL of methyl orange without the catalyst was tied and put in a similar way at another inlet. Then after, UV light irradiation with UV reactor for 8 h. The resulted UV-vis absorption peak reduction at 465 nm for MO solution to which AgmSBA1 was added found to show a color change and difference of color change was observed as shown in figure 6.7. The obtained result is consistent with the results reported in literature [16, 17].

Then similar discoloration test was done for AgmMCM (3 & 15)1 and AgmPMO1 which resulted in no significant change in color. The discoloration percentages were calculated using the following equation [16].

$$\text{discoloration (\%)} = \frac{Co - C}{Co} x100$$

Where, C_0 and C are the initial and the after-treatment dye, concentrations in mg L^{-1}, respectively.

Alternatively, $\text{discoloration (\%)} = \frac{Ao-A}{Ao} x100$ [20].

Where A_o is the initial absorbance of MO. and A is the absorbance at sampling time. Based on the above equations the highest discoloration (%) of MO is found to be 70 %. Furthermore, for AgmSBA1 photodegradation test was done at varying time by taking 166 mg of AgmSBA1 in 500 mL of 10 ppm MO dye [16] under oxygen purge and magnetic stirring in 140 W lamp UV reactor. The observed result shows that there is a slight change of color of MO which may be due to the less dose and as the synthesized catalyst used.The other reason may be due to less power of UV lamp used (150 W) compared 300 W used in the literature [16]. Figure 6.12 shows the color change in the preliminary test and UV-vis spectroscopy result of MO after degradation test at varying time and for different catalysts.

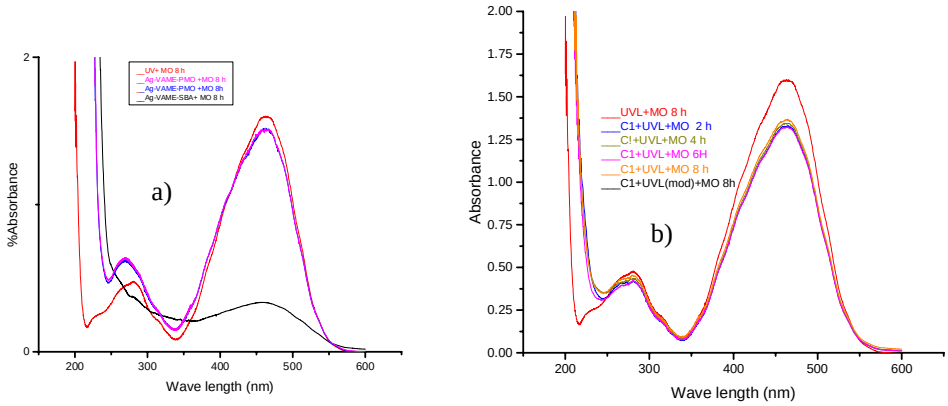

Figure 6. 12: UV-vis spectroscopy of MO after degradation test: a) by AgmMCM, AgmPMO, and presence of only UV light compared with that of AgmSBA1 at preliminary test. b) by AgmSBA1 at a varying time compared with that of its preliminary test result of AgmSBA1

Note that from UV-vis spectrum results, the catalytic degradation capacity of MO dye by the prepared catalyst is in the order AgmSBA1 > AgmMCM(15)1 > AgmPMO1 and hence

AgmSBA1 has highest MO dye degradation capacity which may be due the formation of higher surface area and smaller size silver and silver oxide nanoparticles on the outer surface and pore wall surface of AgmSBA1 whereas the least degradation capacity of MO dye by AgmPMO1 may be due to higher hydrophobicity of PMO that attracts the hydrophobic MO dye. This result can be supported by the characteristic decay curve for the UV-vis spectrum of a small cluster of Ag/AgO nanoparticles (usually less than 10 nm) instead of surface Plasmon resonance from a solution of sample AgmSBA1 emerged in 1M NaOH shown in figure 6.13.

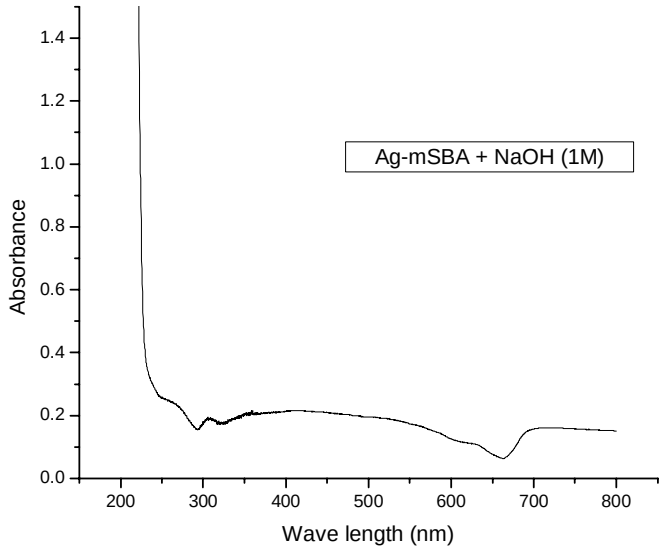

Figure 6. 13: UV-Vis Spectrum of AgmSBA1 in 1M NaOH solution.

6.3.2. chemodegradation of Methylene blue by Silver nanocomposite

Silver loaded on VAME/IFVAME supported OMMs have been tested for their ability to catalyze the reduction of dyes by sodium borohydride ($NaBH_4$) that resulted in a color change of model dye. In the absence of silver nanoparticles, the sample was almost

stationary showing very little or no reduction of the dyes. When silver nanocomposites were added to the solution, the sample rapidly decolorizes the solution. Figure 6.14 shows how the absorbance spectrum of the dyes decreases when the dyes are reduced.

Silver nanoparticles act as an electron relay, aiding in the transfer of electrons from the BH^{-}_{4} ion to the dyes, and thereby causing a reduction of the dyes. BH^{-}_{4} ions are nucleophilic while dyes are electrophilic. It has been proven that nucleophilic ions can donate electrons to metal particles, while an electrophilic can capture electrons from metal particles. It has been shown that BH^{-}_{4} ions and dyes are simultaneously adsorbed on the surface of silver particles when they were present together.

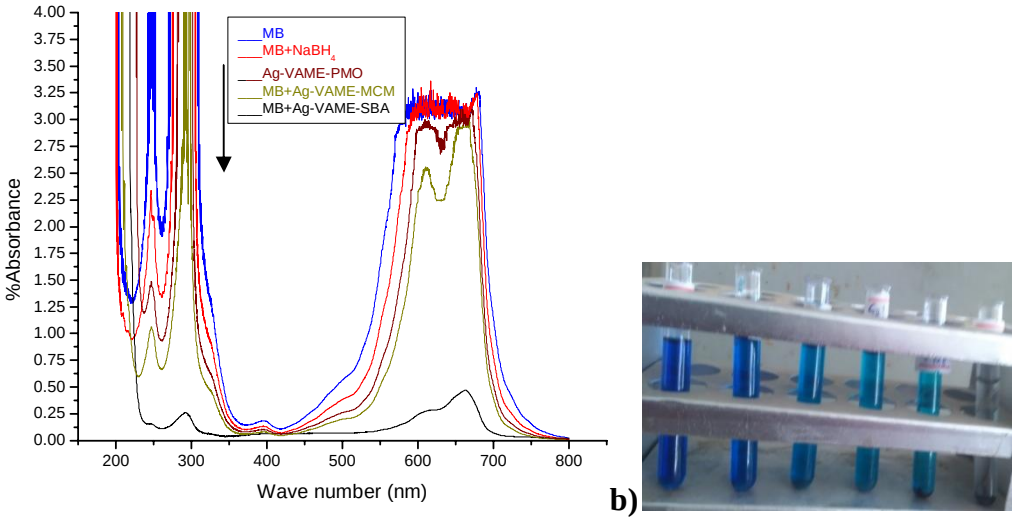

a) **b)**

Figure 6. 14: a) UV-vs spectra of Methylene blue after degradation test by different AgmOMMs (catalyst compared with that of $NaBH_4$ and b) the resulted color changes

In summary, the formation of AgmOMMs and AgifmOMMs was achieved as confirmed by FT-IR spectra, Powder XRD profiles and TEM image. The potential catalytic application test for degradation for model dye MO & MB seems to be promising for AgmSBA1.

6.4. References

1. Yin A, Guo X, Dai W, Fan K: **High activity and selectivity of Ag/SiO_2 catalyst for hydrogenation of dimethyl oxalate**. *Chem Commun (Camb)* 2010, **46**(24):4348-4350.
2. Chen Y, Wang C, Liu H, Qiu J, Bao X: **Ag/SiO_2: a novel catalyst with high activity and selectivity for hydrogenation of chloronitrobenzenes**. *Chem Commun (Camb)* 2005(42):5298-5300.
3. Abou El-Nour KMM, Eftaiha Aa, Al-Warthan A, Ammar RAA: **Synthesis and applications of silver nanoparticles**. *Arabian J. of Chemistry* 2010, **3**(3):135-140.
4. Zienkiewicz-Strzałka M, Błachnio M, Deryło-Marczewska A, Kozakevych RB, Bolbukh YM, Tertykh VA: **Silver nanoparticles deposited on pyrogenic silica solids: Preparation and textural properties**. *Adsorption Sci. & Technology* 2017, **35**(7-8):714-720.
5. Zienkiewicz-Strzałka M, Deryło-Marczewska A, Kozakevych RB: **Silica nanocomposites based on silver nanoparticles-functionalization and pH effect**. *Applied Nanoscience* 2018, **8**(7):1649-1668.
6. Gupta R, Ganesan V: **Gold nanoparticles impregnated mesoporous silica spheres for simultaneous and selective determination of uric acid and ascobic acid**. *Sensor and Actuator B: Chemical* 2015, **218**:139-145.
7. Huang R-S, Hou B-F, Li H-T, Fu X-C, Xie C-G: **Preparation of silver nanoparticles supported mesoporous silica microspheres with**

perpendicularly aligned mesopore channels and their antibacterial activities. *RSC Advances* 2015, **5**(75):61184-61190.

8. Zienkiewicz-Strzałkaa M, Pasieczna-Patkowskab S, Kozakc M, Pikusa. S.: **Silver Nanoparticles Incorporated onto Ordered mesoporous Silica from Tollen's Reagent**. *Applied Surface Sci.* 2013, **266**:337-343.

9. Dorobantu LS, Gossc GG, Robert E. Burrell RE: **Effect of light on physicochemical and biological properties of nanocrystalline silver dressings**. *RSC Advances* 2015, **5**:14294–14304.

10. Zhao Y, Yue Qi Y, Wei Y, Y Zhang Y, Zhang S, Yang Y, Liu Z: **Incorporation of Ag nanostructures into channels of nitrided mesoporous silica**. *Microporous and mesoporous materials* 2008, **111**:300-306.

11. Velu M, Pyong-In Y, Palanivel V, Palaniyappan J, Sung-Chul H, Seong-Ho J, Jeong-Min S, Subpiramaniyam S: **Production, optimization and characterization of silver oxide nanoparticles using Artocarpus heterophyllus rind extract and their antifungal activity**. *African J. of Biotechnology* 2017, **16**(36):1819-1825.

12. Chen CC, Wu HH, Huang HY, Liu CW, Chen YN: **Synthesis of High Valence Silver-Loaded Mesoporous Silica with Strong Antibacterial Properties**. *International J. of environmental research and public health* 2016, **13**(1).

13. Díaz I, García B, Alonso B, Casado CM, Morán M, Losada J, Pérez-Pariente J: **Ferrocenyl Dendrimers Incorporated into Mesoporous Silica: New Hybrid Redox-Active Materials**. *Chemistry of Materials* 2003, **15**(5):1073-1079.

14. Sareen S, Mutreja V, Singha S, Pal B: **Highly dispersed Au, Ag and Cu nanoparticles in mesoporous SBA-15 for highly selective catalytic reduction of nitroaromatics**. *RSC Adv* 2015, **5**:184.

15. Pawar O, Deshpande N, Dagade S, Waghmode S, Nigam P, Joshi N: **Green synthesis of silver nanoparticles from purple acid phosphatase apoenzyme isolated from a new source Limonia acidissima**, 2015, **11**

16. Colpini LMS, Lenzi GG, Urio MB, Kochepka DM, Alves HJ: **Photodiscoloration of textile reactive dyes on Ni/TiO_2 prepared by the impregnation method: Effect of calcination temperature**. *J of Envir Chem Engin* 2014, **2**(4):2365-2371.

17. Zhou R, Srinivasan MP: **Photocatalysis in a packed bed: Degradation of organic dyes by immobilized silver nanoparticles**. *J of Envir Chem Engin* 2015, **3**(2):609-616.

18. Kant R: **Textile dyeing industry an environmental hazard**. *Natural Sci* 2012, **04**(01):22-26.

19. Hadi HN, Wahab HS: **Visible Light Photocatalytic Decolourization of Methyl Orange Using N-Doped TiO_2 Nanoparticles**. *J. of Al-Nahrain University* 2015, **18**(3):1-9.

7. Conclusion

Nowadays, there is a high discharge of dye effluent from textile industry that greatly pollutes our environment as a result of industrialization and population growth which needs remediation. As a result, there is an increasing research interest for the development of more stable and efficient metal nanocatalyst supported on surface functionalized ordered mesoporous silica framework for effective degradation of model organic dyes. In this study, attempts were made to design modified ordered mesoporous nanocomposites by supporting with native vernonia oil derivatives and incorporation of stable silver nanoparticles (AgNPs) as potential photo/chemo-catalysts for degradation of organic dyes. In line with this, in the first part of this work, more active precursor-like vernolic acid and mono alkyl esters such as methyl, ethyl, and propyl esters were derivatized from the less active native vernonia oil (tri-alkyl ester) by hydrolysis and transesterification reactions using an acid catalyst. The resulting monoalkyl esters were further functionalized by methyl mercapto imidazole by thiol-ene coupling reaction in the presence of free radical reaction activator benzophenone) and UV light energy. The presence of major functional groups of the monoalkyl esters and their mercapto imidazole functionalized products were confirmed by FT-IR, ^{1}H & ^{13}C NMR spectroscopy and CHN elemental analysis.

In the second part of this work, VAME/IFVAME-OMMs or (m/ifmOMMs) coordinated nanocomposites were made by supporting VAME/IFVAME on three types of ordered mesoporous nanomaterials (Al-MCM-41(Si/Al=3&15), SBA-15 and PMO). The highest percent yield of VAME/IFVAME incorporation without pore blocking was achieved at their 13 % loading during surface modifications of OMMs. In such surface modifications,

the active site surface hydroxyl groups of the silanol of OMMs react with the carboxylate functional group of the active monoester (VAME/IFVAME) by transesterification reaction mechanism. The retain of 2D hexagonal structure with feasible porosity and surface area of the modified mesoporous material (mOMMs/ifmOMMs) of 13 % VAME/IFVAME loading for impregnation of Ag NPs were confirmed by N_2 adsorption-desorption isotherm, PXRD and TGA studies results. Furthermore, the incorporation of the VAME/IFVAME in the modified OMMs was confirmed by FT-IR and TGA studies result. In the third part of this work, AgmOMMs and AgifmOMMs were made by in-situ wet impregnation of mOMMs and ifmOMMs by metal salt ($AgNO_3$). PXRD and transmission electron microscopy (TEM) image studies confirmed the formation of polydisperse nanocomposites in the inner and outer surface of the VAME/IFVAME grafted OMMs with retaining of their hexagonal mesopore structure with spherical morphology and average particle size of less than 10 nm. FT-IR studies support coordination of AgNPs with carboxylate groups. The formation high distribution of nanoparticle/nanorods for AgifmOMMs from TEM images also confirmed increased functionality, of ifmOMMs that can stabilize AgNPs. The overall AgNPs incorporated nanocomposite can be proposed in the scheme below. Finally, the photocatalytic and chemical degradation potential of sample nanocomposite were tested and found to be promising as shown in the scheme below.

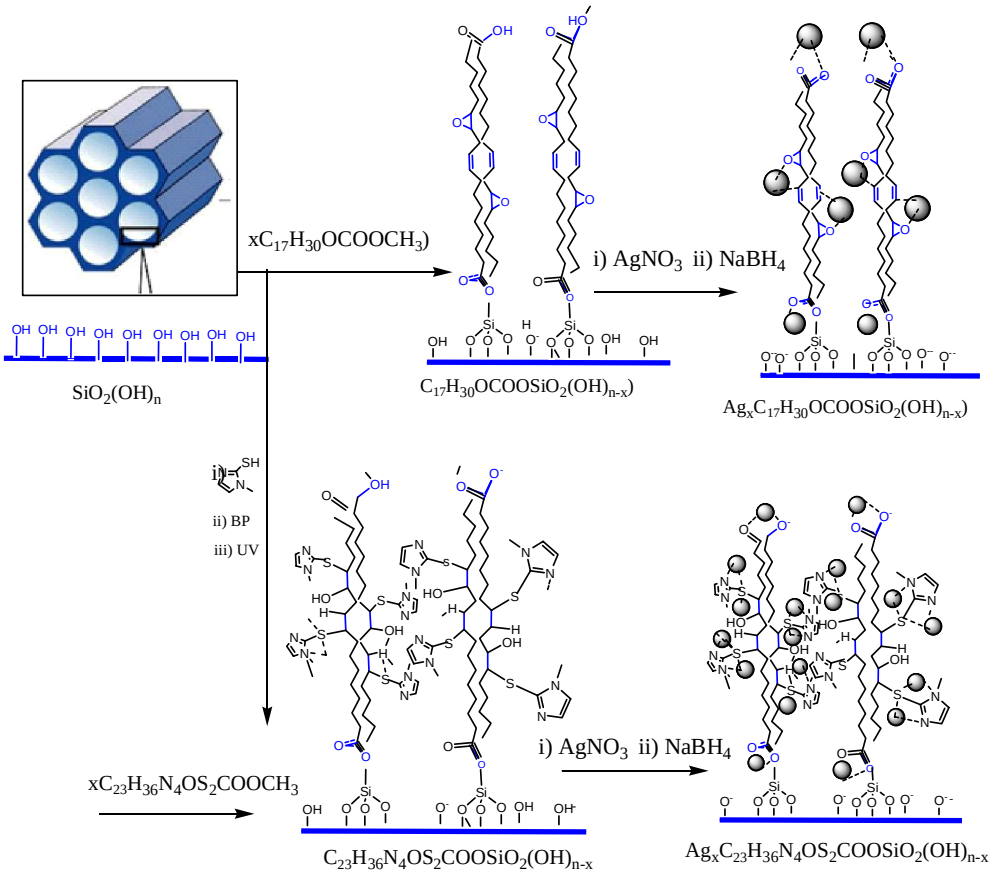

Scheme showing sample support and immobilization of vernonia oil derivative on ordered mesoporous nanomaterial

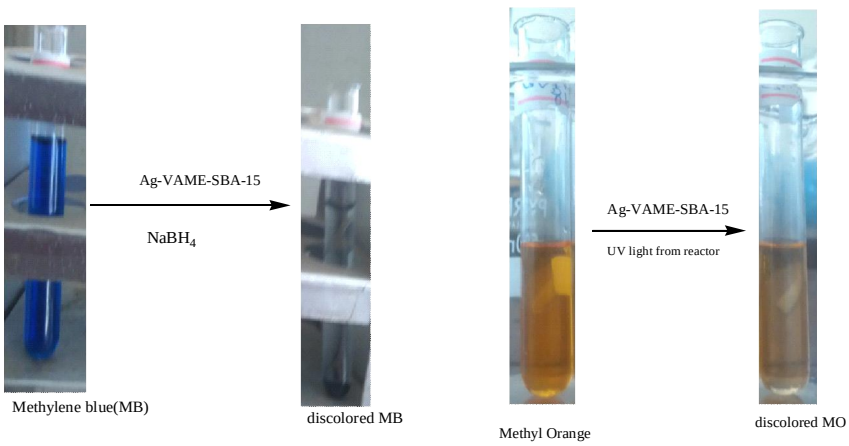

Scheme 7. 1: Schemes showing sample support of vernonia oil derivatives on ordered mesoporous nanomaterials and Ag NPs immobilization (top side) and potentail catalytic degradation test of methylene blue and methyl orange by the synthesized AgmOMM1 nanocomposites (bottom side)

8. Appendices

Appendix 1: ^{1}H & ^{13}C NMR spectra

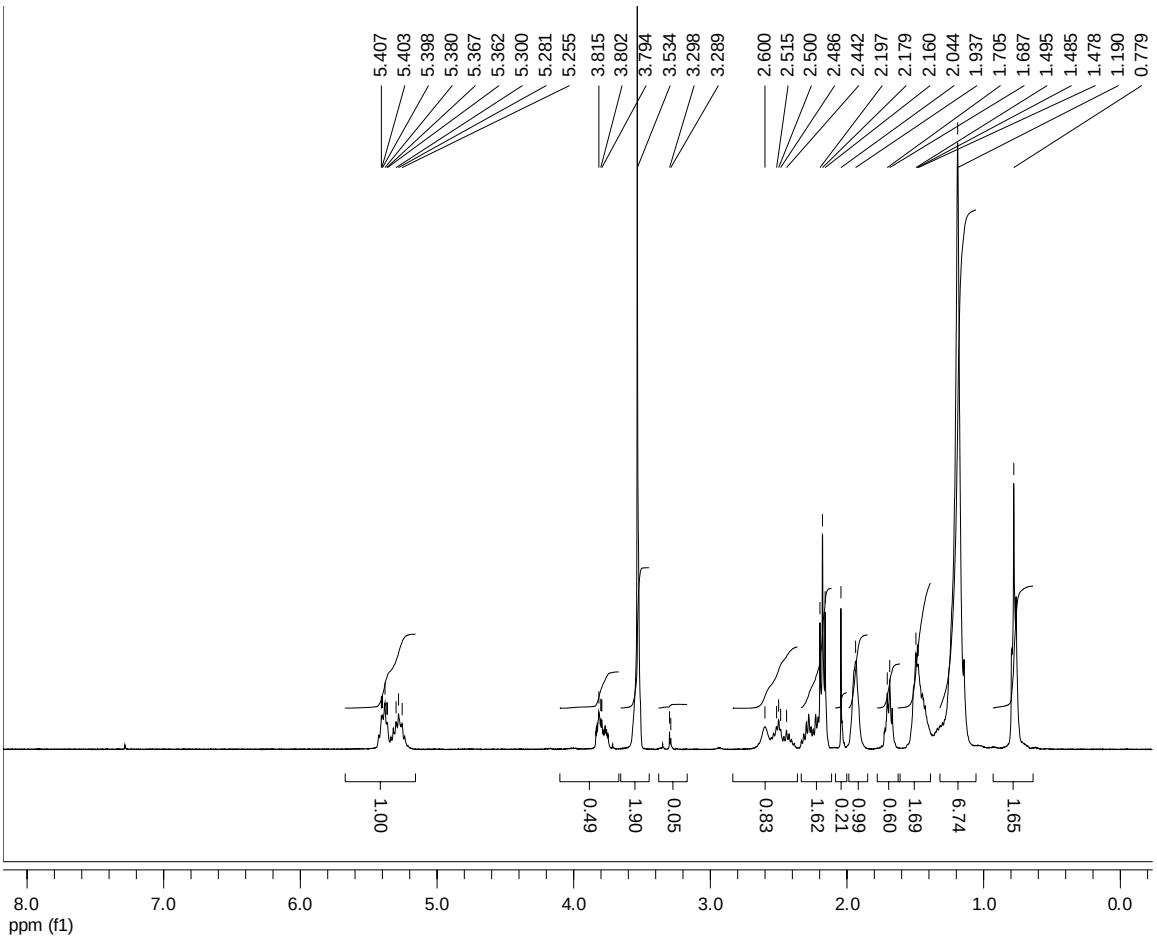

^{1}H NMR spectrum of Vernolic Acid Methyl Ester-VAME

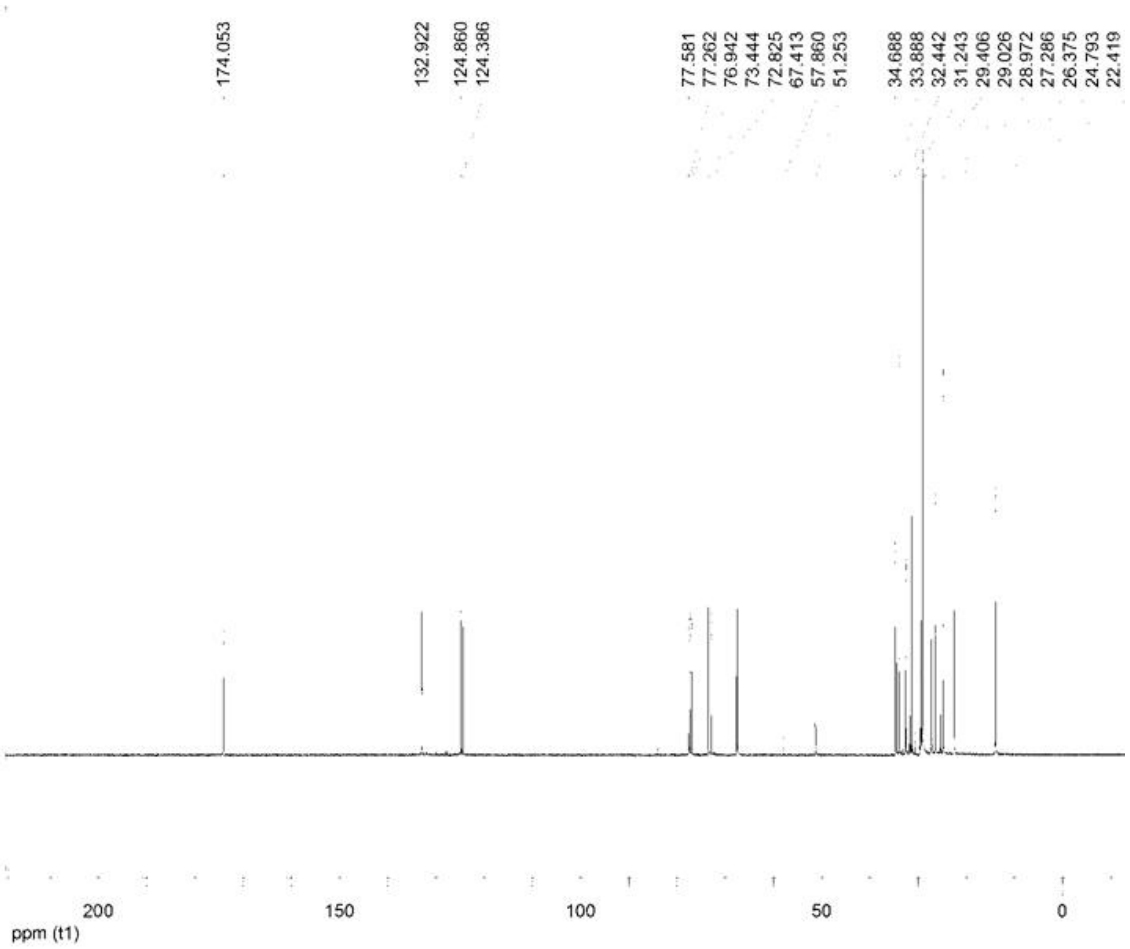

^{13}C NMR spectrum of Vernolic Acid Methyl Ester-VAME

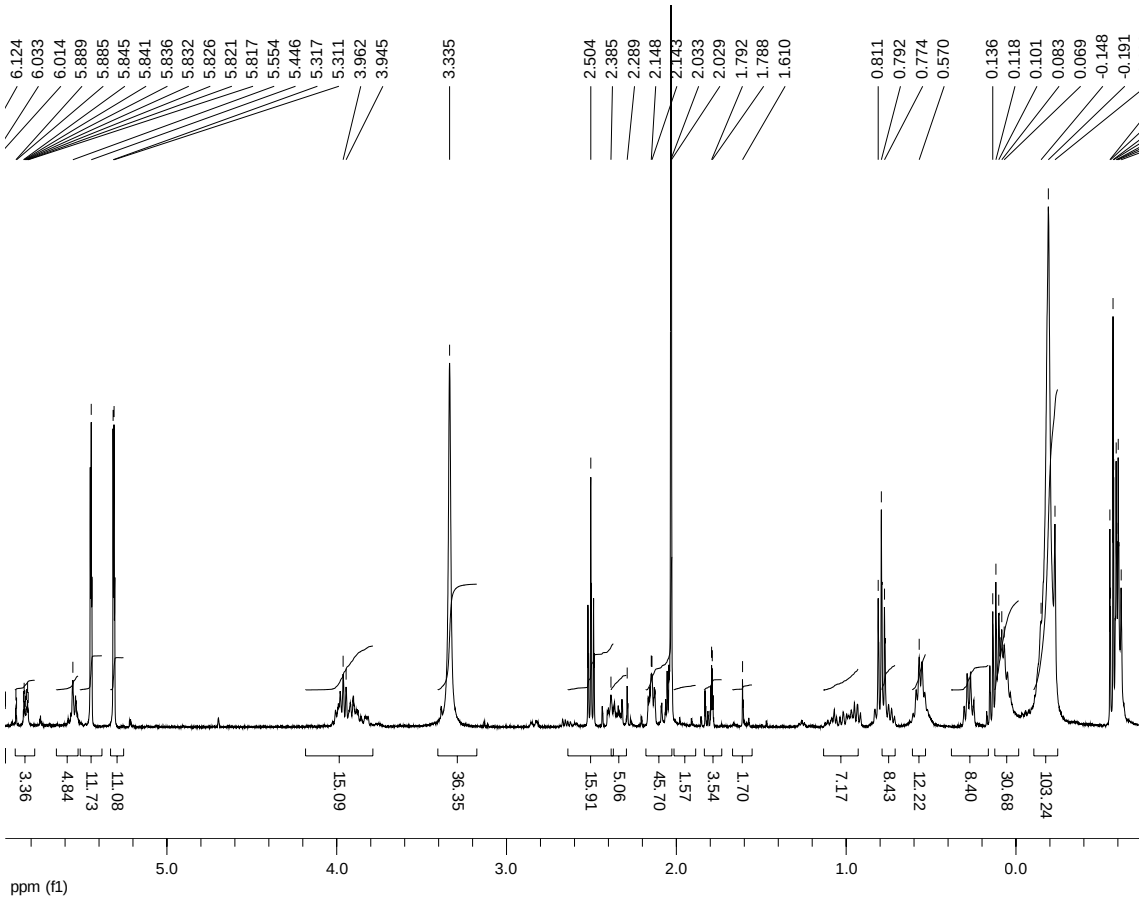

^{1}H NMR spectrum of Vernolic Acid Propyl Ester-VAPE

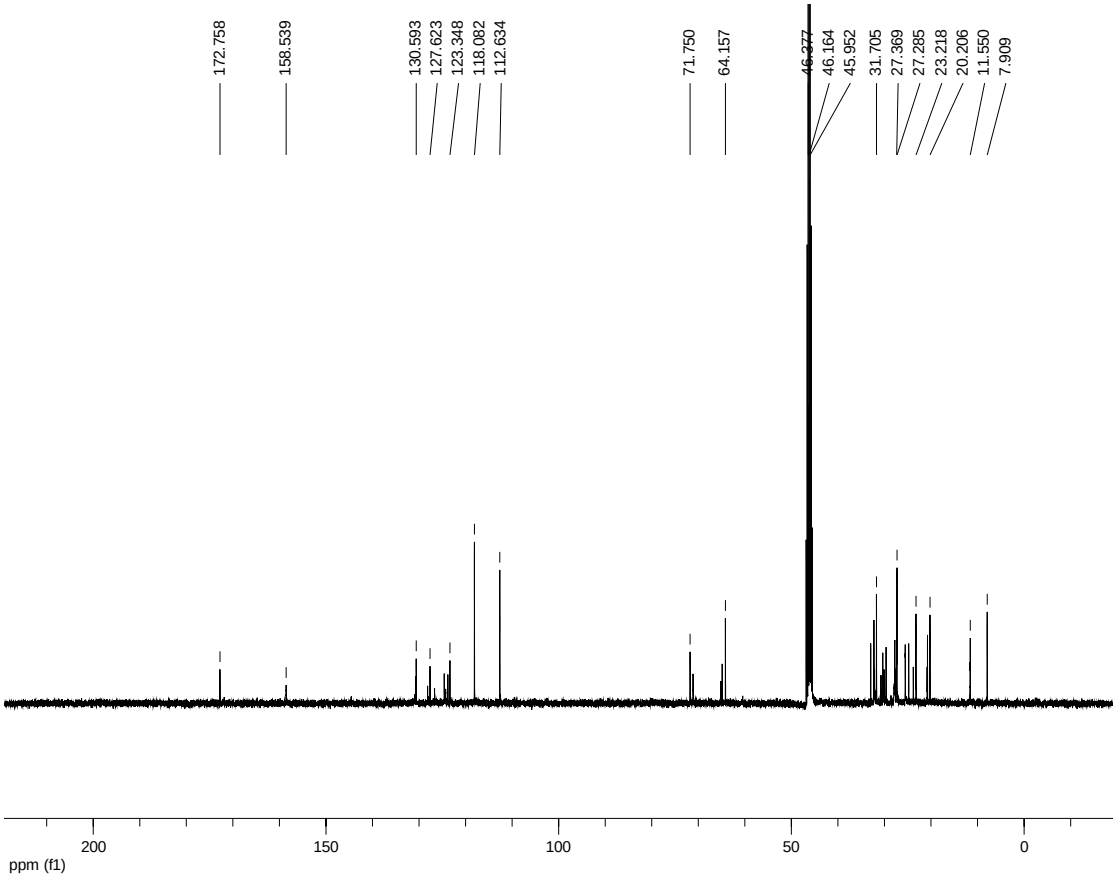

^{13}C NMR spectrum of Vernolic Acid Propyl Ester-VAPE

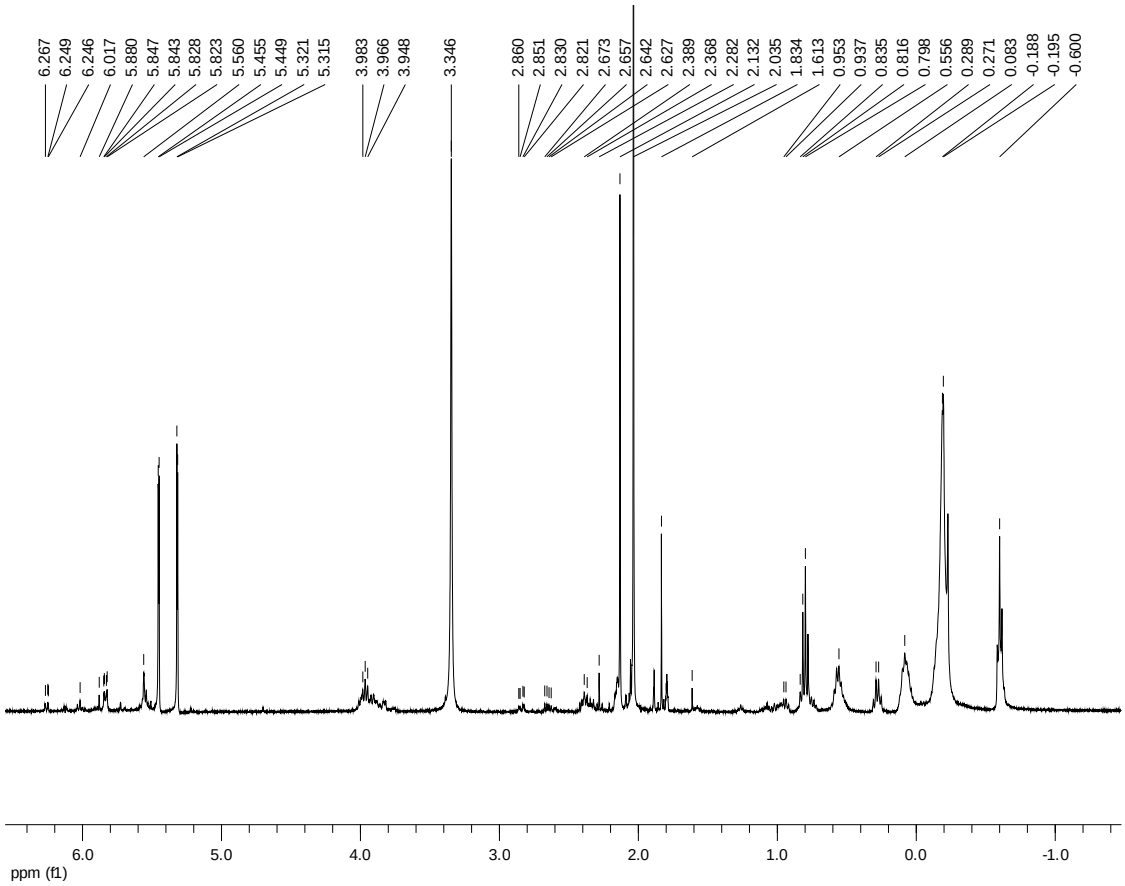

^{1}H NMR spectrum of Mercapto Imidazole functionalized VAME

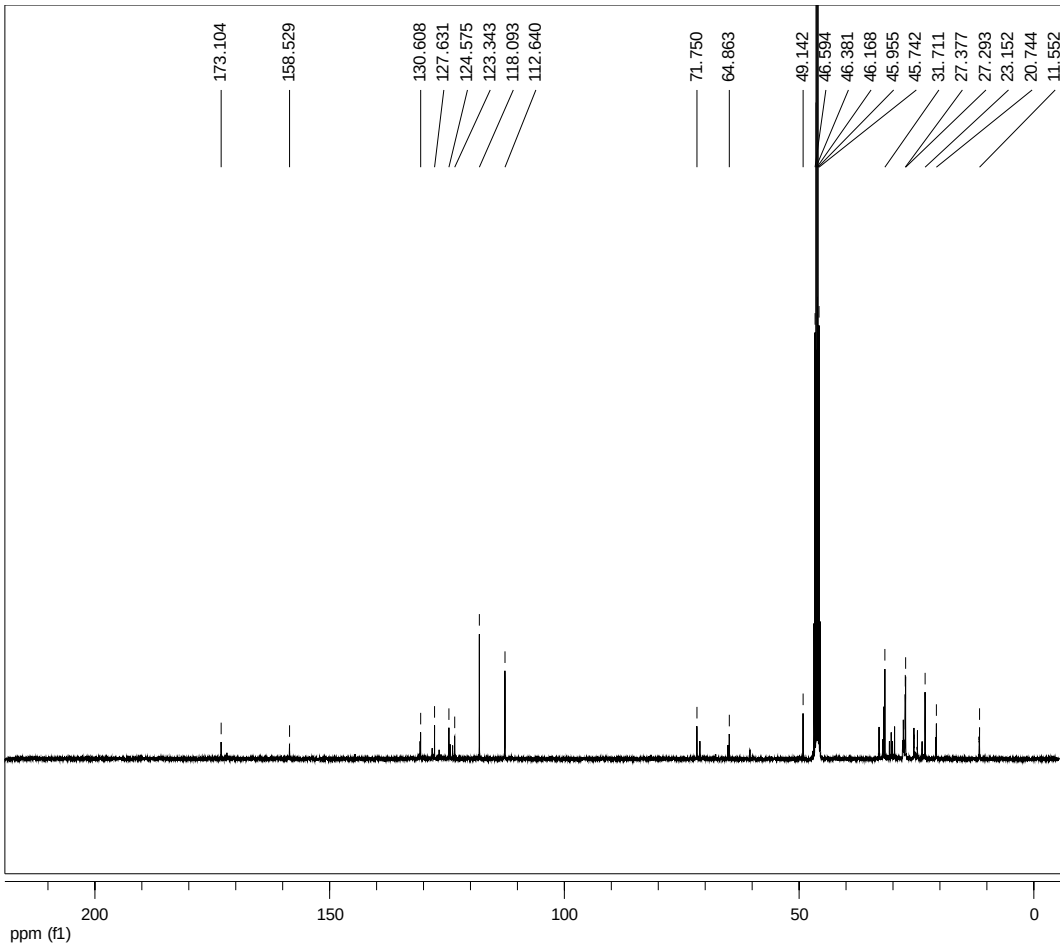

^{13} C NMR spectrum of Imidazole functionalized VAME IFVAME

Appendix 2: FT-IR Spectra

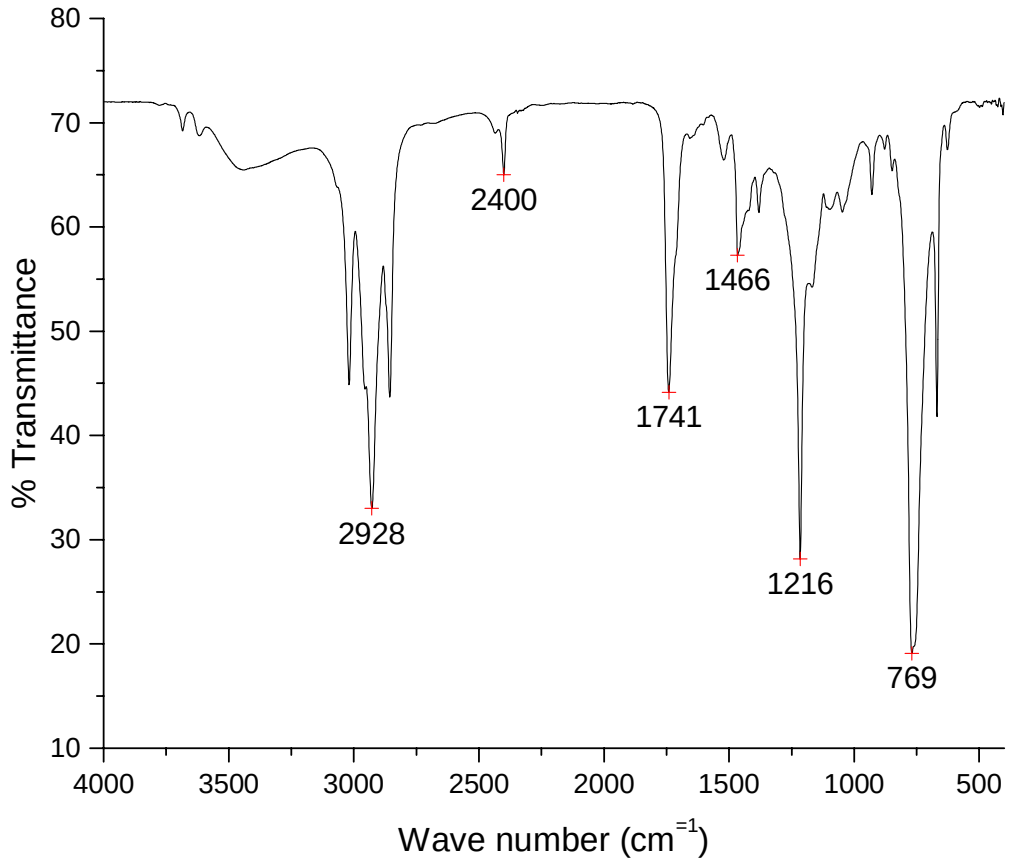

FT-IR spectrum of Crude Vernonia Oil-CVO from fresh V.galamensis seed

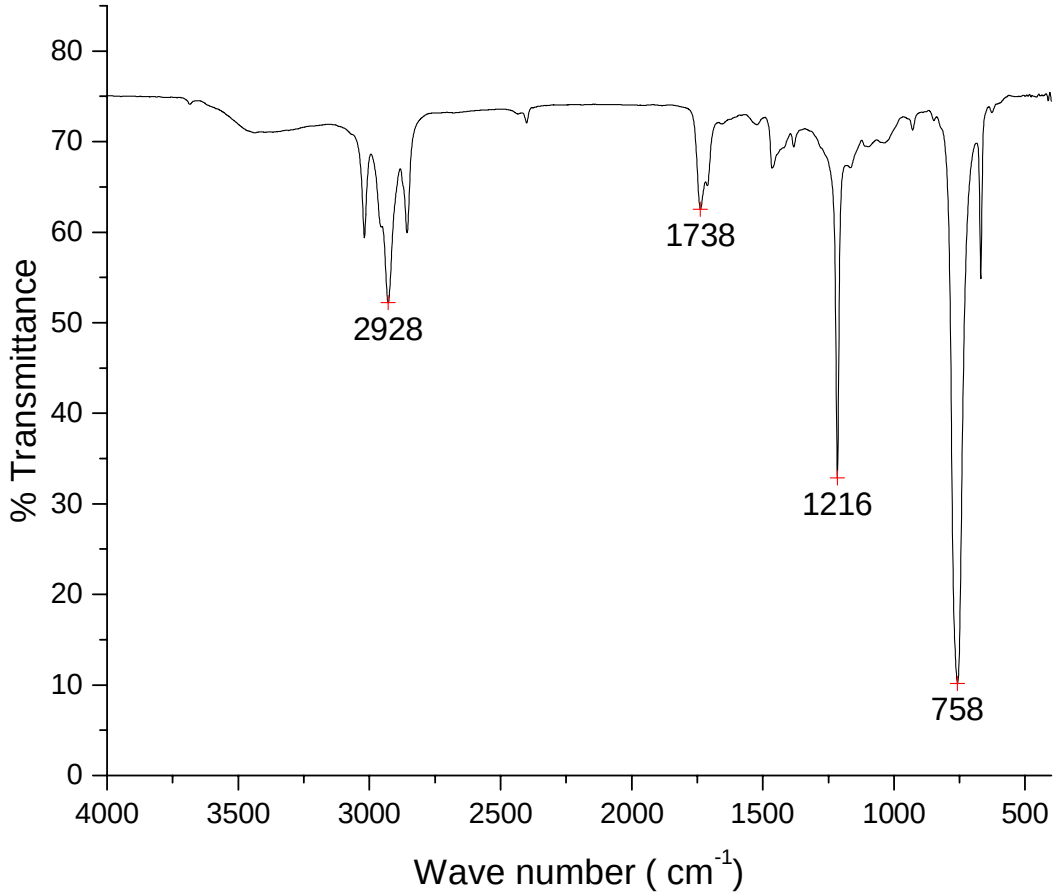

FT-IR spectrum of Neutral Vernonia Oil-NVO from fresh V.galamensis seed

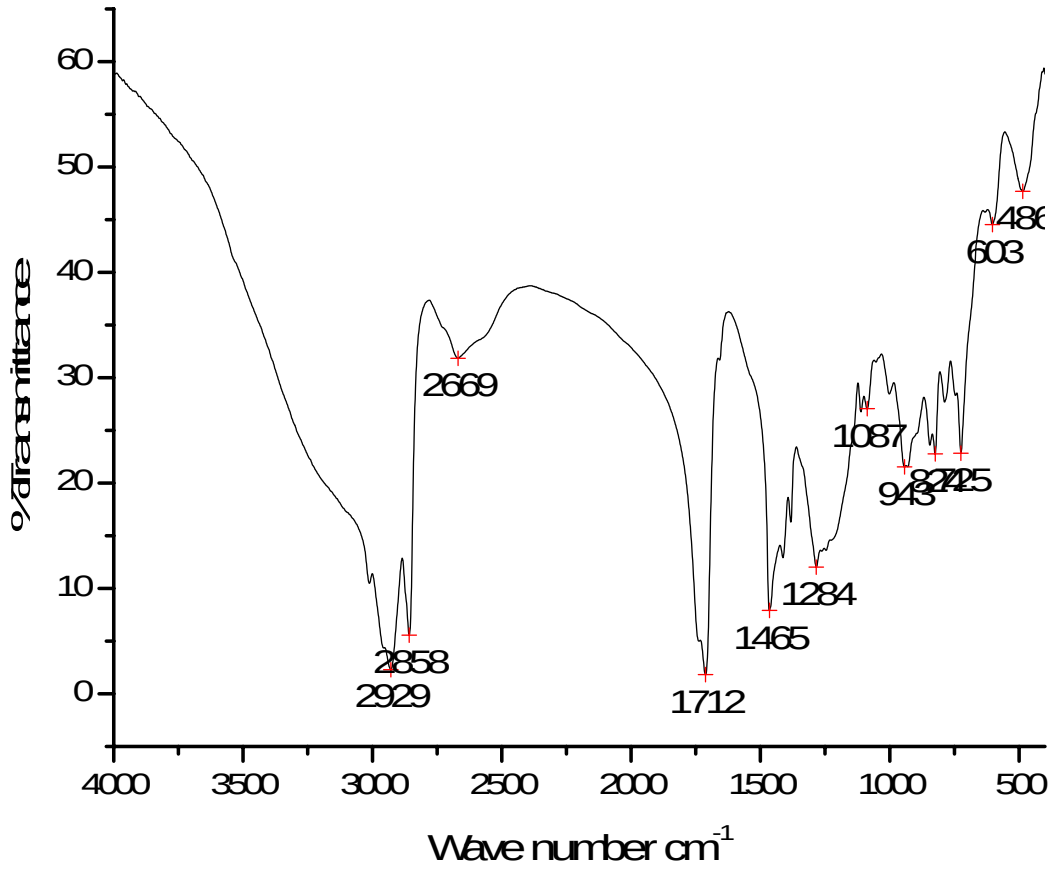

FT-IR spectrum of Vernolic Acid-VA

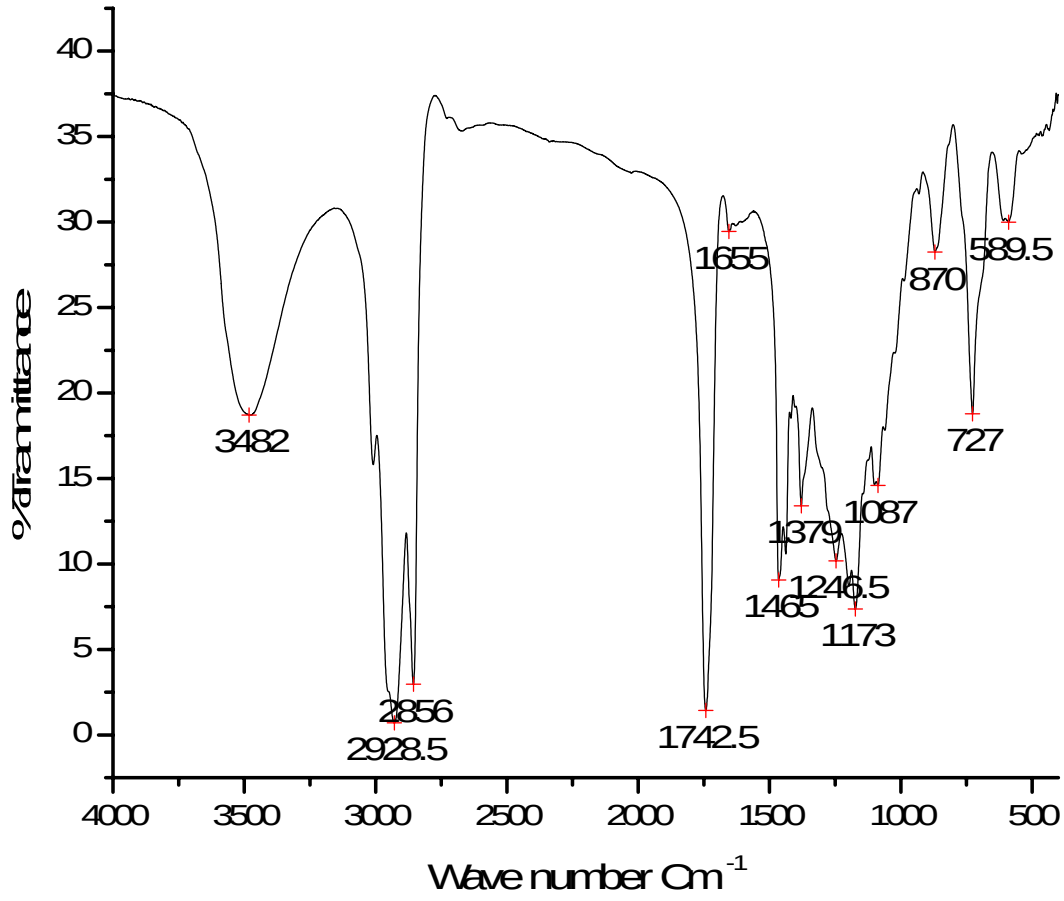

FT-IR spectrum of Vernolic Acid Methyl Ester-VAME

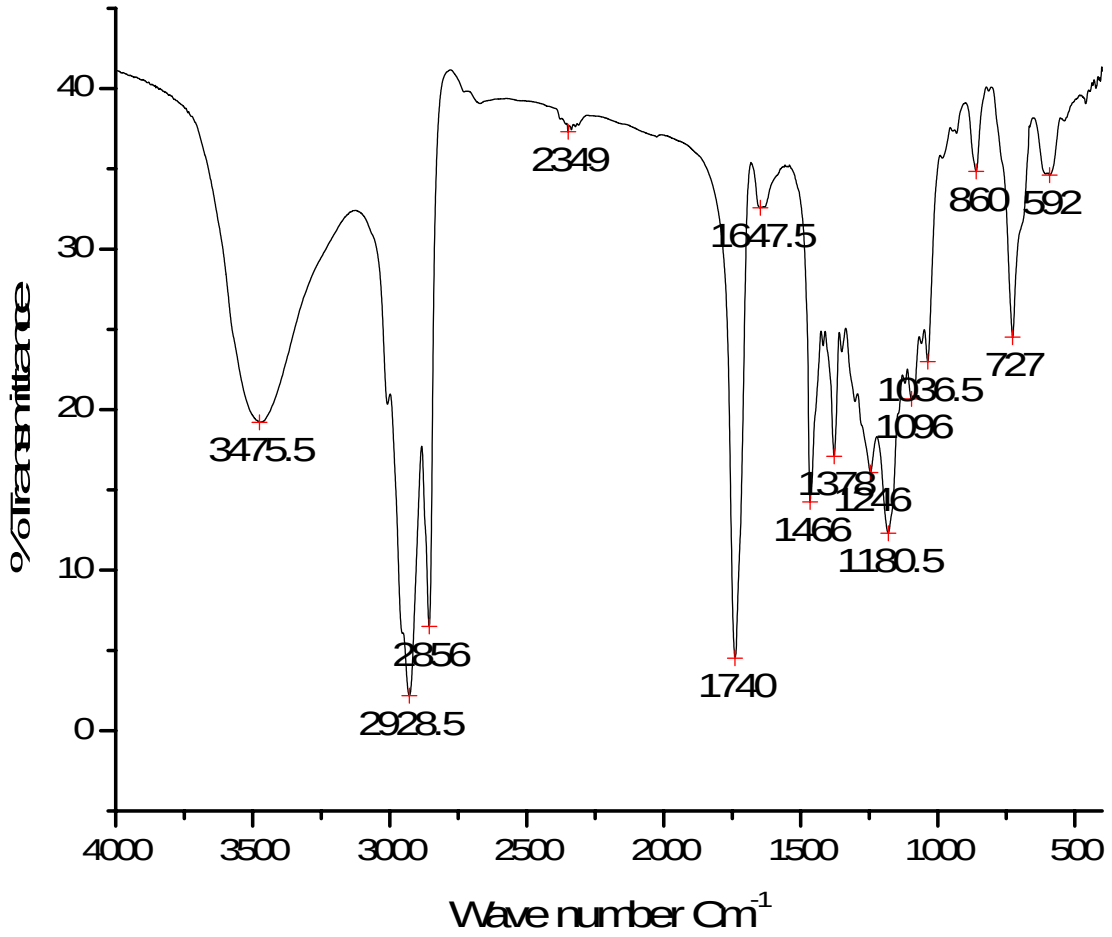

FT-IR spectrum of Vernolic Acid Ethyl Ester-VAEE

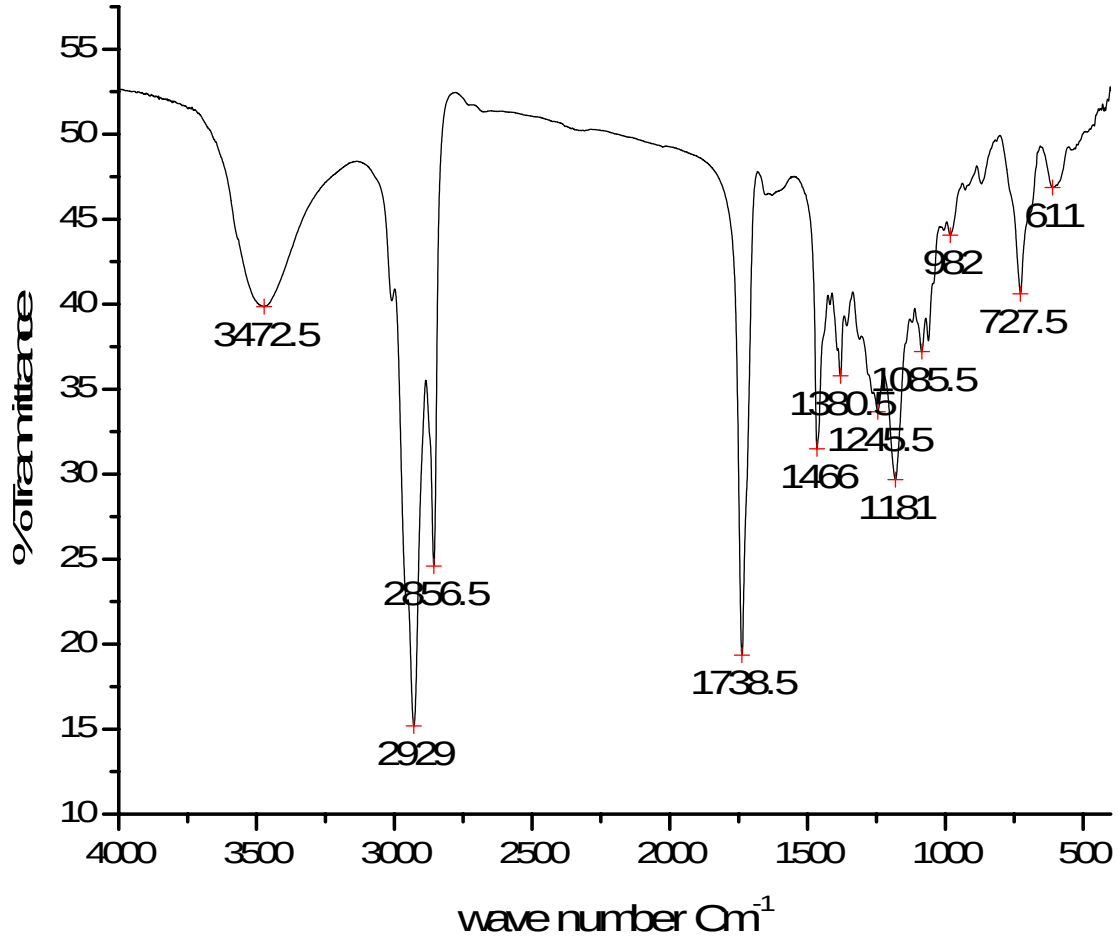

FT-IR spectrum of Vernolic Acid Propyl Ester-VAPE

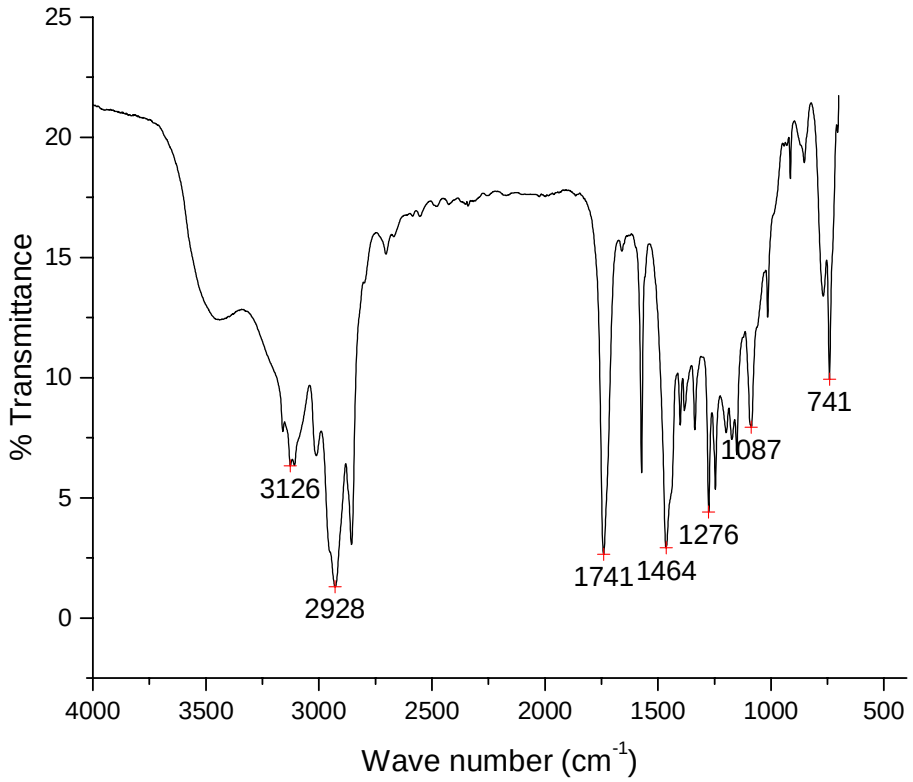

FT-IR spectrum of Mercapto Imidazole functionalized Vernolic acid Methyl Ester-IFVAME

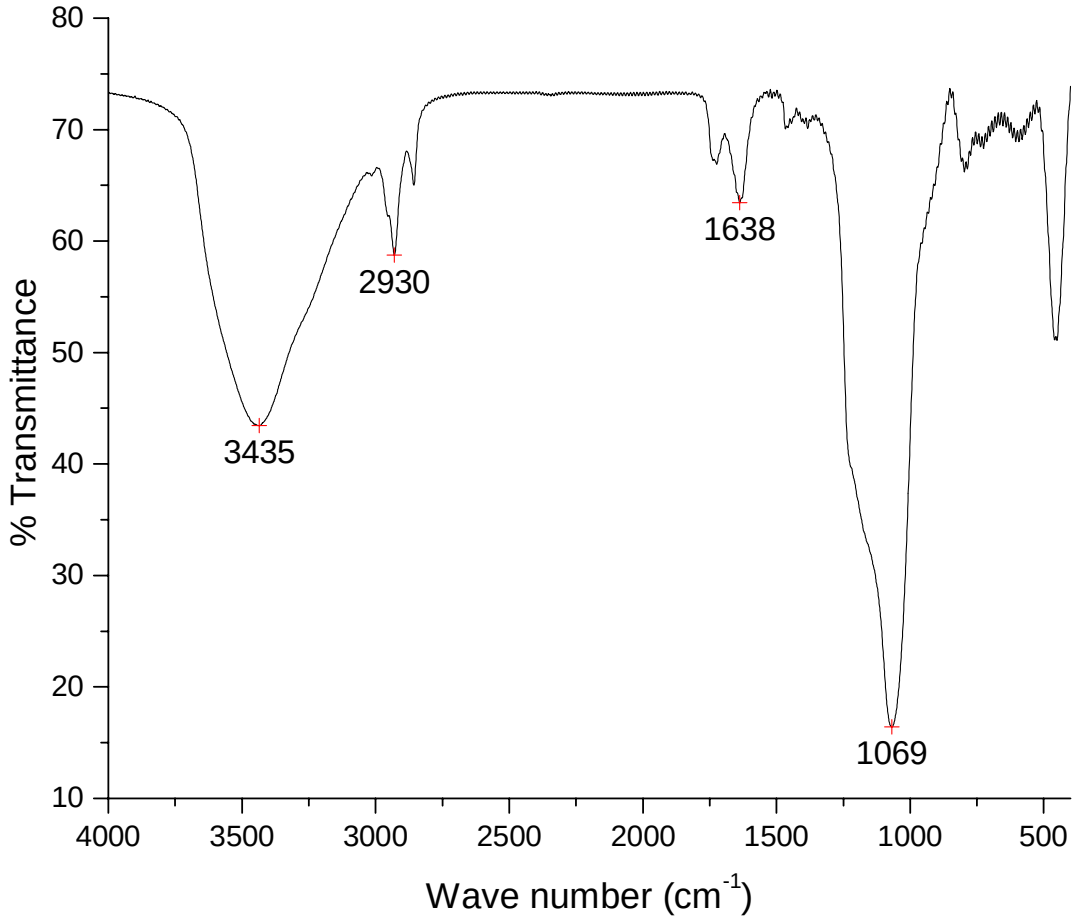

FT-IR spectrum of 13 % VAME loaded Al-MCM-41 (Si/Al=3) (mMCM (3)1)

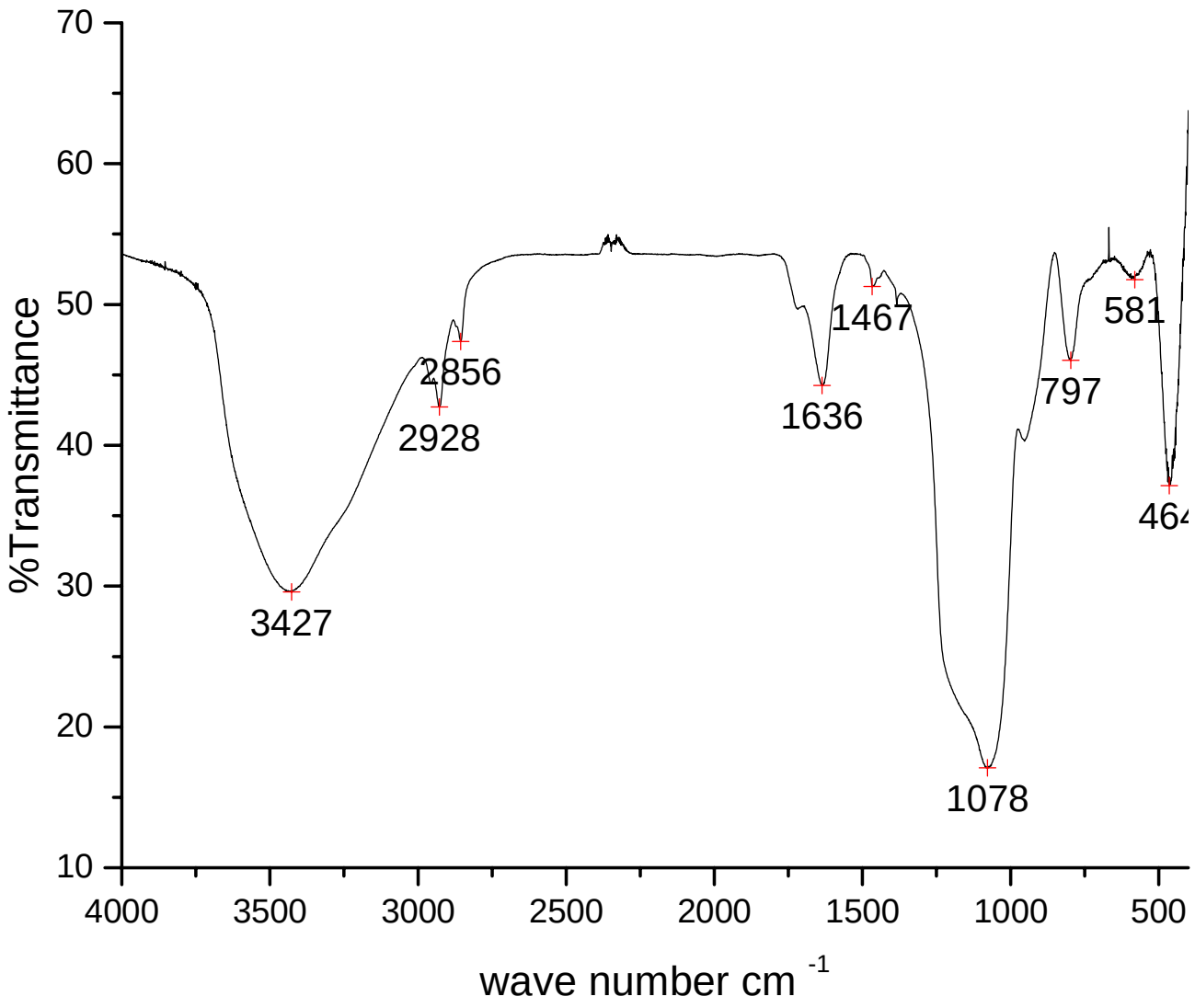

FT-IR spectrum of 13 % VAME loaded Al-MCM-41 (Si/Al=15) (mMCM (15)1)

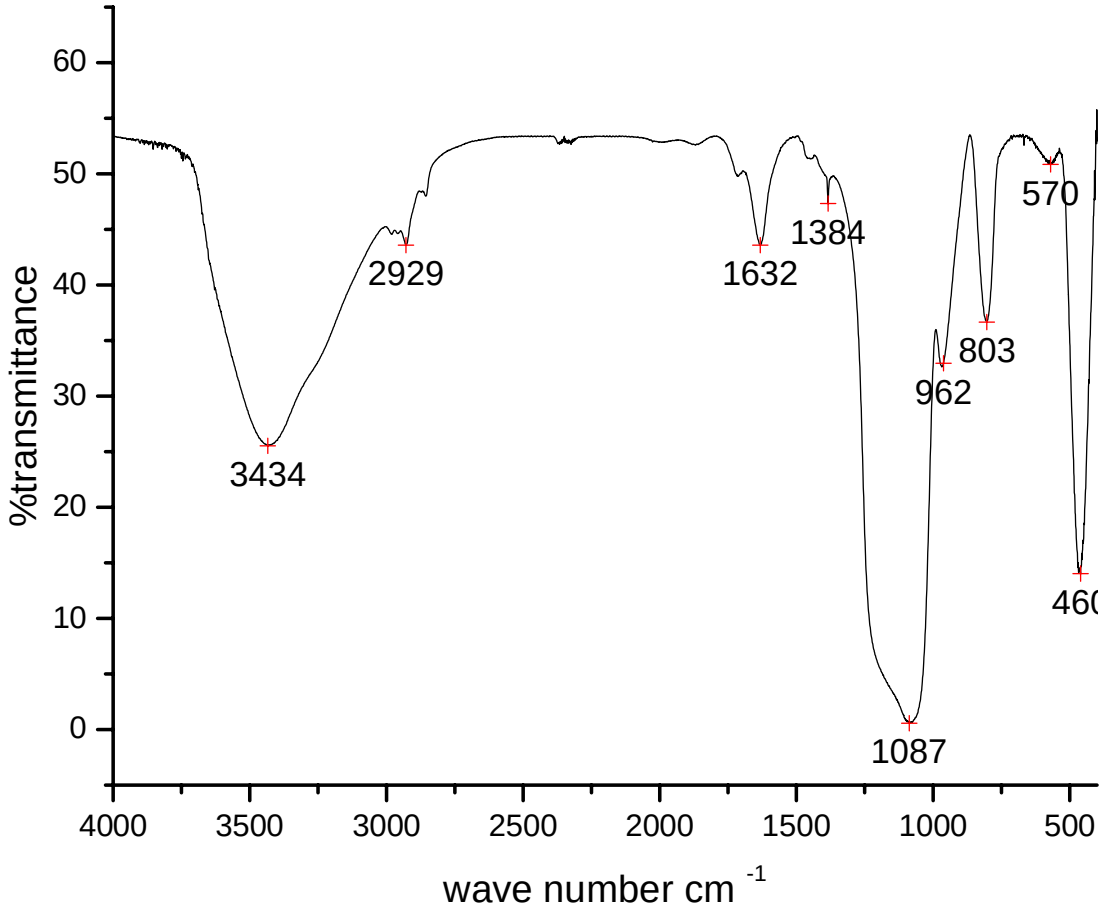

FT-IR spectrum of 13 % VAME loaded SBA-15 (mSBA1)

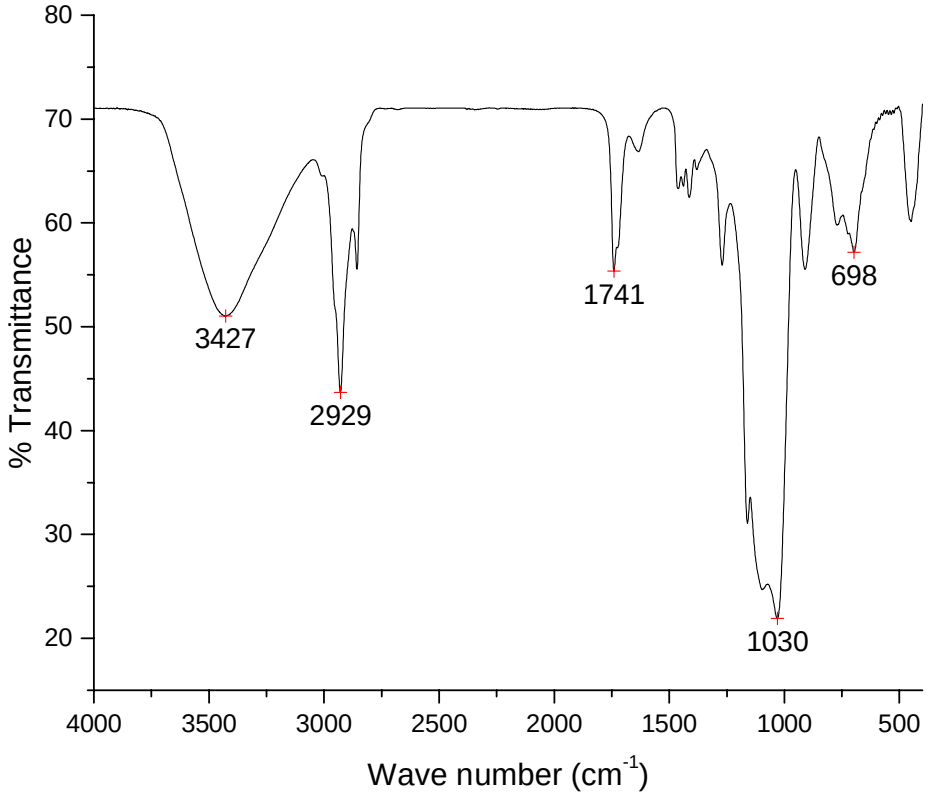

FT-IR spectrum of 13 % VAME loaded PMO (mPMO1)

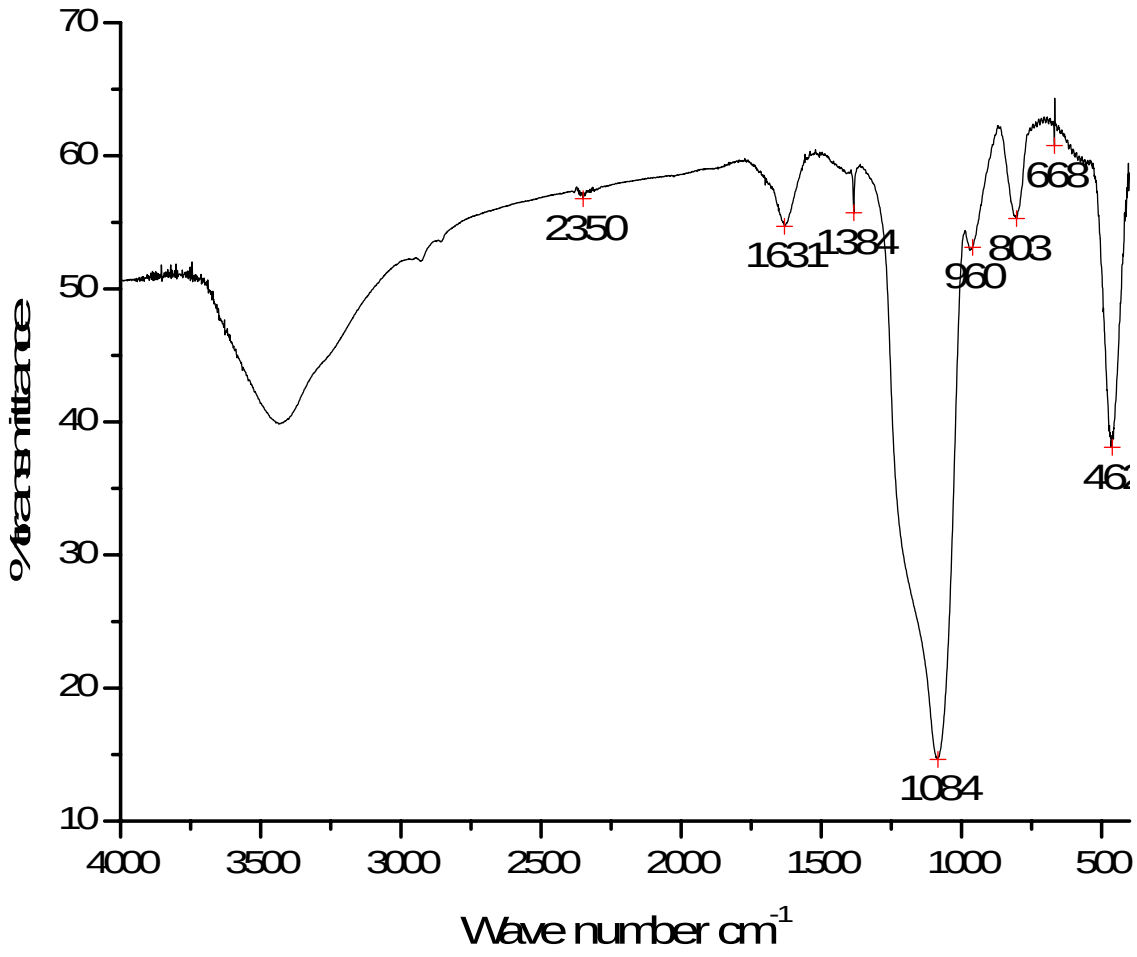

FT-IR spectrum 13 % IFVAME supported SBA-15 (IFVAME-SBA or ifm-SBA)

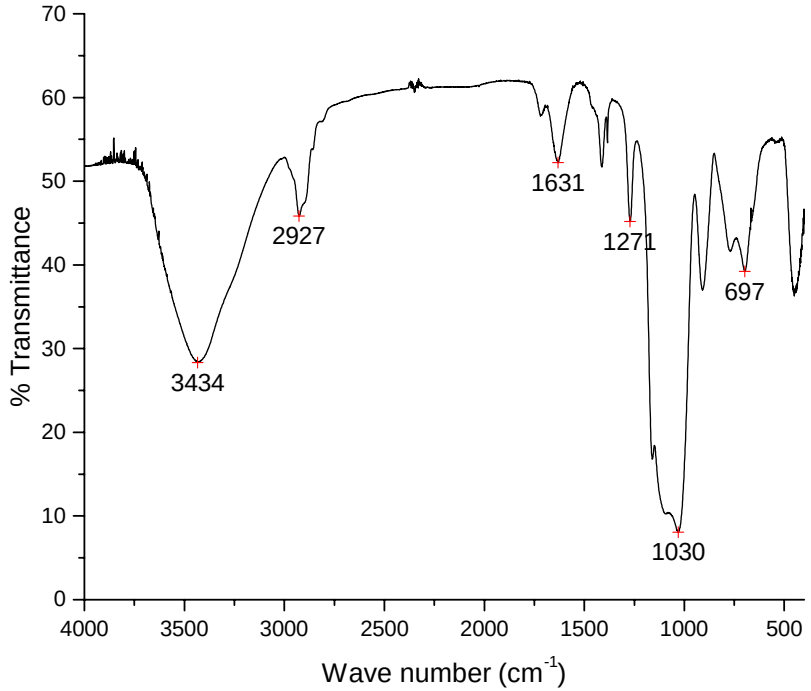

FT-IR spectrum of 13 % IFVAME supported PMO (IFVAME-PMO or ifm-PMO)

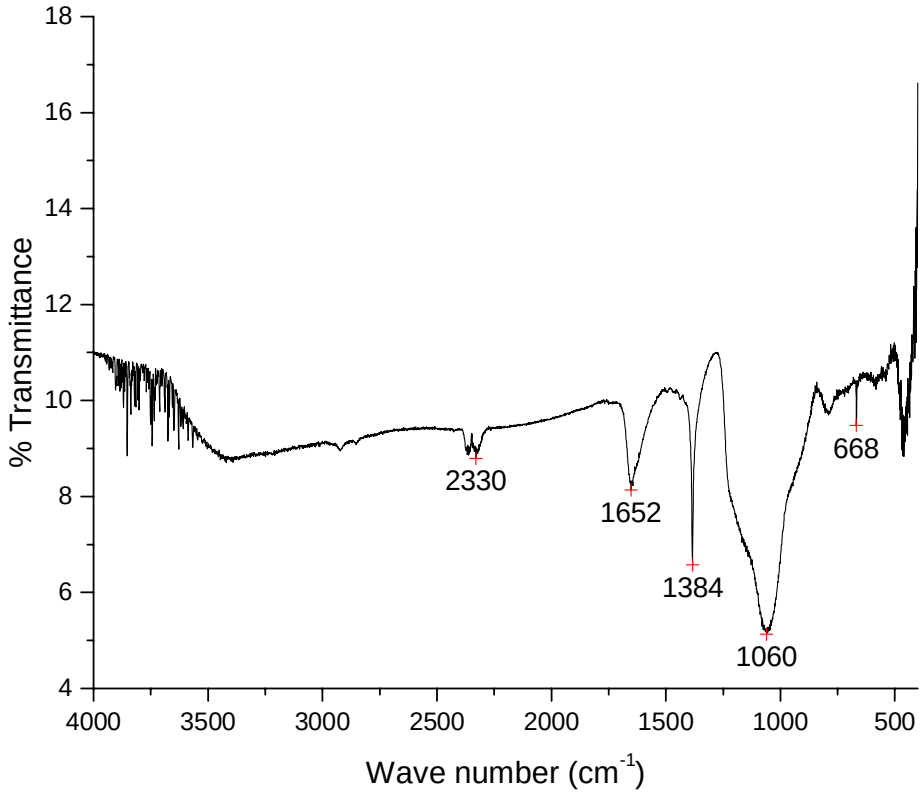

FT-IR spectrum of AgmMCM (3)1

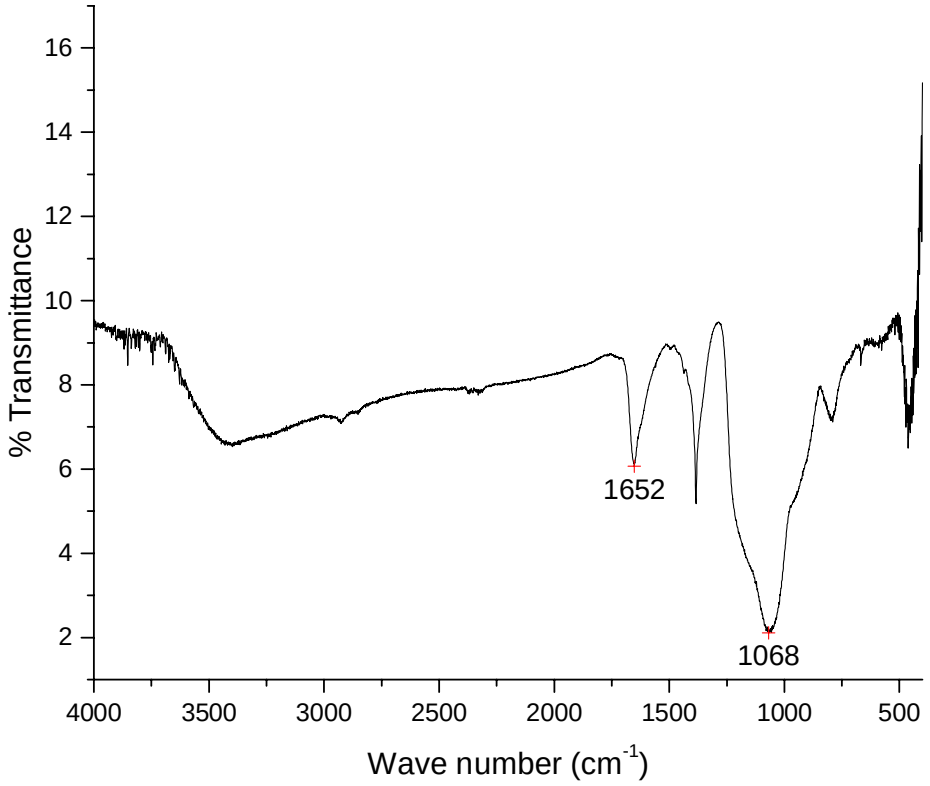

FT-IR spectrum of AgmMCM (15)1

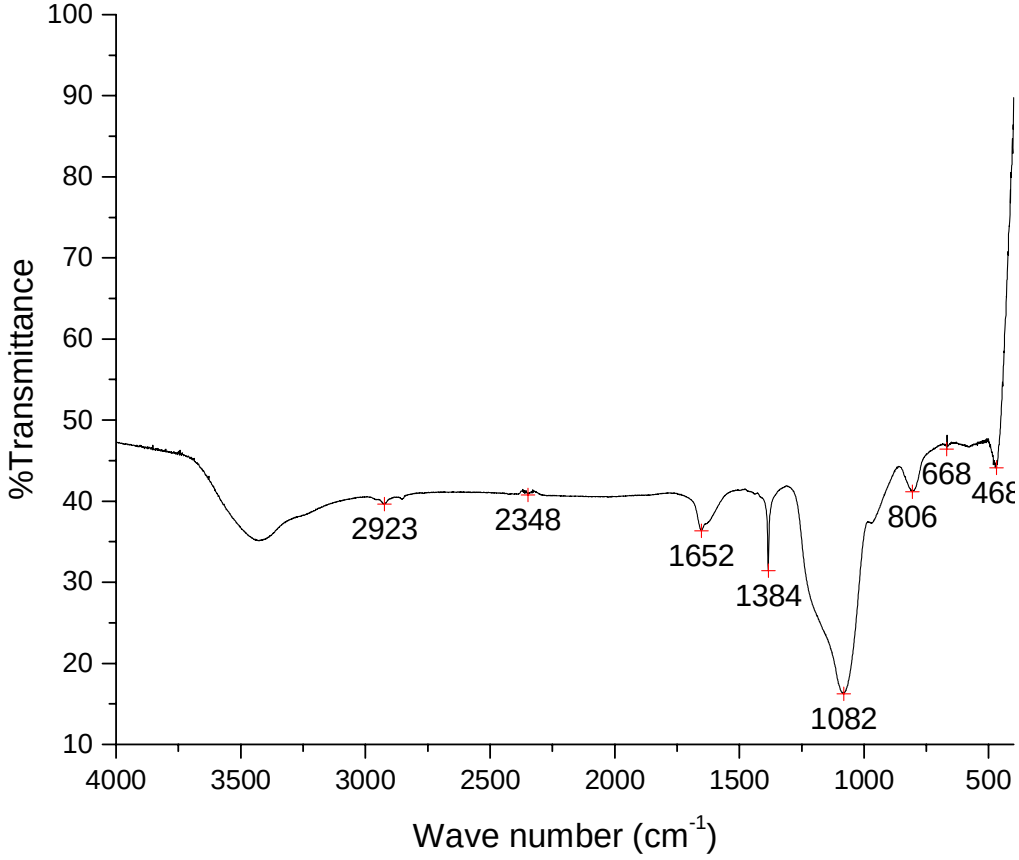

1

FT-IR spectrum of AgmSBA1

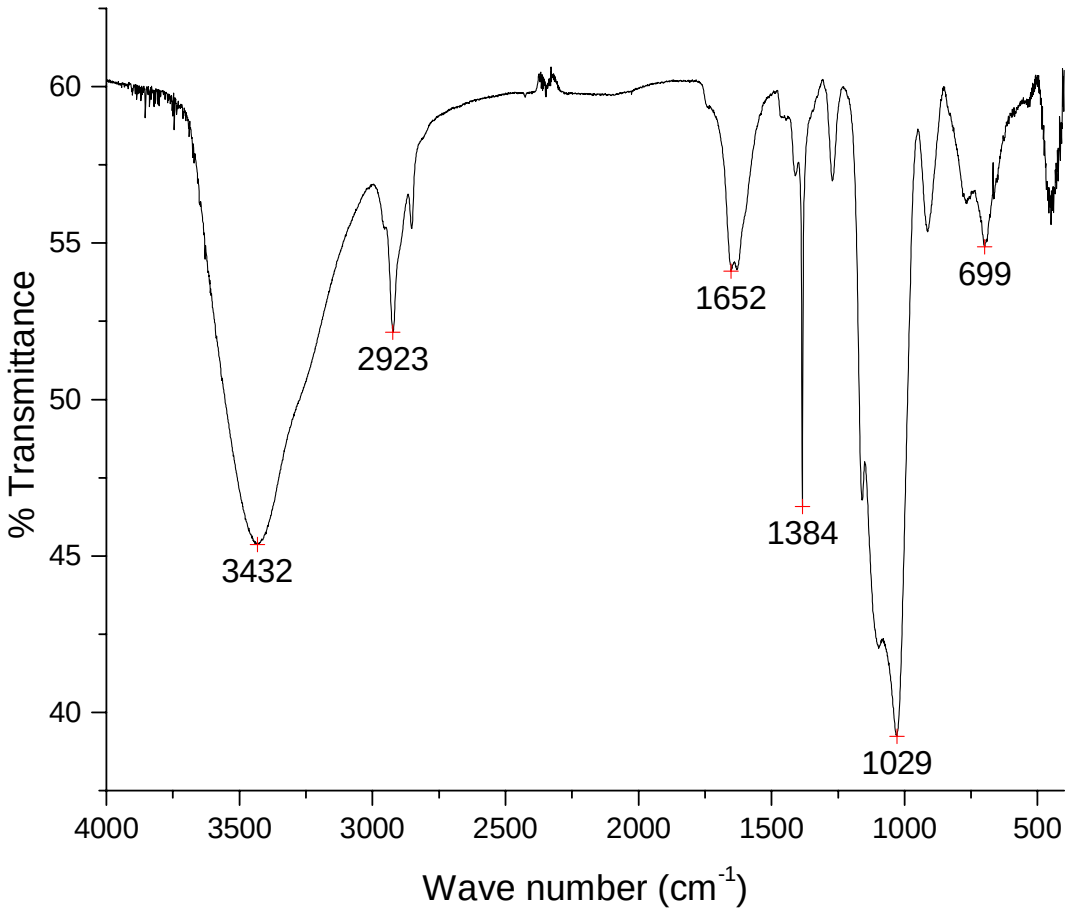

FT-IR spectrum of AgmPMO1

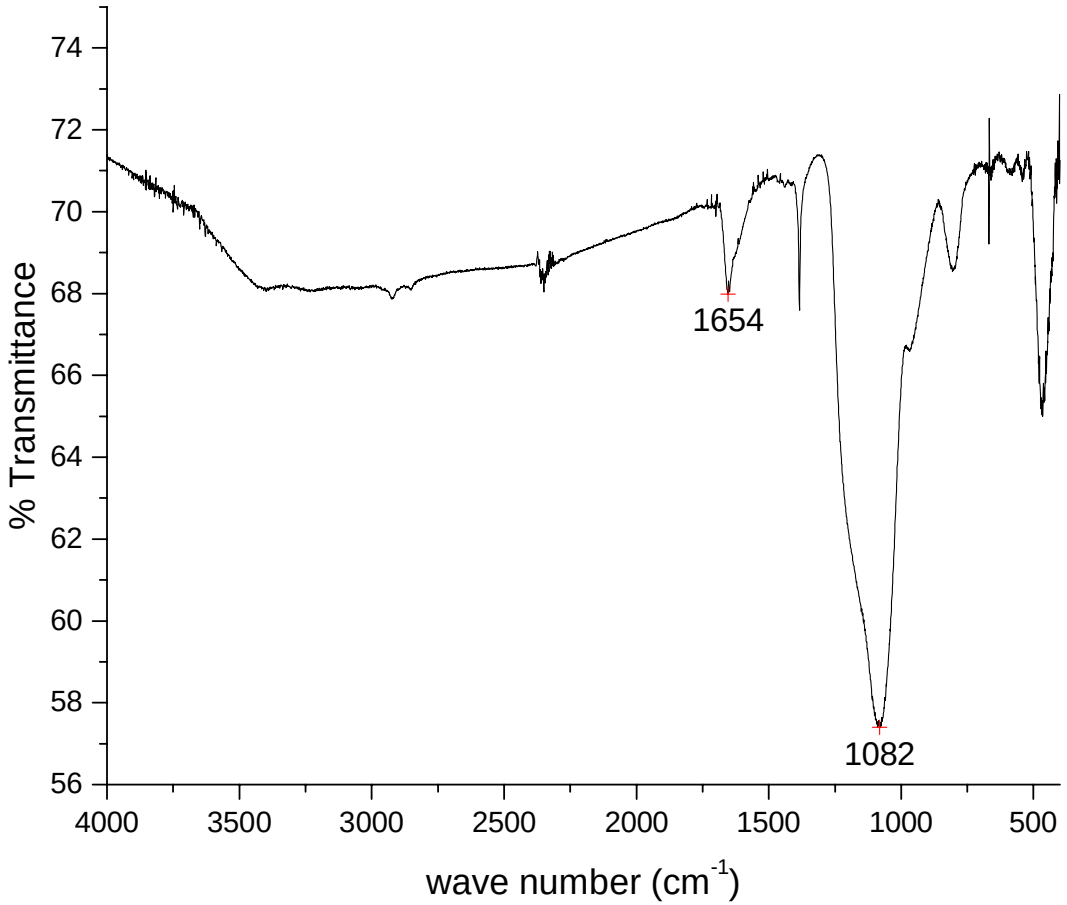

FT-IR spectrum of AgifmSBA1

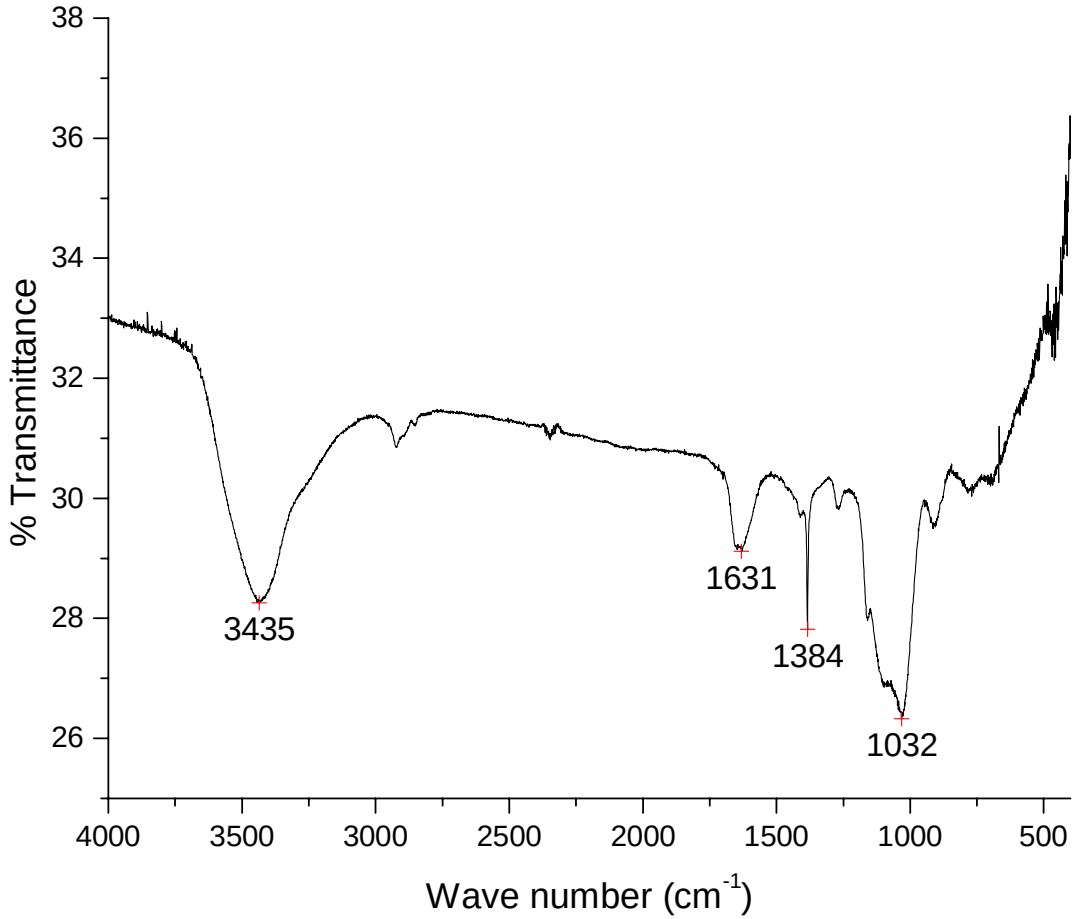

FT-IR spectrum of AgifmPMO1

***Appendix 3**: Powder XRD Diffractogarms or profiles*

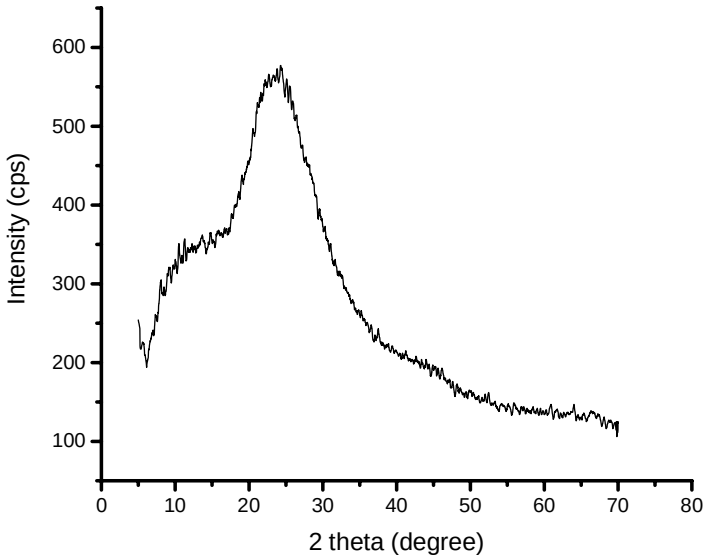

Wide Angle Powder XRD profile of Al-MCM-41 (Si/Al = 3)-MCM (3)

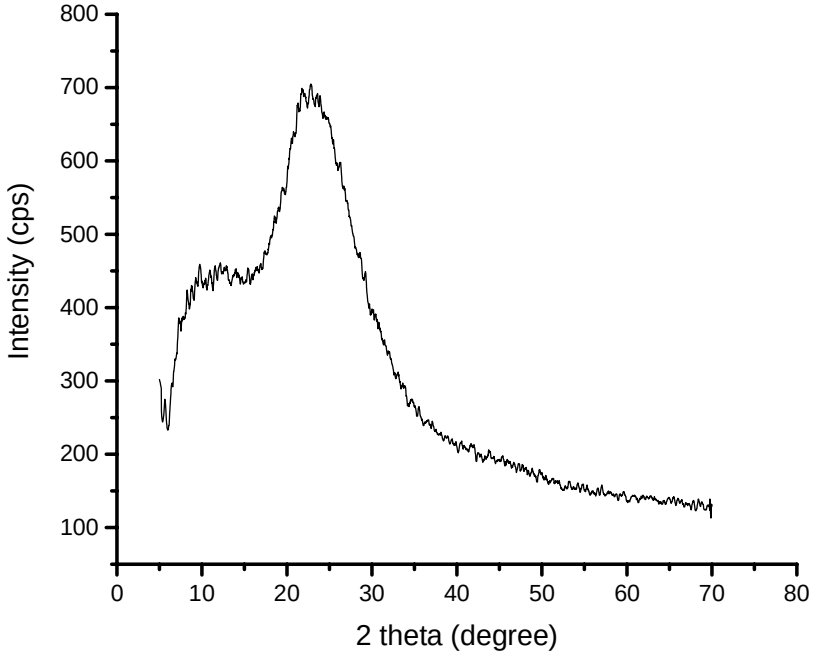

Wide Angle Powder XRD profile of Al-MCM-41(Si/Al =15)-MCM (15)

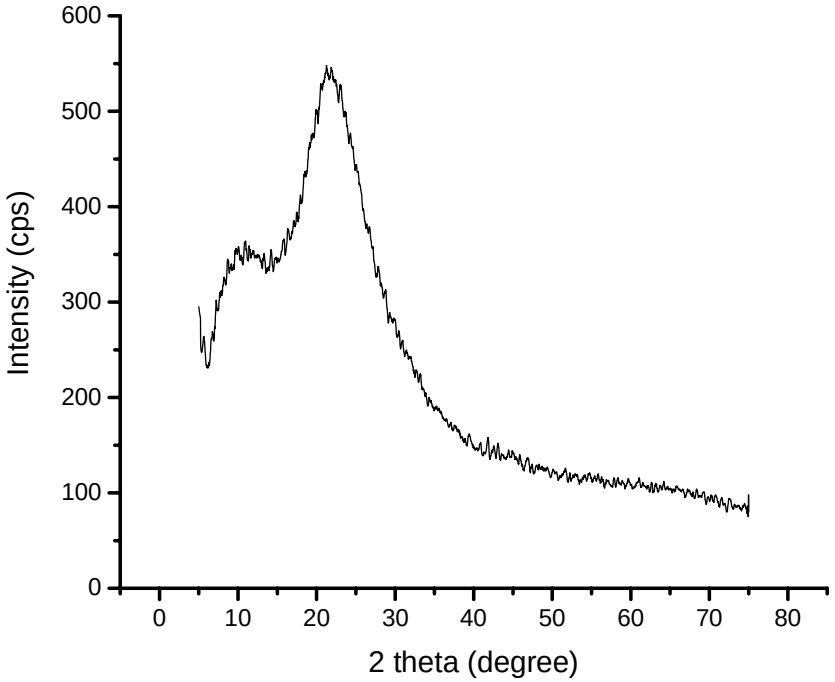

Wide Angle Powder XRD profile of SBA

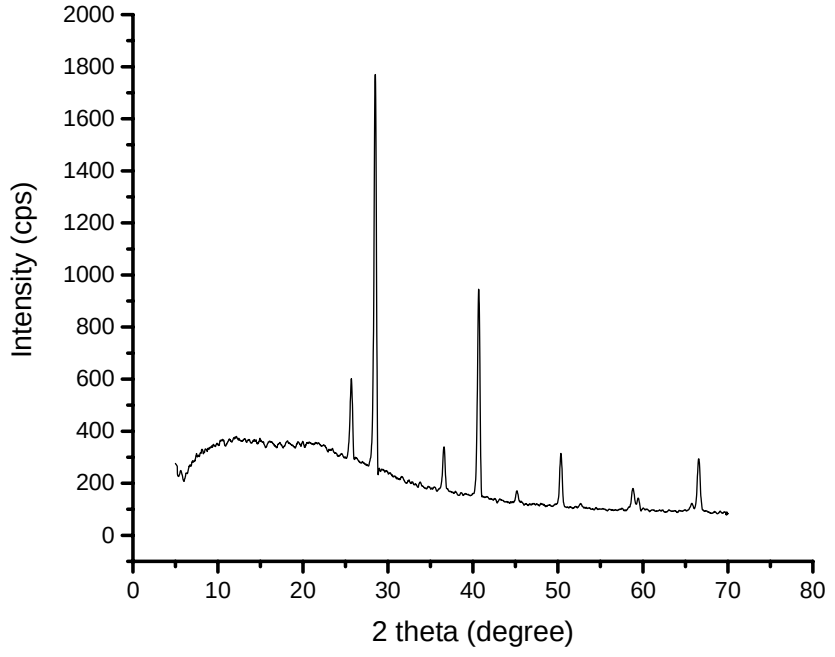

Wide Angle Powder XRD profile of PMO1

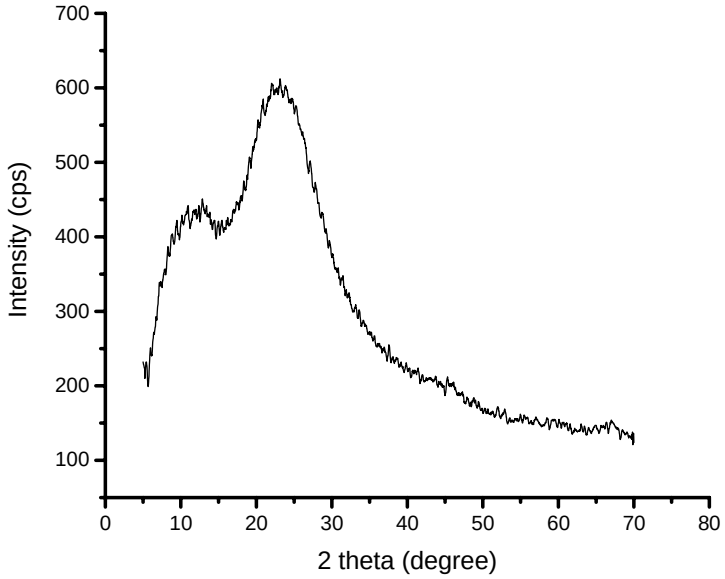

Wide Angle Powder XRD profile of mMCM (3)1

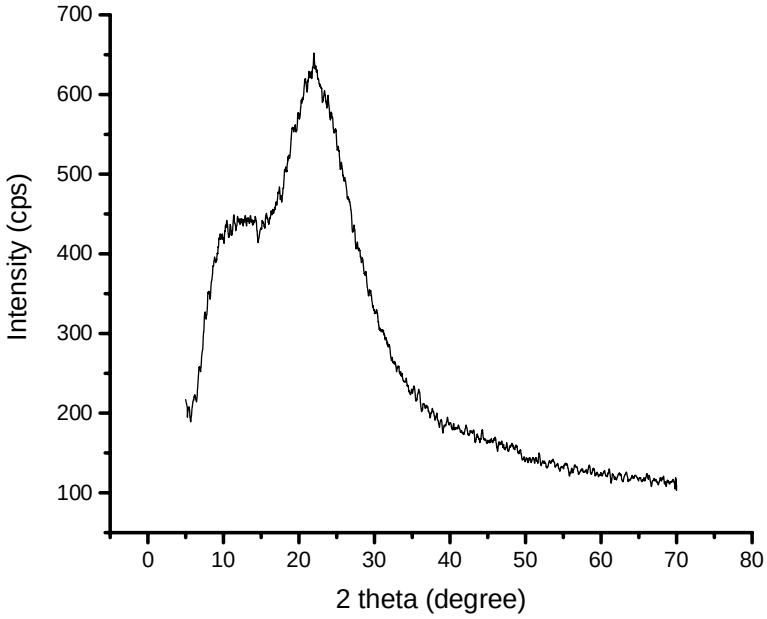

Wide Angle Powder XRD profile of mMCM (15)1

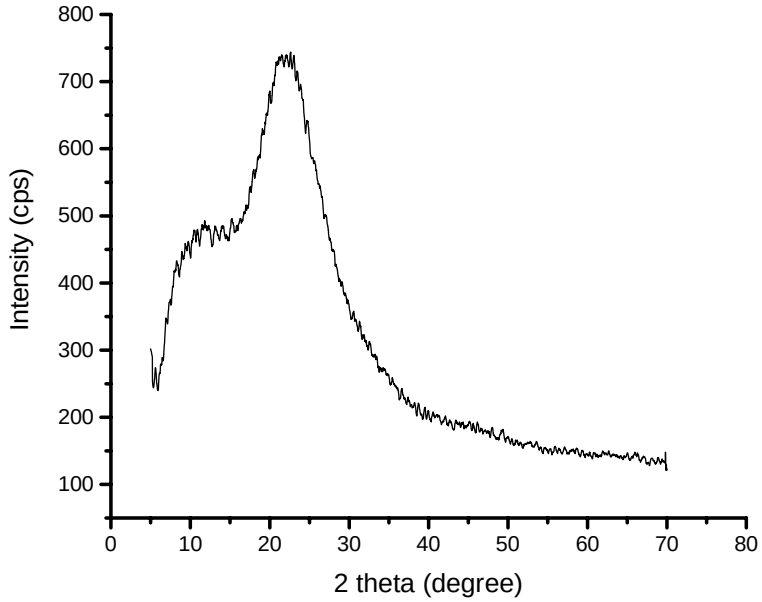

Wide Angle Powder XRD profile of mSBA1

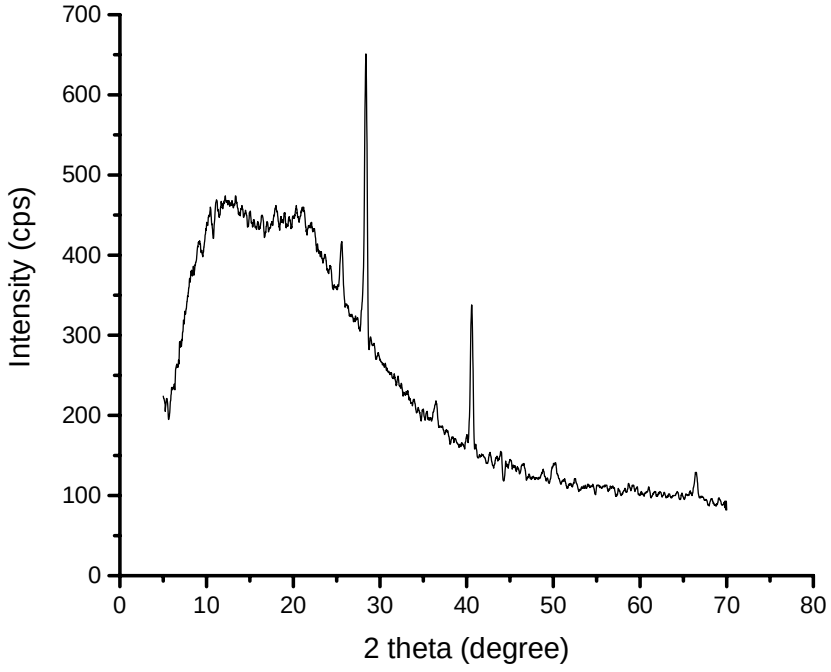

Wide angle Powder XRD profile of mPMO1

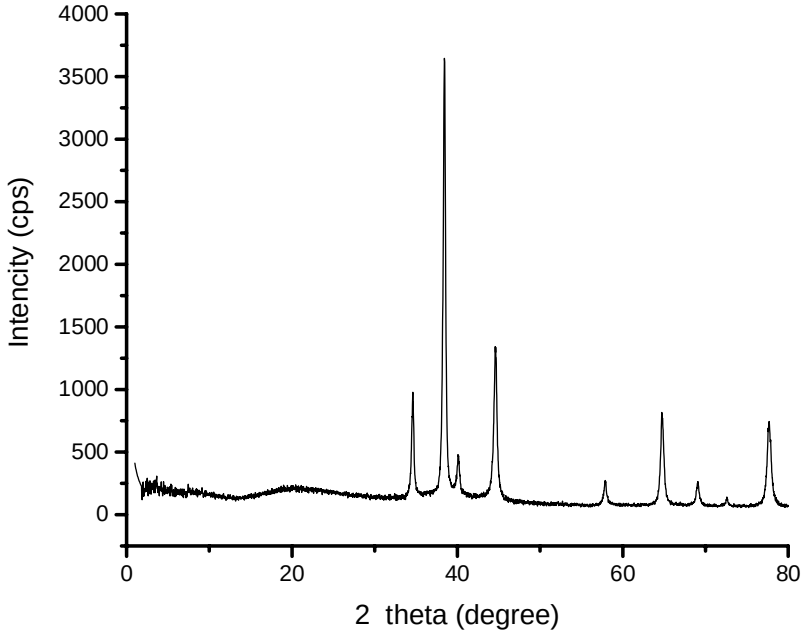

Wide angle Powder XRD profile of AgmMCM (3)1

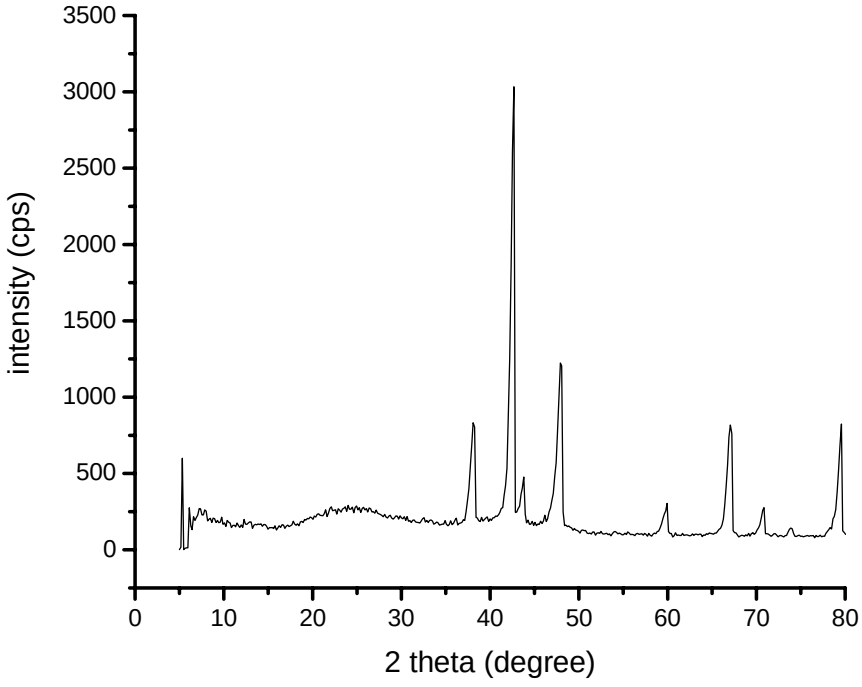

Wide angle PXRD profile of AgmMCM (15)1

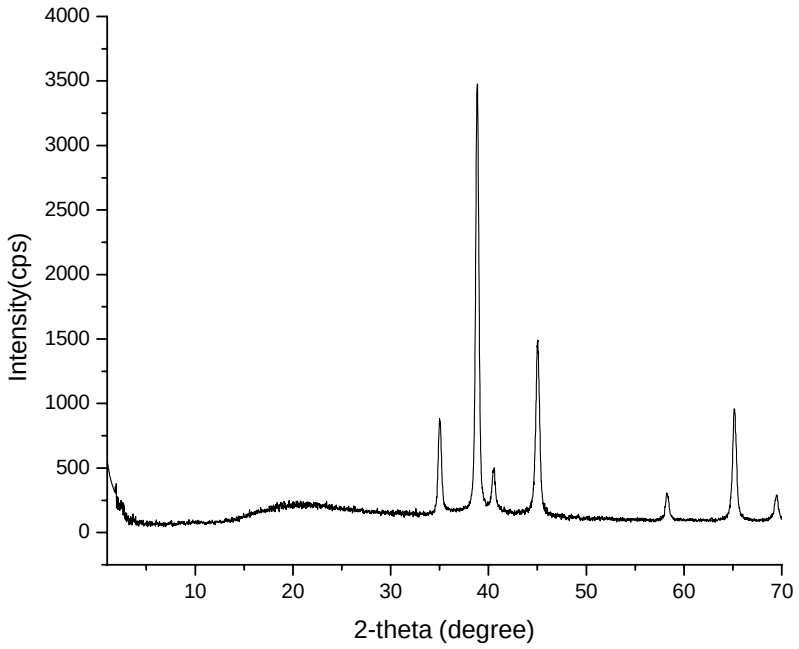

Wide angle Powder XRD profile of AgmSBA1

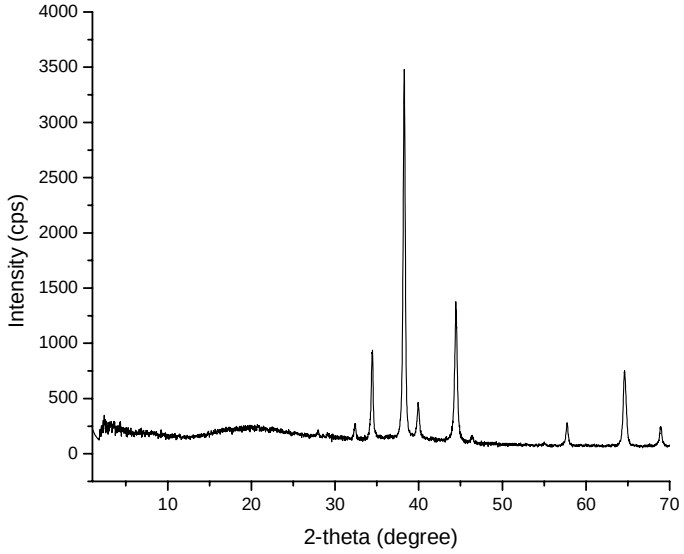

Wide angle Powder XRD profile of AgmPMO1

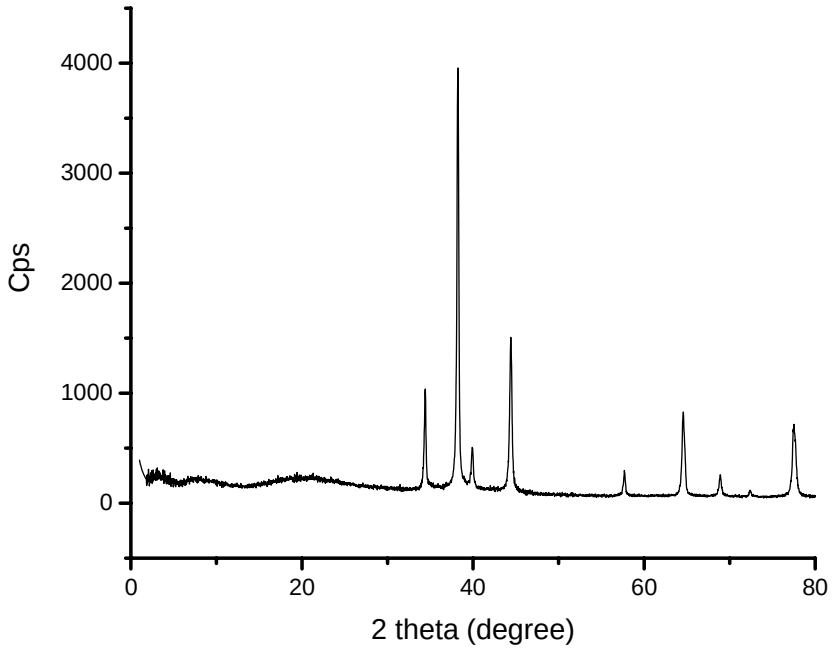

Wide angle Powder XRD profile of Agifm SBA1

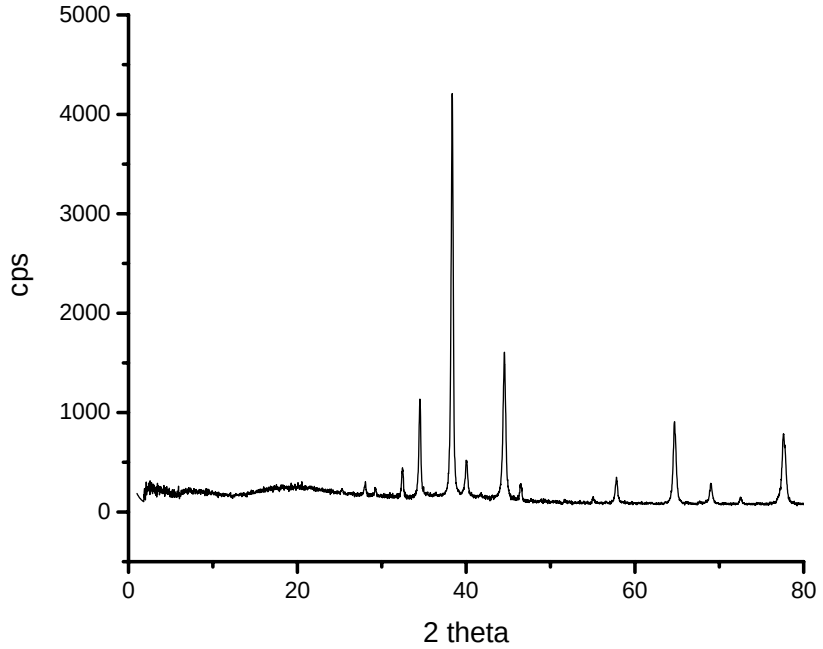

Wide angle Powder XRD profiles of AgifmPMO1

Appendix 4: TGA Profiles

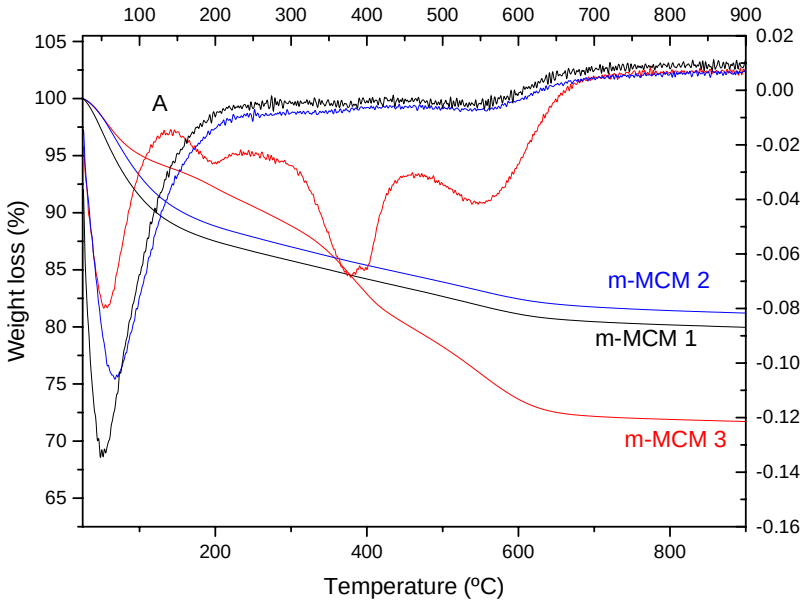

TGA/DTG profiles of mMCM (3)1-3

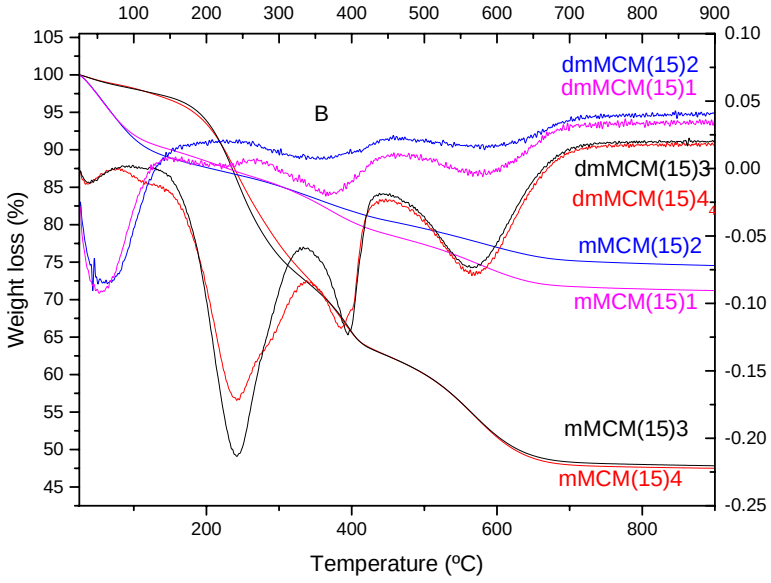

TGA/DTG profiles of.mMCM (15)1-4

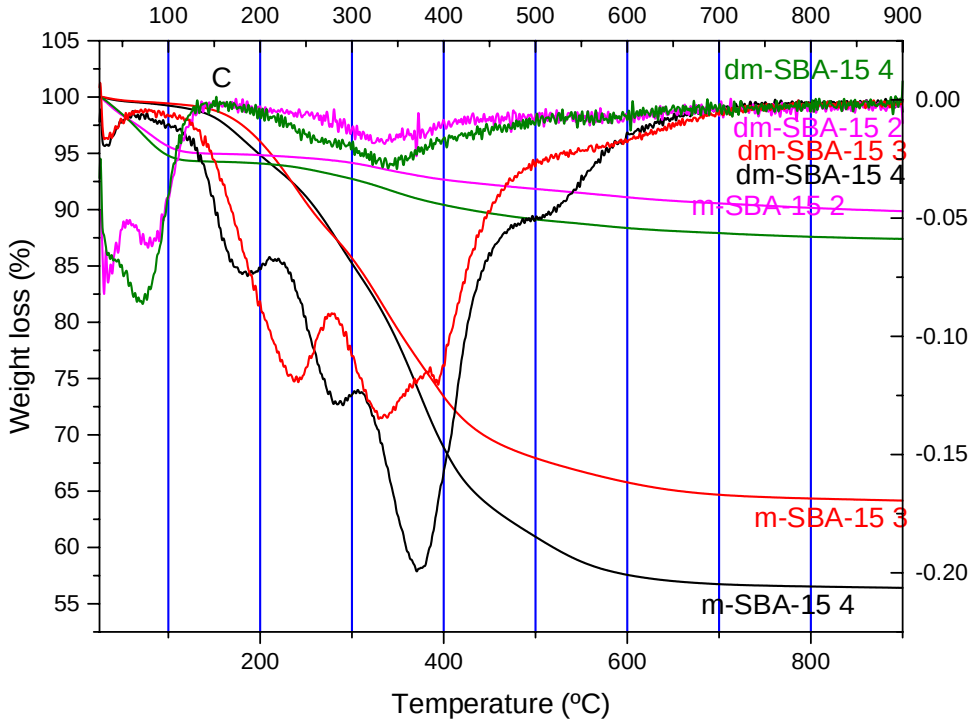

TGA/DTG Profiles of mSBA 1-4

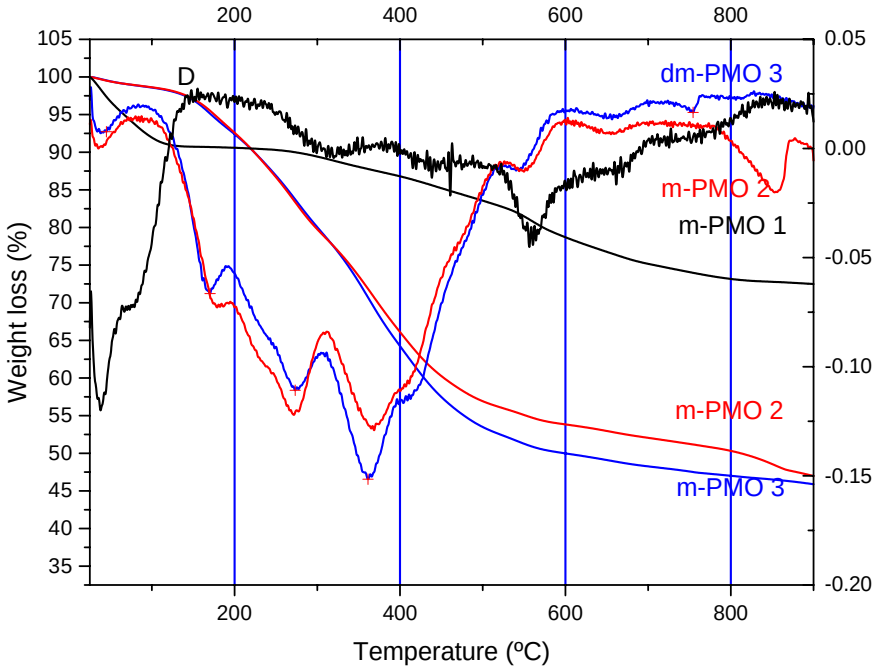

TGA/DTG profile of mPMO) 1-3

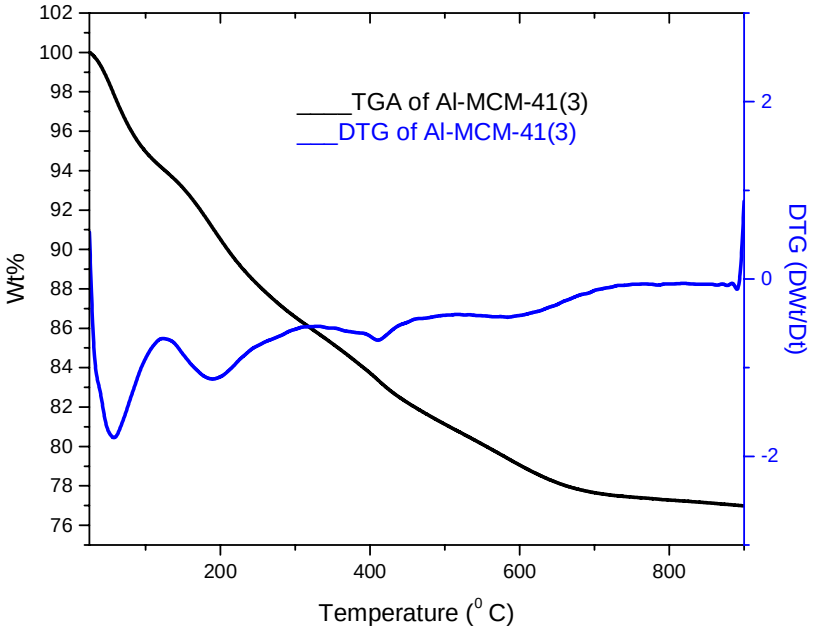

TGA/DTG profile of ifmMCM (3)1

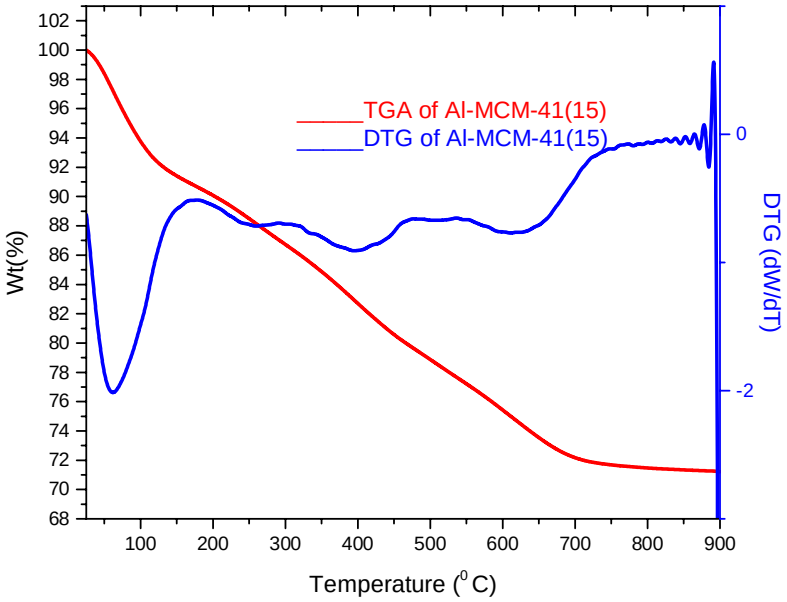

TGA/DTG profile of ifmMCM (15)1

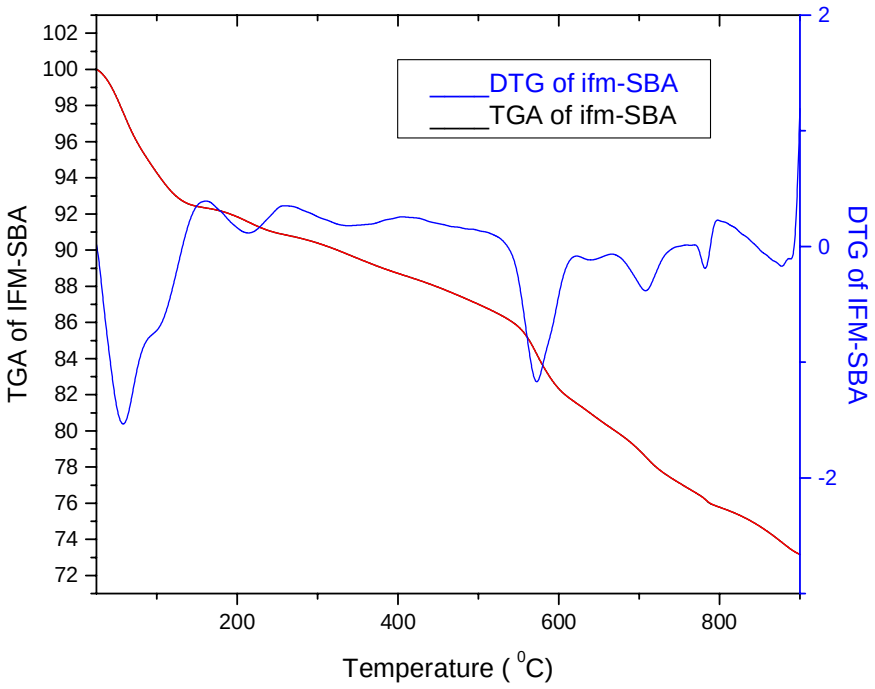

TGA/DTG Profile of ifmSBA1

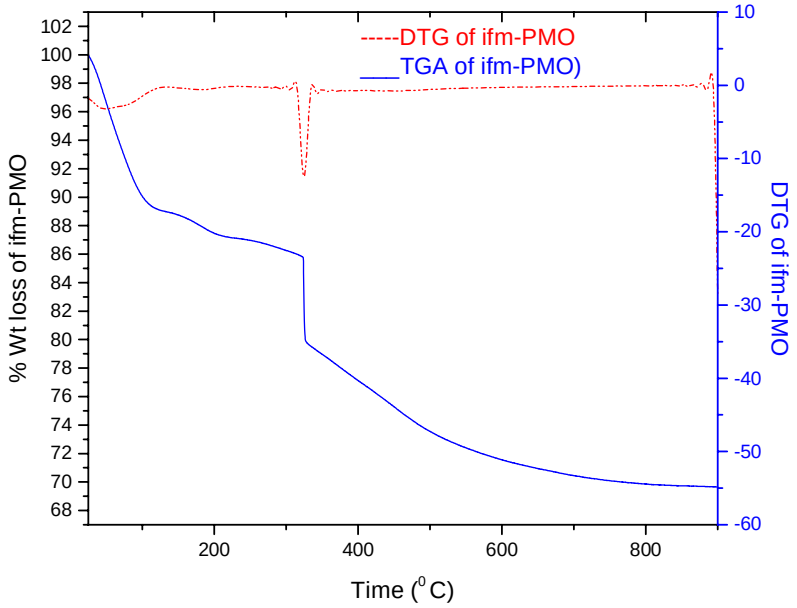

TGA/DTG Profile of ifmPMO

***Appendix 5**: Nitrogen Sorption Isotherms*

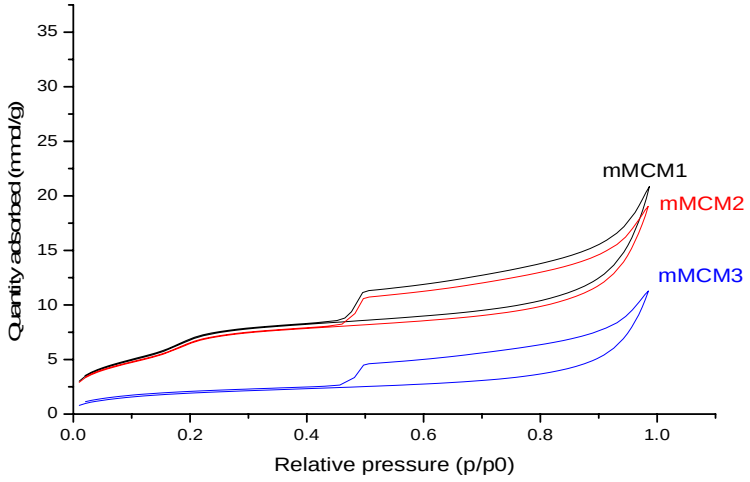

Nitrogen Sorption Isotherms of mMCM (3)1-3

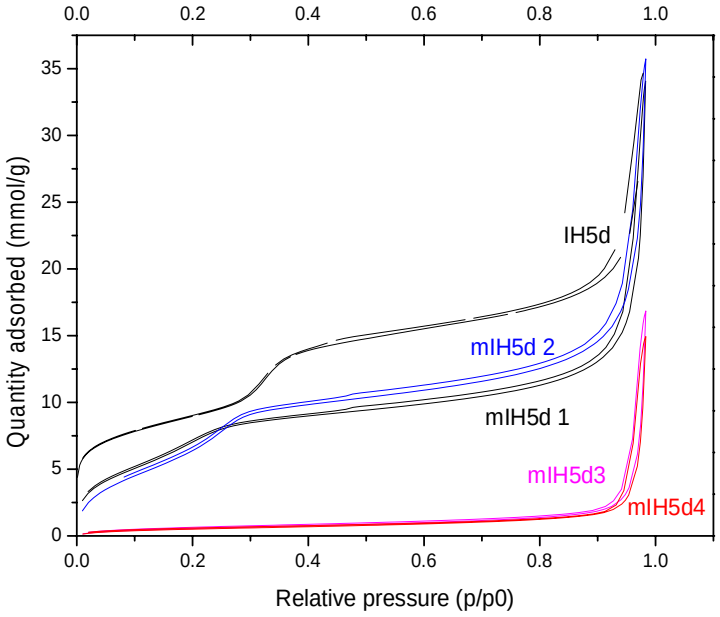

Where IH5d=MCM (15)1

Nitrogen Sorption Isotherms of mMCM (15)1-4

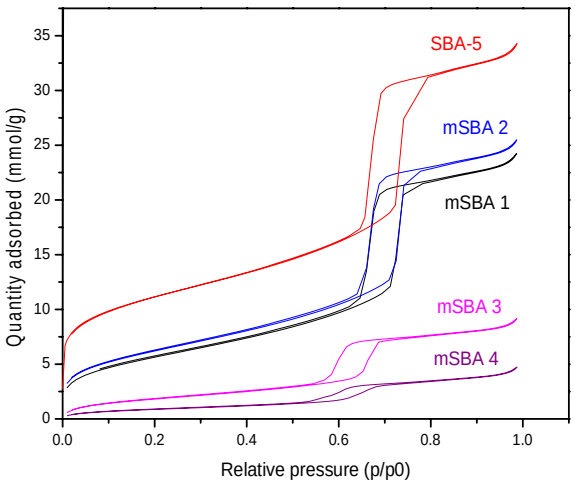

Nitrogen Sorption Isotherms of mSBA 1-4

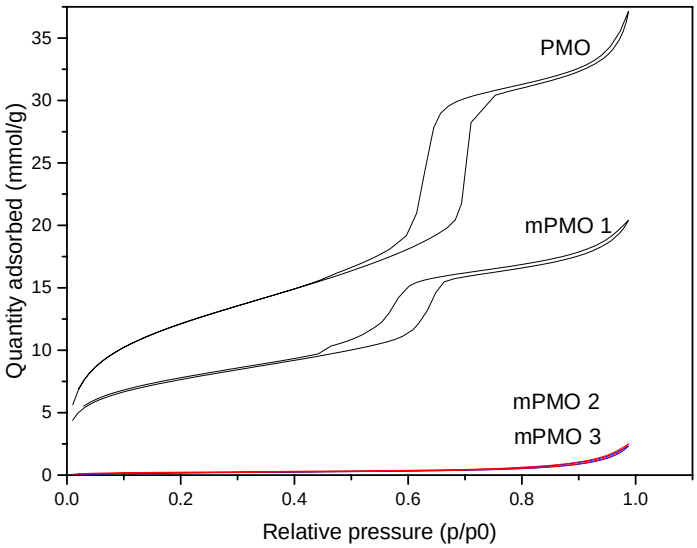

Nitrogen Sorption Isotherms of mPMO 1-3

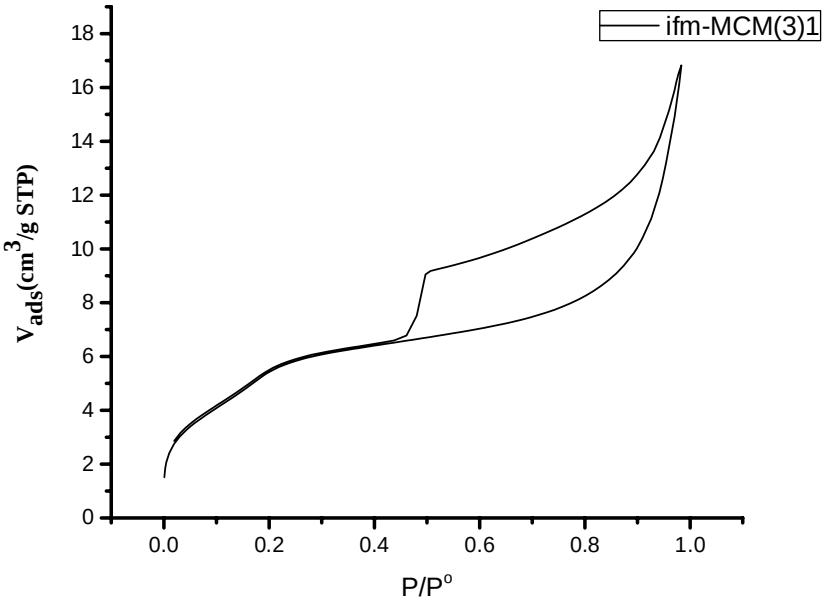

Nitrogen Sorption Isotherm of ifmMCM (3)1

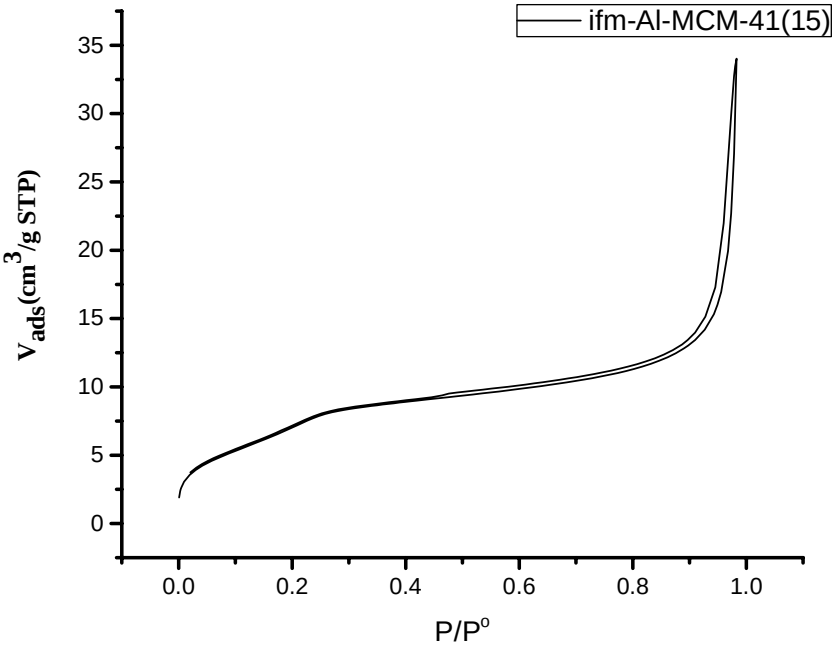

Nitrogen Sorption Isotherm of ifmMCM (15)1

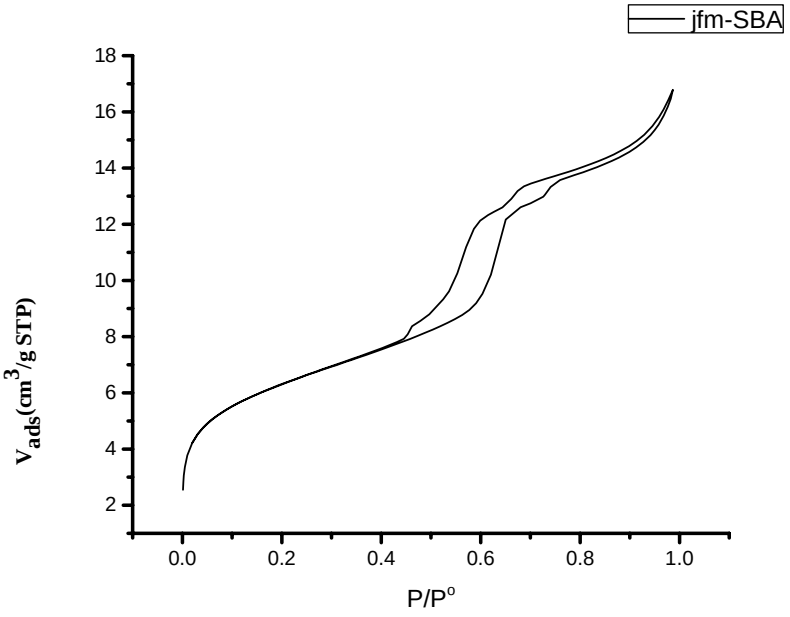

Nitrogen Sorption Isotherm of ifmSBA1

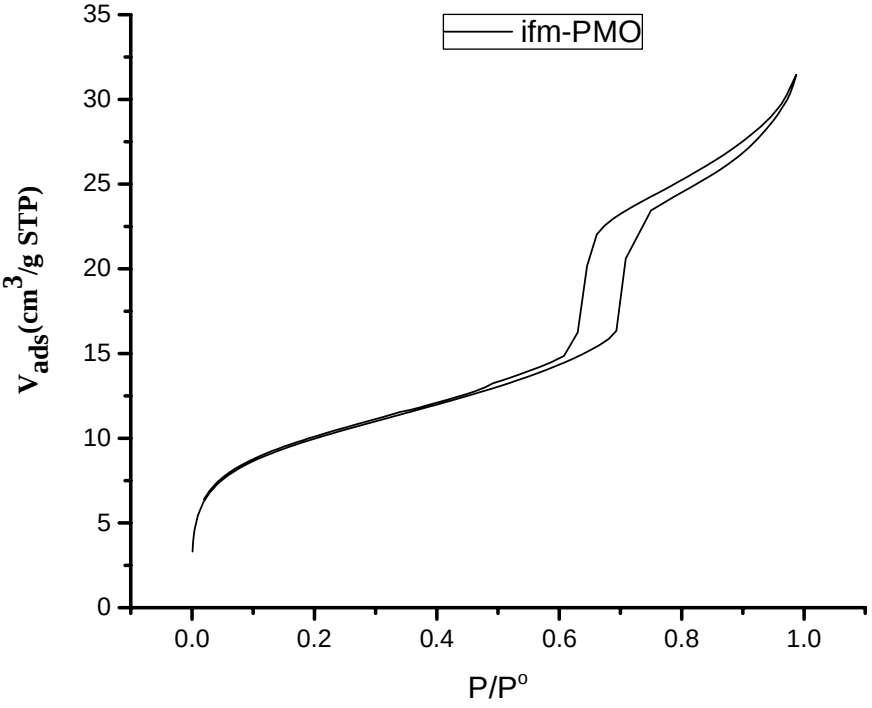

Nitrogen Sorption Isotherm of ifmPMO1